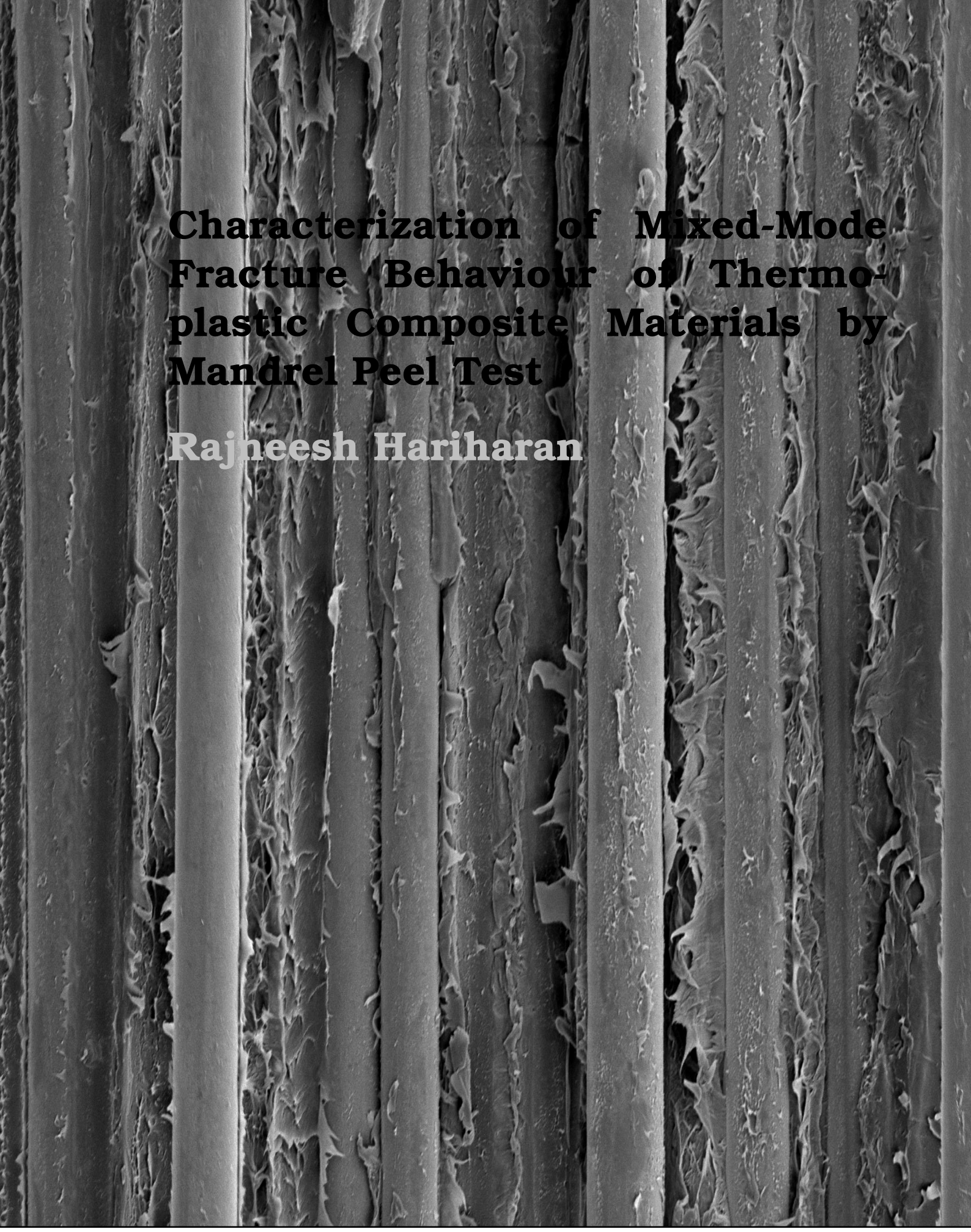


Characterization of Mixed-Mode Fracture Behaviour of Thermoplastic Composite Materials by Mandrel Peel Test

Rajneesh Hariharan

TU Delft Delft University of Technology

Materials Science and Engineering

Characterization of Mixed-Mode Fracture Behaviour of Thermoplastic Composite Materials by Mandrel Peel Test

Master of Science Thesis

For obtaining the degree of Master of Science in Materials Science and Engineering at Delft University of Technology

Rajneesh Hariharan

May 30, 2023

Faculty of Mechanical, Maritime and Materials Engineering (3mE) · Delft University of Technology

The work in this research project was supported by Brightlands Materials Center-TNO. Their cooperation is hereby gratefully acknowledged.





Copyright © Materials Science and Engineering (MSE)
All rights reserved.

Delft University of Technology
Department of Materials Science and Engineering
Materials Science and Engineering (mse)

The undersigned hereby certify that they have read and recommend to the Faculty of Mechanical, Maritime and Materials Engineering (3mE) for acceptance a thesis entitled

Characterization of Mixed-Mode Fracture Behaviour of Thermoplastic Composite Materials by Mandrel Peel Test

by

Rajneesh Hariharan

in partial fulfillment of the requirements for the degree of

Master of Science Materials Science and Engineering

Dated: May 30, 2023

Chairman and Examiner:

Dr. Marcel Hermans, TU Delft

Examiner:

Dr. Iuri B.C.M. Rocha, TU Delft

Supervisor(s):

Dr. Miguel Bessa, TU Delft

Dr. Ali Rezaei, BMC-TNO

Dr. Yibo Su, BMC-TNO

Abstract

Delamination is a significant failure mode that has been the subject of extensive research in laminated structures. The interface in assembly structures often represents the susceptibly weak link and necessitates careful consideration to guarantee structural stability. It is of utmost significance to understand the behaviour of the delamination phenomenon and precisely evaluate the fracture toughness (resistance to delamination) in composites. Numerous test techniques have been established over time, some of which have been recognized and adopted as standards. The complexity associated with the standardized tests (crack tip monitoring, design configuration) and the limitations in the scope of testing various interface configurations have led to favoring of alternative testing methods in recent years.

This thesis primarily aims at exploiting the new potentials of the Mandrel Peel Test method by incorporating the novel **"Multi-Mandrel Concept"** in determining the fracture toughness of the Thermoplastic Composites. Mandrel Peel test, a modified adaptation of the standard 90-degree peel test, presents as a promising technique for the delamination fracture testing of composites by determining the energy necessary for peeling off a flexible adherend (generally referred to as the peel-arm) from a rigid substrate. In this thesis, the objective was to further the understanding of the Mandrel Peel test, investigate the sensitivity of specimen configuration and testing parameters on different thermoplastic materials systems, and evaluate the suitability of the Mandrel Peel test method for establishing a relationship between mandrel roller size and mixed mode fracture behavior. Comparative assessments were conducted between the multi-mandrel radii peel test and standardized tests, including DCB, ENF, and MMB tests. Experimental tests, fractography studies, and numerical validation were performed on UD GF/PP and UD CF/PPS composites.

The results show that the average fracture toughness values are slightly higher and more consistent for 2-ply peel arm specimens compared to 1-ply peel arm specimens. This is attributed to the microstructure (matrix and fiber distribution) at the interface and its influence on damage mechanism and fracture propagation behavior. The thickness of the ply also affects delamination propagation behavior and depends on the microstructure, with thicker plies exhibiting non-uniform fiber and matrix distribution.

The experimental investigation reveals that the fracture toughness values increase as the mandrel radius increases for UD GF/PP and UD CF/PPS composites with a 0|0 interface. The

fracture toughness of CF/PPS peel specimens with a 0|90 interface shows limited variation with respect to the mandrel radius. The relationship between mandrel radius and fracture toughness may not follow a linear trend, and it can depend on other factors such as material thickness, interface orientation, and fracture energy at pure loading modes.

Comparative assessments between standardized tests and mandrel peel tests show similar trends in fracture toughness values with increasing mode mixture and mandrel roller radii. Fractography analysis provides valuable insights into the fracture behavior of tested materials, and a correlation is identified between the failure modes observed in mixed-mode bending (MMB) tests and mandrel peel tests. The mandrel peel test enables establishing a relatively straight crack front during the delamination propagation, controlled by the mandrel's kinematics, resulting in a more uniform distribution of strain energy across the specimen's width, unlike standard tests.

The findings suggest that utilizing the multi-mandrel concept in assessing mixed-mode fracture toughness offers the possibility of extrapolating pure mode I and II fracture toughness values. This approach presents a viable tool for characterizing the fracture energy of composites with non-zero fiber-oriented interfaces that cannot be effectively assessed using classical tests. The results support the claim that mandrel roller size influences the degree of mode-mixity and suggests considering mandrel size when assessing mode-mixity in fracture phenomena.

Overall, this study provides valuable insights into the sensitivity of specimen configuration and testing parameters, the influence of mandrel roller size on mixed-mode fracture behavior, and the potential benefits of the mandrel peel test for delamination studies. By considering these findings, further advancements can be made in understanding and characterizing fracture properties in hybrid material systems.

Keywords: Delamination, fracture toughness, mixed-mode fracture, DCB, ENF, MMB, Mandrel Peel test, thermoplastic composite, GF/PP, CF/PPS, Multi-Mandrel Concept, peel arm, mandrel roller, mode mixity

Preface

I embarked on this remarkable research journey with a profound purpose - to earn my MSc in Materials Science and Engineering. Throughout this experience, I was privileged to delve into various aspects of my field, honing my practical skills and expanding my knowledge. Among the opportunities that came my way, I had the chance to delve into the production and processing of polymer composites, conduct experimental fracture testing, explore the potential of the Mandrel Peel testing method, and immerse myself in the fascinating world of fracture surface characterization. Each step of this research has brought me closer to my academic goal and allowed me to grow both personally and professionally.

First and foremost, I express my sincere appreciation to my supervisors, Dr. Miguel Bessa at the University, Dr. Ali Rezaei, and Dr. Yibo Su at the company where I conducted a significant portion of my research, for their invaluable guidance, wisdom, and continuous encouragement throughout the entire process of this thesis. Their expertise and insights have been instrumental in shaping the direction and quality of this research. They have been very supportive and considerate of my personal circumstances during the research phase.

Additionally, I extend my heartfelt thanks to Jos Linsen and Rick Leuven at the Brightlands Materials Center and Victor Horbowiec, Dave Ruijtenbeek, Alexander Uithol, and Durga Mainali Sharma at the DSAML- TU Delft who generously shared their expertise and assisted me in various testing aspects.

I am also profoundly grateful to Manoj G Reddy, whose unwavering support and guidance in the numerical validation of this work were invaluable. The insights and discussions during the research phase with Manoj greatly enhanced the accuracy and robustness of the results presented in this thesis.

A special thanks to Luc Koote (Ph.D. student); his willingness to clarify technical aspects and engage in fruitful discussions contributed to the overall quality of this work.

I am indebted to Evert Vixseboxse, my study advisor throughout my study period at the 3mE, who has constantly supported and motivated me and listened to all my problems during my most challenging and tough times. Reaching this stage would have been exceedingly difficult without his guidance and motivation.

To my friends at the university, who have become my extended family, I express my heartfelt gratitude. Their positive talks, support, encouragement, and engaging discussions have maintained my enthusiasm and pushed me forward during this journey.

I want to thank my parents, extended family, and friends, whose unwavering support and understanding have sustained me during moments of doubt and exhaustion. Their presence in my life has been a constant source of motivation and encouragement, and I am forever grateful for their love and belief in my abilities.

Delft University of Technology **Rajneesh Hariharan**

Table of Contents

Preface **IX**

1 Introduction **1**
1.1 Motivation for Research 3
1.2 Thesis Objective 4
1.3 Report Structure 4

2 Literature Review **7**
2.1 Delamination 7
2.2 Fracture Mechanisms 7
2.3 Fracture Modes 8
2.4 Damage Mechanisms 9
2.4.1 Damage Zone and Matrix Cracking (Damage Initiation) 9
2.4.2 Damage Propagation 11
2.5 Fracture Mechanics Approach 15
2.6 Interlaminar Fracture Toughness Testing 16
2.6.1 Mode I Fracture Testing 17
2.6.2 Mode II Fracture Testing 17
2.6.3 Mixed Mode I/II Fracture Testing 21
2.6.4 Bi-Material Interface Problems 23
2.7 Peeling Techniques 28
2.7.1 90 and 180 degrees Peel Tests 28
2.7.2 Climbing Drum Peel (CDP) Test 29
2.7.3 Horizontal Drum Peel (HDP) Test 30
2.7.4 Double Drum Peel (DDP) Test 32
2.7.5 Mandrel Peel (MP) Test 33

2.8 Influence of Specimen Geometry and Testing Conditions 35
2.8.1 MP Specimen Interface Configuration 36
2.8.2 MP Specimen Width 39
2.8.3 MP Specimen Thickness 40
2.8.4 Mandrel Roller 42
2.8.5 Crosshead Displacement Rate (Peeling Rate) 44
2.8.6 Alignment Force 45
2.8.7 Friction 46
2.8.8 Mode of Failure 47
2.9 Mixed Mode Propagation Failure Criteria 48
2.10 Mixed Mode Partitioning 49
2.11 Numerical Modelling Approaches 50
2.11.1 Virtual Crack Closure Technique (VCCT) 50
2.11.2 Cohesive Zone Modeling (CZM) 51
2.12 Summary 54

3 Research Framework 57
3.1 Research Objective and Questions 57
3.2 Research Approach and Strategy 58

4 Methodology 61
4.1 Materials 61
4.2 DCB, ENF, and MMB Specimen Design Specifications 61
4.3 Mandrel Peel Test Specimen Considerations 62
4.4 Experimental Test Plan 66
4.5 Manufacturing Process 67
4.6 Specimen Preparation 68
4.7 Experimental Test Set-up and Procedure 70
4.7.1 Double Cantilever Beam Test 70
4.7.2 End-Notched Flexure Test 71
4.7.3 Mixed-Mode Bending Test 72
4.7.4 Mandrel Peel Test 74

5 Data Processing Procedures 77
5.1 Modified Beam Theory (DCB) 77
5.2 Compliance Calibration Method (ENF) 78
5.3 Corrected Beam Theory (MMB) 79
5.4 Energy Balance Approach (MP) 80

6 Experimental Results and Discussions (DCB, ENF, & MMB) 82
6.1 Double Cantilever Beam Tests 82
6.2 End - Notched Flexure Tests 87
6.3 Mixed - Mode Bending Tests 93
6.4 Fractography Studies 97
6.5 Effects of Processing Conditions 101
6.6 Failure Criteria 105

7 Mandrel Peel Tests 108
7.1 Experimental Results 108
7.2 Discussion 112
7.2.1 Effect of Peel-arm Thickness and Mandrel Roller Radius 113
7.2.2 Applicability to 0|90 (Cross-ply) Interface 118
7.2.3 Mode of Failure 121
7.3 Analysis of Fracture Toughness 122
7.4 Comparative Assessment 125
7.4.1 Crack Front 127
7.4.2 Failure Mode 128

8 Numerical Validation 131

9 Conclusions and Recommendations 135

References 138

List of Figures

1.1 Failure mechanisms in composites (left) **[1]** and Composite failure (center) and delamination at the composite-metal interface (right) in Fiber metal laminate(FML) **[2]**. 1

1.2 Various sources of interlaminar fracture **[3]**. 2

2.1 Failure mechanisms in composites (Broad classification -left) **[4]** and detailed ply level fracture mechanisms (right) **[5]**. 8

2.2 Modes of fracture **[6]**. 9

2.3 Illustration of crack growth at (left) $\theta|0$ and (right) $0|0$ ply interfaces showing the crack branching and migration mechanism **[7]**. 10

2.4 Crack tip and the debonding above and below across the interface**[8]**. 11

2.5 Different crack propagation behaviour and the force-displacement response **[9]**. 12

2.6 Effect of plastic damage zone formation and the presence of matrix at the interface on the crack growth behaviour**[10]**. 13

2.7 Illustration of fiber nesting at the interface in 0^o UD composites (left) and Damage zone promoting multiple cracks and triggering fiber bridging (right) **[11]**. 14

2.8 Fiber bridging observed in mode I (left) **[8]** and mode II (right) **[12]**. 15

2.9 Schematic of the standardized DCB Specimen for determining the quasi-static mode I interlaminar fracture toughness. In this schematic, load application is achieved using piano hinges; alternatively, load blocks can also be used **[13]**. 17

2.10 End Notched Flexure (ENF) test **[14]**(left) and End Loaded Split (ELS) test (right)**[15]** 18

2.11 Stabilised End Notched Flexture (SENF) test **[16]**. 19

2.12 Over notched flexure (ONF) test- (left) and Four point bend ENF (4ENF) test - (right) **[14]**. 19

2.13 Schematic of the CENS testing fixture **[17][18]**. 20

2.14 Schematic representation of the force-displacement response of various mode-II testing (left) **[19]** and Frictional resistance as a function of crack propagation at constant friction coefficient for different test methods (right) **[14]**. 21

2.15 Schematic of the mixed mode bending (MMB) configuration for Mixed mode I/II fracture testing **[20]**. 22

2.16 Fixed ratio mixed mode (FRMM) test configuration **[21]**. 22

2.17 Illustration of the single-leg bending (SLB) test **[22]**. 23

2.18 Propagation of crack in a DCB specimen with an adhesive layer showing the crack front curvature and the neglected area **[23]**. 24

2.19 Various specimen configurations for generating different mode mixtures**[24]**. 27

2.20 Schematic illustration of a typical peel test (F - applied force, w - width, θ - peeling angle)**[25].** 28

2.21 Representation of a 90° and 180°peel tests **[25]**. 29

2.22 Schematic illustration of the Climbing Drum Peel test set up: (A) front view, (B) side view, (1) rigid adherend, (2) flexible adherend, (3) drum, (4) loading straps, Fp—externally applied force **[26].** 29

2.23 Schematic illustration of the HDP test (a) and (b) CDP test **[27]**. 31

2.24 DDP test concept (left), and DDP experimental set-up (right) **[28]** . 32

2.25 Schematic illustration of the mandrel peel test set-up **[15]**. 33

2.26 Two distinct fracture behaviors: delamination growth along the interface (interfacial failure) and, in another case, fiber pull-out from the substrate; these behaviors relate to two different processing conditions**[29]**. 38

2.27 Fracture toughness values for different CF/PEEK woven samples (Width and Peeling rate)(left) **[30]**, and Fracture toughness values for UD CF/PEEK values (right) **[31]** . 40

2.28 Adhesive fracture toughness values for different peel-arm thickness (left) **[32]**, and Increasing plastic bending energy with the thickness (right) **[33]**. 41

2.29 Effect of peel-arm thickness on the propagation fracture toughness **[31]**. 41

2.30 Table showing the reducing plastic bending energy (G_p) with increasing mandrel size **[33]**. 43

2.31 Stick-slip behaviour**[34]**. 43

2.32 Schematic representing the peel-arm contact with the mandrel. 44

2.33 Overview of the mean spacings between peaks for the different samples tested at different peeling rates **[30]**. 45

2.34 Schematic representing the conformance (left) and non-conformance (right) as a function of alignment load **[35]**. 45

2.35 Effect of alignment force on the fracture toughness **[31]**. 46

2.36 (a) The ratio of μF_p to F_p - F_a as different value of μ. (b) The fracture toughness as the different measurement value of μ**[35]**. 47

2.37 Fracture surface exhibiting mode I (left), mode II (center) features and MP specimen (right) showing features similar to mode I **[36]**. 48

2.38 Representation of VCCT **[37]**. 51

2.39 Bi-linear constitutive law for the mixed mode loading condition **[38]**. 52

3.1 Flowchart of the approach and strategy employed in this research. 59

4.1 Illustration of the DCB, ENF and MMB specimen geometry. 62
4.2 Illustration of the mandrel peel specimen configuration. 63
4.3 Illustration of the Bending strain vs. mandrel radius for different peel arm thicknesses. Solid circles indicate the corresponding critical mandrel radius. 64
4.4 Relation between the mandrel radius and the peel arm length requirements. 64
4.5 Geometric specification of the mandrel peel specimen. 65
4.6 Pressure-Temperature cycle for the consolidation process 68
4.7 Schematic view of the layup of the laminate, detailing the cut for the DCB, ENF, and MMB specimens 69
4.8 Schematic view of the layup of the laminates, detailing the cut for the Mandrel Peel specimens. 69
4.9 Illustration of the DCB test configuration showing a specimen attached to a combination of loading tabs. 70
4.10 ENF test setup and configuration for compliance calibration and NPC fracture test. 71
4.11 MMB test setup with high-resolution camera and crack monitoring system. 72
4.12 MMB test configuration for different mode mixtures (CF/PPS). 73
4.13 Mandrel Peel Test setup at the BMC facility. 74
4.14 Illustration of the alignment load optimization procedure to achieve conformity. 75

6.1 Characteristic force-displacement plots for UD GF/PP and UD CF/PPS DCB specimen. 83
6.2 Mode I interlaminar fracture toughness 83
6.3 Mode I fracture toughness as a function of crack length (R-curve) of UD GF/PP specimens. Increasing resistance due to large scale bridging. 84
6.4 Mode I fracture toughness as a function of crack length (R-curve) of UD CF/PPS specimens. Converges to a steady state propagation around crack length 50 mm. 84
6.5 Image shows the crack path of the GF/PP specimen with the resin-rich region and broken fiber. 85
6.6 Fiber bridging observed in the CF/PPS specimen. 86
6.7 Side-views of the GF/PP specimens displaying fiber bridging density with crack propagation. 86
6.8 Typical ENF Force vs. Displacement plot of UD GF/PP specimens 87
6.9 Typical ENF Force vs. Displacement plot UD CF/PPS specimens 88
6.10 Fracture process zone near the crack tip exhibiting matrix microcracking (insert film) - GF/PP (x500) 89
6.11 Typical ENF Force vs. Displacement plots for different specimen geometries - GF/PP 89
6.12 Condition of the crack tip near the starter film region and the corresponding fracture surface. 90
6.13 Indication of the force drop magnitude and the corresponding crack growth for the ENF specimens. 91
6.14 Macroscopic images of the ENF test of GF/PP composite 92
6.15 Macroscopic images of the ENF test of CF/PPS composite 92
6.16 Mode II Interlaminar fracture toughness of the two composite systems (NPC) 93

6.17 Typical MMB Force vs. Displacement plots for GF/PP specimens at various mode mixtures 94
6.18 Typical MMB Force vs. Displacement plots for CF/PPS specimens at various mode mixtures. 95
6.19 Side-view of the GF/PP specimens displaying fiber bridging during MMB experiments. 95
6.20 Mixed-mode interlaminar fracture toughness of the UD GF/PP and UD CF/PPS composites. 96
6.21 Fracture surface of mode I UD GF/PP and UD CF/PPS specimens indicating the tortuous path with fiber bundles and broken fibers. 97
6.22 SEM micrographs of Mode I delaminated fracture surfaces of GF/PP. 98
6.23 SEM micrographs of Mode I delaminated fracture surfaces of CF/PPS. 99
6.24 SEM micrographs of Mode II delaminated fracture surfaces. 99
6.25 Fracture surface of the UD GF/PP ENF specimen indicating the fiber domination in the upper and fiber imprints in the lower arm, respectively. 100
6.26 SEM micrographs of delaminated fracture surface of GF/PP in various mode mixtures. 101
6.27 SEM micrographs of delaminated fracture surface of CF/PPS in various mode mixtures. 102
6.28 Correlation of Interlaminar fracture toughness of GF/PP and the degree of crystallinity **[39][40][41][42][43][44, 45]**. 103
6.29 Correlation of Interlaminar fracture toughness of CF/PPS and the degree of crystallinity **[46][47][48][10][36]**. 104
6.30 Fracture toughness as a function of different mixed mode ratios establishing the B-K delamination failure criterion for GF/PP and CF/PPS. 106
6.31 Mode II vs. Mode I (components of the various mixed mode ratios) and the Power Law curve fit for delamination behavior prediction. 107

7.1 Peel force-displacement plots of 1-ply UD GF/PP peel specimens with 0|0 interface for various mandrel radii. 109
7.2 Peel force-displacement plots of 1-ply UD CF/PPS peel specimens with 0|0 interface for various mandrel radii. 110
7.3 Peel force-displacement plots of 2-ply UD GF/PP peel specimens with 0|0 interface for various mandrel radii. 111
7.4 Peel force-displacement plots of 2-ply UD CF/PPS peel specimens with 0|0 interface for various mandrel radii. 112
7.5 Peel force-displacement plots of 1-ply UD GF/PP peel specimens with 0|90 interface for various mandrel radii. 112
7.6 Peel force-displacement plots of 1-ply UD CF/PPS peel specimens with 0|90 interface for various mandrel radii. 113
7.7 Fracture surface of the UD GF/PP 1-ply peel arm and substrate indicating fibers of the peel arm adhering to the substrate. 114
7.8 Peel force-displacement plots of 1-ply UD GF/PP and UD CF/PPS peel specimens with 0|0 interface showing gradually increasing peel force for tests with R10. 116
7.9 Crack propagation behavior of 1-ply UD GF/PP and UD CF/PPS peel specimens with 0|0 interface showing bundled fibers peeled and pulled increasing peel force for tests with small mandrel radius. 116

7.10 Crack propagation behavior of 1-ply UD GF/PP peel specimens with 0|0 interface showing fiber peeling and breakage resulting in a relatively stable behavior for R50 and R75. 117
7.11 Peeling behavior of 1-ply GF/PP specimens with 0|90 interface with different mandrel roller. 118
7.12 Fracture surface of the peel arm and substrate of the GF/PP specimen with a 0|90 interface, showing the fibers adhering on the peel arm (left), SEM image of the substrate exhibiting the corresponding region (right). 119
7.13 Schematic illustration of the crack propagation path in 0|90 GF/PP peel specimens indicating both interlaminar and intralaminar failure. 120
7.14 Fracture surface of the peel arm and substrate of the CF/PPS specimen with a 0|90 interface, showing no migration or fiber bridging trace. 120
7.15 Schematic illustration of the crack propagation path in 0|90 CF/PPS peel specimens. 121
7.16 SEM micrographs of the delaminated fracture surface of UD GF/PP in various mandrel radii. 122
7.17 SEM micrographs of the delaminated fracture surface of UD CF/PPS in various mandrel radii. 122
7.18 Propagation fracture toughness of 1 and 2-ply peel specimens as a function of various mandrel radii for UD GF/PP and UD CF/PPS composites. 124
7.19 Propagation fracture toughness of GF/PP and CF/PPS peel specimens with 0|90 interface as a function of various mandrel radii. 124
7.20 Critical failure envelope comparison for the GF/PP material system based on various testing methods. 126
7.21 Critical failure envelope comparison for the CF/PPS material system based on various testing methods. 126
7.22 Propagation of crack in CF/PPS ENF specimen showing the crack front curvature. 127
7.23 Propagation of crack in GF/PP mandrel peel specimens showing relatively straight crack front. 128
7.24 Micrography images of the fracture surface of DCB, MMB, ENF specimens, and the MP specimens of UD GF/PP composite. 129
7.25 Micrography images of the fracture surface of DCB, MMB, ENF specimens, and the MP specimens of UD CF/PPS composite. 129

8.1 FE model (2D) of the Mandrel Peel test configuration with boundary conditions. 131
8.2 Numerically simulated fracture toughness for various mandrel radius compared with the experimental results of the UD GF/PP composite. B-K criterion (left) and Power Law criterion (right). 132
8.3 Numerically simulated fracture toughness for various mandrel radius compared with the experimental results of the UD CF/PPS composite. B-K criterion (left) and Power Law criterion (right). 132
8.4 Simulated fracture toughness represented as Mode II vs. Mode I for UD GF/PP peel tests indicating the mode mixity: B-K criterion (left) and Power Law criterion (right). 133
8.5 Simulated fracture toughness represented as Mode II vs. Mode I for UD CF/PPS peel tests indicating the mode mixity: B-K criterion (left) and Power Law criterion (right). 133

List of Tables

2.1 Summary of the mandrel peel tests in the literature used for determining the fracture toughness. 39

4.1 Material properties at Room temperature 61

4.2 Experimental test matrix for the DCB, ENF, and MMB tests. 67

4.3 Experimental test matrix for the Mandrel Peel tests. 67

4.4 Loading arm length for different mode mixtures for UD GF/PP and UD CF/PPS specimens. 73

6.1 Values of the peak forces (P_{max}) recorded during the mode II ENF tests of UD GF/PP and UD CF/PPS. 90

6.2 Mode II Interlaminar fracture toughness, G_{IIc} data 93

6.3 Summary of the experimental values of the mixed mode fracture energies from MMB tests. 96

6.4 Experimentally determined Interlaminar fracture toughness of UD GF/PP and UD CF/PPS composite laminates. The average initiation fracture toughness values are presented. 106

Chapter 1

Introduction

Composite materials have been extensively employed in the aerospace sector for many years. Their utilization has been rapidly expanding across industries for various applications in recent times as they offer several benefits, including lightweight, high strength and stiffness to weight ratio, exceptional resistance to erosion, and flexibility in design.

Fiber-reinforced polymer composites (FRPCs), especially, are attractive for both secondary and load-carrying structural applications. The hybridization of composites, particularly the bonding of composites to composites and fiber-reinforced polymer composites with metals, is also increasingly common and gaining attention, as it allows for optimal maximized utilization of their respective material characteristics and reduces their drawbacks. Given the criticality of these layered structures' functionality, as they play a crucial role, it is vital to comprehend and anticipate their load-carrying capability and failure mechanisms for better design.

Composites may experience functional failure due to various dominant failure mechanisms, including but not limited to fiber breakage, matrix cracking, fiber peel-off, delamination, and transverse cracking, which depends on the stacking sequence, ply orientation, intrinsic material properties, and loading conditions. In layered material systems such as laminated composites and bonded joints (composite-composite, metal-composite), delamination is the prominent failure mechanism (Figure 1.1).

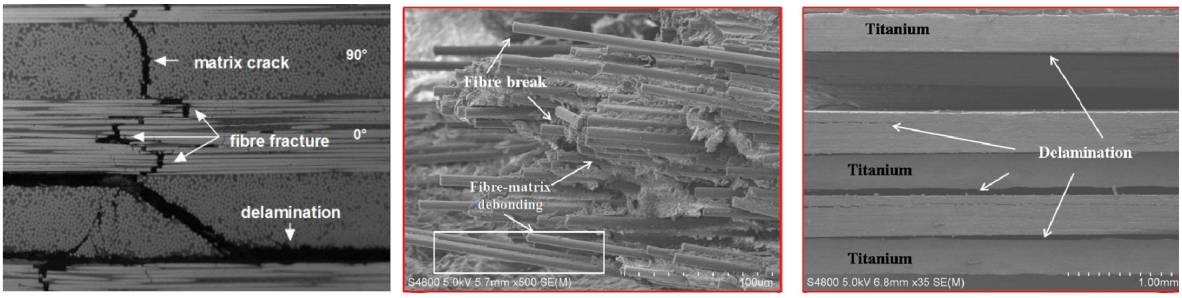


Figure 1.1: Failure mechanisms in composites (left) **[1]** and Composite failure (center) and delamination at the composite-metal interface (right) in Fiber metal laminate(FML) **[2]**.

Typically, delamination is referred to as the interfacial failure/damage between two adjoining layers as a result of loss of adhesion, eventually causing debonding of layers and stiffness and strength reduction. The delamination phenomenon within a composite laminate can arise due to various reasons. The formation of a crack(s) between the adjacent layers, or delamination as it is known, represents a significant fracture mechanism in composite laminates that can manifest at various stages during the structure's lifespan. Such stages may include the manufacturing, transportation, mounting, and in-service operational phases (Figure 1.2).

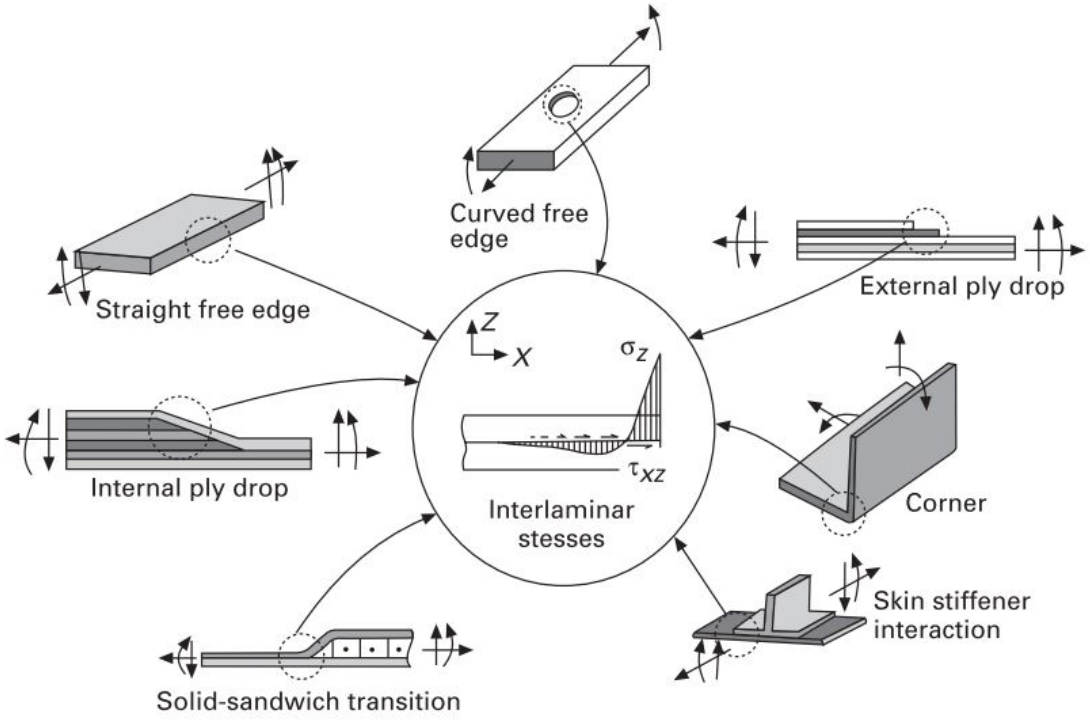


Figure 1.2: Various sources of interlaminar fracture **[3]**.

The initial classification relates to delamination occurrences that arise from curved geometries, for example, those found in curved regions, tubular sections, cylindrical and spherical structures, and pressurized containers/vessels. In each scenario, the stresses normal to the interface between two adjoining layers may cause adhesion loss/de-bonding and the onset of interlaminar cracking. The second categorization involves sharp sectional discontinuities of structure, for instance, ply drop-offs, free edges, stiffeners- plates connection, sandwich structures, and adhesively bonded and mechanically fastened joints. Apart from this, another classification associated with the influence of temperature and moisture must also be considered. The dissimilar thermal coefficients of the matrix and reinforcement cause contractions across the plies/layers during the curing/consolidation phase, potentially leading to residual stress development that can trigger delamination[49]. Likewise, the uneven expansion of plies during moisture absorption could also contribute to delamination.

Delamination may prevalently occur during the manufacturing process, attributing to various reasons including but not limited to matrix shrinkage, localized formation of regions with an excess of resin due to poor ply-placement (or hand layup) or prepreg quality, foreign bodies,

and other related factors. Furthermore, impact events represent another significant source of delamination in laminated structures. The crack may initiate due to the damage generated internally at the interface as a result of an impact during the fabrication, repairing activities, bird strikes (aircraft and wind turbine blades)[50], collisions. Following the delamination onset or the delamination initiation, the crack will propagate, drastically reducing the load-bearing capacity of the structure and its stability.

1.1 Motivation for Research

It is of utmost significance to understand the behaviour of the delamination phenomenon and precisely evaluate the fracture toughness (resistance to delamination) in composites to better the structural performance. To accurately model delamination, it is essential to incorporate the critical strain energy release rates (G_c) corresponding to various crack propagation modes. These (G_c) values are crucial input parameters for most delamination models. Generally, the fracture toughness is presumed to be purely dependent on the material system and must be evaluated experimentally. The experimental exploration of interlaminar fracture has been a subject of investigation for several years. Consequently, numerous test techniques have been established over time, some of which have been recognized and adopted as standards officially by diverse standardization committees.

The fracture toughness thus can be obtained by complying with standard test procedures, and the existing standards for assessing the delamination behavior of composites primarily focus on determining the fracture energy, (G_c), under conditions of pure-modes or mixed-mode loading. The pure mode I, mode II, and mixed-mode I/II fracture toughness can be determined through the standardized ASTM D5528/D5528M [51], ASTM D7905/D7905M [52] and, ASTM D6671/D6671M [53], respectively. However, the standards established so far are primarily intended for unidirectionally fiber-reinforced polymer matrix composites and these standards impose certain limitations on the testing specimen geometry and configuration. Additionally, the loading must exhibit symmetric or antisymmetric characteristics to isolate the contributions of mode I and mode II. As a result of these constraints, a variety of potentially intriguing interface configurations cannot be effectively tested using the current standards, thus limiting the scope.

The Double Cantilever Beam (DCB) test is utilized for mode I, while the End-Notched Flexure and Mixed-Mode Bending (MMB) tests are for mode II and mixed mode I/II. These tests necessitate for symmetric interface for crack propagation, and the global stiffness of the specimen arm plays a significant role. Nonetheless, from a fracture point of view, the developed DCB, ENF, and tests fail to successfully assess the performance of non-symmetric (0°- θ°, specimen arm thickness) interface and hybrid interface (such as metal-polymer laminate). It presents challenges such as but not limited to non-uniform strain energy distribution, crack front curvature, residual thermal stresses, and delamination migration when employed to determine the interlaminar fracture toughness of various other specimen stacking (interface and global) configurations (Section 2.6.4).

Despite following several guidelines by designing and modeling at the ply level to design the optimal layup configuration to minimize the issues and effectively utilize the standard delamination test, undesired effects are still observed and remain unsolved. It should be noted that

the critical energy release rate formulations (DCB, ENF, and MMB tests) often fail to consider certain pertinent factors, leading to an overestimation of the fracture toughness value. Moreover, to conduct standard tests, it is essential to maintain constant knowledge of the crack tip position and length throughout the experiment. Despite its importance, actively monitoring and determining the precise position of the crack tip during testing can prove challenging. Alternative testing methods that do not require such extensively rigorous procedures in the design of stacking sequences, specimen geometry, and crack extension measurements have been favored in recent studies.

The peel tests have been more interesting in recent years for several reasons. Peel tests are a well-established technique for determining the energy necessary for peeling off a flexible adherend (generally referred to as the peel-arm) from a rigid substrate (Figure **2.20**). The peel test is most often used to characterize the fracture toughness and the mixed-mode behavior. They are of more interest as they accommodate the variations and demonstrate the ability to assess the performance successfully. Among the various peel tests developed and proposed, the literature indicates the promising potential of the mandrel peel test as a testing method for determining the interlaminar/interfacial properties of various interesting configurations employed in real-engineering structures. The mandrel peel test, a roller-assisted modified version of the 90^{o} peel, offers many advantages, is of more interest, and is gaining attention because of its various advantages (Section **2.7.5**).

1.2 Thesis Objective

This thesis majorly aims at exploiting the new potentials of the Mandrel Peel Test method by incorporating the novel **"Multi-Mandrel Concept"** in determining the fracture toughness of the Thermoplastic Composites. The objective is to further the understanding of the Mandrel Peel test, explore the influence of specimen configuration and testing parameters on various thermoplastic materials, and evaluate the applicability of this test for establishing a correlation between mandrel roller size and mixed-mode fracture behavior. The study is structured into distinct phases, each contributing to the investigation. The initial phase involves a comprehensive examination of the critical factors associated with the mandrel peel test. In the subsequent phase, mandrel peel experiments are performed on different thermoplastic composite systems, based on the preliminary knowledge acquired, to analyze the sensitivity of crucial parameters. Furthermore, standardized tests for the same material systems are conducted in the third phase, enabling a comparative assessment with the mandrel peel test. Fractography-based studies and a numerical finite element analysis (FEA) approach are employed to qualitatively comprehend the mixed-mode fracture behavior and quantitatively evaluate the mode components of the energy release rate in the mandrel peel tests. By combining experimental and numerical techniques, this study aims to comprehensively understand the mandrel peel test and its relationship to fracture toughness for various material systems.

1.3 Report Structure

The report is structured into chapters, each addressing specific aspects of the research topic. Starting with the literature review (Chapter **2**) provides a comprehensive overview of the

existing knowledge and research in the field. Following the literature review, the research framework (Chapter 3) is presented, outlining the conceptual framework and theoretical basis for the study. Chapter 4, Methodology, describes the materials, specimen design specifications, and considerations for the experimental tests. It also covers the manufacturing process and specimen preparation, along with the experimental test setup and procedures. Chapter 5 explains the different methods used for processing the collected experimental data. Next, the experimental results and discussions for the standardized double cantilever beam (DCB), end-notched flexure (ENF), and mixed-mode bending (MMB) tests are presented (Chapter 6). Chapter 7 focuses on the Mandrel Peel Tests, including the experimental results, discussion, comparative assessment, and fracture toughness analysis. The subsequent chapters include numerical validation (Chapter 8) to assess the accuracy and reliability of the experimental findings, and finally, conclusions and recommendations (Chapter 9) based on the findings of the study.

Chapter 2

Literature Review

This literature review provides a comprehensive overview of the studies conducted on interface crack problems to gain a deeper understanding of delamination behavior, specifically focusing on the fundamentals of fracture mechanics and the implementation of fracture mechanics approaches in delamination characterization and analysis. Various aspects of the delamination, including damage initiation and damage propagation, fracture modes, and micro-mechanistic damage mechanisms prevalent under varying loading conditions, are discussed. From an experiment standpoint, overview and analysis of the existing standard tests that are commonly employed in research and industry for interlaminar fracture toughness determination under static loading conditions and also the applicability of various peel testing techniques (as well as newly proposed concepts), particularly the potential **mandrel peel test** that is gaining more attention in the recent years. A more fundamental analysis of the two prominent numerical simulation modeling approaches for delamination, namely the virtual crack closure technique (VCCT) and the cohesive zone model (CZM), is presented on a broader level. The study describes the implementation methodology of both methods with their respective strengths and limitations.

2.1 Delamination

This section provides a comprehensive overview of fundamental aspects related to composite delamination. Specifically, it aims to examine the underlying principles of delamination mechanics and the initiation and progression of interlaminar cracks under static loading conditions. Additionally, this review addresses the synergy between delamination and other micromechanisms in composite laminates. With this, a deeper comprehension of the phenomenon can be attained.

2.2 Fracture Mechanisms

Within a layered composite laminate, the damage creation/initiation (thus, the fracture toughness) and propagation will be influenced by the stacking configuration of plies/lay-

ers under specific loading conditions, as will be discussed further (Section 2.3). Inevitably, the failure of the composite will be dictated by either one or a synergistic combination of the failure mechanisms at the ply level. Laminated composites display various modes of failure, which can be broadly classified into three distinct categories: interlaminar (delamination), intralaminar, and translaminar fracture (Figure 2.1).

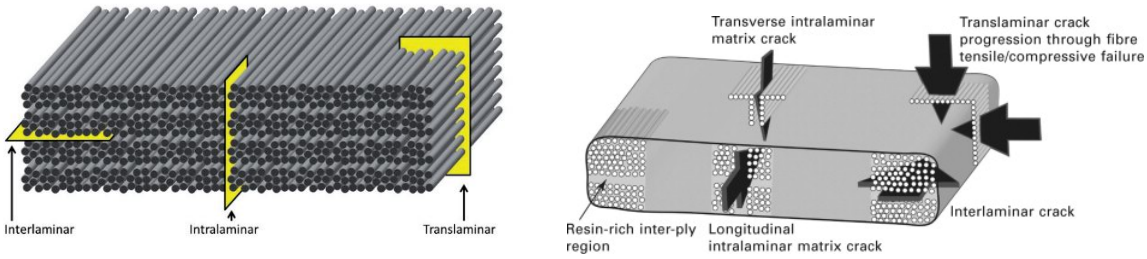


Figure 2.1: Failure mechanisms in composites (Broad classification -left) **[4]** and detailed ply level fracture mechanisms (right) **[5]**.

Interlaminar Fracture

Interlaminar fracture, also commonly known as delamination, is a phenomenon that involves the separation of two adjacent layers of laminated material. A high interfacial strength between fiber and matrix, coupled with a relatively low toughness of the matrix, yields a cohesive mode of interlaminar fracture. The parallel alignment of fibers along the direction of crack propagation impedes the migration of cracks to the adjacent neighboring layers, thus ensuring the maintenance of fiber-matrix bonding. Conversely, a weak fiber/matrix interface promotes crack propagation at the interface of fiber/matrix, leading to partial or complete detachment of fibers from the matrix.

Intralaminar Fracture

In instances where the interfacial properties between the fiber and matrix are very poor, the debonding of the fiber/matrix will exhibit severe behavior, leading to the migration of fracture into the neighboring layer. This occurrence causes the crack front to become (partially) intralaminar. Large-scale fiber bridging is a characteristic feature of longitudinal intralaminar fracture. Also, the growth of matrix cracks can occur perpendicular to the plane of the plies, i.e., through the laminate thickness, instead of propagating between the layers [5].

Translaminar Fracture

Another category of fracture is a translaminar fracture. Composite laminates are typically designed to maximize the concentration of fibers in the directions experiencing the highest stress levels. This failure mode is associated with the propagation of a through-the-thickness crack which inevitably requires the rupture of fibers, either tensile or compressive. To cause a translaminar fracture, the fiber/matrix interface must exhibit exceptional strength, in addition to the matrix's strength relative to that of the fiber [54].

2.3 Fracture Modes

In accordance with the principles of fracture mechanics, the crack may propagate from various modes of loading such as mode I, mode II, and mode III or a combination of these, known as

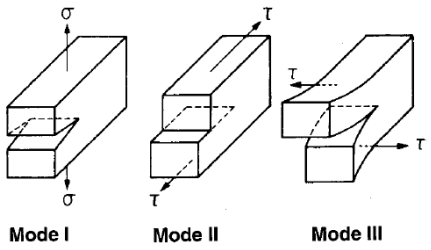


Figure 2.2: Modes of fracture **[6]**.

mixed mode crack (Figure **2.2**).

- In **mode I**, the delamination propagates because of the tensile forces acting perpendicular to the delamination plane. Mode I is generally also called the opening mode of crack.
- In **mode II**, the delamination propagates because of the in-plane shear forces exerted in a direction parallel to the delamination plane. This mode is usually called the shearing or in-plane sliding mode of crack.
- In **mode III**, the delamination propagates because of the out-of-plane (antiplane) shear forces acting in a direction parallel to the delamination plane but normal to the direction of propagation. It is further known as the tearing mode of crack.

Generally, the distribution of stress at the crack tip is superimposed, and it is noteworthy that these three loading modes are commonly present in real-world engineering scenarios. Understanding their individual contributions to the overall stress distribution is crucial for predicting crack growth and failure.

Numerous experimental studies indicate that the fracture mode typically influences the fracture toughness (G_c) value [55][56][57][58]. Furthermore, it has been shown that the path of crack growth or failure loci can be affected by the loading type. The investigation of composite delamination has focused chiefly on pure mode I, pure mode II, and mixed mode I/II. Within the composite research, although it is acknowledged that the contribution of mode III is insignificant in the delamination growth, mode III has been of more interest in recent years—nevertheless, this review limits the discussion to only mode I, mode II, and its combination. Henceforth, throughout this report, the term mixed mode (mode mixity) refers to the mixed mode I/II state.

2.4 Damage Mechanisms

2.4.1 Damage Zone and Matrix Cracking (Damage Initiation)

The delamination crack propagation is generally known to be preceded by damage zone formation at the front of the crack tip, and this particular damage zone is distinguished by the development of microcracks with the resin-enriched regions observed between the layers/plies

at a microscopic scale. Accordingly, microscopically, the matrix may be perceived as a material with isotropic and homogeneous properties, which typically undergoes cracking solely under local tensile loads, as suggested by Greenhalgh et al. [7]. Consequently, microcracks within the matrix are likely to originate and propagate in the plane exposed to the highest tensile stress state.

In the case of mixed mode loading, the microcracks are observed to develop at an inclination relative to the plane of plies at the interface ahead of the crack tip and propagate in that direction. If such microcracks appear at the interface of plies oriented in $\theta|0$ direction, the fibers within the off-axis ply facilitate and promote the progression of microcracks through the ply (intra-ply). As a result, the delamination **crack tip migration** through the ply oriented at an angle occurs. In general, if the tip of the crack confronts the adjacent ply at the interface, a shift in the crack propagation plane may be attained, complicating the interlaminar delamination behavior. Conversely, at the $0|0$ interface, the crack growth through the plies is expected to be impeded by the 0^{o} oriented fibers in both plies. Consequently, the delamination crack is constrained to remain adjacent to the ply fibers, and ideally, no shift from the intended crack plane should be observed. The mechanism of crack growth and migration at $\theta|0$ and $0|0$ interfaces are depicted in Figure 2.6. However, the actual scenario is different during the delamination testing of $0|0$ interface specimens due to the occurrence of another phenomenon known as fiber bridging, which will be discussed in Section 2.4.2 [59].

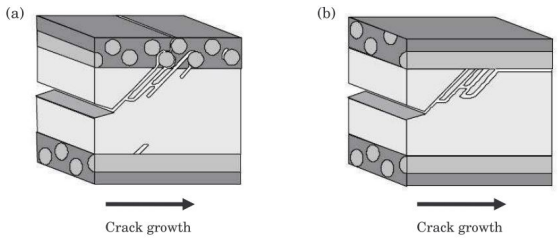


Figure 2.3: Illustration of crack growth at (left) $\theta|0$ and (right) $0|0$ ply interfaces showing the crack branching and migration mechanism **[7]**.

Continuing on the damage zone, the growth of the interlaminar crack emerges from the matrix cracks coalescences, based on Purslow's observation [60]. With mode I domination, matrix microcracks tend to propagate parallel to the plies' plane while gradually shifting towards one of the interply boundaries, and in this region, the existence of fibers alters the fracture process zone preceding the crack tip, yielding the delamination progression by peeling off the matrix (from the fibers). Whereas, with the dominance of mode II, it is observed that the degree of the damage process zone expands, and microcracks in the matrix begin to manifest at a significantly greater distance in front of the crack tip. Furthermore, the orientation of the microcracks to the interface (plies) plane exhibits an inclination of up to 45^{o}. Subsequently, the delamination propagates with irregular, tortuous surfaces ensuing from the matrix crack coalescence.

Importantly, as the damage zone grows to a critical size and initiation occurs, in such a situation, the toughness (G_c) determined signifies the amount of energy absorbed within the damage zone, which in turn is shown to be influenced by the orientation of adjacent and sub-adjacent plies relative the crack propagation direction. Various studies demonstrate that both the plastic matrix deformation and the cracking around the crack tip affect the initiation and

propagation fracture toughness values, indicating that these mechanisms primarily govern the initiation toughness[61][62].

Figure 2.4 shows the cracks and debonding ahead of the delamination crack tip, where it is notably representing an unstable initiation such that the cracks developed are not confined to the interface and can be seen instead following an alternate path above and below the delamination plane, indicating such initiation behavior could promote the possibility of the localized crack jumps away from the intended path of crack growth [8].

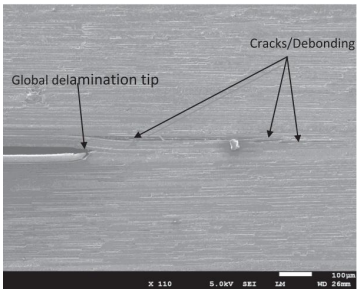


Figure 2.4: Crack tip and the debonding above and below across the interface**[8]**.

To obtain reliable interlaminar fracture toughness values, preventing a shift in the delamination path upon crack initiation at the intended interface is essential. However, this is particularly challenging when the intended delamination interface is not parallelly aligned with the fiber orientation, as the delamination propagation interface tends to shift frequently for multidirectional, woven fabric, cross-ply, bi-material, and unidirectional interfaces. Therefore, it is crucial to comprehend the propagation behavior and aspects that affect delamination growth since they can significantly influence the propagation path.

2.4.2 Damage Propagation

An integral aspect in the assessment of the interlamination fracture toughness of composites involves a crucial element of investigating the propagation and its behavior. The analysis of force-displacement curves of the tested specimens serves as the primary tool for macroscopic characterization of crack growth, strain energy release rate (SERR)/ fracture toughness, G_c.

The characteristics of the interlaminar crack propagation behavior can be categorized into three distinct types: **stable, unstable, and hybrid**. Figure 2.6 provides a visual illustration of the load-displacement response in correlation with the respective fracture surface topography.

In certain materials, when experiencing continuous and steady-state crack growth, there is a gradual decrease in force as the displacement increases (machine cross-head). However, in some cases, the crack may propagate in an unstable manner, characterized by intermittent intervals with either no (or slow rate of) crack growth followed by abrupt and rapid propagation of the crack, resulting in a significant drop in the force-displacement response. Typically, these rapid growths are succeeded by periods of arrest and subsequent reloadings, ultimately leading to a localized peak force as crack propagation reinitiates. This phenomenon is generally known as **stick-slip** displaying saw-teeth-like force-displacement plots [63]. In

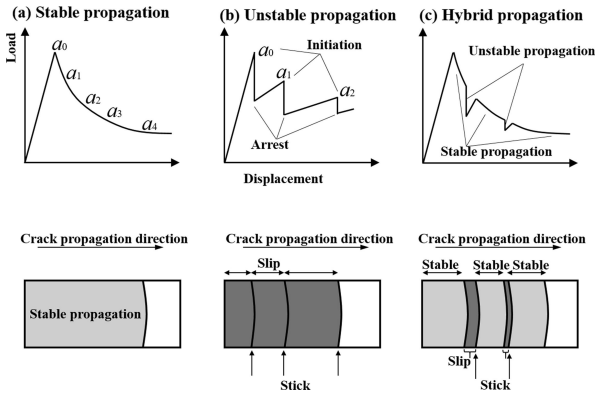


Figure 2.5: Different crack propagation behaviour and the force-displacement response **[9]**.

literature, this behavior is also referred to as crack jump, crack path migration [62], or non-smooth growth [64]. Hybrid propagation relates to the growth that combines the behavior of the stable and unstable modes.

Delamination migration is one of the biggest concerns, and delamination migration pertains to the growth of the crack in a direction other than the intended interface. From the previous section, it was understood that the damage zone at the crack tip could also influence the delamination migration. Further to this, the fiber volume fraction in composite laminates is also a crucial factor in determining crack propagation behavior. The presence of a matrix-rich region near the crack tip can lead to an increase in fracture toughness, even if the crack does not grow through that path [10]. This observation is commonly associated with the plastic yield zone and its size (radius, $\mathbf{r_y}$) ahead of the crack tip. While high energy of dissipation, evidenced by high fracture toughness, is observed for interfaces enriched with a matrix that facilitates a larger plastic-deformation zone, it has been further postulated that if the size of the plastic zone exceeds the resin-rich region, the crack may potentially propagate by migrating towards the weakest region of the interface, eventually leading to unstable crack growth behavior. The size of the plastic zone depends on the mode of fractures. An estimation of the plastic zone size in mode I and mode II for a neat polymer can be determined based on Irwin's plastic zone model for plane strain as outlined in the work of Ozdil and Carlsson (mode I)[65] and Aksoy and Carlsson (mode II) [66] as expressed in Equation 2.1 and 2.2 respectively.

$$\mathrm{r_y} = \frac{1}{4\pi}\left(\frac{\mathrm{K_{Ic}}}{\sigma_\mathrm{y}}\right)^2\left(\frac{3}{2} + (1-2\nu^2)\right) \tag{2.1}$$

$$\mathrm{h_p} = \frac{0.448{\mathrm{K_{IIc}}}^2}{\pi{\sigma_\mathrm{y}}^2} \tag{2.2}$$

where $\mathrm{K_{Ic}}$ and $\mathrm{K_{IIc}}$ are the mode I and mode II stress intensity factors, σ_y is the polymer yield stress, ν denotes the Poisson's ratio, and $\mathrm{h_p} = 2\mathrm{r}_y \sin\theta$ ($\theta = 42.3^\mathrm{o}$) represents the height of the plastic zone in mode II.

In case the interface with the matrix becomes larger than the radius of the plastic zone, the crack growth will be confined within this region enriched with resin. In fact, it is also proposed

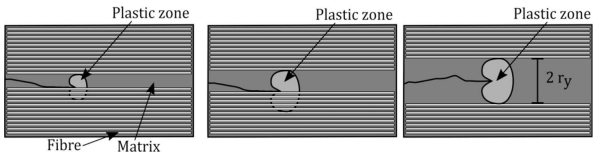


Figure 2.6: Effect of plastic damage zone formation and the presence of matrix at the interface on the crack growth behaviour**[10]**.

that the highest theoretically possible fracture toughness value is attained when the thickness of the resin-rich area equals or exceeds twice the plastic zone radius ($2\mathbf{r_y}$), representing the intrinsic fracture toughness of the neat polymer without any additives [65][66].

Next, the fracture toughness is shown to exhibit a continued increase with a proportional increase in the thickness of the matrix bond line at the interface. It has been demonstrated that regions with a higher concentration of matrix material exhibit superior toughness compared to fiber-rich regions. Consequently, non-uniform distribution (disparities in fiber volume) within the composite laminate can influence the progression of cracks affecting the overall toughness of the system.

In scenarios where the propagation of a crack occurs through (or proximate to) regions abundant in the matrix, the physical characteristics of the material undergo variations leading to an abrupt rise in toughness, thereby impacting the fracture behavior. Moreover, the heterogeneity of matrix-rich regions is a significant contributor to the instability of crack propagation, making the behavior unpredictable. It is a well-established fact that the growth of a crack from a zone with high toughness (resistance) to a zone with low toughness (resistance) results in an accumulation of elastic energy within the sample that exceeds the threshold for stable crack growth, subsequently promoting an unstable mode of crack progression and the phenomenon of so-called **stick-slip**[67][10][68][69].

The manner in which a crack grows heavily depends on the material's nature through which it propagates, ultimately influencing the type of failure mechanism that occurs[68][69]. With that, it is the manufacturing processing parameters that can also essentially control the properties of the material. Considering semi-crystalline thermoplastic as a case, this polymer undergoes changes in its crystalline structure (degree of crystallinity) in response to variations in cooling rate during manufacturing, signifying differences within matrix properties. In particular, the production of large structures may involve unavoidable non-uniform cooling due to fluctuations in the rate of cooling, which can ultimately lead to disparities in material properties and, in turn, in fracture propagation behavior. In this aspect, Purslow [70], from his fractographic investigation on the CF/PEEK specimen (DCB), reported three different types of failure mechanisms, namely **slow-ductile**, **intermediate-brittle**, and **fast-brittle** failure showing transition behavior within the same specimen (fracture surface), and interestingly for the same type of fracture (mode I peeling) and similarly for mode II shear in this work [71], based on the variations on the surface morphology.

Fiber Bridging

Another typical behavior frequently observed during the delamination is that fibers from the adjacent plies at the interface at the crack tip vicinity nest together, termed **fiber bridging**. This mechanism has a tendency to impede or resist delamination growth. The UD composites, with the fiber orientation in the longitudinal direction (0^o), are generally more susceptible

to fiber nesting. In the case of the multidirectional composites, the plies (fiber) oriented in a different direction could be determined straightforwardly at a microscopic level due to the presence of a small layer of resin free from the fiber between the reinforced matrix. However, this distinct separation may be significantly less, particularly for the UD composites. Mainly caused during the manufacturing process, it is possible for the fibers to migrate (partially) within the adjacent plies or at the interface, eventually leading to the bridging of fibers (Figure 2.8- left). Such a phenomenon can result in the absence of a well-defined path for the interlaminar fracture to propagate. The impact of ply/fiber orientation on fiber bridging remains a topic of debate among researchers. Altering the interface's stacking configuration may enhance or minimize the fiber-bridging phenomenon. Specifically, relatively increasing the ply orientation deviates the crack growth direction such that it is no longer parallel to the fiber orientation, eventually causing the crack to shift from the primarily intended path to the adjacent layers inducing the fibers to bridge within the crack path [72][73]. Another possible additional mechanism that could be attributed to the cause for the bridging of fibers was suggested by Bradley et al. [74], associating it with the damage zone formation. With resin matrices exhibiting high toughness, the formation of the plastic yield zone at the vicinity of the delamination tip may extend to multiple layers (adjacent and sub-adjacent) across the interface, as shown in Figure 2.8(right), and leading to multiple cracks and debonding sites within these plies, subsequently as the delamination grows, the fiber bundles within these layers function as bridging fibers. This behavior could also be more appropriately related to the multidirectional laminates [11][74].

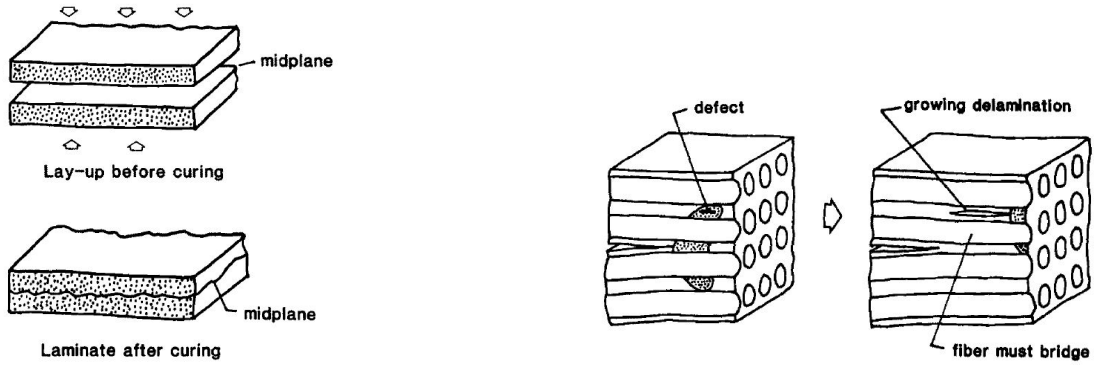


Figure 2.7: Illustration of fiber nesting at the interface in 0^o UD composites (left) and Damage zone promoting multiple cracks and triggering fiber bridging (right) **[11]**.

In cases of fiber bridging, the progression of a crack, in reality, entails the peeling off of the bridged fibers from the matrix and eventual fiber fracture. The crack extension directly influences the degree of the fiber bridging, and as the crack length increases, a more significant number of fibers bridge, and this phenomenon results in an increase in the material's resistance to fracture as a function of the increment of the crack, what is known as the **R-curve effect**. The presence of the bridged fibers leads to a substantial increase in delamination resistance and, in some cases, results in (mode I) propagation fracture toughness that can be up to four times higher than the initiation toughness [75]. In the absence of fiber bridging, the fracture toughness has been found to remain constant with steady propagation. Nevertheless, if the fibers bridge at the crack front, the fracture toughness ceases to remain constant and exhibits a rising trend with crack propagation length indicating the toughening effect. This was clearly

observed and reported by De Moura et al. [76] from the experimental investigation on UD CF/epoxy composites, during which the fibers bridging the crack were deliberately cut to study the fiber bridging effects.

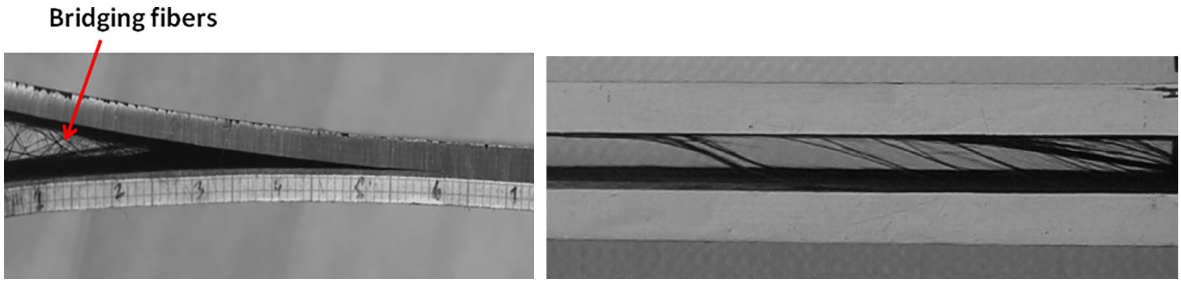


Figure 2.8: Fiber bridging observed in mode I (left) **[8]** and mode II (right) **[12]**.

Experimental observations have indicated that the significance of this particular phenomenon is greater in fractures primarily dominated by the higher contribution of mode I. Likewise, the occurrence of fiber bridging has also been noted in mode II delamination (Figure **2.8**- right) and as well may lead to a noticeable R-curve effect for the fracture toughness, as reported in a few studies [77][12].

2.5 Fracture Mechanics Approach

Fracture mechanics is a field of study that focuses on the failure of materials that are primarily governed by cracks, and delamination is a specific type of fracture mechanism that occurs in composite laminates. Given this, fracture mechanics presents itself as an appropriate approach to investigate the delamination onset and propagation problems in laminated composite material systems.

Griffith and Irwin's contributions allowed for the quantification of a material's resistance to fracture. Specifically, Griffith [78] pioneered a quantitative relationship between the strength and size of any crack in a material(for brittle materials). Following this, Irwin [79] further refined this correlation by taking into account the presence of a small localized plastic zone in the crack tip vicinity and proposed a method for deriving the critical strain energy release rate, which serves as a fundamental material property in characterizing fracture toughness. The concept of critical strain energy release rate, or SERR as commonly referred to, continues to be utilized to assess the fracture properties in metallic and laminated composite structures. Nevertheless, implementing linear elastic fracture mechanics (LEFM) fundamental principles is constrained to composite materials featuring relatively localized plastic fracture process zone at the crack tip and no other energy dissipation mechanisms.

The interlaminar fracture toughness expressed in terms of the strain energy release rate follows the global energy balance approach, based on the fundamental assumption that in order for a crack to initiate or propagate, the overall energy within the system should either stay constant or reduce. In the case of elastic behavior, the resultant energy balance can be mathematically described as a function of external work done by the forces (U_{ext}) and the strain energy stored (U_s) for an incremental crack area increase (da). As such, the energy release rate for a crack with a length of a and a width of b can be represented as:

$$G_c = \frac{1}{b}\left(\frac{dU_{ext}}{da} - \frac{dU_s}{da}\right) \tag{2.3}$$

Kanninen et al. [80] suggested a compliance calibration method to experimentally calculate the strain energy release rate (SERR) as a function of crack length for various specimen geometries based on the Irwin-Kies relation [81]. The reduction of compliance (C) for beam-like specimens generally involves the utilization of beam theories like direct beam theory and corrected/modified beam theory to derive closed-form formulations.

$$G_c = \frac{P^2}{2B}\frac{dC}{da} \tag{2.4}$$

where G_c is the SERR, P is the force, B is the specimen width, C is the compliance, and a is the crack length.

The overall fracture toughness/critical energy release rate (G_c), particularly in composite material systems (FRPs), can be regarded as a function of various mechanisms in the form of pure interfacial or interlaminar debonding (G_c^{Int}), deformation of matrix (G_c^{Mat}), fiber breakage (G_c^{Fb}), bridged fiber/matrix peeling (G_c^{Fp}) and can be expressed as in the following equation[82][83]:

$$G_c = G_c^{Int} + G_c^{Mat} + G_c^{Fb} + G_c^{Fp} \tag{2.5}$$

The dissipation of energy resulting from the deformation of the matrix, breakage of fibers, and debonding of fiber/matrix is presumably considered negligible, leading to a fracture toughness value of $G_c = G_c^{Int}$, according to Irwin's theory. However, the case of composites with tough polymer resins is known to exhibit extensive plastic deformation, which contributes significantly to the overall resistance to fracture. Moreover, the phenomenon of bridging fibers intensifies the fracture resistance by creating additional mechanisms that resist crack propagation in the form of fiber/matrix pull-out and fiber breakage.

The fundamental premise that the energy is exclusively directed toward delamination is no longer tenable. To accurately estimate the conservative G_c value, avoiding or quantifying the severity of the (plastic) matrix deformation and influence of bridging fibers is necessary. However, this presents a significant challenge as the energy contributions from these failure mechanisms (matrix deformation, fiber breakage, and fiber pull-out) exhibit substantial variability and pose difficulties in corresponding quantitative measurements. It should be emphasized that the contribution of each (either) of these failure mechanisms also depends on the mode of fracture/loading.

2.6 Interlaminar Fracture Toughness Testing

The experimental exploration of interlaminar fracture has been a subject of investigation for several years. Consequently, numerous test techniques have been established over time, some of which have been recognized and adopted as standards officially by diverse standardization committees. This section aims to review and discuss several of the most widely utilized fracture testing methods, commencing with the pure modes and advancing to the mixed modes (I/II).

2.6.1 Mode I Fracture Testing

The double cantilever beam (DCB) test is the most commonly employed testing technique for evaluating the mode I interlaminar fracture toughness. This test determines the longitudinal fracture toughness when a crack propagates in the direction parallel to the fiber between two adjacent layers/plies. The test specimen features a pre-crack generated in the mid-plane and is loaded through the piano hinges or end blocks (Figure 2.9). The experimental configuration allows for straightforward data analysis, relying on fundamental concepts odf beam mechanics.

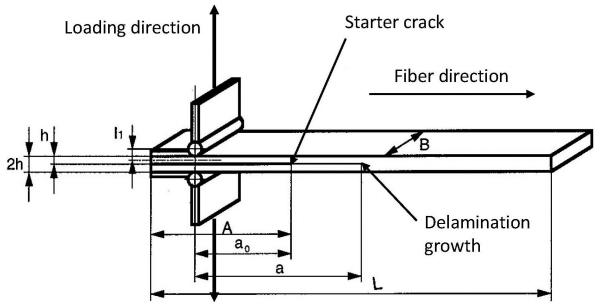


Figure 2.9: Schematic of the standardized DCB Specimen for determining the quasi-static mode I interlaminar fracture toughness. In this schematic, load application is achieved using piano hinges; alternatively, load blocks can also be used **[13]**.

DCB is a standardized test method [51][84], and it is noteworthy, however, that these standardizations are applicable only to the testing of the unidirectional (UD) composite systems, and certain challenges are encountered when implementing the DCB test on other composite materials. Instability (unstable) in the propagation of crack has been reported in several studies for UD fiber-reinforced composites and various woven fabric-reinforced and multidirectional composite systems [30][34]. Additionally, there are reports indicating that; the mode I critical energy release rate (G_{Ic}) can exhibit considerable variation. This variability depends on factors such as the stacking sequence of plies, the orientation of fiber, and the geometry of the specimen. As a result, assessing the properties of the intended interface accurately and effectively comparing findings across various studies becomes challenging. This is discussed in detail in Section 2.6.4.

2.6.2 Mode II Fracture Testing

Various testing methods exist to assess quasi-static Mode II fracture toughness [85]. Typically, most of these approaches employ bending to generate shear loading on the specimen. In developing such tests, the primary objective was to achieve reproducible and consistent outcomes through an easily straightforward and manageable procedure.

Compared to mode I, the assessment of mode II interlaminar fracture has only recently become standardized, as outlined by the ASTM standard D7905-14 [52]. The key hindrance to the development of a standardized methodology is the challenge of determining the crack propagation length under in-plane shear loading conditions due to the contact between the crack interfaces.

The End Notched Flexure (ENF) test (Figure 2.10-left), as per ASTM's suggestions, is standardized [52] for evaluating Mode II fracture toughness. The testing is primarily based on the

3-point bending technique. It should be noted that this test mainly yields initiation fracture toughness values due to unstable crack propagation. However, there are reports stating that stable crack propagation can be achieved for initial pre-crack lengths that are significantly large, with an aspect ratio $a_o/L > 0.7$ [86][87][88]. As in practice, most experimental configurations employ comparably shorter initial pre-cracks, and delamination propagation tends to be unstable, making it difficult to obtain a possible R-curve[86][89].

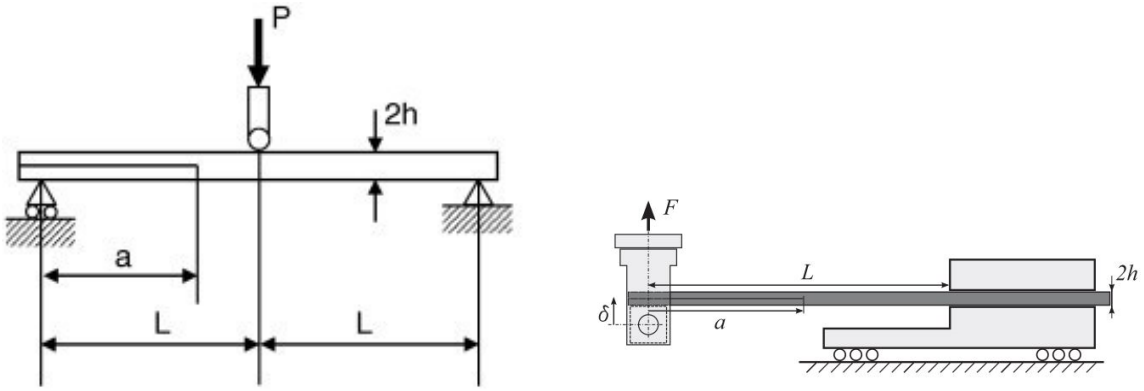


Figure 2.10: End Notched Flexure (ENF) test **[14]**(left) and End Loaded Split (ELS) test (right)**[15]**

The End Loaded Split (ELS) test (Figure 2.10-right), initially utilized in the work of P S Vanderkley [90], represents another standardized technique by **ISO 15114** [91] that is used for achieving pure mode II conditions. This testing method closely resembles the ENF test, with the specimen being clamped at the non-delaminated end and subjected to loading at the pre-cracked end while both arms undergo bending in the same direction.

The ELS test provides steady crack propagation, which is enabled by the utilization of a reasonably complicated sliding fixture. Martin et al.[92] and Wang H et al. [93] reported that crack growth exhibits stable behavior as the crack length attains 55% ($a_o/L > 0.55$) of the specimen length. There are studies indicating that low aspect ratios (a_o/L) yield an unstable propagation of the crack, emphasizing the requirement for a larger initial crack length [89][56]. Although the ELS configuration facilitates large crack propagation, it is adversely impacted by the challenges related to inconsistency in the clamping device. To obtain comparable outcomes, it is necessary to adjust for the compliance of the fixture, which introduces further intricacy into the testing process.

The stabilized end notched flexure (SENF) test, four-point end notched flexure (4ENF) test, and the over-notched flexure (ONF) test are the other adapted versions of the standardized 3-point end notched flexure (3ENF) test.

The SENF test method (Figure 2.11) proposed by Kageyama et al. [94] accomplishes stable crack growth by evaluating the shear displacement of a crack and regulating the corresponding rate of that displacement. Subsequently, this measurement is employed to direct the loading of the test specimen in real-time through the integration of the signal with the control system of the testing apparatus, ensuring that a steady rate of crack sliding displacement is maintained that cannot be reliably assured through a 3ENF test [94][95]. As the test involves incorporating the measuring system for the shear displacement of the crack, the testing procedure is more sophisticated comparatively.

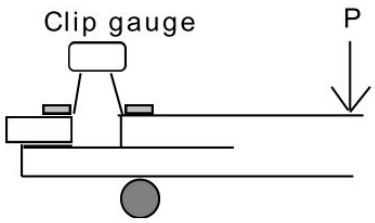


Figure 2.11: Stabilised End Notched Flexture (SENF) test **[16]**.

Aiming to address the shortcomings, Martin et al. [96] introduced the 4ENF test method. The 4ENF test demonstrates stability in the delamination propagation, and the experimental set-up is uncomplicated to deal with. The testing is similar to the principle of the ENF, but loading under a 4-point bending technique (Figure 2.12-right). In this configuration, the crack tip can be positioned either towards the left of the loading roller or between the two inner loading rollers, such that the loading point is always over the initial precrack. Moreover, the assembly of the loading fixture to the machine's cross-head load frame can either be fixed or pinned. It has been established that the pinned arrangement is more advantageous for practical purposes. Specifically, it is considered that in the case of a pinned configuration with the pre-crack front positioned within the inner span of the loading rollers, the shear force becomes zero while the bending moment remains constant, eventually presuming an outcome with minimization of frictional effects at the crack faces, comparatively.

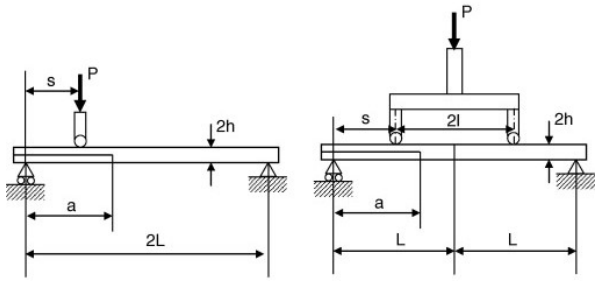


Figure 2.12: Over notched flexure (ONF) test- (left) and Four point bend ENF (4ENF) test - (right) **[14]**.

Similar to this, another test was recommended by Tanaka et al. [97], known as the Over notched flexure (ONF) test (Figure 2.12-left). In fact, this test utilizes the same test setup as the ENF test and also works on the 3-point bending technique. However, the characteristic aspect of the ONF test is that the loading roller is over the pre-crack, more similar to the 4ENF configuration. It is shown that the testing also generates stable delamination growth. It is also believed that the friction between the crack interface can potentially influence the experimental fracture energy determination due to the positioning of the loading. Francesco Caimmi et al. [17] developed the Compact Edge - Notched Shear Specimen (CENS) test as a mode II test specifically designed to be utilized in high loading rates. In this particular geometric configuration (Figure 2.13), the specimen being tested is fixed to two metallic fixtures utilized for loading. One of the fixtures is held stationary, while the other is subjected to a controlled load rate. As a result of this loading configuration, a shear stress state is

generated at the crack tip in the specimen.

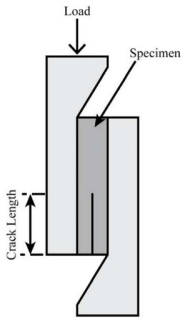


Figure 2.13: Schematic of the CENS testing fixture **[17][18]**.

The objective was to minimize the frictional influence in pure mode II testing. The extent to which friction affects ENF testing is disputed in the literature, with evaluations varying from 3%[86] to 15% [98]. However, some investigations suggest that friction only affects the region near the loading roller, which is inconsistent with numerical analysis demonstrating the compressive stresses at the tip [99]. The CENS test exhibited negligible friction and predominantly pure mode II behavior. Nevertheless, the authors suggest that further improvements are necessary for this test. No further work is found in the literature pertinent to this testing method.

The phenomenon of friction at the crack interfaces plays a critical role in evaluating the mode II behavior. Various testing procedures display distinct loading responses as illustrated by the force-displacement plot (Figure 2.14 - left). Numerous studies have been conducted to examine the influence of friction on fracture toughness. Notably, the fracture toughness values derived from 4ENF tests have been found to be in the range of 9-17% [96][100], while it is almost 60% (ONF tests)[97] higher in comparison with the values attained in the ENF test. Another work from Schuecker et al.[101], exploring the frictional impact at the interface in ENF and 4ENF testing, reported that the friction influence was estimated to be a maximum of 5% in 4ENF, whereas 2% in ENF, on the determined fracture energy, provided that data processing is done through a compliance calibration procedure. Additionally, their results suggest that the frictional effects become more pronounced as the span ratio increases.

Davidson et al.[102] performed experiments to determine and quantify the coefficient of friction of carbon-reinforced epoxy composites, reporting that the investigated materials had friction coefficient values of 0.374 and 0.345. It was also concluded that friction had approximately a 5% impact on the fracture toughness data. In numerical analysis, [103] researching the potential impact of geometric nonlinearities as well as the friction on the ENF and 4ENF tests showed that for a coefficient of friction varying between 0.3 and 0.5, the friction affected the mode II energy release rate by 3.6-6% in the ENF test, while it was found to be 8-12% in the 4ENF test. Furthermore, they also emphasized that the frictional impact is dependent on the span length along with the geometry of the specimen. According to the experimental findings of Wang et al.[14], the ENF testing provided a more dependable fracture initiation value with a minimal degree of statistical variation, while the toughness value derived from the 4ENF test is relatively higher (2%) than the ENF value. In contrast to the ONF test, where the friction effect is observed to increase as the crack propagates, the influence of friction is

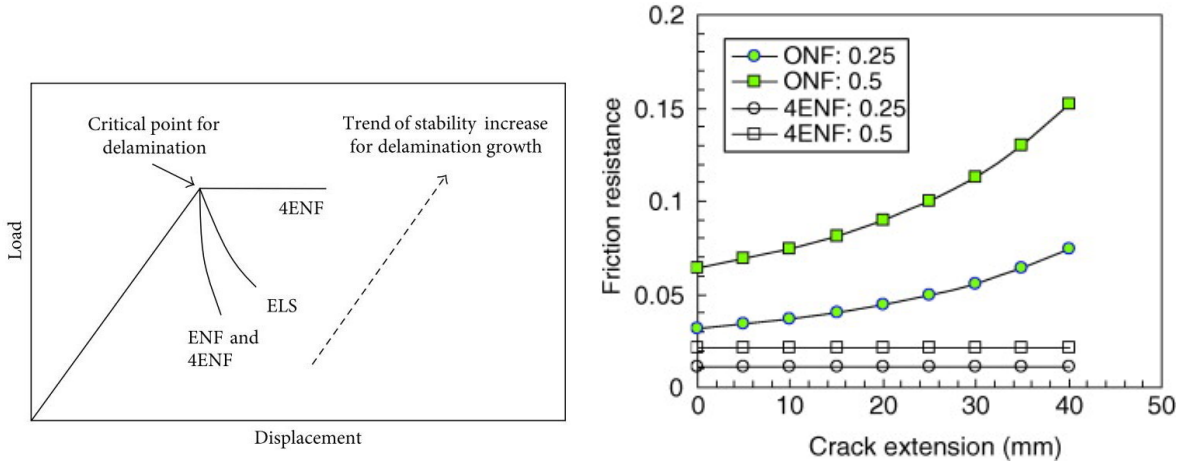


Figure 2.14: Schematic representation of the force-displacement response of various mode-II testing (left) **[19]** and Frictional resistance as a function of crack propagation at constant friction coefficient for different test methods (right) **[14]**.

significantly lower in 4ENF testing (Figure **2.14** - right).

Andras et al.[104] showed that open notched flexure (ONF) test represents a more suitable approach for assessing the mode-II toughness of composite materials characterized by low flexural modulus, compared to the ELS test, as it experiences large displacements, limiting the feasibility of executing the propagation test and generating the R-curve.

2.6.3 Mixed Mode I/II Fracture Testing

In composite structures and bi-material interfaces (hybrid joints and also multidirectional laminates), delamination is a complex phenomenon that typically does not occur under pure mode I or II loading conditions but rather a combination of modes I, II, and III. This section focuses exclusively on the discussion of mixed mode I/II fracture testing.

In scientific literature, within the framework of characterizing mixed mode fracture phenomena, two commonly employed terms are mixed mode ratio and mode mixity. It is advantageous to offer some explanation to facilitate a better understanding of these terms.

- **Mixed mode ratio**: Refers to the ratio of the mode II strain energy release rate (SERR) G_{II} to the total SERR G_T ($G_I + G_{II}$), expressed as G_{II}/G_T.
- **Mode mixity**: Also known as phase angle ψ, is a function of G_I and G_{II}, represented as $\psi = \arctan\left(\sqrt{\frac{G_{II}}{G_I}}\right)$ or $\arctan\left(\frac{K_{II}}{K_I}\right)$, where K_{II} and K_I denotes the mode II and mode I stress intensify factors (SIFs), respectively.

A range of experimental fixtures is developed for the mixed mode tests. Multiple specimen configurations and loading conditions have been widely utilized to investigate mixed mode failure, and these include the mixed mode bending (MMB) test, the asymmetric double cantilever beam (ADCB) test, fixed ratio mixed mode (FRMM) test, and the single-leg bending (SLB) test, among others.

A typical experimental configuration for conducting mixed mode fracture testing, commonly referred to as the Mixed mode bending (MMB) test, is shown in Figure 2.15. Reeder and Crews [99] initially introduced the MMB test, which was subsequently re-designed to address the limitations of the earlier version [105]. The MMB test (ASTM) has been standardized for unidirectional fiber-reinforced composites, specifically specimens exhibiting symmetry along the interface [?]. The MMB test integrates the key characteristics of the mode I DCB and mode II ENF configurations to generate the mixed mode I/II loading conditions at the crack's tip. In this test configuration, by adjusting the length (distance) of the loading arm lever (c), practically any mode mixities can be feasibly attained (with symmetric arms).

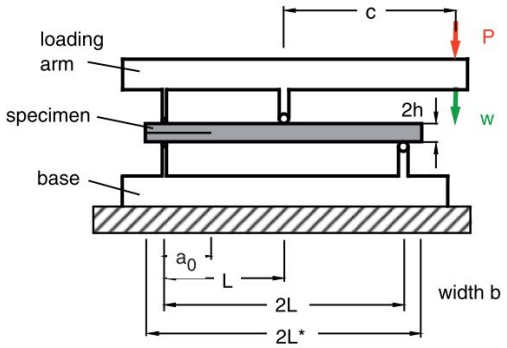


Figure 2.15: Schematic of the mixed mode bending (MMB) configuration for Mixed mode I/II fracture testing **[20]**.

The fixed ratio mixed mode (FRMM) test proposed by Hashemi et al.[106] utilizes a clamping fixture that is similar to the mode II ELS test set up; however, only one arm is subjected to loading in this particular configuration (Figure 2.16). It is also referred to as mixed mode end loaded split (ELS) test [59]. The mixed mode ratio resulting from this test is nearly unaffected and not a function of crack length, while the mode ratio depends on the mechanical properties and relative specimen thickness [58]. In the case of the symmetric specimens, the generated mode ratio is equivalent to 0.429. However, for specimens with geometric asymmetry (different thicknesses), the fracture modes estimated based on the various mode-partition theories established in the literature do not seem to produce consistent results, which is one limitation of this test. It should be noted that the clamping mechanism needs to be calibrated, and inaccuracies may occur in the measurements of crack length during testing due to bending induced in the specimens, as previously noted for the pure mode II situation[85].

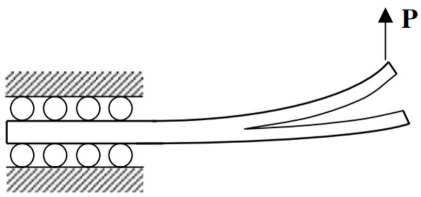


Figure 2.16: Fixed ratio mixed mode (FRMM) test configuration **[21]**.

The mixed mode flexure (MMF) test, also popularly known as the single leg bending (SLB) test, is comparable to the ENF test, utilizing a three-point bending setup, where the application of load is exclusive to the upper arm of the specimen (Figure 2.17). The SLB test can yield a distinctive mixed mode ratio of 0.429 for symmetric specimens, which aligns with that found in the FRMM condition and the notched 4ENF test [21]. With material (modulus ratios) or geometrical asymmetric features (such as the thickness ratios) in the specimens, investigations suggest that reasonably various mode mixtures can be realized in this test [107]. Nevertheless, the intentional non-balanced, non-symmetric design of specimens (also the underlying concept of ADCB tests) can pose challenges as it raises concerns regarding mode partitioning [108].

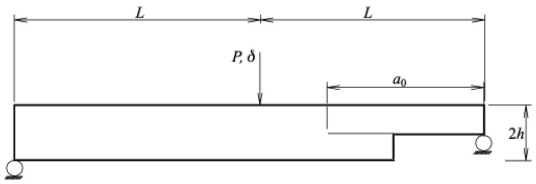


Figure 2.17: Illustration of the single-leg bending (SLB) test **[22]**.

2.6.4 Bi-Material Interface Problems

In precise terms, the failure at the interface between a bi-material is not exclusively limited to interfacial failure between two different materials, such as metal – composite, composite – composite joints. Instead, it also involves a delamination failure between the interface of two adjacent plies with fibers oriented at different directions ($\theta^o - \theta^o$) within a composite. The unequal stiffness between these delaminated layers, resulting from their distinct fiber orientations, creates a crack interface between two asymmetrical arms. Therefore, it is also appropriately classified as a bi-material interfacial crack failure.

The scope of the ASTM standards discussed in the previous section is limited to the fracture toughness evaluation exclusively in unidirectionally reinforced fiber polymer composite specimens. However, research has demonstrated that the fracture toughness may exhibit variability based on the stacking configuration of the specimen. When attempting to determine fracture toughness utilizing the established standardized techniques like the DCB, ENF, or MMB in a bi-material interface or multidirectional composite laminates, problems may arise in comparison to unidirectional composite testing. This section deals with the discussion focusing on addressing the undesired issues associated with employing these testing methodologies for the testing of multidirectional composites and bonded joints, which are actually used in real-world engineering structures.

- The **distribution of strain energy release rate** along the delamination front across the specimen width is non-uniform, and this non-uniformity is characterized by its asymmetry. In their work, researchers Sun et al. [109] have established a correlation between this asymmetry and the bending-twisting coupling phenomenon, defined by a parameter $\mathbf{B_t}$ $\left(\left|\frac{D_{16}}{D_{11}}\right|\right)$. On the other hand, the difference between the strain energy values at the specimen edges and its center has been associated with the non-dimensional ratio referred to as $\mathbf{D_c}$ representing the bending stiffness under plane strain/stress conditions

by Davidson et al.[110]. This parameter $\mathbf{D_c}$ $\left(\frac{D_{12}^2}{D_{11}D_{22}}\right)$, derived from the components of the ABD matrix exhibits a strong dependence on the lay-up sequence of the laminates. Conventionally, it was presumed that the non-uniformity could be disregarded when the D_c value was insignificantly small. Nonetheless, empirical findings have demonstrated that the non-uniformity remains influential even in laminates with a small D_c, as reported in many studies [111][62][61]. Multidirectional laminates can exhibit bending-twisting coupling unless they possess an asymmetric configuration. Compared to UD composites, the presence of fewer plies oriented at 0° leads to a reduction in bending stiffness. As a consequence of these factors, the strain energy release rate distribution (multidirectional laminates) is anticipated to be non-uniform. Therefore, experimental determination of fracture toughness can yield imprecise results, as beam theory assumes a uniform distribution, and fracture toughness is typically determined based on delamination propagation length at the edges rather than the center [109]. In addition, the non-uniformity factor also poses challenges in visually monitoring the delamination growth, as it results in uneven propagation of crack front along the specimen width. Eventually, variations in the visually recorded crack tip positions may be obtained from either side of the specimen (Figure 2.18).

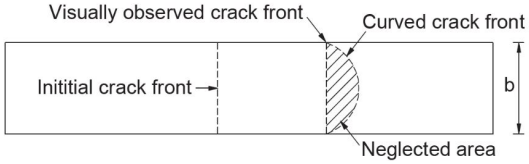


Figure 2.18: Propagation of crack in a DCB specimen with an adhesive layer showing the crack front curvature and the neglected area **[23]**.

Moreover, the non-uniformity in fracture toughness is influenced by the aspect ratios of the specimen, specifically the ratio of initial crack length to width (a_0/w) and the ratio of thickness to width (t/w)[61]. The curvature and skewness of the crack front are also dependent on the stacking sequence of the specimen and may contribute to the observed variation in fracture toughness with respect to lay-up. Thus, it is imperative to minimize variation and skewness in the specimen design, restricting the design boundaries [109].

- The Resistance curve, often called the **R-curve**, relates to the fracture toughness behavior (fluctuations) with the crack propagation. Numerous studies have suggested that the R-curve cannot invariably be regarded as the intrinsic material property, as it is influenced by the specimen's geometry and damage mechanism, such as fiber-bridging. With this objective, Sorensen et al. [112] performed DCB tests on the UD carbon-epoxy specimens with varying thicknesses of the specimen. The results indicated that as the thickness of the specimens increased, the obtained R-curves started exhibiting a low rate of fracture growth. However, the steady state (plateau) fracture toughness was similar in all cases, and no significant changes were noticed. In order words, the findings revealed that the thicker specimens reached the steady state after a large propagation of crack length. The underlying reason for this observation was stated by the fact that thinner specimens are anticipated to have a greater opening for a similar crack propagation length. Other researchers have reported comparable findings for thickness effects [113][114]. Interestingly, on the other hand, in recent studies, Farmand et al. [115]

noted the mode I fracture toughness (propagation) to be increasing with the specimen thickness (DCB), whereas the onset fracture toughness remained insensitive, similar to what Shokrieh et al. observed [116]. The R-curve effects have been observed to be significant, with varying anti-symmetric interface layups exhibiting considerable irregularities in the crack propagation, resulting in higher fracture toughness compared with the UD interface [117].

- The phenomenon of **delamination(crack) migration** pertains to the growth of delamination in a direction other than the intended interface (specimens' mid-plane). It has been shown that this phenomenon is facilitated by the growth of delamination at the interface between adjacent layers/plies of varying orientations [118][119]. While Sebaey et al.[120] have inferred from their experimental analysis of various interfaces and stacking sequences that the probability of delamination migration is higher with decreasing specimen bending stiffness. The shift of the crack path (migration) has been observed to impact the fracture toughness propagation values due to the partial utilization of the released strain energy in this process [121]. Also, the migration may potentially result in the mode-mixity locally at the crack tip, even during the pure mode tests. This is primarily attributable to the asymmetry generated in the specimen arms causing variations in the thickness as the delamination grows away from the desired interface and the initial symmetrical condition of the specimen is not maintained anymore.In this work [122], it is elaborated that the contribution of both tensile (peel) and shear stress promotes the migration of cracks. According to the authors, migration is predicted to occur in both the upper and lower planes of the interface in mode I, whereas in mode II loading conditions, the path of delamination migration is determined by the direction of the interlaminar shear stress. So indicates that the configuration of the specimen plays a crucial role in determining the direction of delamination migration if it lacks symmetry relative to the specimens' mid-plane. The propagation of delamination is impeded in 0° plies due to the alignment of fibers in the ply perpendicular to the crack front and the force driving the mechanism [119]. In a study by Pereira et al. [123], the ENF and MMB specimens were strategically positioned within the fixture to induce compressive stresses on the non-zero oriented ply at the interface, thereby promoting the migration directed toward the ply oriented in 0°.

- Further **intralaminar fracture** has also been observed in experimental investigations of multidirectional composites, wherein the crack growth occurs within a ply (intra-ply) at the interface (Section 2.2), as reported by several studies [124][117][120]. This failure behavior deviates from the traditional interlaminar failure mechanism and will likely impact fracture toughness values.

- In laminated composite with asymmetric stacking sequence, each constituent layer exhibits distinct mechanical properties, leading to distinct behavior of individual arms. Pereira and de Morais [123] highlighted that conventional fracture tests such as double cantilever beam (DCB) and end notched flexure (ENF) cannot establish pure mode conditions in such multi-directionally laminated composite systems. Additionally, mixed mode bending (MMB) tests may yield **different mode mixity** than that is anticipated for unidirectional laminates, as no analytical model exists that can determine the mode mixture for asymmetrical specimens and subsequently determine the appropriate loading arm length (c).

- From the aspect of **stacking sequence and the global stiffness** of the whole specimen and the sub-laminate, various investigations have been documented with respect to the impact of the orientation of the fiber (or ply angle) adjacent to the intended crack propagation interface on the delamination behavior [61]. In one of the studies, Bin Mohamed Rehan et al. [62] investigated the outcomes of the impact of fiber orientation/ply angle on delamination propagation. The findings indicated that varying lay-up configurations (adjacent and sub-adjacent layers) for a given specific crack interface leads to a substantial difference in the initiation fracture toughness, thereby suggesting that the variation in the stacking sequence of plies near (above and below) the delamination faces also plays a crucial role in determining delamination toughness.
- As multidirectional composites are composed of plies with varying orientations and thermal and chemical expansion coefficients, **residual thermal stress** can be developed upon cooling subsequent to the manufacturing (consolidation/curing) process, which is shown to affect the released strain energy and, eventually, the fracture toughness [125]. The numerical analysis of mode I fracture of multidirectional specimens conducted by Sebaey et al. [111] established that although the force-displacement response was not affected by the induced residual stresses, the migration of crack was promoted.

As per the ASTM protocols, if evident crack migration or significant variations in delamination growth occur on either side of the specimen, the test results are deemed invalid. In the case of unidirectional specimens, it is crucial to avoid such occurrences, as it may suggest inaccuracies in the testing fixture's alignment or the specimen's fabrication process. However, it is more challenging to prevent these issues when testing multidirectional coupons, and their presence does not necessarily imply an incorrect test execution. To mitigate these issues, most research studies investigating the impact of ply orientation on the interfacial fracture toughness evaluation modify the lay-up sequence to minimize the above-discussed concerns.

In this aspect, several guidelines are outlined and followed in the literature in the design of the layup configuration, which includes: reducing the parameters $\mathbf{B_t}$ and $\mathbf{D_c}$, enhancing the specimen bending stiffness, ensuring equivalent stiffness of the two arms, eliminating or minimizing the flexural/-torsional (bending/twisting) coupling, utilizing doublers (for thin – specimens) to avoid bending failure, prevent non-uniform cooling or significant thermal gradients during processing.

When it comes to bi-material interface testing, in particular, the metal-composite, composite–composite bonded joints, the established conventional experimental testing methods have been extended for testing the bonded joints; the dissimilarity in Young's moduli between the adherends, along with the asymmetrical nature of material results in a limitation in the effective applicability of the test and data analysis procedures for crack problems.

While the fracture toughness dependence on the mode mixity is extensively acknowledged and understood, however, for a bi-material interface crack, it is known to be rigorous and challenging to partition the contribution of each mode, primarily due to the fact that this type of crack intrinsically experiences mixed mode loading [126][24][127]. As a result, deriving pure fracture toughness values (mode I and mode II) and mode mixities for mixed mode tests can be problematic from an experimental standpoint.

One of the primary challenges in experimentally achieving different mode-mixtures and developing comprehensive fracture envelope for various bonded joints is the absence of a single

test specimen geometry or the loading fixture capable of effectively characterizing the entire spectrum of in-plane fracture conditions (Figure 2.19). Although with MMB tests, adjusting the length (distance) of the loading arm lever (c) practically any mode mixities can be feasibly attained, it is only for unidirectional composites. An analytical model that can determine the mode mixture for asymmetrical specimens and subsequently determine the appropriate loading arm length remains elusive.

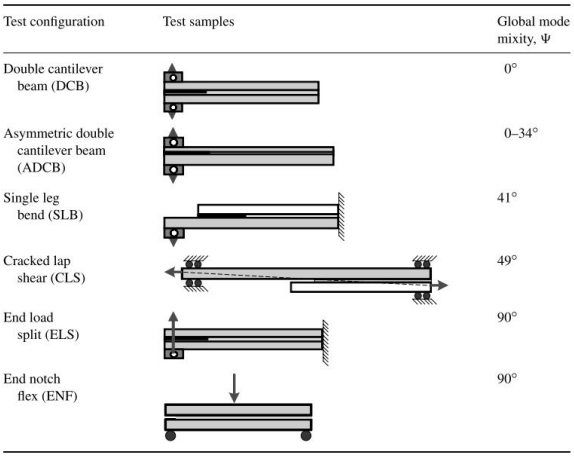


Figure 2.19: Various specimen configurations for generating different mode mixtures[24].

Another critical issue is associated with the specimen design configuration, with no definite guidelines. The research findings have demonstrated that using the phenomenological design approach, which involves having equal bending stiffness of each arm along the interface in the bi-material joints, does not generate loading conditions for pure mode I and II failure.

The experimental determination of fracture toughness typically generates either mode I or mode II dominant values, in general. As the experiments only yield the total energy release rate, to determine the mode mixity of a mixed mode test, various theoretical and analytical frameworks have been proposed and suggested for partitioning the mode components. More importantly, the impact of residual stresses has been largely overlooked and not taken into account in the majority of the experimental procedures and energy release rate formulations. The scientific community has not yet reached a consensus on which theoretical approach yields the most precise predictions for bi-material interface crack mode mixity. A standard that can provide guidelines for specimen design and tests and the analysis of the results is lacking [127].

Despite following several guidelines by designing and modeling at the ply level to design the optimal layup configuration to minimize the issues and effectively utilize the standard delamination test, undesired effects are still observed and remain unsolved. It should be noted that the critical energy release rate formulations (DCB, ENF, MMB, and even other tests) often fail to consider certain pertinent factors, leading to an overestimation of the fracture toughness value. Moreover, to conduct standard tests, it is essential to maintain constant knowledge of the crack tip position and length throughout the experiment. Despite its importance, actively monitoring and determining the precise position of the crack tip during testing can prove challenging. Alternative testing methods that do not require such extensively rigorous procedures in the design of stacking sequences, specimen geometry, and

crack extension measurements have been favored in recent studies.

2.7 Peeling Techniques

Peel tests are a well-established technique for determining the energy necessary for peeling off a flexible adherend (generally referred to as the peel-arm) from a rigid substrate (Figure 2.20). The peel test methods offer several appealing advantages over the currently standardized tests for the delamination fracture testing of the composites, namely the DCB, MMB, and ENF tests. In recent years, the peel tests have been more interesting, as they present a promising potential in testing varying ranges of interface configurations in combination with simple specimen design. More importantly, the tests enable greater control over the delamination rate and the failure loci, facilitating a simple experimental process overall. Peel test methods are categorized according to fixture configurations and vary in terms of the application of load onto the specimen. Nevertheless, fundamental principles underlying these methods exhibit many commonalities. Many peel test methods have been developed, and few have been standardized. This section provides an overview and analyzes various peel testing techniques that are commonly employed (as well as newly proposed concepts) in research and industry.



Figure 2.20: Schematic illustration of a typical peel test (F - applied force, w - width, θ - peeling angle)**[25].**

2.7.1 90 and 180 degrees Peel Tests

The 90 degrees peel test technique (Figure 2.21 - left), as described in various standards [128][129], may be feasibly utilized in testing the adhesively bonded assembly if either of the two adherend arms exhibit flexibility. The 180 degrees test (Figure 2.21 - right) [130] can be suitably employed to evaluate the integrity of the bonded joints (rigid-flexible), provided they can be bent to meet the necessary 180° angle specifications for load application . Amongst these two, the 90 degree peel has been found to be highly advantageous in conditions where the substrates/adherends demonstrate reduced flexibility and the resistance to peel cannot be evaluated by applying load at 180 degrees due to the possibility of cracking or adherend failure [26]. Certain significant limitations are associated with the utilization of these techniques due to their inherent shortcomings. Firstly, the testing equipment lacks the capability to ensure the maintenance of a consistently constant peeling angle [26]. Secondly, the failure loci can exhibit instability at the peel front, leading to the inconclusive characterization of results [131]. In addition, the peel arm undergoes bending during peeling, resulting in a certain radius of curvature, which cannot be controlled and may cause issues. In particular, if the interface under investigation is relatively tough compared to the peel-arm (composite),

the radius of curvature may exceed the acceptable range, ultimately ensuing in a peel-arm failure before/during peeling [132].

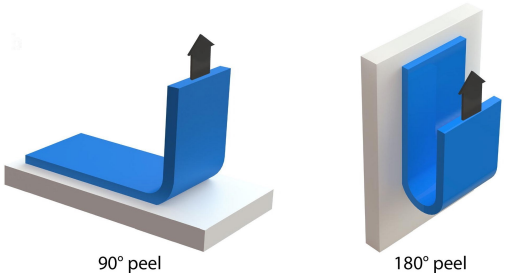


Figure 2.21: Representation of a 90° and 180°peel tests **[25]**.

2.7.2 Climbing Drum Peel (CDP) Test

The Climbing Drum Peel (CDP) test was initially conceptualized for evaluating the adhesive strength within bonded and sandwich structures, specifically in the context of flexible and rigid adherends. In general, this test method which is standardized **(ASTM D1781 - 98)** [133] aims to quantify the adhesive performance of the interface between the two types of adherends in terms of their ability to withstand peel forces. The climbing drum peel experimental test set-up (Figure 2.22) consists of a drum with flanges such that the radius of the flanges is greater than the drum radius. The flexible adherend often referred to as the peel - arm, is affixed by bending around the drum at a constant curvature. Two loading straps are positioned on the flanges to apply the torque for the drum to progress, roll along the specimen, and initiate debonding. This is achieved by clamping the specimen at the non-delaminated end to the upper grips, whereas the bottom end of the loading straps is fixed to the lower grip of the universal testing machine, and as the cross-head moves upwards an external force is exerted, generating the torque.

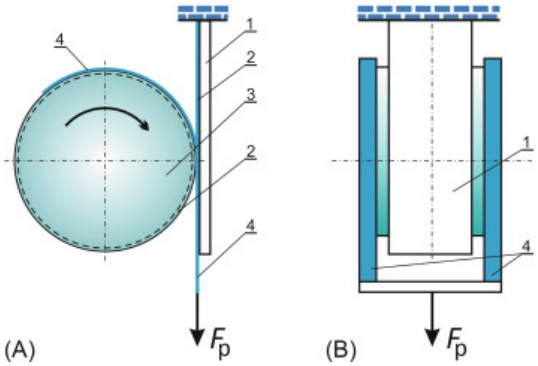


Figure 2.22: Schematic illustration of the Climbing Drum Peel test set up: (A) front view, (B) side view, (1) rigid adherend, (2) flexible adherend, (3) drum, (4) loading straps, Fp—externally applied force **[26].**

The conventional utilization of this technique does not entail the critical strain energy evaluation, a crucial design factor in the composites. Instead, as mentioned earlier, peel force/torque

is measured, which is influenced by the geometric configuration of the peel setup. Initial research by Okada et al.[134] and others on the sandwich structures established a correlation between the peel force and the critical strain energy release/fracture toughness from the CDP test. Following the same concept, Daghia et al.[135] explored the applicability of the CDP test in evaluating the fracture toughness of the monolithic composite laminates. This work, presuming the fracture energy outcome from the CDP tests as mode I dominant, was compared as an alternate for the classical DCB tests. While similarly comparable fracture energy values were observed for the non-zero interfaces from the two tests, the specimens tested with 0/0 interface exhibited significant differences, with higher values obtained from CDP test. Although the authors explain that the fracture surfaces of the tested specimens (0/0 interface) display different propagation paths, however do not concretely indicate the possible reason for the variation.

The CDP tests prove to be efficient in maintaining a relatively straight delamination front to that of the DCB tests.The drum/roller offers the benefit of regulating the peel - arm's curvature radius over the other non-roller-assisted standardized 90 and 180-peel tests. It is also possible that a fracture of the peel tape might develop before the actual peeling during the CDP test due to inadequate tape conformance to the drum[136][35]. Furthermore, there are other drawbacks associated with the CPT test, as it necessitates specific experimental conditions, such as peel - arm flexibility, a drum with a larger radius (a minimum radius of 50 mm [137]), and a higher applied force during bending, to improve conformance. Moreover, the extent of peeling (delamination) is constrained by geometrical factors, which dictate a maximum peeling length equivalent to approximately two-thirds of the circumference of the drum. This limitation arises from the fact that the wound layer of the sample is bound to collide with the non-delaminated portion of the peel sample when 2/3 of the initial round of the drum is complete. As there exists a correlation between the diameter of the drum and its weight, which is directly influenced by the thickness of the peel-arm, a higher drum weight complicates the practical handling of the experimental set-up[135]. Apart from this, the specimen's vertical misalignment may potentially cause the rotation of the specimen, and further considerations are essential to reduce the variations by maintaining the alignment during the loading.

From a perspective of the loading mode achieved in the CDP tests, it is by far considered to be mode I dominant, and this stems from the only fact that the determined fracture energy from the CDP tests results in more or less comparable values to those obtained from the DCB [138][135] and SCB tests [139]. Nevertheless, detailed studies pertaining to the dominance of mode I load in the CDP tests are still sparse.

2.7.3 Horizontal Drum Peel (HDP) Test

In 2018, Canas et al.[27] proposed a new peel testing configuration known as the Horizontal Drum Peel (HDP) test to circumvent the unfeasibility of the DCB and CDP tests to perform "in situ", as it necessitates the utilization of the Universal testing machine for load application. The design aimed at featuring the following attributes: no requirement to determine the crack length, simplicity of execution, direct evaluation of fracture energy (G_c), and finally, the feasibility of conducting the test "in situ."

The HDP test, primarily based on the principles of the CDP tests, consists of a drum posi-

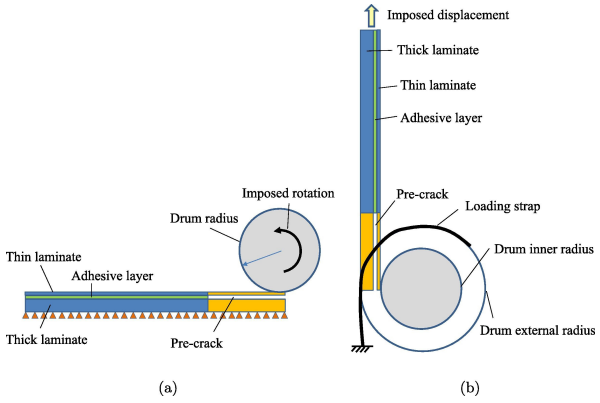


Figure 2.23: Schematic illustration of the HDP test (a) and (b) CDP test **[27]**.

tioned horizontally (Figure **2.23**-a). Unlike the CDP tests, the HDP test is executed without employing the Universal testing machine. To this end, a motor-driven kinematic chain is utilized to directly translate the rotational force to the drum and eventually attain the desired rotational speed. Within this HDP configuration, the testing procedure consists of two stages: initially, the flexible layer is wound around the drum, and subsequently, as the torque is applied, the combination of winding and debonding initiates. It is noteworthy to realize that the bending moment (M) induced in the thin, flexible peel - arm at the crack front governs the propagation of crack. It should be emphasized that if this moment remains below the critical threshold, debonding will not take place. The crucial fact to be noted during the testing with the HDP configuration is that the thin flexible adherend conforms to the radius of the drum during the initial winding step, and as the delamination proceeds, the flexible arm detaches away from the drum losing the curvature of the drum.

The critical threshold moment (M), which causes the delamination, is correlated to the critical radius (R). In this testing, the critical radius of the thin arm cannot be effectively controlled; despite the variations in the curvature, it is believed that corresponding bending moments induced across other regions of the laminate do not influence the progression of crack.

The authors from their experimental outcome indicate that the fracture energy (G_c) results from both the tests (HDP and CDP) seem to agree reasonably well, with a difference of around 4%. Further to this, their numerical analysis establishes that the fracture behavior observed is a mixed mode in both test cases, with the mode mixity angle determined to vary with the two different adhesively bonded laminates (UD tape and fabric) tested, indicating that the degree of mode-mixity depends on the material system investigated. However, the mode- mixity is lower for HDP tests than for CDP tests.

The very evident fact that there is no control over the radius of curvature is a significant drawback in itself. Moreover, this could potentially prevent the testing applicability for other interesting interface configurations, such as the delamination of multidirectional laminates and bi-material interface to a large extent in which the delamination behavior is known to be more susceptible to phenomena such as delamination migration, stick-slip, and could lead to the failure of the peel - arm. Notably, the reproducibility remains highly questionable.

2.7.4 Double Drum Peel (DDP) Test

The concept of the Double Drum Peel (DDP) test originated at Cetim [28], intending to facilitate the experimental analysis of the bonding quality (delamination behavior) in the Laser Assisted Tape placement rings with a particular focus on the impact of various processing parameters. In this testing, the specimen is cylindrical, fabricated by winding a composite tape circumferentially around a mandrel (R1), such that the end region of the tape remains intentionally unattached from the rest of the specimen (acts as a peel-arm) to serve as a pre-crack to conduct the standard peeling delamination propagation tests (Figure 2.24 - left).

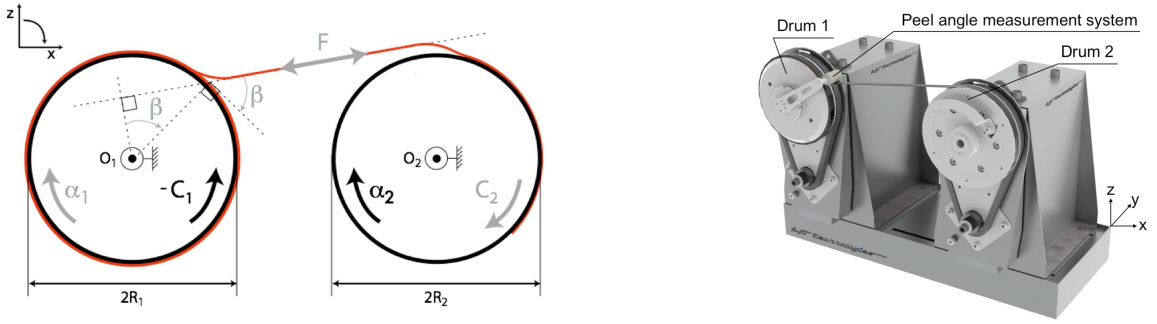


Figure 2.24: DDP test concept (left), and DDP experimental set-up (right) **[28]** .

The test configuration is comprised of two rotating drums or mandrels (R1 and R2), generally with equal radii. During a test, the specimen being evaluated is fixed to drum 1; meanwhile, the peel arm's end is attached to drum 2. Within this experimental setup, the cylindrical specimen is clamped to drum 1 using an elastomeric ring that expands radially, and the peel arm is inserted into a slit and secured with an internal clamp to drum 2. Subsequently, drum 2 is initiated with a steady angular velocity (α) while a motor applies a couple ($C_2 > 0$) to the drum to sustain the prescribed velocity, and its measurement is simultaneously recorded. The resultant rotation exerts a force on the peel arm, thereby initiating the propagation of delamination. In addition, a resisting torque ($C_1 < 0$) is implemented on drum 1 via a feedback control system, which facilitates the selection and maintenance of a consistent and appropriate peeling angle β throughout the experiment. The measurement of angle β, which is necessary for the control loop, is continuously monitored during the test through the use of a measuring arm positioned on the specimen (Figure 2.24 - right).

The authors validated the DDP concept by executing the tests on CF/PEEK rings fabricated by (LATP) and considering various configurations, with peel angles (β) ranging from 30° to 50°. It is to be mentioned that the tensile and bending strength of the material (peel arm) under investigation limits the peeling angle range. The findings in this study highlight that the tests with angles 30° and 50° experienced unstable crack propagation, while the 40° peel specimens exhibited delamination with steady couple measurements. It is further stated that unstable delamination resulted in reduced stable propagation region for effectively evaluating the fracture energy, suggesting that the DDP test is unsuitable for small peel angles ($\beta < 30°$). Next to that, the DDP specimens tested at $\beta = 50°$, which displayed irregularities (sudden force rise and torque decrease) was, attributed to the considerable fracture observed in the peel specimen in the form of fiber breakage and transverse crack due to the local bending, indicating that the peeling angle is also not so applicable for fracture energy characterization.

Their analysis based on the analogical principles of the classical peel test showed that the mode mixity was calculated to be constant $G_{II} = 0.6G_I$ for the peel angle range within this test, thereby expecting constant fracture toughness irrespective of the tests. According to the authors, the above hypothesis agrees reasonably well with the results showing more or less similar fracture toughness of around 2 kJ/m^2 for the various peel angles tested with exceptions.

Although the DDP looks likely optimistic for testing the delamination properties of curved and cylindrical structures, in a broader sense, it still appears to suffer from similar issues associated with the classical variable angle peel test, more notably the challenges in controlling the peel angle and peel-arm failure (tough materials). Nonetheless, it is still very early to comment exclusively on the basis of one study.

2.7.5 Mandrel Peel (MP) Test

Mandrel Peel (MP) test was developed and established by Kawashita. et.al [140][141] as an alternative method which was predominately utilized for metal-polymer laminates in the determination of adhesive fracture toughness. In the last few years, the potential applicability of the mandrel peel test for characterizing the interlaminar/interfacial fracture toughness has been explored and demonstrated due to the inapplicability of standard peel tests. Figure 4.13a is the graphical representation of the mandrel peel test configuration.

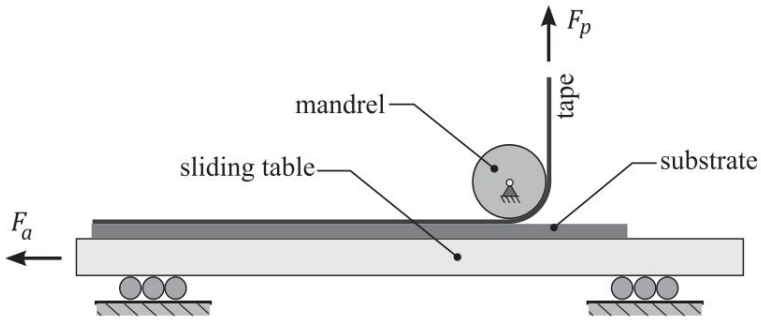


Figure 2.25: Schematic illustration of the mandrel peel test set-up [15].

As can be seen, the substrate (rigid adherend) of the specimen is fixed to the set-up's sliding table, which is attached to the Universal testing machine. The peel - arm of the specimen, which is flexible, is bent around a cylindrical mandrel. The mandrel acts as a bearing capable of rotating around a fixed shaft. One characteristic feature that distinguishes the mandrel peel test from the various roller-assisted techniques is the application of alignment or balancing force that can be adjustable along the sliding table to ensure and attain peel - arm conformity with the mandrel. After ensuring conformity, a tensile force is eventually exerted to peel off the peel-arm from the rigid fixed arm. Furthermore, the mandrel roller radius can be varied to achieve desirable experimental conditions. The experimental protocol encompasses two peeling cycles. In the initial first cycle, the peel arm is separated from the laminate to a pre-determined delamination length. After the first cycle, the unbonded peeled specimen (G_c

=0) is subjected to another peeling process to determine the friction coefficient, μ, in the mandrel peel set-up.

Critical Strain Energy Release Rate (SERR) Formulation for the MP Test

To comprehensively characterize the delamination behavior of composites (and bonded/hybrid joints) at a global level, it is vital to establish a precise methodology for determining the overall critical energy release rate (G_c) based on experimental data. This section will revisit the fundamental energy balance principles essentially utilized by Grouve et al.[36] in evaluating the critical strain energy release rate.

The interlaminar fracture toughness/energy release rate determined by the mandrel peel test is represented in terms of strain energy change per unit area of crack growth [36].

$$G = \frac{1}{b}\left(\frac{dU_{ext}}{da} - \frac{dU_d}{da} - \frac{dU_s}{da}\right) \tag{2.6}$$

where U_{ext} is the external work, U_d is the dissipated energy during peel test and U_s is the strain energy stored in the peel arm. The crack area change is |bda| in which b is the width of the peel arm, and da is the crack length increment.

In addition, the residual stress induced during the manufacturing is also taken into account in the analysis. The external work due to the crack growth da corresponds to

$$dU_{ext} = -F_a da + F_p da + F_p da(\epsilon_m - \epsilon_r) = (F_p - F_a)da + \frac{F_p^2}{bhE}da - \frac{F_p \sigma_r}{E}da \tag{2.7}$$

where h and E are the thickness and Young's modulus of the peel arm, respectively. ϵ_m corresponds to the elastic strain in the peel arm and whereas ϵ_r denotes the pre- strain in the peel arm caused by a residual stress σ_r.

The dissipation of energy during the peeling involves the plastic deformation of the peel arm and the friction in the test set-up. Further, for a peel arm with UD reinforcement, the dissipated energy via plastic work is generally considered to be negligible. Therefore, during the peeling test, only friction is accounted for and taken into consideration, which is proportional to the peel force, F_p and is given as:

$$dU_d = \mu F_p da \tag{2.8}$$

The strain energy U_s of the global system comprises the tensile strain energy stored in the peel arm and substrate and the residual strain energy stored in the bonded part of the peel arm and substrate. The change in strain energy associated with incremental crack growth is represented as:

$$dU_s = \frac{1}{2}\sigma_m \epsilon_m bhda - \frac{1}{2}\sigma_r \epsilon_r bhda = \frac{1}{2}\frac{F_p^2}{bhE}da - \frac{1}{2}\frac{bh\sigma_r^2}{E}da \tag{2.9}$$

The energy release rate is finally expressed as:

$$G = \frac{1}{b}\left[F_p(1-\mu) - F_a + \frac{1}{2}\frac{F_p^2}{bhE} + \frac{1}{2}\frac{bh\sigma_r^2}{E} - \frac{F_p\sigma_r}{E}\right] \tag{2.10}$$

Besides, if the contribution of stored strain energy and the residual stress in the peel arm to the overall strain energy release rate is significantly negligible. Consequently, both the terms can be ignored during the calculation; eventually, Equation 5.18 can be rewritten as:

$$G = \frac{1}{b}\left[F_p(1-\mu) - F_a\right] \tag{2.11}$$

A more detailed formulation of the contribution of residual thermal stresses and the tensile strain energy can be found in [35].

Advantages of Mandrel Peel Test

- In terms of practicality, the mandrel peel experiments prove to be comparably simple to execute, with straightforward, uncomplicated data processing formulation.
- The mandrel peel test enables to characterize the interlaminar/interfacial properties of various interesting interface configurations [composite (0^o-0^o,$0^o-\theta^\circ$, $\theta^o-\theta^o$) composite – composite, metal – composite] with simple and economical specimen design.
- The mandrel roller, combined with the alignment force, effectively maintains the peel-arm curvature, minimizing the likelihood of peel-arm failure, and the peel front angle can be controlled precisely (over other peel tests).
- The kinematics of the mandrel peel test (mandrel roller) enables establishing a relatively straight crack growth front controlling the crack tip location.
- The mandrel peel test typically generates more fracture data as the mandrel tends to arrest any unstable crack propagation, thereby increasing the statistical reliability and relevance of the test results (compared with the DCB test).
- The tests do not require monitoring and measuring the crack tip propagation, unlike the classical DCB, ENF and MMB tests.
- The critical energy release rate formulation considers the effects (contribution) of residual thermal stresses.

2.8 Influence of Specimen Geometry and Testing Conditions

The preceding section presented the mandrel peel test as a promising alternative testing methodology for evaluating the interlaminar/interfacial properties. Despite ongoing efforts to explore its efficiency in assessing the fracture toughness properties of laminated materials, the MP test remains in its nascent stage of development. This section examines and presents a discussion on the effects of the MP specimen design geometry and the testing conditions and parameters on fracture toughness and behavior.

2.8.1 MP Specimen Interface Configuration

This section briefly presents a review of the application of the mandrel peel tests on various interface configurations. Table 4.3 shows the summary of the mandrel peel tests from the literature.

Grouve et al. [36]conducted an experimental study to investigate the feasibility of employing the mandrel peel test to evaluate thermoplastic composites' fracture toughness (Gc). This was achieved by comparing the results obtained from the MP test with those from the DCB and ELS tests, which measure the pure mode I and II fracture toughness, respectively. For this purpose, UD CF/PPS and CF/PPS hybrid composite with woven fabric - UD ply as interface were analyzed for the testing, and the experimental setup for the MP test featured a mandrel roller of 5 mm radius and an alignment force of approximately 75 N with a peeling rate of 15 mm/min. The mandrel peel results showed an approximate 20% reduction in the propagation fracture toughness relative to the mode I DCB and mode II ELS specimens for the UD interface. Further, a low degree of scatter in the mandrel peel tests was observed, consistent with that of the DCB and ELS specimens. The authors attributed the cause for the reduced fracture toughness to the relatively low-scale fiber-bridging effects during the peeling test in comparison with the DCB tests based on the photographic analysis. Whereas for the specimens featuring a hybrid interface, both the DCB and ELS tests failed to yield the results due to the migration of the crack front towards the UD CF/PPS ply. During the ELS testing, the specimens exhibited highly unstable crack growth after the crack onset. Nonetheless, the study revealed that the fracture toughness of the hybrid specimens could be quantified by applying the mandrel peel test, demonstrating acceptable repeatability with low SD.

To assess the weld strength and the degree of bonding of thermoplastic composites, Grouve et al. [142][15]utilized the mandrel peel test to evaluate the interface properties between the UD thermoplastic CF/PPS tape and CF/PPS woven laminate in terms of fracture toughness as a metric to compare the efficacy of the laser-assisted tape placement process with traditional press molding technique. The results illustrate that the tape-placed specimens exhibit higher interfacial fracture toughness than those produced through press molding. More importantly, the authors conclude from the study that the mandrel peel test successfully allowed to examine the effects, such as the degree of crystallinity and the weld interface induced by the process parameters on the interfacial properties, highlighting the potential of mandrel peel test as an effective means for characterization and enabling parametric optimization of the manufacturing process.

With peel tests being proven to be a compelling option for measuring the interfacial properties (fracture toughness) of hybrid joints as they can accommodate tailored specimen design configurations such as (not limited to) co-consolidation of a layer of UD thermoplastic composite onto a metallic substrate, Yibo et al. [35] proposed mandrel peel test for investigating the fracture toughness of Titanium – CF/PEEK co-consolidated joints. The experiments established that the assessment of interfaces exhibiting high toughness could be well accomplished, which in fact, is not feasible with standardized conventional peel tests due to the occurrence of tape failure. Notably, it was also shown that friction influences the measurements in the mandrel peel tests. Continuing on this, Yibo et al. [143] further extended the work on Titanium- CF/PAEK joints; however, this study involved examining the influence of surface treatments on the titanium on the interfacial fracture properties, utilizing the mandrel peel test as a quantifying means for the joint quality. According to this study, two different modes

of failure were noted. While all the Ti-CF/PEEK and Ti-CF/PEKK (anodized/untreated) specimens exhibited interfacial fracture behavior, the grit-blasted Ti-CF/PEKK joints failed at the CF/PEKK interface, basically intralaminar fracture, leading to a partial UD tape failure along the fiber direction (normal to the Ti - CF/PEKK interface). It is said that the contribution of this localized peel arm fracture energy was approximated to be around 5-10% of the determined fracture energy during the test. Based on the bonding mechanism observations and evidence, the authors affirm that the surface treatment and the thermoplastic tape type play a substantial role in the interfacial properties of the metal-thermoplastic composite joints.

Similarly, based on the works of Grouve et al.[36] and Yibo et al.[143], Peters et al.[144] focused on studying the process (selective tape placement) parameters effects, specifically the processing temperature on the interfacial bond strength between the GF/Polyamide UD thermoplastic composite tape and the (laser textured) steel hybrid-joint using the mandrel peel test. In this work, it has been reported that the mode of failure is interfacial with traces of resin found in the textured cavities. The authors show that the initial macroscopic observation and fracture surface and cross-sectional analysis of the steel substrate after the mandrel peeling test, which reveals the bonding mechanism (mechanical interlocking) of the resin into the textured cavities and the corresponding fracture toughness, yields an understanding on the process parameter influence and enables for further optimization of the tape placement process.

The need for the fastener-free metal-TPCs hybrid joints and the rising advent of co-consolidation as a potential alternative for the conventional joining methods motivated Vanessa et al. [145] to perform research on the influence of surface treatment (grit-blasting) on the interfacial fracture properties of the co-consolidated Ti- UD CF/PEKK hybrid joints. The mandrel peel test characterized the fracture toughness properties, and the results signified that the surface topography (roughness) governs the mechanism of failure, and a transition from interfacial to intraply was found by the authors. It has been argued that the correlation between fracture toughness from the mandrel peel test and the microscopy examinations on the fracture surface enabled quantifying the critical surface roughness value where the transition in the failure behavior was noticed.

The suitability of quantifying the fracture toughness of CF/PEEK woven fabric thermoplastic composites by the mandrel peel test was explored by Sacchetti et al.[30]. This study's mandrel peel experiments involved studying the peel specimen width and peeling rate effects on the determined fracture toughness. The outcome indicated no peeling rate influence, while wider specimen width exhibited relatively lower toughness values. Based on the analysis, the authors deduced that the mandrel peel test was more efficiently straightforward and reliable than DCB. This is supported by the evidence that both tests generated comparable fracture toughness data and exhibited consistent stick-slip fracture propagation phenomena. Moreover, the findings reveal that utilization of the mandrel enabled restricting the unstable crack growth and generated around 20 times more data points per unit crack increment than the DCB test.

Followingly, Sacchetti et al.[34] extended the applicability studies on the same CF/PEEK woven fabric laminates as the previous studies. However, the main focus of this investigation involved evaluating the interlaminar fracture toughness in the parallel and perpendicular direction to the fiber orientation at the interface and comparison with the DCB and ELS

experimental results. This research presents that both the DCB and the mandrel peel specimens display instability in the crack growth characterized by the stick-slip behavior, whereas the crack grows steadily in the ELS specimens. The propagation fracture toughness measurements are found to be comparable to the DCB toughness data for both tested interfaces; however, it is also proposed by the authors that the occurrence of pronounced stick-slip phenomena during the DCB testing leads to an overestimation of fracture energy values. It was further confirmed again that the mandrel could limit the instability by suppressing the unstable growth of cracks, eventually creating multiple re-initiation of cracks, thereby enhancing the statistical significance and reliability of the mandrel peel test.

In recent work, Andreas et al.[29] displayed the potentiality of the mandrel peel test as an appropriate and viable approach for conducting tests on thermoplastic tapes consolidated on thermoplastic substrates. According to the studies, the tested UD GFPP – GF/PP mat peel specimens have exhibited two distinct fracture behaviors: delamination growth along the interface (interfacial failure) and, in another case, fiber pull-out from the substrate; these behaviors relate to two different processing conditions (Figure 2.26). Varying orientation (IR-Roll direction, NR- perpendicular to IR) of the GF/PP mat substrate relative to the UD GF/PP tape generates different fracture toughness values, with IR exhibiting higher toughness comparatively. However, it has been reported that localized bending of the substrate found during the peeling of IR specimens resulted in the overestimation of the fracture energy values, in contrast to the NR peel specimens, where there were no such behaviors. As the process parameters (pressure, consolidation temperature, and time) effects on the fracture energy were investigated, with this work, the authors concluded that the possibilities of developing a processing window based on the interface properties determined by the mandrel peel test are promising.

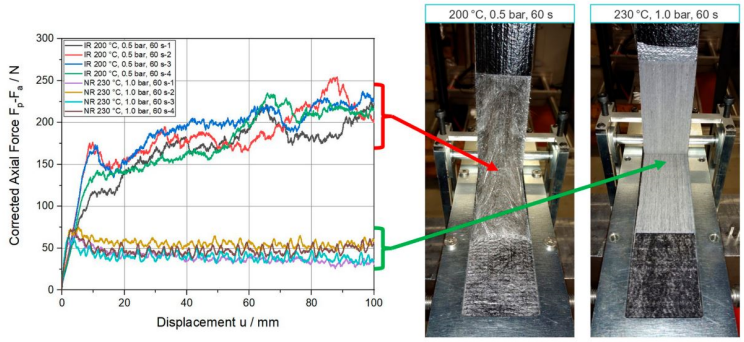


Figure 2.26: Two distinct fracture behaviors: delamination growth along the interface (interfacial failure) and, in another case, fiber pull-out from the substrate; these behaviors relate to two different processing conditions**[29]**.

In 2023, as a part of ESIS TC4 round-robin testing, a comparative assessment of the climbing drum peel (CDP) test and mandrel peel (MP) test in determining the interlaminar fracture toughness with the standard DCB tests was published [137]. In this round-robin evaluation, various types of material systems were tested: (Epoxy laminates (partly and fully cured) –(0|0) interface and CF/PAEK laminate - (0|0), (0|90) interface)). The experiments' findings for both epoxy and CF/PAEK laminates featuring the unidirectional interface (0|0) indicate that the propagation fracture toughness to be in agreement with a variance of approximately 20%.

Testing of CF/PAEK - 0|90 interfaces with crack propagating unstable (stick-slip behavior), the mandrel peel testing has been found to be more consistent over the delamination length, compared to the climbing drum peel test, which displayed a decreasing trend in the R-curve. Moreover, it is shown that high repeatability (low scatter -13%) could be achieved with the peel tests than the DCB tests, which exhibited a scatter of around 17%. Nonetheless, the authors declare that more research is underway within the round-robin tests (various material systems, interface configurations) as it necessitates investigating the reproducibility of the Mandrel peel tests and will be addressed in the subsequent studies.

Material	Stacking Sequence	Interface	Mandrel radius (mm)	Peel-arm thickness (plies)	Width (mm)	Peeling rate (mm/min)	Reference
UD CF/PPS	$[0\|0_{19}]$	0|0	5	1	8	15	[36]
CF/PPS woven fabric	$[0\|(F_{2s}/0/0/F/0/F_{2s}/0)]$	0|(90/0)	5	1	8	15	[36]
UD CF/PEEK - Titanium	[0|Ti]	TPC | Metal	10	1	10	15	[35][143]
CF/PEEK woven	$[(0/90)/(0/90)_r]_{4s}$	(0/90)|(90/0)	10	1	10, 18	3, 30	[30]
CF/PEEK woven	$[(0/90)/(0/90)_r]_{4s}$	(0/90)|(90/0)	10	1	10	30	[34]
UD CF/PEEK	$[0\|\ (\theta/0_{14}/\theta\ /0)]$	0|0, 0|30, 0|45, 0|60, 0|90	10	1	10	15	[31]
GF/Polyamide - Steel	[0|Steel]	TPC | Metal	10	1	25	20	[144]
UD CF/PEKK - Titanium	[0|Ti]	TPC | Metal	10	1	10	15	[145]
UD GF/PP - GF/PP Mat	[0|GFPP mat]	TPC |TPC(mat)	Not available	1	44	1	[29]
UD CF/Epoxy	$[0\|0_6]$	0|0	20	1	10	Not available	[137]
UD CF/PAEK	$[0\|0_{14}], [0\|(90/0)_7]$	0|0 , 0|90	20	1	10	Not available	[137]

Table 2.1: Summary of the mandrel peel tests in the literature used for determining the fracture toughness.

2.8.2 MP Specimen Width

Sacchetti et al.[30] was the first to explore the MP specimen width effects on fracture toughness. The results of the MP tests for C/PEEK 5 harness woven specimens of width 10 and 18 mm at a constant peeling rate of 30 mm/min revealed that the wider peel specimens (18 mm) exhibit a marginally reduced toughness with a relatively low standard deviation, comparatively (Figure 2.27 -left). As stick-slip failure behavior was observed irrespective of the specimen width, the study also highlighted that the spacing between instabilities (distance between two peaks) indicated a reduction with increasing specimen width (Figure 2.27).At the same time, no explanation was provided for the observed effects.

On the other hand, from the works of Grafen [31] for the UD CF/PEEK, the analysis demonstrates that the calculated fracture toughness, (G_c) remains unaffected by variations in the specimen width size. This is evident from (Figure 2.27 -right), which shows that the mean (G_c) values for specimens with widths of 10 mm and 17 mm are 1.58 kJ/m^2 and 1.59 kJ/m^2, respectively. Furthermore, the standard deviation for a width of 10 mm is 0.1663, while it is 0.1645 for a width of 17 mm. However, from the experimental observations, Grafen also found a twisting effect on the 17 mm wide peel specimens, which was attributed to vertical alignment issues since the comparatively smaller clamping grips (attached to the machine) presented challenges, leading to a twisted clamping and alignment. Suggesting that the wider peel specimens might be less appropriate for the mandrel peel tests as this twisting phenomenon could generate a non-uniform distribution of force at the peeling front that might potentially impede the propagation of crack along the intended path.

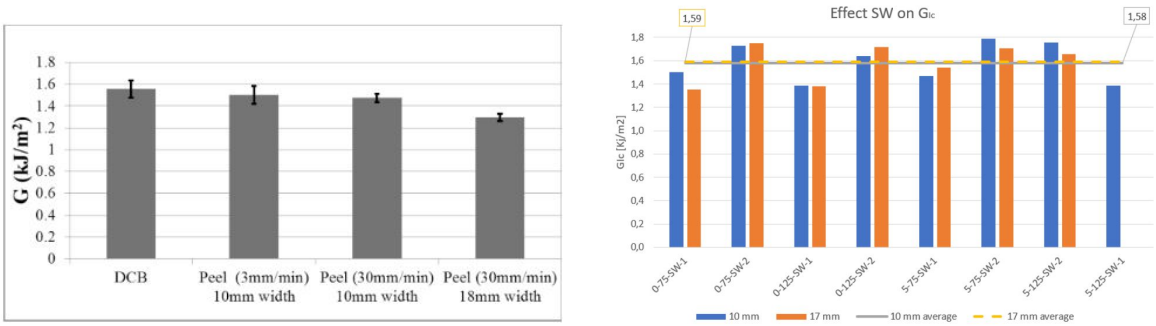


Figure 2.27: Fracture toughness values for different CF/PEEK woven samples (Width and Peeling rate)(left) **[30]**, and Fracture toughness values for UD CF/PEEK values (right) **[31]** .

From the energy balance equation, the fracture toughness determined as the effective peel force per width apparently implies that the fracture toughness value should essentially remain uninfluenced by the width of the specimen. Discussing from the perspective of the effect of the peel specimen width on the crack front curvature, it can be considered to be minimal as the kinematics of the mandrel peel test enables establishing a relatively straight crack growth front controlling the crack failure location, leading to a better strain energy distribution across the width, unlike the standard tests. From this aspect, the width size effect on the strain energy release rate can be expected to be non-critical in mandrel peel tests.

2.8.3 MP Specimen Thickness

The composite mandrel peel specimen's thickness can be expressed as a function of the variables, namely the thickness of individual plies and the total number of plies, and this applies to both the substrate and the peel - arm. While in the case of hybrid joints with metallic peel - arms or substrates, it is just representative in terms of the thickness of the metal. Studies related to different kinds of material systems can be found in the literature, and in most of the research on mandrel peel test of monolithic composite materials (also metal-thermoplastic hybrid joints with composite peel - arm), the peel - arm thickness is discussed in terms of the number of plies. Henceforth, the same representation will be followed in this section.

Initial works pertaining to the mandrel peel test method involved characterizing the adhesive fracture toughness of various metal-polymer laminates. Some of these studies also aimed at

exploring the specimen thickness effects. Kawashita et al. [33] performed mandrel peel tests with a mandrel size of 20 mm for peel-arm thicknesses of 0.63, 1.635 and 2 mm to examine its effects on the fracture toughness of adhesively bonded aluminum laminates. From their tests, it was shown that the cohesive plane of failure was observed in all the cases. Further, aggregable toughness values (compared to other test methods) were obtained only for higher alignment loads, as no peel-arm to mandrel conformance was achieved for low alignment loads, whereas 0.63 mm thick peel-arm failed to attain any conformation irrespective of the alignment load. This study also highlighted (including practical test complications) that peel-arm with increasing thickness would demonstrate a higher degree of plastic energy due to bending, necessitating large alignment loads (external energy) to conform to the mandrel (Figure 2.28- right).

In another work [32] on the effects of peel-arm thickness on the fracture toughness of adhesive, it was noted that the adhesive exhibited no significant sensitivity to variations in peel-arm thickness (0.5, 1, and 1.5 mm), with the exception of a comparatively low adhesive toughness for 0.5 mm thick peel-arm (Figure 2.28- left). This behavior was attributed to the plausibility of interfacial fracture occurring at this thickness value.

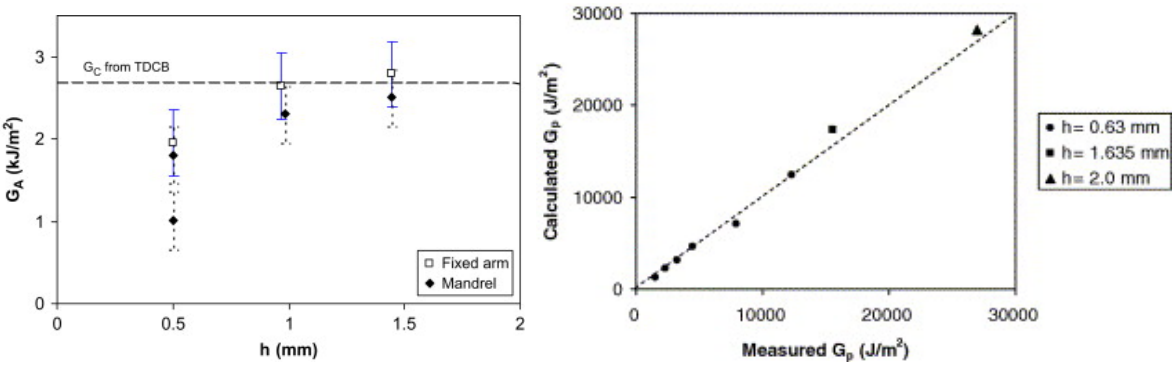


Figure 2.28: Adhesive fracture toughness values for different peel-arm thickness (left) **[32]**, and Increasing plastic bending energy with the thickness (right) **[33]**.

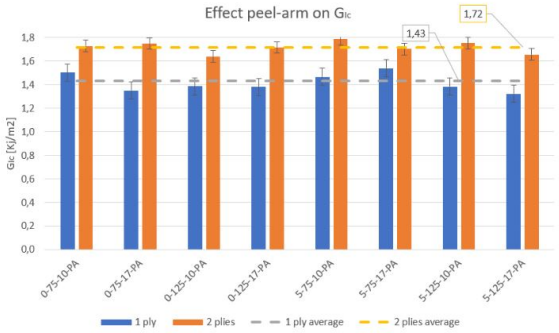


Figure 2.29: Effect of peel-arm thickness on the propagation fracture toughness **[31]**.

Recently, Grafen [31] investigated the influence of the peel-arm thickness on the fracture toughness of the UD CF/PEEK composite material system. The mandrel peel tests were performed for peel-arm thicknesses of one ply and two plies using a 10 mm mandrel radius.

The study reported the average propagation fracture toughness values to be 1.43 ± 0.072 kJ/m^2 and 1.72 ± 0.049 kJ/m^2 for one-ply and two plies thick peel-arms, respectively, indicating a possible sensitive correlation between fracture toughness and the peel-arm thickness (Figure 2.29). However, the author also speculates the observed fracture toughness variation by attributing to the two different laminates employed to fabricate the specimens. Apart from this, it is argued that this effect might also arise due to differences in the global stiffness of peel-arm or increased migration of fibers.

More importantly, it is stated that the migration of cracks can occur, and there was no clear relation between the specimen geometric/testing parameters and crack growth behavior observed. It is also mentioned that peel testing of two-plies thick specimens caused challenges associated with the clamping to the machine's grips due to higher stiffness, proving challenging to bend and conform to the mandrel roller and consequently slightly misaligned and peel-arm twisting were observed.

While it is understood that the specimens with metallic peel-arm also involve dissipation of plastic energy due to the bending of the peel-arm over the mandrel, influencing the fracture toughness, this could be anticipated to be less applicable in the case of a peel-arm (fiber-reinforced polymer composites) with a fiber orientation along the peeling force. Regardless, the effect of peel-arm thickness on the fracture toughness measurement using mandrel peel tests lacks significant understanding.

2.8.4 Mandrel Roller

The mandrel roller, combined with the alignment force, effectively controls the peel-arm curvature [141][146]. As mentioned earlier, the characteristic advantage is that the mandrel roller size can be varied in accordance with the materials being tested. The mandrel roller size and the mandrel's vertical position are the variables associated with the mandrel.

Earlier works of Kawashita et al.[33] analyze the mandrel roller size influence on the fracture toughness of the polymer-metal laminates. This particular experimental study utilized a range of mandrel radii (5, 7.5, 10, 15, 20 mm) for the mandrel peel tests with a peel-arm (metal) thickness of 0.635 mm. It was reported that in all the test cases, there was no conformity of the peel-arm to the mandrel, irrespective of the alignment load, except with a 5 mm radius where the conformation was achieved at high alignment loads. The results showed a transition in the fracture plane from cohesive to interfacial behavior for the 5 mm radius, whereas the peel specimens failed in a cohesive mode for the other mandrel radius. The fracture behavior observed with a 5 mm radius was attributed to the generation of highly localized interfacial stresses due to the conformance. The findings revealed that the non-conformance greatly influenced the measured adhesive fracture toughness, indicating the importance of appropriate mandrel roller size selection. Nonetheless, plastic bending energy dissipation was minimized with increasing roller radius (Figure 2.30- reduction is unrelated to the non-conformance). The authors further established an empirical relation between the peel-arm curvature radius (R_0) and mandrel radius (R_1), suggesting that to attain peel-arm conformity, the condition $R_0 > R_1$ should be satisfied.

In another work by Kawashita et al.[147], peel tests with a 1 mm peel arm (metal) for two mandrel radius sizes of 10 and 15 mm, based on their analysis, it was stated that mandrel radius size is unlikely to affect the fracture toughness measurements. Despite observing a

G_A, G_P and plastic corrections for 0.635 mm AA 2024 T3/Adhesive F from mandrel tests exhibiting cohesive fracture

Mandrel roller radius (mm)	Mean G_A (J/m^2)	Measured G_P (J/m^2)	Plastic correction (X) (%)
5	3000	12,300	80
7.5	4660	7930	65
10	4660	4490	50
15	5650	2320	29
20	6870	1550	18

Figure 2.30: Table showing the reducing plastic bending energy (G_p) with increasing mandrel size **[33]**.

difference of around 15% among the tests, the authors drew no conclusive inferences, which were limited by the errors involved.

When testing specimen configurations with composite peel-arm, it is shown that the selection of the mandrel size plays a crucial role, as the roller radius affects the bending strain of the peel arm, which is bent around the mandrel roller [35]. As such, the bending strain, which is dependent on the mandrel radius (R) and the thickness of the peel arm (t), can be estimated through the empirical relation:

$$\epsilon = \frac{t}{2R} \tag{2.12}$$

All the studies thus far have employed mandrel radius (for a given peel-arm thickness) such that the bending strain does not exceed the maximum strain of the peel-arm (basically the fibers) to prevent the flexible peel-arm from failure.

Besides the potential advantage of the mandrel in controlling the location of the crack front, another aspect is that according to the research by Sacchetti et al.[30], in the case of unstable crack growth, the spacing between the instabilities is restricted compared to that of the conventional DCB tests. The mandrel roller assists in impeding the unstable propagation of crack upon each occurrence, necessarily leading to offering multiple crack re-initiations per unit crack increment [30][34] and the most effective explanation can be found through the illustrative depiction in Figure 2.31.

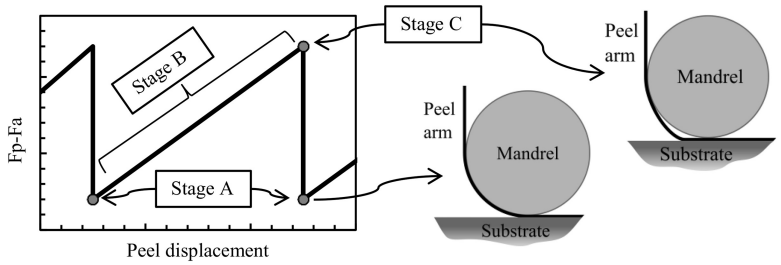


Figure 2.31: Stick-slip behaviour**[34]**.

During the initial loading step of the peel testing, the peel - arm exhibits conformity to the mandrel. With a gradual increase in the load, stick behavior is noticed, as the advancement of crack does not occur, and consequently, the peel - arm fails to sustain and loses its conformation around the mandrel. Upon further increase in the applied load, eventually attaining

the maximum force, the amount of energy stored within the system becomes sufficient to re-initiate the crack growth, and this leads to instability in the crack growth with an instantaneously abrupt load drop referred to as slip. As the sudden growth of the crack terminates, the peel - arm regains its conformation with the mandrel.

Next, the vertical positioning or the contact of the mandrel roller relative to the peel specimen plays a significant role since it not only might have an influence on the peel-arm breakage but also the friction because of the rolling line contact of the mandrel with the specimen (Figure 2.32).

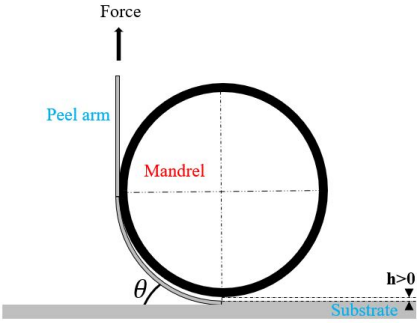


Figure 2.32: Schematic representing the peel-arm contact with the mandrel.

When there is no initial contact between the mandrel and the specimen at the crack front, the mandrel is positioned (vertically) too away from the base of the specimen, which is fixed rigidly, and as a consequence, the specimen experiences deflection, which causes internal stresses. Besides, the chances of peel-arm breakage are higher due to the peeling force and the alignment force combined with the generated peel angle. If the mandrel is in firm contact with the specimen, though the probability of the breakage of the peel arm gets minimized, the prospect of an increase in the overall friction of the set-up is more due to the high contact pressure. The ideal and preferred condition is when the mandrel is in frictionless or low frictional contact with the specimen at the crack front. Thus, it is essential to adjust the mandrel's vertical position to achieve the preferred condition before the test.

While it is apparently clear that the issues, such as the non-conformance and plastic bending energy, associated with the testing of metal-laminates is known to have affected the adhesive fracture toughness evaluation, no comprehensive insights could be obtained from the literature exploring the mandrel size effects in the mandrel peel testing. As far as the limited literature available on the testing of the composites utilizing the mandrel peel test for the evaluation of the fracture toughness, there are no studies focused on exploring the mandrel size effects on the fracture toughness.

2.8.5 Crosshead Displacement Rate (Peeling Rate)

Sacchetti et al.[30] investigated the influence of the displacement rate (peeling rate) on the fracture energy (G_c) of C/PEEK woven fabric laminates determined using the mandrel peel tests. With this purpose, the peeling tests were performed with a specimen width of 10mm

at two displacement rates of 3 mm/min and 30 mm/min. The experimental results showed no displacement/peeling rate effect on the fracture toughness measured (Figure 2.27 -left). In this study, the fracture behavior exhibited a stick-slip phenomenon, and interestingly, the findings suggest that an increase in the peeling rate leads to a decrease in the spacing between instabilities during mandrel peel tests (Figure 2.33). The authors propose for additional investigation to comprehend these occurrences. No conclusion can be derived from this only study related to the peeling rate effects on fracture toughness.

Sample	Average distance between peaks	Standard deviation
DCB	20.3 mm	2.2 mm
3mm/min 10 mm W	0.94 mm	0.1 mm
30mm/min 10 mm W	0.83 mm	0.07 mm
30mm/min 18 mm W	0.72 mm	0.06 mm

Figure 2.33: Overview of the mean spacings between peaks for the different samples tested at different peeling rates **[30]**.

2.8.6 Alignment Force

Typically, the alignment force facilitates the peel-arm and mandrel conformation. The alignment force requirement depends on several factors, such as the radius of the mandrel, the material system, the peel-arms' width and thickness, and the material's fracture toughness properties. A poor and improper peel-arm conformation with the mandrel might be attributed to the inadequate alignment force, which could have a consequence on the stick-slip behavior or the other way around. Further, the stick-slip behavior may cause irregularities in the crack propagation rate/velocity and even a shift from the intended plane. Though the reason for slip-slip behavior involves several factors, it is nevertheless vital to prevent the stick-slip phenomenon caused due to imperfect mandrel conformation. Figure 2.34 shows the schematic of the effect of alignment force on the peel–arm–mandrel conformation behavior.

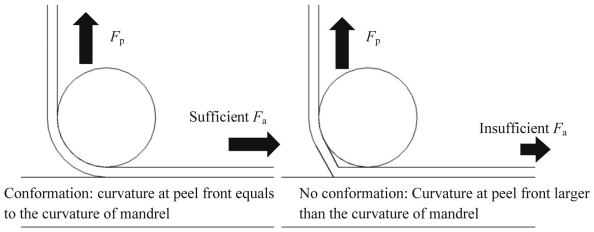


Figure 2.34: Schematic representing the conformance (left) and non-conformance (right) as a function of alignment load **[35]**.

Kawashita et al.[33][32] discovered that during the testing of metallic-peel arm polymer laminates, an increase in alignment loads resulted in a more uniform peel crack propagation along the intended plane. However, this phenomenon was also associated with decreased fracture toughness value for various reasons (at low alignment loads, a transition from interfacial to cohesive failure was noticed, while high alignment force caused the interfacial failure). while high alignment force caused the interfacial failure). Grouve et al.[36], in the initial study for UD CF-PPS composite, performed the mandrel peel experiments with two alignment loads of 75 N and 150 N to explore the alignment load effects on the measured interlaminar fracture

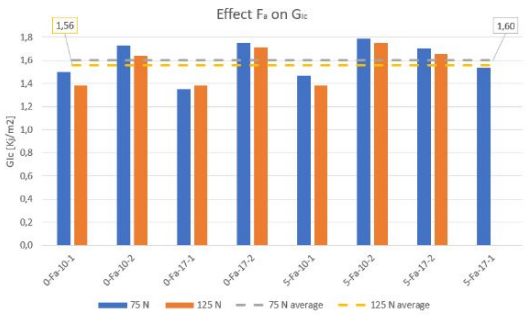


Figure 2.35: Effect of alignment force on the fracture toughness **[31]**.

toughness. The average steady-state propagation fracture toughness was found to be around 853 ± 51 J/m^2 for 75 N alignment force, and in the case of 150 N, it was determined as 829 J/m^2. Based on the evidence, the authors state that the fracture toughness is unlikely to be influenced by the alignment force.

Similarly, with the same objective, Grafen [31] chose the alignment force of 75 N and 125 N for the UD CF/PEEK peel specimens (for one ply and two plies peel-arm thicknesses). From the findings, it was suggested that the propagation fracture toughness remains unaffected primarily irrespective of the alignment force in both the peel-arm cases. The argument was considering the data, which revealed that the mean fracture toughness for the specimens subjected to an alignment force of 75 N was only 0.07 kJ/m^2 compared to what was observed for 125 N. Moreover, the standard deviation was found to be around 0.159 and 0.169 for 75N and 125 N alignment force, respectively (Figure 2.35). Notably, it is also reported that the few specimens tested with 75 N alignment force exhibited intralaminar fracture propagation behavior, despite observing proper peel-arm conformance to the mandrel. This further indicates that the higher alignment force limits the possibilities of delamination migration (similar to the observations of Kawashita et al.).

It is clear that the alignment force is a critical factor, and optimizing the required optimal alignment load for achieving the proper peel–arm–mandrel conformation is purely based on trial-and-error experiments, as no theoretical and analytical relations have been established yet to determine the alignment load.

2.8.7 Friction

Typical with other experimental configurations, the mandrel peel testing setup also encounters friction-related challenges within the associated internal moving parts. According to the mandrel peel test protocol [140], it is recommended that the overall friction of the system does not surpass 5% in order to prevent any potential impact on the accuracy of the results. To minimize friction to the greatest extent possible, the sliding table in the mandrel peel design configuration incorporates a linear motion bearing system, while the mandrel shaft acts on a bearing as outlined in the protocol. The alignment and peel forces influence the coefficient of friction,μ. As mentioned earlier, the frictional coefficient value is determined by performing the peeling test again on the un-bonded specimen, and the correlation between

the alignment (F_a) and peel forces (F_p) is established as follows:

$$\mu = \frac{F_p - F_a}{F_p} \tag{2.13}$$

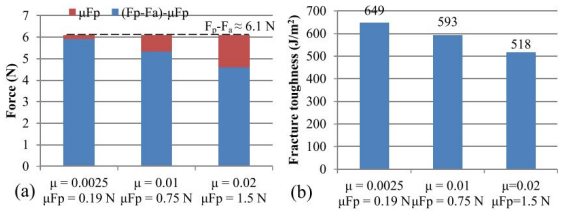


Figure 2.36: (a) The ratio of μF_p to F_p - F_a as different value of μ. (b) The fracture toughness as the different measurement value of μ**[35]**.

The fracture energy relation clearly signifies that the coefficient of friction determination governs the toughness evaluation. In actuality, the value of μ exhibits variation from each tested peel specimen and the experimental set-up. Yibo et al.[35], in their experimental work on the interfacial toughness characterization of metal-thermoplastic composite joints, studied the frictional effects in the mandrel peel test. It was shown that considering a range of μ values obtained for the utilized test set-up, for an average effective peel force (F_p - F_a), the corresponding (F_p - F_a - μF_p) force value after correction for friction varies, consequently impacting the determined fracture toughness. Figure 2.36 apparently indicates the disparity in the fracture energy measurements, thus emphasizing that friction plays a key role, specifically in the case of interfaces exhibiting low fracture toughness.

2.8.8 Mode of Failure

In general, the peel test experimental techniques to determine the fracture toughness is widely considered a combination of mode I and mode II fracture conditions [148][149]. It is worth mentioning that the fracture toughness assessment obtained from the mandrel peel test also basically indicates mixed mode fracture propagation[150]. As such, this implies that the interlaminar/interfacial fracture toughness measurements derived from the mandrel peel test are essentially anticipated to be within the range between the pure mode I and pure mode II fracture values. The limited literature compares the mandrel peel test results for the material system investigated to the pure mode I DCB and pure mode II ELS experiments. While Grouve et al. [36] found that the mode I and mode II values to be similar with stable crack propagation for UD CF/PPS material, in the case of Sacchetti et al. [34] for the CF/PEEK woven fabric laminates investigated, the DCB and mandrel peel tests demonstrated unstable crack growth. In contrast, the crack propagated steadily in the ELS tests with higher fracture toughness. The findings demonstrate that the mandrel peel fracture toughness exhibits a similar correlation with the pure mode I value (DCB tests), whereas they deviate from the pure mode II results (ELS tests). Additionally, complementing the fractographic analysis using the microscopy technique to ascertain the failure mode mechanisms during the mandrel peel testing, it was shown that the fracture surfaces of the mandrel peel specimens exhibit distinctive features of tensile opening mode I failure comparable to DCB while on the other hand, aspects of shear mode failure have been observed in ELS specimens (Figure **2.37**).

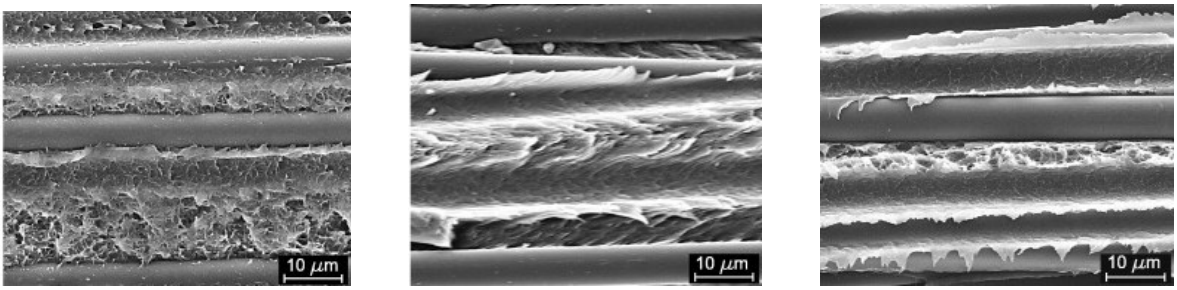


Figure 2.37: Fracture surface exhibiting mode I (left), mode II (center) features and MP specimen (right) showing features similar to mode I **[36]**.

Based on the evidence (toughness value and fracture features), it has been corroborated and considered that the degree of mode mixity is low in the mandrel peel test, more toward mode I loading conditions. Henceforward, all the recent works on the mandrel peel test in the literature have been compared to the DCB tests, including the round-robin tests. Nevertheless, the degree of mode mixity (G_{II}/G_I) factor remains unknown and has not been addressed.

2.9 Mixed Mode Propagation Failure Criteria

The assessment of crack propagation is commonly approached based on the fracture mechanics theory. In the case of pure mode delamination, the crack starts to propagate as the critical value of the energy release rate in mode I or mode II is attained (Equation **2.14**). Standardized test methods, can be used to determine the critical strain energy release rate for different modes. In actuality, most delamination problems are characterized by mixed mode behavior, necessitating the development of a mixed mode criterion to account for the synergetic effects of different modes.

$$G_i \geq G_{ic} \tag{2.14}$$

where i = I, II, and III represents the pure modes.

As previously mentioned, the fracture toughness, G_c, is normally dependent on the mode mix. Given that testing is not feasible for all possible mode ratios, the fracture behavior is inferred from the extrapolation based on the limited test cases, necessitating the selection of an appropriate criterion to model the experimental test data. The precision of the predictions relies on the quality of the initial measurements and the effectiveness of the chosen criterion for approximation.

Extensive studies have been conducted to explore the criteria for delamination under mixed mode conditions, considering various mixed mode ratios. Further, these criteria generally incorporate the mixed mode ratio as a variable(G_{II}/G_T), which can be determined by either employing the stress intensity factor or the strain energy release rate. Some of the noteworthy mixed mode failure criteria have been outlined below:

Linear law: The linear criterion involves normalizing individual mode components of fracture toughness and formulating a linear relationship between the critical values of mode I and mode II fracture toughness, denoted by G_{Ic} and G_{IIc}, respectively.

$$\left(\frac{G_I}{G_{Ic}}\right) + \left(\frac{G_{II}}{G_{IIc}}\right) \geq 1 \tag{2.15}$$

Power law: The power law criterion constitutes a broader extension of the linear criterion that accounts for the non-linearities in the fracture toughness locus. To use this criterion, it is necessary to determine the values of fitting parameters α and β through experimentation. A convex failure locus is observed when the values of α and β exceed unity, whereas a concave failure locus is obtained when α and β are less than 1. When β is greater than α, the failure locus is inclined towards the mode I axis. The linear criterion corresponds to the condition where α equals β equals 1. The criterion developed by Wu and Reuter [151] can be expressed as follows:

$$\left(\frac{G_I}{G_{Ic}}\right)^{\alpha} + \left(\frac{G_{II}}{G_{IIc}}\right)^{\beta} \geq 1 \tag{2.16}$$

Benzeggagh and Kenane (B-K) criterion: As suggested by Benzeggagh and Kenane [152], the B-K criterion is formulated based on the stress intensity factor at the vicinity of the delamination crack tip and is mathematically represented in terms of the energy release rates. The parameter η is determined experimentally.

$$\frac{G_T}{G_{Ic} + (G_{IIc} - G_{Ic})\left(\frac{G_{II}}{G_T}\right)^{\eta}} \geq 1 \tag{2.17}$$

While the linear law is comparatively straightforward to apply, its accuracy may be compromised in cases where the failure loci of composite materials exhibit a convexity. In such cases, the use of a power law with values of α and β greater than one can adequately capture the convexity. The linear law is subject to a few limitations with respect to its applicability, specifically that the values of mode I fracture toughness (G_I) and mode II fracture toughness (G_{II}) must satisfy the conditions $\mathbf{G_I < G_{Ic}}$ and $\mathbf{G_{II} < G_{IIc}}$. Furthermore, it has been documented that the linear law criterion is inadequate to account for the mode mixity variation effects on mixed mode fracture toughness. In contrast, B-K law offers an added advantage over other criteria in that it necessitates computing only one fitting parameter based on the experiments. According to previous research [153][154], the B-K law has demonstrated the ability to represent changes in mixed mode ratio effectively. The B-K law's proficiency in this aspect and other favorable attributes have established it as the predominant criterion for delamination propagation in both the Virtual Crack Closure Technique (VCCT) and the Cohesive Zone Model (CZM).

2.10 Mixed Mode Partitioning

The overall fracture energy, G_c, can be separated into different mode components, and this partition process is known as **mode partitioning**.

As highlighted in the preceding sections, the fracture toughness dependence on the mode mixity is extensively acknowledged, moreover understood, while, for an interface crack, the total fracture toughness is relatively straightforward to determine; however, it is known to

be rigorous and challenging to partition the contribution of each mode, primarily due to the fact that this type of crack intrinsically experiences mixed mode loading. A commonly adopted customary scientific practice in fracture testing is to employ the **critical failure envelop method**, which involves estimating the fracture toughness of various mixed mode ratio combinations by extrapolating based on limited mixed mode test cases. Nevertheless, as mentioned earlier, one of the primary challenges in experimentally achieving a comprehensive fracture envelope for laminated composites and the various bonded joints is the absence of a single test specimen geometry or the loading fixture capable of effectively characterizing the entire spectrum of in-plane fracture conditions.

Several analytical mode partitioning models have been proposed and developed based on the beam theories categorized as **global methods** and based on stress intensity factors classified as **local methods** to mention a few (Williams [55], Suo and Hutchinson [155], Thouless [156] [157], Davidson [158], Wang and Harvey [159], Reeders and Crew Jr [99]). The models derived from the abovementioned approach have been employed for diverse specimen geometries such as DCB, ENF, MMB, ADCB, SLB, peel tests (and other geometries) to experimentally investigate the fracture toughness and interfacial behavior under various (mixed) failure modes and validate the theories.

Numerous previous studies have documented that various partition theories generate comparable (total) fracture energy values; however, the mode mixity prediction does not agree well [160][159], even exhibiting substantial differences [161]. Despite extensive research in interface crack problems, a definitive theoretical model that can accurately predict crack behavior has not been established. While several theories have been proposed, none have yet been proven to possess a high degree of accuracy or a physical framework. The scientific community has not yet reached a consensus on which theoretical approach yields the most precise predictions for interface crack mode mixity. Furthermore, the absence of a universally accepted reliable benchmark complicates the evaluation and comparison of different approaches [127][162].

At the same time, many researchers have worked following the numerical front based on the finite element method to calculate the total fracture energy using the various specimen geometries (test configurations) and validation. Notably, FE modeling has been widely used as a means of approach for mode partitioning.

2.11 Numerical Modelling Approaches

This section provides an introductory overview of the finite element analysis-based simulation of the laminated structures' delamination initiation and propagation behavior. The numerical modeling of the delamination behavior utilizes two primary approaches: the Virtual Crack Closure technique, the so-called VCCT, and the Cohesive Zone modeling technique (CZM) to predict the damage behavior and are discussed followingly.

2.11.1 Virtual Crack Closure Technique (VCCT)

The VCCT approach is extensively employed for applying the delamination failure criteria based on the theories of fracture mechanics. Initially developed for two-dimensional analysis

by Rybicki and Kanninen [163], this technique presents a simple and uncomplicated approach for evaluating the strain energy release rate without requiring singular elements at the crack's tip. Accordingly, the VCCT works on the basis of two fundamental presumptions:

- As the crack grows by a small increment, the energy necessary to initiate the crack opening is equivalent to the energy required for crack closing over the same crack increment.
- A small crack length increment does not considerably alter the crack tip condition/position (da).

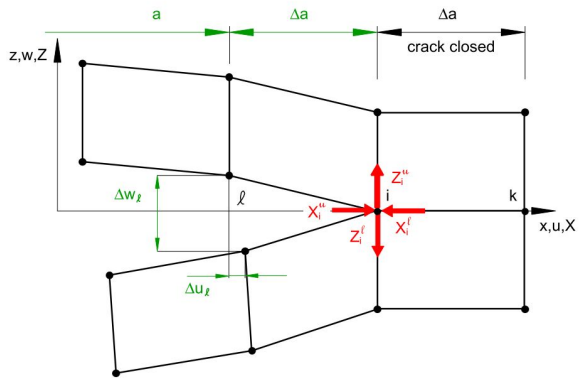


Figure 2.38: Representation of VCCT [37].

The energy release rate can be determined from the derivative function of the strain energy with respect to the crack area. An estimation of the energy released can be derived from computing the product of forces acting at the crack tip node and the corresponding displacement from the previous crack tip position (crack increment) (Figure 2.38). Given the availability of force and displacement values at the corresponding crack tip nodes in all three directions, the VCCT technique enables the partition of energy release rate components in all modes of fracture at the crack tip [37][20][123][164][165][166].

2.11.2 Cohesive Zone Modeling (CZM)

The Cohesive Zone Modelling, also known as CZM, was initially proposed to address the process zone that occurs in front of the crack tip. By integrating the principles of Damage mechanics and Fracture mechanics, this modeling approach can simulate both the initiation/onset and propagation of delamination without being constrained by a minimal fracture process zone. The cohesive zone model postulates the existence of a process zone in which tractions act at the virtual interface near the crack front and necessitates a cohesive constitutive law that correlates the traction and the separation within this zone. This law is based on two key factors: a **damage variable (d)** and a **penalty stiffness parameter (K)**. As the damage advances within this zone, the damage variable is utilized to simulate the subsequent changes in the constitutive behavior. In the absence of any damage, the penalty stiffness parameter exclusively defines the behavior. As the damage initiates, the traction attains a maximum critical value, followed by a gradual decrease complying with the damage variable

until it reaches zero. In the case of mixed mode loadings, damage initiates as the displacement jumps for each mode exceed a specific damage threshold, which varies depending on the material system [167].

The constitutive laws, also referred to as cohesive laws, may also be classified based on their shapes, including bilinear, exponential, and trapezoidal laws. Amongst these, bi-linear law is one of the widely utilized cohesive laws. Further, in these laws, the damage variable is defined in a manner that upon damage initiation, with increasing displacement jumps, the cohesive traction descends in a linear trend until the traction within the element reaches zero.

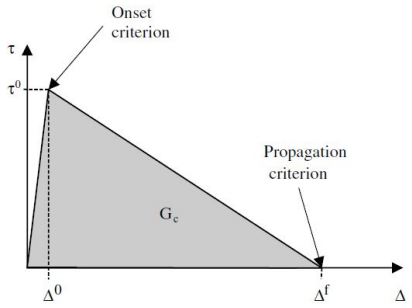


Figure 2.39: Bi-linear constitutive law for the mixed mode loading condition **[38]**.

To characterize this bi-linear model, it is essential to specify the penalty stiffness parameter that determines the initial slope, the onset criterion that defines the threshold traction or initiation of damage, and the propagation criterion regarding the final displacement jump or complete decohesion [168].

The criterion for propagation is generally established on the basis of strain energy release rate. The damage starts to grow as the energy release rate attains a maximum critical value, known as the fracture toughness, specific for each mode under pure mode loading conditions. In the traction-separation (displacement jump) response, the area under the curve represents the corresponding fracture toughness. Formulating the displacement jumps (for complete decohesion) is not required in case the fracture toughness is specified.

Damage is said to initiate under pure mode loading conditions as the cohesive traction elements reach and exceed the corresponding threshold interfacial strength. A model considering the effects of different modes is necessary for mixed mode behavior. The stress-based quadratic criterion expressed in the equation is one such model initially introduced by Ye [169] and suggested by Turon et al.[167] that can be utilized to predict the delamination onset.

$$\left(\frac{\tau_3}{\tau_3^0}\right)^2 + \left(\frac{\tau_2}{\tau_2^0}\right)^2 + \left(\frac{\tau_1}{\tau_1^0}\right)^2 = 1 \tag{2.18}$$

where τ_i denotes the interfacial traction and ${\tau_\mathrm{i}}^0$ represents the corressponding interfacial strengths at each loading directions. Whereas, for simulating the mixed mode behavior, it is necessary to consider appropriate energy-based mixed mode criterion (Section **2.9**) to account for the synergetic effects of different modes and control the damage propagation.

The CZM has been well developed for simulating the propagation behavior, including damage mechanisms such as plastic deformation and fiber bridging effects implemented with various

deformation and bridging laws, proving to result in relatively realistic outcomes to a large extent. However, the mode-partitioning with CZM is not that well established as compared to VCCT. The discussion on the detailed procedures (models and approaches) and the associated complexities of CZM on mode-partitioning is out of the scope of this literature review. Nevertheless, an attempt has been made to briefly discuss the recent development of CZM-based mode decomposition on a broader level.

In this regard, Conroy et al.[161] proposed a semi-analytical cohesive analysis (SACA) approach for the mixed mode decomposition, where the method considers the damage state at the crack tip's vicinity by including a length scale parameter to the cohesive zone length. As there is no crack tip singularity, the computation of the fracture energy mode partition is enabled by integrating over the cohesive surfaces after the damage process zone fully develops. Canas et al. [27] followed the same CZM approach to post-process the numerical analysis and determine the mode mixity for the horizontal peel testing. As emphasized earlier, in addition to the interface cohesive strength properties in pure modes and penalty stiffness, defining the failure locus in mixed mode is necessary. The above studies used the B-K criterion and linear law, respectively.

Recently, Moreira et al.[170] suggested a novel CZM-based mode partitioning approach. The mode mixity is determined by simulating the mixed mode tests (ADCB, SLB of unknown mode mixtures) by randomly assigning the failure criterion parameter value to the failure criterion considered. The force vs. displacement response obtained based on the numerical simulation is then used to predict the fracture energy from the analytical model. For every value of the failure criterion and the numerically estimated fracture toughness, there exists a distinct mode mixity. This study used an energy–based power law criterion for the mixed mode propagation behavior. Interestingly, the studies showed that the mode -mixity and the corresponding estimated fracture energy for a particular specimen geometry with various power-law values resulted in relatively same values. This study indicated that the mode-partitioning approach could be utilized to estimate the mode-mixity for the mixed mode tests for adhesively bonded joints. While Francis et al. [171] performed the ADCB and SLB tests for UD composite laminates and employed the same partitioning approach performing numerically and reporting similar observations.

Nanditha [172], with an objective to validate the mode partitioning approach suggested by Moreira et al. [170], performed the numerical simulations implementing the B-K law failure criterion to check for the predictions. While the power law (parameter value between 1.5 and 2.5) simulations resulted in comparably approximate fracture toughness and mode-mixity, on the other hand, the simulations with B-K law failure criterion (value between 1.5 and 2.5) showed disagreement with variations in the estimations of both the mode-mixity as well as fracture toughness. Also, it was reported that for some values of the B-K law parameter, the mode ratio and the fracture toughness predictions demonstrate similarity with the estimations obtained using power law. Furthermore, it is also recommended to implement the mode-partitioning approach to the MMB tests (since mode ratios can be predefined) for further validation of the method.

While both the VCCT and the CZM techniques can be utilized to simulate the onset/initiation and delamination progression, only the CZM approach is capable of predicting the damage initiation. It is imperative to have prior knowledge of any existing crack in terms of location and size if VCCT is implemented. VCCT may thus be effectively implemented to simulate

delamination in cases where the location of the crack is predetermined, such as in experiments involving inserts within the specimen. However, in situations where the crack initiation site is unknown, VCCT may not be applicable [173].

It has been found to have limitations in capturing plasticity during the delamination due to its conceptual development on the structure of Linear Elastic Fracture Mechanics; nonetheless, if the fracture process zone is insignificant relative to the size of the specimen, VCCT still remains appropriate. On the other hand, the utilization of cohesive elements is not limited to the postulations of LEFM, and therefore, it can yield more precise outcomes where nonlinearities dominate, specifically in ductile fracture.

In the context of incorporating these techniques within the commercial finite element modeling software, the VCCT approach enables the acquisition of the values of distinct components of fracture energy acting at individual nodes across the delamination front, whereas the CZM method does not directly facilitate and generate details on the strain energy rate distribution of each mode. It depends on the formulation of cohesive zone and is not straightforward to implement. Another aspect is that VCCT is computationally cost-effective compared to CZM due to the requirement of a minimum number of cohesive elements with high mesh refinement at the cohesive zone to simulate the delamination. Nonetheless, the recent CZM-based mode-partitioning appears to be promising.

Understanding and evaluating the fracture energy distribution can be crucial, as it may not be uniformly distributed in actual structures, thus potentially invalidating certain assumptions. In that sense, the literature shows that numerical simulation enables a greater analysis (in combination with experimental data) and could be achieved by incorporating the precise specimen geometry, material characteristics, and loading conditions of the tests and assessing the local loading conditions or mode mixity through the implementation of methodologies such as VCCT (LEFM) and (or) CZM (which considers damage process zone).

2.12 Summary

The initial primary aspect of delamination testing involves determining an appropriate experimental setup to ensure the steady propagation of cracks in the specimen. The scope of standardized tests established so far is limited to testing unidirectionally reinforced fiber polymer composites. It presents challenges such as but not limited to non-uniform strain energy distribution, crack front curvature, residual thermal stresses, and delamination migration when employed to determine the interlaminar fracture toughness of various other specimen stacking (interface and global) configurations. However, it should be noted that the critical energy release rate formulations (DCB, ENF, MMB, and even other tests) often fail to take into consideration certain pertinent factors, leading to an overestimation of the fracture toughness value. In order to minimize the issues and effectively utilize the standard delamination test, several guidelines are followed in the literature to design the optimal layup configuration. Despite this rigorous designing and modeling at the ply level, the difficulties and issues are still observed and remain unsolved. Moreover, to conduct standard tests, it is essential to maintain constant knowledge of the crack tip position and length throughout the experiment. Despite its importance, actively monitoring and determining the precise position of the crack tip during testing can prove challenging. As a result, alternative testing methods

that do not require such extensively rigorous procedures in the design of stacking sequences and crack extension measurements have been favored in recent studies.

The peel tests have been more interesting in recent years for several reasons. Among the various peel tests developed and proposed, the literature indicates the promising potential of the mandrel peel test as a testing method for determining the interlaminar/interfacial properties of various interesting configurations employed in real-engineering structures. The mandrel peel test, a roller-assisted modified version of the 90^{o} peel, offers many advantages and is of more interest and is gaining attention because of the simple and economical specimen design. The experiment is simple to perform and can be controlled precisely. Earlier research has demonstrated that the mandrel peel test can characterize the fracture toughness of UD-UD, UD-woven, and UD-metal interface configurations.

The MP test is in its nascent stage of development, and efforts to explore its efficiency in assessing the fracture toughness properties of laminated materials with a long-term goal of establishing standardization are ongoing.

From the available literature, it could be understood that there are several specimen geometry aspects and the parameters associated with the mandrel peel test setup necessary for the measurement of the interfacial/interlaminar fracture toughness. These factors include the peel-arm thickness, peel specimen width, peeling rate, mandrel roller radius, and alignment force which might influence the determined fracture toughness.

However, the effects of the MP specimen design geometry and the testing conditions and parameters on fracture toughness have not been well established, particularly the damage mechanism. Additionally, it is unclear and lacks understanding of the sensitivity of the behavior of different material systems and interface configurations to testing variations, specifically, the mandrel roller size. Notably, the degree of mode mixity (G_{II}/G_{I}) factor remains unknown and has not been addressed.

To this end, to be able to draw reliable conclusions and gain insights about the sensitivity of these parameters, extensive experimental tests on various materials systems (high toughness matrix, different fiber reinforcement, and thereof) should be performed to evaluate the repeatability and reproducibility, and assess an appropriate approach (numerical simulations or analytical models) to partition the fracture mode and the investigation should focus on the questions to be addressed.

Finally, this literature review lays a cornerstone for defining and formulating the research framework.

Chapter 3

Research Framework

This chapter provides an overview of the framework that underpins the research, outlines the research questions and hypotheses, and presents the methodological approach and strategy employed to address them.

The standard interlaminar fracture test methods face challenges and limitations according to the literature. The mandrel peel (MP) test has shown promise as a potential testing method for evaluating the interlaminar/interfacial properties of various configurations found in real engineering structures. Despite being in its early stages of development, ongoing efforts are being made to explore the efficiency of the MP test in assessing the fracture toughness properties of laminated materials, with the long-term goal of establishing standardization. Existing literature highlights the importance of several factors in the mandrel peel test setup that influence the measurement of interfacial/interlaminar fracture toughness. These factors include the thickness of the peel arm, the width of the peel specimen, the peeling rate, the radius of the mandrel roller, and alignment force. Understanding the influence of these specimen geometry aspects and testing conditions on fracture toughness and the associated damage mechanism remains limited.

Furthermore, the sensitivity of different material systems and interface configurations to variations in testing, specifically the size of the mandrel roller, is not well understood. The degree of the mode mixity factor, which plays a significant role in fracture toughness, has not been adequately addressed in the available literature. This lays a cornerstone for defining and formulating the research framework.

3.1 Research Objective and Questions

The research objective has been defined by addressing the existing gaps gleaned from the limited published scientific articles.

This thesis primarily aims at exploiting the new potentials of the Mandrel Peel Test method by incorporating the novel **"Multi-Mandrel Concept"** in determining the fracture toughness of the Thermoplastic Composites.

- "To gain insights about the sensitivity of the specimen configuration and testing parameters on various materials systems and study the applicability of the Mandrel Peel test method to establish a relation between the mandrel roller size and the mixed mode fracture behavior."

- "Comparative **"multi-mandrel concept"** peel test assessment with the standardized DCB, ENF, and MMB tests."

With the motive of realizing the research objective, the following research questions and sub-questions are formulated that need to be addressed.

Main Research Questions:

- How does the mandrel roller size influence the mixed-mode fracture behavior?

  The **hypothesis** in this thesis is that "*It is expected that the degree of the mode-mixity changes with increasing mandrel size.*"

- How can the degree of mode-mixity be validated and quantified?

- Can the Mandrel Peel test generate a range of mixed-mode fracture data?

- Is the Mandrel peel test applicable for measuring the fracture energy of the 0°- θ interface, and can it successfully generate mixed-mode fracture data?

Sub-Research Questions:

- How does the specimen's geometry, including peel arm thickness, width, and overall thickness, influence the measured fracture energy and the crack propagation path?

- What is the effect of the peeling rate on the measured fracture energy?

- How does the balancing load affect the measured fracture energy?

- What are the effects of the Mandrel peel set-up on the measured fracture energy and the crack propagation path?

3.2 Research Approach and Strategy

The research approach and strategy employed in this study were determined based on an extensive review of the existing literature and the research questions framed. The primary aim was to achieve the research objective and validate the hypothesis, necessitating an experimental and numerical approach. This approach was structured into several key steps, each contributing to the overall research process (Figure 3.1).

- **Step 1** involved conducting an initial study to comprehensively understand the critical factors associated with the mandrel peel test. The objective was to analyze the impact of various parameters, such as the thickness of the peel arm and weight for conformation, on the measured fracture energy. This preliminary investigation allowed the knowledge gained to be applied to optimizing the mandrel peel test setup and specimen design.

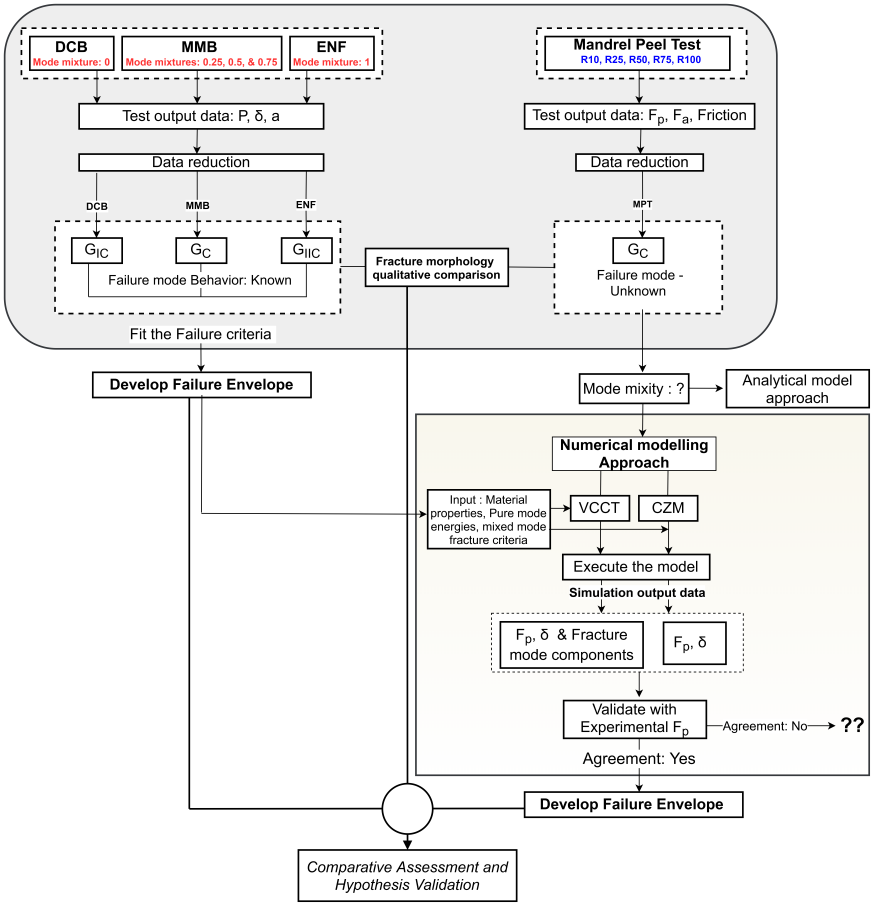


Figure 3.1: Flowchart of the approach and strategy employed in this research.

- To experimentally validate the hypothesis, **Step 2** focused on performing mandrel peel tests on Unidirectional Fiber-Reinforced Polymer Composites (FRPC). This choice enabled a comparison with standardized tests. The intention was to establish a correlation between the fracture energy observed during the mandrel peel tests and the fracture toughness obtained from DCB (Double Cantilever Beam), ENF (End-Notched Flexure), and MMB (Mixed-Mode Bending) standardized tests conducted on the same material system.

- Building upon the experimental data obtained, **Step 3** involved the development of a failure envelope based on a mixed-mode failure criterion utilizing Power Law and B-K law. This approach allowed for a comprehensive analysis and comparison of the fracture energy results obtained from the standardized tests and mandrel peel test.

- To gain further insights and understand the mode components of the energy release rate in the mandrel peel tests, **Step 4** employed qualitative fractography-based studies and a numerical approach involving FEA modeling. A developed numerical model of the DCB, ENF, and mandrel peel test was utilized to simulate the load-displacement behavior of the GF/PP (Glass Fiber/ Polypropylene) and CF/PPS (Carbon Fiber/ Polyphenylene Sulfide) specimens that were experimentally tested.

- To study the mandrel peel test's applicability, additional tests were conducted on the two material systems with a 0°-90° interface. The objective was to assess the performance of the mandrel peel test in this specific configuration and evaluate its effectiveness in capturing fracture behavior.

By employing this systematic research approach and strategy, combining experimental and numerical techniques, the study aimed to provide a comprehensive understanding of the mandrel peel test and its relationship to fracture toughness for different material systems.

Chapter 4

Methodology

In this chapter, the material used, manufacturing process, specimen preparation, and the experimental procedures followed to characterize the interlaminar fracture toughness are described:

4.1 Materials

To effectively assess the applicability of the mandrel peel testing and subsequently validate the hypothesis: two Fiber- Reinforced Thermoplastic Composite materials currently used in automotive and aerospace applications were considered. Unidirectional Glass fiber pre-impregnated with Polypropylene resin designated as UDMAX^{TM} **GPP 45-70 TAPE** by the manufacturer SABIC, and Unidirectional Carbon-fiber pre-impregnated with Polyphenylene sulfide resin designated as **Toray Cetex TC1100 PPS** by Toray Advanced Composites were used in this study. Table 4.1 summarizes the properties of the two material systems at room temperature. The different fiber and matrix types would allow for a comparison between the stiffness and resin-dominated interfacial properties.

	T_m [°C]	t_{ply} [mm]	v_f [%]	E_{11} [GPa]	E_{22} [GPa]	G_{12} [GPa]	ν_{12} [-]
UD GF/PP	163	0.25	45	35	3.3	1.74	0.32
UD CF/PPS	280	0.21	59	134	10	3.5	0.33

Table 4.1: Material properties at Room temperature

4.2 DCB, ENF, and MMB Specimen Design Specifications

The following section deals with the specimen design specification for the DCB, MMB, and ENF fracture tests. The literature search showed that the ASTM D5528/D5528M [51], ASTM D6671/D6671M [53], and ASTM D7905/D7905M [52] standards correlate well with

the current literature findings. Consequently, these standards have complied with minor deviations.

As addressed in Section 2.5, the resistance to delamination/fracture, or the critical strain energy release rate at different modes, is quantified assuming the Linear Elastic Fracture Mechanics Theory based on the studies of Irwin and Griffith. Highlighting the fact that the strain energy release rates, G_c, are determined as a function of the crack length; layup, initial delamination length, specimen width, thickness, and the overall length of the specimen, among others, are the critical design factors that could possibly affect the delamination growth and the delamination front curvature. In the calculation of the G_c, the delamination front is presumed to be straight. For highly curved delamination fronts, this would ensue in a considerable overestimation of the strain energy, as the typical area of the delamination is calculated as the average width of the specimen times the length of the delamination measured at the edge of the specimen. Therefore, the specimen design factors are intended to reduce these effects to a large extent, which eventually results in the following specimen geometry prescribed in the ASTM standards (Figure 4.1).

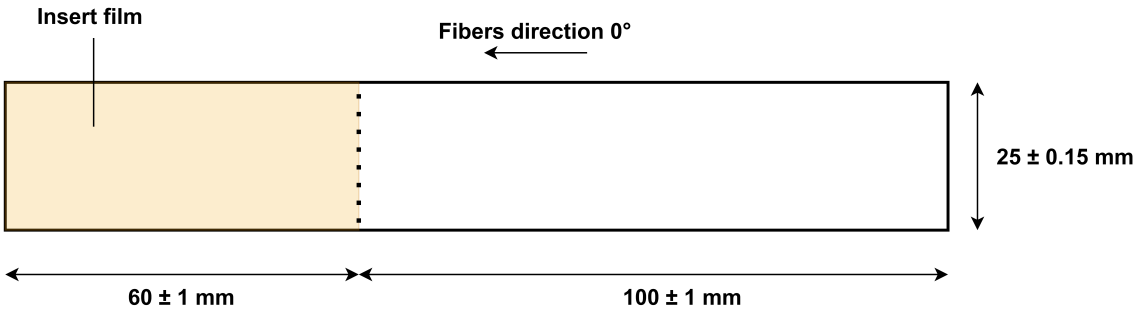


Figure 4.1: Illustration of the DCB, ENF and MMB specimen geometry.

4.3 Mandrel Peel Test Specimen Considerations

The application of the Mandrel Peel test to monolithic specimens lacks established guidelines for selecting the layup and specimen design configuration. Based on the literature review and the preliminary analysis, the following factors are considered crucial. Firstly, the two sub laminates referred to as "peel arm" and "substrate" on either side of the delaminated plane, as shown in Figure 4.2, have distinct stiffness requirements. The peel arm should be flexible to minimize the energy needed for bending around the mandrel roller, while the substrate should exhibit high stiffness during peeling. In this regard, the primary critical considerations for the mandrel peel specimen design are the width, peel-arm thickness, and a total thickness of the sample.

Peel arm Thickness

Another distinctive feature of the mandrel peel test is the mandrel roller. The applicability of the mandrel facilitates efficient control of the peel-arm curvature, further sustaining the elongation of the fibers in the FRP peel arm within the fracture threshold, thus suppressing the breakage of the peel-arm tape. The selection of the mandrel size plays a crucial role, as

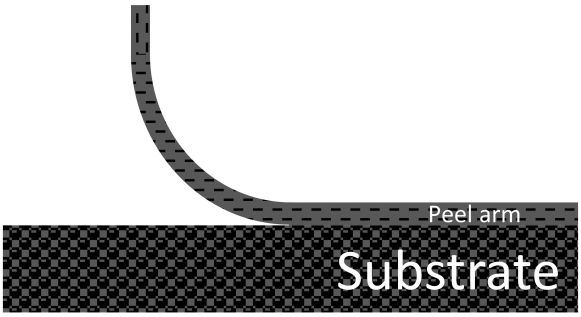


Figure 4.2: Illustration of the mandrel peel specimen configuration.

the roller radius affects the bending strain of the peel arm, which is bent around the mandrel roller. The peak strain sustained by the peel arm during the bending to achieve conformity can be estimated using Equation 4.1, which is a function of both the mandrel radius, R, and the thickness of the peel arm, t.

$$\epsilon = \frac{t}{2R} \tag{4.1}$$

Nevertheless, to assure that the fibers of the peel arm do not strain beyond its elongation threshold and fail, the size of the mandrel is limited for a given thickness, and this critical size is found based on the relation expressed in Equation 4.2.

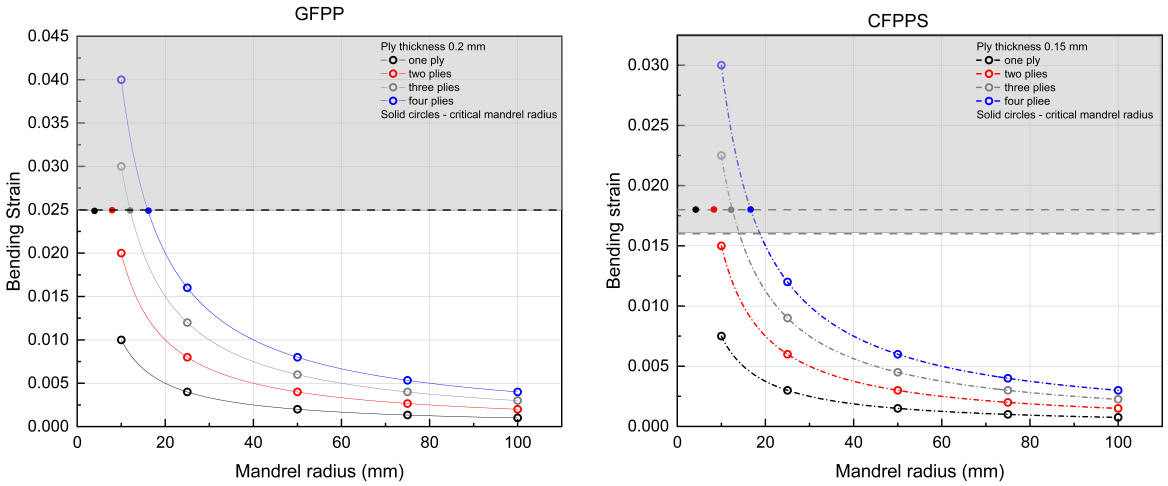
$$R > \frac{t}{2\epsilon} \tag{4.2}$$

The elongation threshold for the E-glass fibers used in the UD GFPP tape supplied by SABIC is around 2.5 - 4%, whereas for the UD CFPPS tape from the Toray Advanced Composites utilizes AS4A type carbon fibers, the failure strain is estimated to be within 1.6 – 1.8%.

Figure 4.3 shows the bending strain of the peel-arm as a function of mandrel radius for different peel-arm thicknesses for UD GF/PP and UD CF/PPS material systems. The critical mandrel size required to keep the peel-arm from breakage increases as the peel-arm thickness increase, as indicated by the solid circles (Figure 4.3). Mandrel rollers of radii 10, 25, 50, 75, and 100 mm were available for this research. It is aimed at utilizing all the mandrel sizes to achieve desirable experimental conditions. However, from the above prediction, the bending strain (peel arm) is expected to be higher than the threshold value for three plies and four plies thick peel arm for a roller radius of 10 mm, thus, limiting its usage. Further, during the preliminary study, the test with a peel-arm thickness of four plies resulted in fiber breakage for a radius of 10 mm due to the higher strain. Therefore, mandrel peel specimens with a peel-arm thickness of one ply and two plies are considered for this test campaign. Although the bending strain of the two-ply thick CFPPS peel arm for the 10 mm radius is closer to the failure strain, it will still remain part of the experimental testing plan.

Peel arm Length

Although there is nothing much discussed regarding the length of the peel arm in the literature, this is one of the essential design considerations that need to be taken into account in

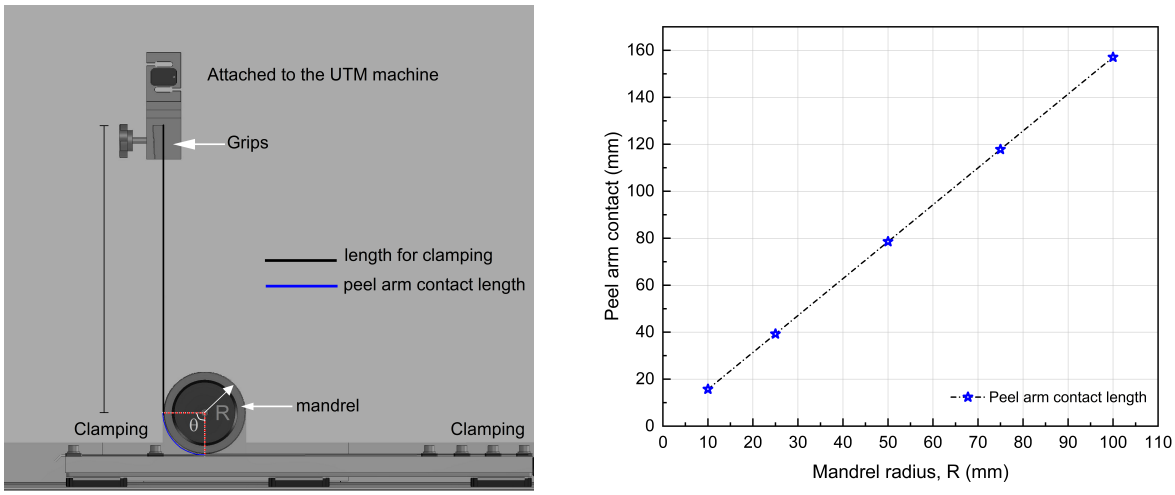


(a) GF/PP **(b)** CF/PPS

Figure 4.3: Illustration of the Bending strain vs. mandrel radius for different peel arm thicknesses. Solid circles indicate the corresponding critical mandrel radius.

this test campaign, and this is due to the fact that the earlier works reported on the mandrel peel test so far have been studied only for smaller roller radii (max radius 20 mm).

Figure 4.4a illustrates the schematic of the peel arm conformed with the mandrel. In the mandrel peel configuration the angle between the applied peel force and the vertical is 90°. The arc length of the peel arm that is in contact with the mandrel for an arc angle of 90° depends basically on the radius of the mandrel roller, and this can be determined using the relation:



(a) Schematic (side-view) of the mandrel peel detailing the peel arm configuration.

(b) Increasing Peel arm contact length as a function of mandrel radius.

Figure 4.4: Relation between the mandrel radius and the peel arm length requirements.

$$p = R * \theta \tag{4.3}$$

It can be seen that (Figure 4.4b), the peel arm length in contact with the roller increases for varying (increasing) ranges of the mandrel roller radius. Correspondingly, the total peel arm length, which includes the peel arm contact length and the length necessary for clamping to the grips of the Universal testing machine, is essentially higher than the indicated values in Figure 4.4b.

Accordingly, considering a maximum peeling distance (crack propagation) of 50 mm, and to satisfy the total peel length requirements and also to facilitate proper clamping of the substrate to the sliding table of the peel setup at two ends (insert film and non-delaminated end) with sufficient spacings, the initial delaminated length (insert film) should be minimum 150 mm long. Taking into account the dimensions of the laminate that could be manufactured, a maximum length of 290 mm could be achieved after trimming the edges and allowing for a delaminated length of around 150 mm, which acts as a peel arm would yield a non-delaminated region of around 140 mm which should be sufficient for peeling and clamping. However, the above-configured specimen design considerations meet all the essential requirements for mandrel peel testing only up to a mandrel size of 50 mm, since, for a mandrel roller radius of above 50 mm, the peel arm length of 150 mm is not sufficient and necessitates a longer peel arm length.This limitation was overcome by extending the length of the peel arm by thermally welding with a consolidated laminate of similar thickness.

MP Specimen Width

As discussed in Section 2.8.2, the effect of the peel specimen width on the crack front curvature can be considered to be minimal as the kinematics of the mandrel peel test enables establishing a relatively straight crack growth front controlling the crack tip location, leading to a better strain energy distribution across the width, unlike the standard tests. From this aspect, the width size effect on the strain energy release rate is expected to be non-critical.

Generally, the mandrel roller width limits the width of the specimen that could be employed. However, the two other critical, decisive factors which control the mandrel peel specimen width considerations are the alignment force and the mandrel radius. More-wide specimens will have higher stiffness, necessitating a larger alignment force to achieve the proper conformation with the mandrel. Secondly, as the mandrel size increases, the alignment force requirement increases for a given specimen width. Therefore, within the context of this research, it is prudent to take these into account, and based on these practical considerations, it was decided to perform the tests with a peel specimen width of 10 mm. The final geometric specification of the mandrel peel specimen based on the above-discussed criteria is shown in Figure 4.5

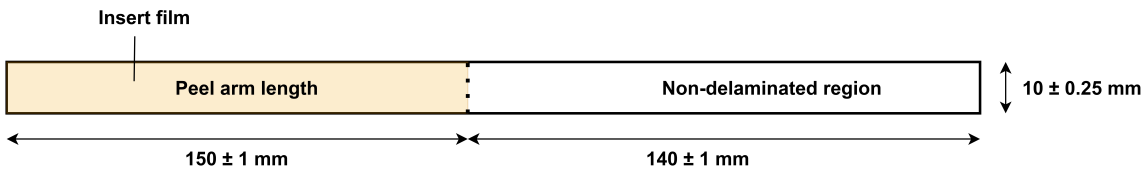


Figure 4.5: Geometric specification of the mandrel peel specimen.

4.4 Experimental Test Plan

The experimental testing plan was defined and finalized based on the specific bounds and criteria discussed in the Section 4.3. The initial part of the research aims to study the pure modes I/II and mixed mode fracture behavior of GF/PP and CF/PPS, and the classical test methods chosen indicate the delamination fracture behavior. For this purpose, five loading ratios were considered. The specimens are labeled as M-T-mXXX-I, where M stands for the Material, T for the test method, m for mode-ratio, and I indicates the interface. The choice of five different mandrel rollers with different interface configurations and material systems enables exploiting the Mandrel peel test and examining the hypothesis. Next, two thickness variations are experimentally analyzed to determine the correlation between fracture toughness (G_c) and peel arm thickness. For the Mandrel peel tests, the specimens are labeled as M-MPT-RXXX-I-PXX, where M again stands for the Material, MP for Mandrel Peel, R for the mandrel radius in millimeters, I indicates the interface and P for the peel arm thickness in plies.

Lay-up Configuration

Multiple recommendations guide the layup configuration of the DCB, ENF, and MMB specimens. To ensure that the delamination occurs under the desired loading conditions, the two arms of the delaminated plane need equivalent stiffness. To achieve this, the pre-crack is introduced at the laminates' midplane. Additionally, it is necessary to minimize the flexural/-torsional (bending/twisting) coupling and warping effects (due to residual thermal stresses) to obtain a fracture behavior with a relatively straight crack front during propagation. For this reason, the layup sequence $[0]_n$ was considered, as it presents a minimal variation of strain energy along the crack front with the skewness parameter (B_t) equal to zero. In addition to the curvature effect, utilizing unidirectional specimens enhances the overall testing procedure by mitigating thermal shrinkage phenomena during consolidation. The criteria necessary to achieve beam-like characteristics are anticipated to have a reduced significance in the context of the Mandrel peel test, where the mandrel roller predominantly dictates the kinematics of the specimen. Further, in accordance with the evaluation of the factors performed in the Section 4.3, the following sequences were selected for the UD plies utilized in the study.

- $[0_1||0_{19}]$ and $[0_2||0_{18}]$ - 0/0 delamination interface: This layup configuration allows the exploitation of Mandrel peel tests to validate the hypothesis and simultaneously enable comprehensive comparison between the MPT and the standardized DCB, ENF, and the MMB tests.
- $[(0||90)/(0/90)_{9s}]$ – 0/90 delamination interface: This layup configuration extends the investigation of a multidirectional interface to assess the applicability and validate the hypothesis.

The preference for the 0|90 (cross-ply) interface configuration over the other angled orientations is attributed to its applicability in industries, particularly automotive. Specifically, the 0|90 sequencing can be utilized as a straightforward outer layer for the beam as a shield in over-molded automotive structures such as car bumpers. These configurations meet most of the requirements for the MP specimens. The balanced symmetric lay-up is expected to mitigate warping effects, minimizing any internal stresses that might be caused during the

testing (especially clamping). The notation || denotes the position of the pre-crack in the specimen lay-up. Tables 4.2 and 4.3 show the experimental test matrix.

	Material(M)	Test(T)	Mode-ratio(m)	Interface (I)
M-DCB-m0-I(0|0)	GF/PP, CF/PPS	DCB	0	(0|0)
M-MMB-m0.25-I(0|0)	GF/PP, CF/PPS	MMB	0..25	(0|0)
M-MMB-m0.5-I(0|0)	GF/PP, CF/PPS	MMB	0.5	(0|0)
M-MMB-m0.75-I(0|0)	GF/PP, CF/PPS	MMB	0.75	(0|0)
M-ENF-m1-I(0|0)	GF/PP, CF/PPS	ENF	1	(0|0)

Table 4.2: Experimental test matrix for the DCB, ENF, and MMB tests.

	Material(M)	Test(T)	Interface (I)	Mandrel radius,R (mm)	Peel arm thickness, P (plies)
M-MP-R-I-P	GF/PP, CF/PPS	MPT	(0|0)	10, 25, 50,75,100	1, 2
M-MP-R-I-P	GF/PP, CF/PPS	MPT	(0|90)	10, 25, 50,75,100	1

Table 4.3: Experimental test matrix for the Mandrel Peel tests.

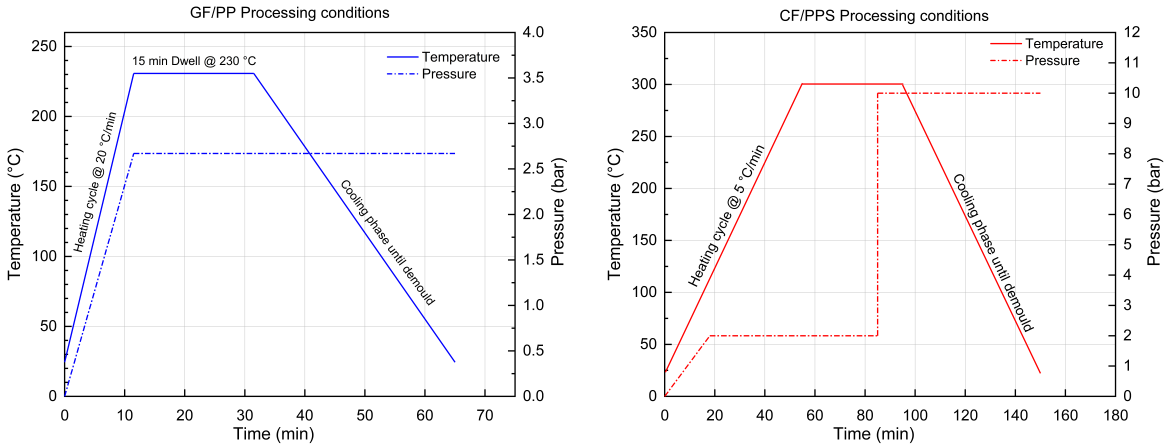
Specimen Sampling and Sample Size

To generate reliable results, it is necessary to test at least five to six specimens, ideally from one composite panel. Taking into account the size of the laminate and the additional discardable area along the edges, however, it was essential to produce multiple laminates (three) to machine the intended desirable number of specimens to perform all the standardized DCB, ENF, and MMB (3 mode - mixtures) tests. Within this study, for each set of tests, the specimens were randomized between the laminates following the practice suggested in the ASTM standard E122 [174] for more statistically consistent qualitative and quantitative data comparison. Similarly, in mandrel peel testing, the specimens were randomized within the same composite panel produced for each separate configuration.

4.5 Manufacturing Process

The manufacturing process of the composite panels is detailed. The hot press consolidation technique at the BMC facility used a two-part picture-frame mold system to manufacture the laminates. Prior to the hand layup process, in order to ensure that the consolidated laminate does not adhere to the mold and facilitate easy part release post the consolidation cycle, the entire mold was cleaned thoroughly using the isopropanol, and a Teflon sheet was placed on the bottom part/plate of the mold. The pre-preg materials supplied by the manufacturers in the form of the wide roll were cut manually according to the preferred orientation and the mold cavity area dimensions, and eventually, the pre-preg plies were stacked by hand. During the layup process, polyimide film was inserted at the laminates' mid-plane to introduce initial artificial delamination for the standardized DCB, ENF, and MMB specimens. Whereas correspondingly, for the production of mandrel peel test specimens, the starter film was inserted at the intended interface according to the design considerations (peel arm thickness). The process conditions were followed per the manufacturer's recommendations, and Figure 4.6a and 4.6b shows the time-temperature and pressure cycle of the consolidation process for the GF/PP and CF/PPS composite material system. The CF/PPS laminates were consolidated

at 300 °C instead of the recommended temperature of 310 °C since the hot press could only be operated to a maximum temperature of 300 °C. Furthermore, it is pertinent to mention that precise control of the cooling rate could not be achieved, and the profile is not linear as depicted.



(a) GF/PP **(b)** CF/PPS

Figure 4.6: Pressure-Temperature cycle for the consolidation process

After the completion of the heating and pressure cycle, the mold is allowed to cool to room temperature, and laminate is removed from the mold manually. Finally, the edges of the laminate are trimmed before machining the specimens.

4.6 Specimen Preparation

The DCB, ENF, and MMB specimens were machined from the laminates (Figure 4.7) using the water-cooled diamond abrasive cut-off wheel facility at the DASML, TU Delft. The specimens' thickness and width were measured precisely using a micrometer screw gauge at three different points. For all the tested specimens, the sides of the specimens were coated with a thin layer of white typewriter liquid corrector to visualize the propagation of the crack. As described in the ASTM standard, markings were made every 1 mm for the initial 5 mm and at every 5 mm up to 60 mm from the insert end to ease the determination of mode I delamination onset and propagation of the DCB specimens. Similarly, the markings were made up to 25 mm for the MMB specimens. The compliance calibration markings were made at a distance of 20, 30, and 40 mm from the insert tip end for the ENF-tested specimens. Next, the aluminum loading tabs were bonded to the DCB and MMB specimens using the Henkel EA3425 epoxy adhesive and cured at room temperature for 12 hours minimum. Prior to the bonding process, the bonding surface of loading tabs was grit blasted while either surface of the specimens was ground with SiC abrasive paper to promote better adhesion. Also, the loading tabs differ since the testing fixtures employed for the DCB and MMB tests differ.

Mandrel peel specimens with a 10 mm width were cut using a rotary saw facility at the BMC from press-molded laminates of varying peel arm thickness (Figure 4.8). The edges

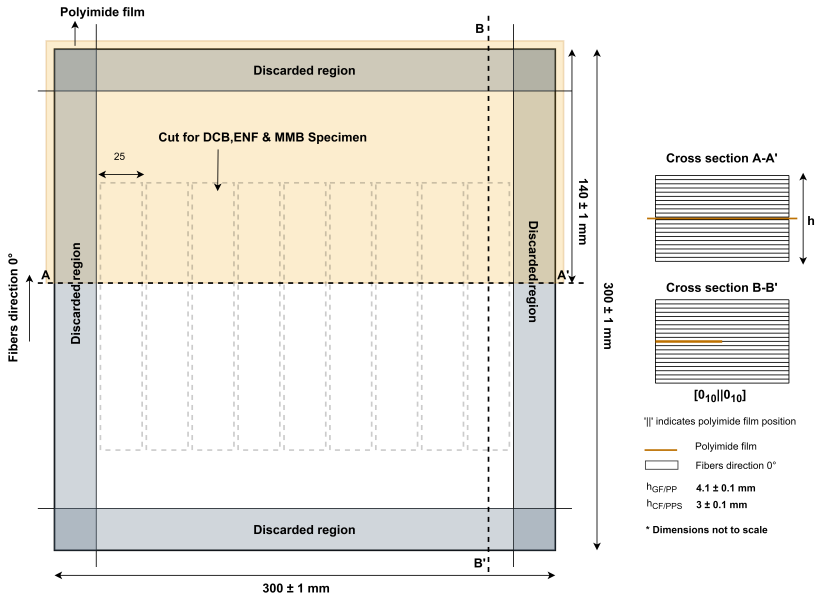


Figure 4.7: Schematic view of the layup of the laminate, detailing the cut for the DCB, ENF, and MMB specimens

were then polished with fine-grit sandpaper to achieve a smooth surface finish. In contrast to the classical tests, markings are unnecessary, as no accurate monitoring of the crack front propagation is required in the MPT.

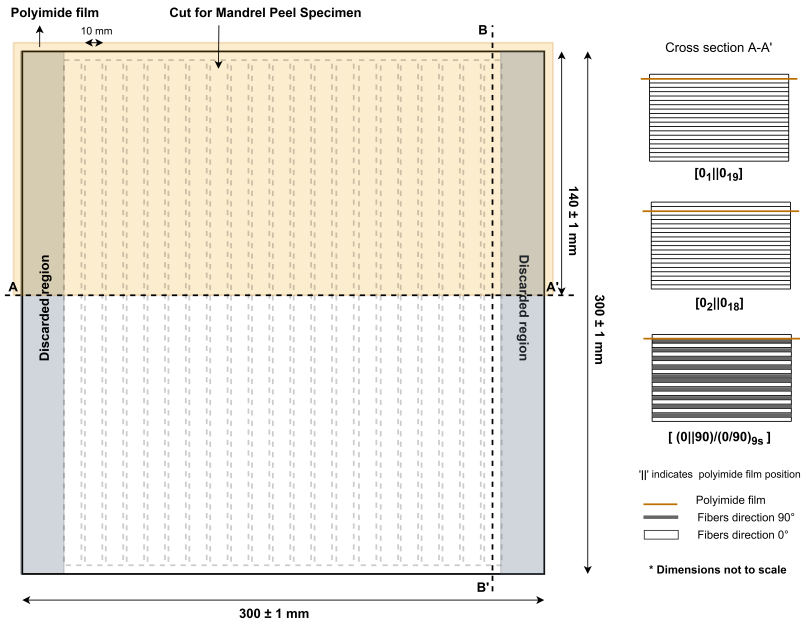


Figure 4.8: Schematic view of the layup of the laminates, detailing the cut for the Mandrel Peel specimens.

4.7 Experimental Test Set-up and Procedure

4.7.1 Double Cantilever Beam Test

The configuration for the DCB tests is shown in Figure 4.9. The automated camera system and the light sources are installed on the front side of the testing machine (similar to Figure 4.11). The testing fixture clamped to the machine's grips consists of two thick metallic plates with a through-hole at either end, via which the specimens are pinned to the combination of specially designed loading tabs referred to as "B" and "S." The loading tabs "B" are adhesively bonded to the specimens and, in turn, attached to the loading tab "S" through a screw, which is reused for series of tests.

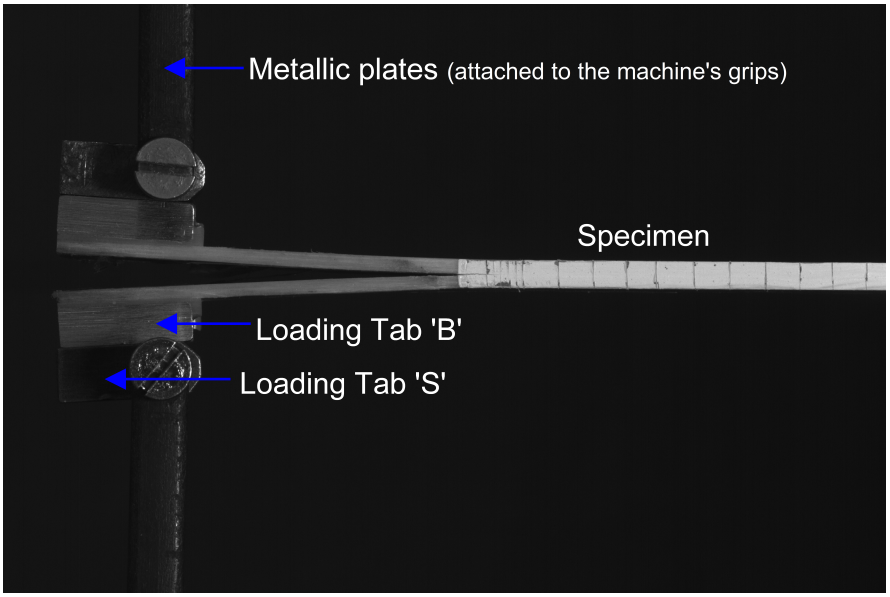


Figure 4.9: Illustration of the DCB test configuration showing a specimen attached to a combination of loading tabs.

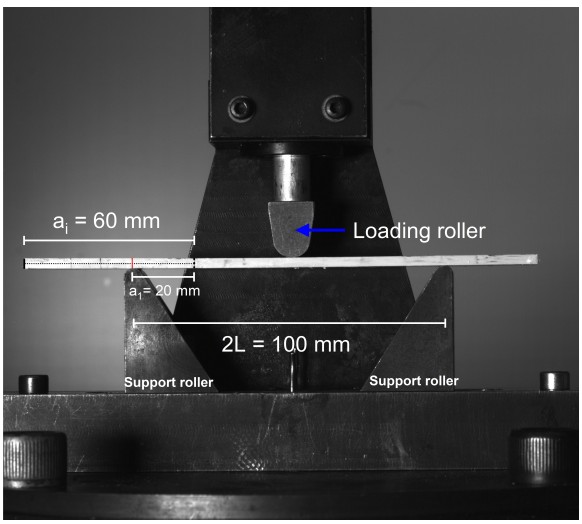
The mode I fracture is attained by "opening" the DCB specimen. Within this testing set-up, this is accomplished by moving the lower arm of the fixture fixed to the cross-head down, thus exerting tensile opening forces on the DCB specimen in a direction perpendicular to the delamination plane.

For all the DCB tests, the specimens were loaded at a displacement rate of 1 mm/min; meanwhile, the camera instantaneously captured the images of the crack propagation at an interval of 3 seconds. As per the ASTM standards, the specimen was initially loaded and unloaded until the delamination propagated, ensuring a crack growth within the 3 to 5 mm range, generally referred to as precracking. After the precracking, the specimen was reloaded up to a delamination crack length of 50 mm beyond the precrack tip.

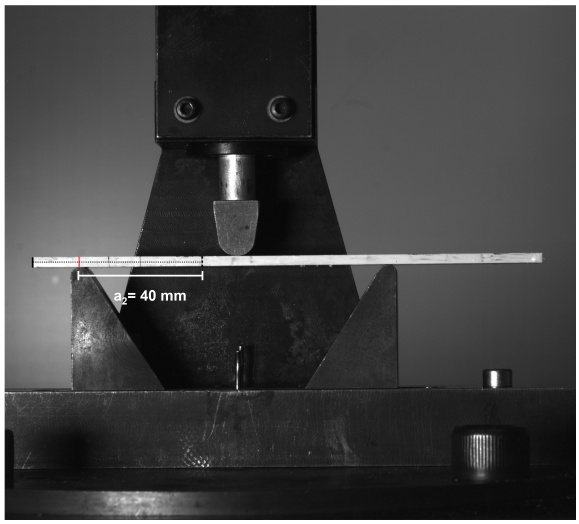
Further to this, the data acquisition and synchronization software generated a file with assigned labeling for each image stored, enabling it to co-relate with the applied force (P) and crack opening displacement (δ) values at the corresponding crack length (a) during the post-processing.

4.7.2 End-Notched Flexure Test

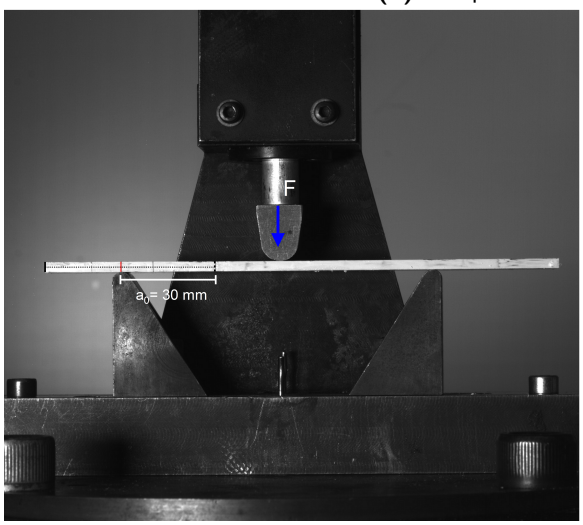
The ENF tests were performed according to the **ASTM D7905/7905 M** test method using a **ZWICK Universal testing machine** incorporated with a 1kN load cell and displacement transducer. The ENF testing is primarily based on the 3-point bending technique. The testing fixture consists of three rollers: two support rollers and a loading roller such that the loading roller is always positioned midspan between the two support rollers with a nominal span length (2L) of 100mm. The support and loading rollers/noses have a radius of 3 mm and 6 mm, respectively and are fixed. During the testing, the position of the loading roller ensures that the point of load application is at the center and perpendicular to the plane of delamination.



(a) Compliance calibration at a = 20 mm



(b) Compliance calibration at a = 40 mm



(c) NPC fracture test at a = 30 mm

Figure 4.10: ENF test setup and configuration for compliance calibration and NPC fracture test.

The Mode II ILFT is derived by applying the Compliance Calibration (CC) method and is discussed in Section 5.2. Before the tests, all the specimens were in the non-precracked

condition, and the test involved three loadings (and unloading) for each specimen carried out in displacement-controlled mode at a rate of 0.5 mm/min. The initial two loadings and the subsequent unloading were essentially needed for the compliance calibration, and the specimen was loaded to 50% of the anticipated peak force at crack length "a," corresponding to 20 mm and 40 mm, ensuring that the crack does not extend due to overloading.

Following the calibration tests, the specimen was reloaded at crack length "a", equal to 30 mm, until the delamination progressed and the eventual failure was observed, referred to as the Non-precracked fracture test. For the Compliance Calibration tests and the final fracture test, the specimen is positioned such that the respective CC markings are over one of the lower support rollers as shown in Figure 4.10.

4.7.3 Mixed-Mode Bending Test

Figure 4.11 illustrates the MMB test apparatus. The loading forces are exerted on the MMB specimen through the specially designed loading tabs attached (bonded) at the insert end of the specimen and via rollers that are in contact with the specimen. The base (bottom part) of the MMB fixture is connected to the bottom loading tab of the specimen and also supports the specimen keeping it stationary with the roller far away towards the right, whereas the lever (top part) is pinned to the top loading tab of the specimen and loads the specimen at the midspan between the loading tabs and the roller at the bottom. Further, the top lever also incorporates a saddle (black) that is always under the loading yoke (blue) and is parallel to the axis. While the base moves upwards during the testing, the yoke remains stationary, thus causing the lever arm, due to the lever roller which functions as a fulcrum, to rotate, eventually generating fracture in tensile opening mode at the loading tabs, and the sliding mode of fracture as the lever roller pushes the specimen downwards opposite the loading tab, thereby producing mixed mode fracture. The saddle position: the absolute length of the loading lever arm ‘c’ determines the delamination mode mixture.

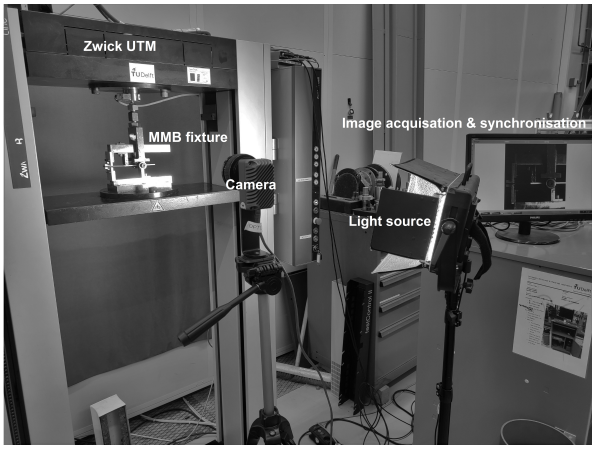


Figure 4.11: MMB test setup with high-resolution camera and crack monitoring system.

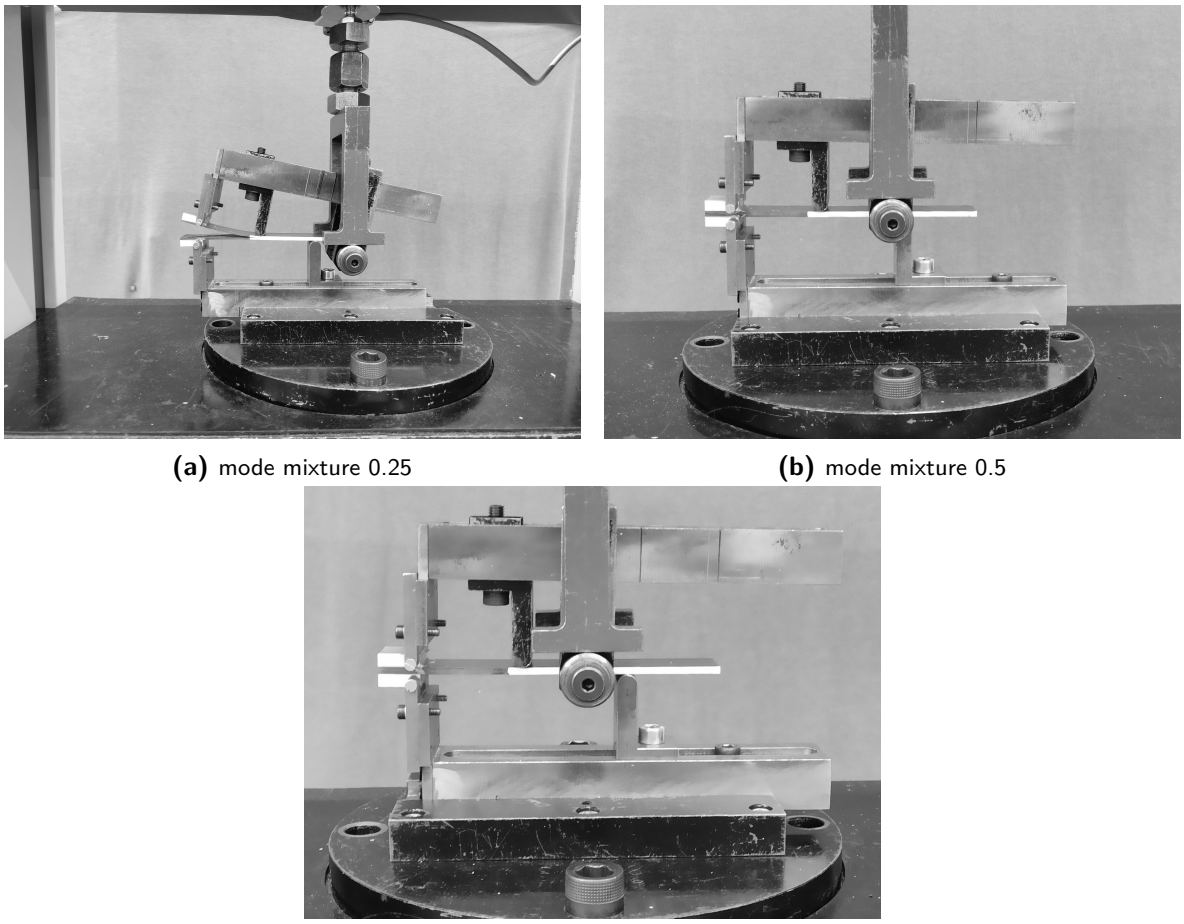
The MMB tests were performed for three-mode mixtures of 0.25, 0.5, and 0.75. The desired mixed mode fracture was achieved by determining the length of the loading lever arm ’c’ from the analytical relation expressed in Equation 4.4 based on the properties of the material

system. Table 4.4 shows the lever length, and Figure 4.13 illustrates the MMB testing configuration for different mode mixtures with corresponding saddle positions.

$$c = \frac{12\beta^2 + 3\alpha + 8\beta(\sqrt{3\alpha})}{36\beta^2 - 3\alpha} L \tag{4.4}$$

	Loading arm length, c (mm)		
Mode mixture	0.25	0.5	0.75
GF/PP	75.59	41.44	28.95
CF/PPS	78.06	42.18	29.27

Table 4.4: Loading arm length for different mode mixtures for UD GF/PP and UD CF/PPS specimens.



(a) mode mixture 0.25 **(b)** mode mixture 0.5

(c) mode mixture 0.75

Figure 4.12: MMB test configuration for different mode mixtures (CF/PPS).

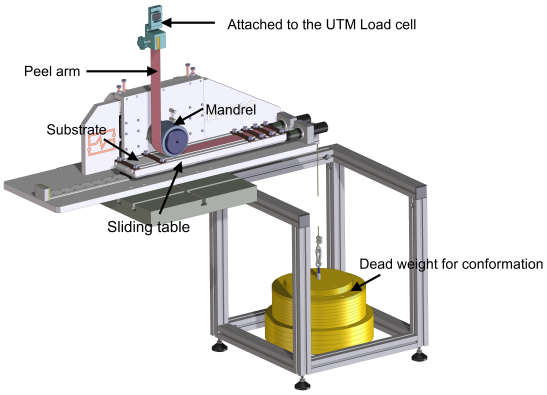
All the MMB experiments were loaded in a displacement-controlled mode at a rate of 0.5 mm/min. The ASTM standard does not suggest pre-cracking in contrast to the DCB tests. Since the delamination propagation may exhibit either stable or unstable behavior, which is

primarily controlled by the mode-mixture in the MMB tests. Thus, the testing was limited to the crack initiation values, and the propagation option was not considered. Further, the tests were stopped when the extended crack reached underneath the central roller.

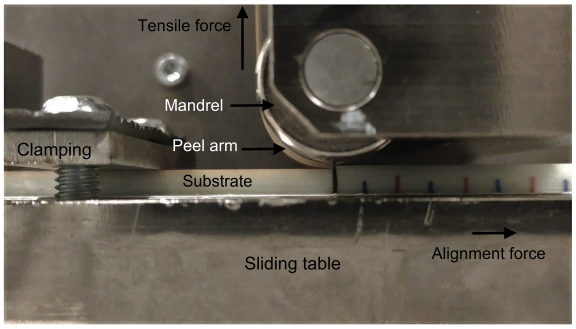
4.7.4 Mandrel Peel Test

The mandrel peel tests were executed employing the mandrel peel set-up (Figure 4.13a) at the Lightweight materials lab, Brightlands Materials Center (BMC)- TNO. As can be seen, the rigid base/substrate of the specimen is fixed to the sliding table of the set-up. The peel arm of the specimen, which is flexible, is bent around a cylindrical mandrel. So as to achieve the peel arm conformity with the mandrel roller, the alignment force was applied using the dead weight plates. A tensile force is eventually exerted to peel off the peel arm from the rigidly fixed arm.

The mandrel peel experimental apparatus (side view) as shown in Figure 4.13b was attached to an Instron 5966 Universal testing machine incorporated with a 1kN load cell and displacement transducers to measure the peel force, alignment force, and peeling rate.



(a) Schematic of the mandrel peel test setup



(b) Side-view of the mandrel peel apparatus showing the test configuration

Figure 4.13: Mandrel Peel Test setup at the BMC facility.

In this study, mandrel rollers of radii ranging between 10mm - 100mm were employed to characterize the interlaminar fracture behavior for two different material systems. Additionally, the alignment load required to achieve conformity for a given specimen thickness and the mandrel roller radius was optimized experimentally (trial and error) prior to the actual experiments. An example of the procedure is shown in Figure 4.14. Furthermore, a camera device was utilized to monitor the peel arm conformation relative to the mandrel, positioned parallel to the setup, recording the complete peeling process.

The experimental protocol encompasses two peeling cycles. In the initial first cycle, the peel arm is separated from the laminate to a pre-determined delamination length. After the first cycle, the unbonded peeled specimen (G_c =0) is subjected to another peeling process to determine the friction coefficient, μ, in the mandrel peel set-up. The experiments were performed at a constant peeling rate of 12.5 mm/min, and the data were recorded for a minimum peel distance of 50 mm. The mandrel peel test entails the measurement of the

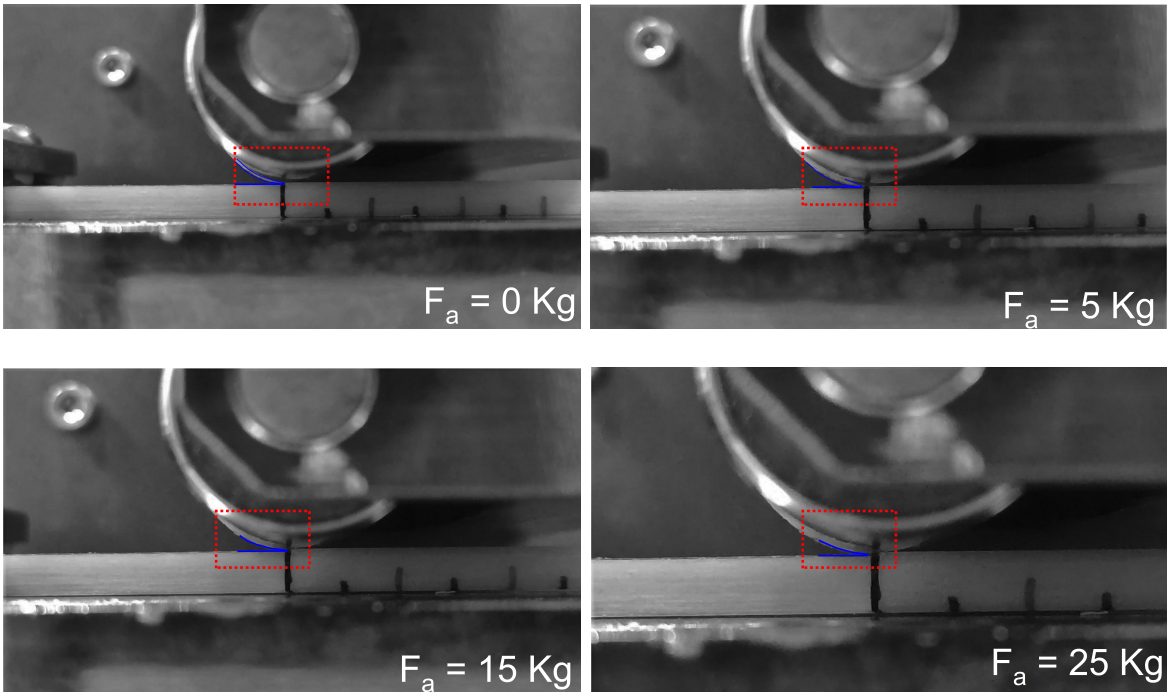


Figure 4.14: Illustration of the alignment load optimization procedure to achieve conformity.

alignment (F_a) and peel force (F_p), and from the force-displacement analysis, the friction co-efficient in the set-up and the interlaminar fracture toughness are determined based on the energy balance approach discussed in Section 5.4.

Another crucial section of this experimental campaign is the fractography studies of specimens to understand the nature of the fracture behavior and substantiate the experimental findings. Optical, Wide angle Laser Confocal and Scanning Electron Microscopy have been utilized to observe and co-relate. The resultant data output obtained from the various experiments is further processed using the reduction procedures described in Chapter 5.

Chapter 5

Data Processing Procedures

5.1 Modified Beam Theory (DCB)

The ASTM specifies three different data reduction procedures for calculating the mode I critical SERR, G_{I_c} as a function of delamination length, which is based on the Irwin - Kies [81] relation as in Equation 5.1.

$$G_{I_c} = \frac{P^2}{2b}\frac{dC}{da} \tag{5.1}$$

Modified Beam Theory (MBT), Compliance Calibration (CC), and Modified Compliance Calibration (MCC) are the three methods. The assumption of specimen compliance of the cantilever beam and its corresponding change with the delamination length forms the primary distinction. Out of these, the ASTM proposes that the MBT reduction method yields more conservative G_{I_c} data. Thus, only the MBT method will be elaborated on in detail.

Modified Beam Theory

According to the beam theory, the critical SERR is expressed as in Equation 5.2, which is calculated for a double cantilever beam fixed at the crack front.

$$G_{I_c} = \frac{3P\delta}{2ba} \tag{5.2}$$

where b is the specimen width, a is the crack length (delamination length), P is the applied force, and δ is the load point displacement. The derivation of critical SERR based on the Beam Theory assumes that no rotation takes place at the crack front. However, in actual reality, crack-tip rotation occurs. As per the standard, the Modified beam theory (MBT) data reduction method, which considers marginally larger delamination, to compensate for this effect was employed to determine the Mode I Interlaminar fracture toughness (ILFT), G_{I_c} using the Equation 5.3, which would provide more realistic and conservative values.

$$G_{I_c} = \frac{3P\delta}{2b(a + |\Delta|)} \tag{5.3}$$

A correction factor 'Δ' accounts for deflection and crack-tip rotation since the beam considered is not perfectly built-in in practice. The correction factor is derived experimentally from the linear regression analysis of the cube root of compliance and delamination length. The corresponding extrapolation of the linear fit generates the negative intercept of x, the value 'Δ' for which the corresponding compliance is zero.

From the above data reduction approach, the flexural stiffness of the material system can also be derived from Equation **5.4**.

$$E_{1f} = \frac{64P(a + |\Delta|)^3}{\delta b h^3} \tag{5.4}$$

For the determined correction factor, the stiffness should remain approximately constant over the entire crack propagation length. However, that is not the case when the fiber bridging mechanism is observed; instead, an increase in the bending modulus will be encountered.

5.2 Compliance Calibration Method (ENF)

The data reduction is based on the conventional compliance calibration method to determine the Mode II critical Strain energy release rate, G_{II_c}. An alternative approach to reduce the G_{II_c} data is using the Classical Beam theory analytical expressions. However, as per the ASTM, compliance calibration is the only method acceptable for the data reduction of the ENF tests.

Compliance Calibration Method

In this method, the compliance of the specimen at each particular crack length was determined by the slope inverse of the linear section of the force-displacement plot derived from the linear regression analysis. Further, the linear regression analysis of the form in Equation **5.5** was applied to fit the compliance vs. crack length data to obtain the compliance calibration coefficients for each specimen. The advantage of this method is that it does not necessitate any derivation of analytical equations for compliance as the compliance vs. crack length data is generated experimentally.

$$C = A + ma^3 \tag{5.5}$$

The parameters A and m are the compliance coefficients, where A is the intercept and m is the slope. The Strain energy release rate, G_Q (Non-precracked) based on the the compliance calibration method is given in the Equation **5.6**.

$$G_Q = \frac{3mP_{max}^2 a_0^2}{2b} \tag{5.6}$$

where the width of the spcimen is b, P_{max} is the peak force registered, a_0 is the crack length used in the **NPC! (NPC!)** fracture test. Finally, the determined G_Q is checked for validity. If found valid, then $G_{II_c} = G_Q$

The acceptability and reliability of the candidate fracture toughness are further evaluated for validation by determining the percentages of G_Q ($\%G_Q$) attained during the corresponding compliance calibration using the expression **5.7**:

$$\%G_{Qi} = \left[\frac{100(P_i a_i)^2}{(P_{max} a_o)^2}\right]; i = 1, 2 \tag{5.7}$$

where P_i is the value of the peak force used during the compliance calibration at a_i, a_i is the i^{th} crack length. Typically, the two forces and corresponding crack lengths: a_1= 20 mm and a_2 = 40 mm considered during compliance calibration for every test.

The fracture toughness of the tested specimen is accepted if the two values determined satisfy the criteria, $15 \leq \%\mathbf{G}_Q \leq 35$. Or else, the obtained test results are excluded/discarded and the CC forces are modified suitably for further testing.

The toughness for any of the specimens where the candidate's toughness is accepted and valid:

$$G_{II_c} = G_Q \tag{5.8}$$

5.3 Corrected Beam Theory (MMB)

The ASTM standard recommends the **Corrected Beam Theory** as the data reduction method for calculating mixed mode I-mode II interlaminar fracture toughness of composites.

Accordingly, the following equations are proposed in the ASTM standard for determining the fracture toughness and mixed mode components.

$$G_{I_{MMB}} = \frac{12(a + \chi h)^2[P(3c - L)]^2}{16b^2 E_{1f} h^3 L^2} \tag{5.9}$$

$$G_{II_{MMB}} = \frac{9(a + 0.42\chi h)^2[P(3c - L)]^2}{16b^2 E_{1f} h^3 L^2} \tag{5.10}$$

Where P is the applied force, b is the specimen width, a is the crack length (delamination length), χ is the crack length correction parameter, c is the length of the loading arm lever, E_{1f} is the flexural modulus along the fibre-direction, h denotes half of the specimen thickness, and finally L is the half-span length of the MMB testing apparatus.

As per the standard, if the weight of the loading arm lever and the testing apparatus is more than 3% of the applied force, this may overload the specimen and eventually affect the calculated fracture toughness. Thus, to account for this effect, the ASTM standard proposes the weight corrections which must be considered.

Introducing the weight corrections to the above equations, yields the following expressions:

$$G_{I_{MMBg}} = \frac{12(a + \chi h)^2[P(3c - L) + P_g(3c_g - L)]^2}{16b^2 E_{1f} h^3 L^2} \tag{5.11}$$

$$G_{II_{MMBg}} = \frac{9(a + 0.42\chi h)^2[P(3c - L) + P_g(3c_g - L)]^2}{16b^2 E_{1f} h^3 L^2} \tag{5.12}$$

where P_g is the weight of the loading arm lever and the testing fixture, and c_g denotes the distance from the lever roller (at the top) to the center of the gravity of the lever arm, and it varies with the length of the loading arm lever.

In addition, the discussed corrected beam theory can also be employed to the mode I DCB. The difference is that the correction factor for the crack-tip rotation would be determined analytically based on the material properties instead of the compliance measured during the DCB testing. The equation for the Mode I Interlaminar fracture toughness would then be expressed as:

$$G_I = \frac{12P^2(a+\chi h)^2}{16b^2E_{1f}h} \tag{5.13}$$

5.4 Energy Balance Approach (MP)

It is important to state that there are currently no standards for the Mandrel peel test method recommending the procedure for data reduction. **Grouve et al.** [36] in their study described the data reduction scheme on the basis of the energy balance approach. Accordingly, the below-discussed data reduction procedure will be followed for calculating the strain energy release rate in the present work.

The mandrel peel test determines the total strain energy release rate in terms of strain energy change per unit area of crack advancement.

$$G = \frac{1}{b}\left(\frac{dU_{ext}}{da} - \frac{dU_d}{da} - \frac{dU_s}{da}\right) \tag{5.14}$$

where U_{ext} is the external work, U_d is the dissipated energy during peel test and U_s is the strain energy stored in the peel arm. |bda| represents the change in the crack area in which |b| is the peel arm width and 'da' denotes the increment in the crack length.

In addition, the residual stress induced during the manufacturing is also taken into account in the analysis. The external work due to the crack propagation corresponds to Equation **5.15**

$$dU_{ext} = -F_a da + F_p da + F_p da(\epsilon_m - \epsilon_r) = (F_p - F_a)da + \frac{F_p^2}{bhE}da - \frac{F_p\sigma_r}{E}da \tag{5.15}$$

where h and E are the thickness and Young's modulus of the peel arm, respectively. ϵ_m corresponds to the elastic strain in the peel arm and whereas ϵ_r denotes the pre-strain in the peel arm due to the residual stress σ_r.

The dissipation of energy during the peeling might involve the plastic deformation of the peel arm as well as the friction in the test set-up. However, for a peel arm with fiber reinforcement in the 0° direction, the dissipated energy via plastic work is generally considered to be negligible. Moreover, the mandrel size is considered such that the bending strain does not exceed, ensuring no plastic deformation occurs due to bending. Therefore, during the peeling test, only friction is accounted for and taken into consideration which is proportional to the peel force, F_p, and is expressed as in Equation **5.16**:

$$dU_d = \mu F_p da \tag{5.16}$$

where μ is the friction. Further, the strain energy U_s comprises the tensile strain energy stored in the peel arm and substrate and the residual strain energy stored in the bonded part of the peel arm and substrate. The change in strain energy associated with incremental crack growth is represented as given in Equation **5.17**:

$$dU_s = \frac{1}{2}\sigma_m \epsilon_m bhda - \frac{1}{2}\sigma_r \epsilon_r bhda = \frac{1}{2}\frac{F_p^2}{bhE}da - \frac{1}{2}\frac{bh\sigma_r^2}{E}da \tag{5.17}$$

Substituting the relation for dU_{ext}, dU_d and dU_s into Equation 5.14 leads to Equation 5.18, which represents the energy release rate.

$$G = \frac{1}{b}\left[F_p(1-\mu) - F_a + \frac{1}{2}\frac{F_p^2}{bhE} + \frac{1}{2}\frac{bh\sigma_r^2}{E} - \frac{F_p\sigma_r}{E}\right] \tag{5.18}$$

Besides, the contribution of stored strain energy and the residual stress in the peel arm to the overall strain energy release rate is significantly negligible. Consequently, both the terms are ignored during the calculation; eventually, Equation **5.18** can be rewritten as:

$$G = \frac{1}{b}\left[F_p(1-\mu) - F_a\right] \tag{5.19}$$

The energy release rate (**5.19**) can now be determined from the peel force, alignment force, frictional coefficient, and the peel arm width.

Chapter 6

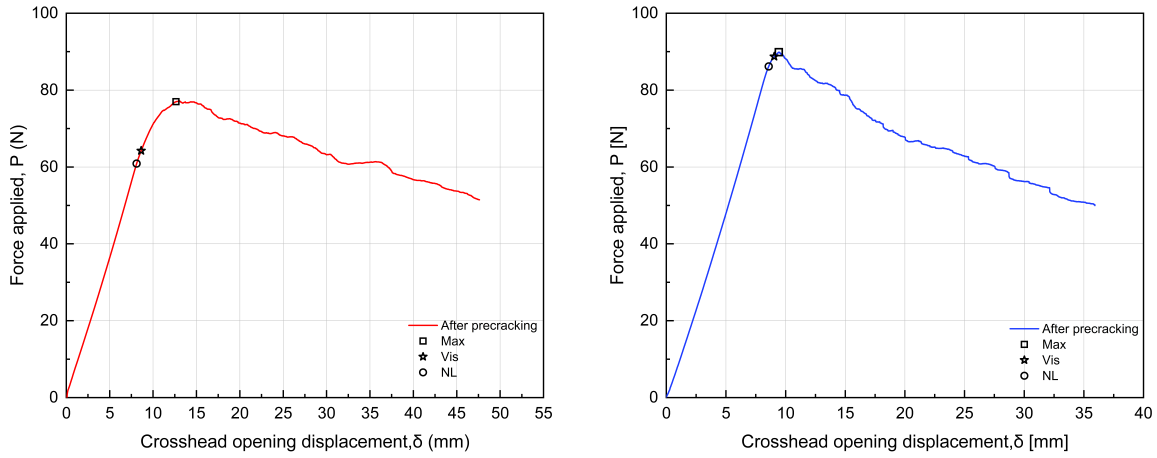
Experimental Results and Discussions (DCB, ENF, & MMB)

The present chapter provides the experimental results of the DCB, ENF, and MMB tests performed for UD GF/PP and CF/PPS composite materials. The results are analyzed and discussed in separate sections. Fractography studies using Optical and Laser confocal microscopy have been conducted to understand the fracture behavior and substantiate the experimental findings.

6.1 Double Cantilever Beam Tests

This section provides the details of the DCB mode I fracture test results. The characteristic force versus displacement plots for both the UD GF-PP and UD CF-PPS DCB specimens are illustrated in Figure 6.1. Notably, these force-displacement curves represent the response obtained during reloading after the pre-cracking, and in each of these cases, the pre-cracked length varies slightly (± 1 mm). Initially, the force-displacement response exhibits a linear trend, followed by the non-linearity; it can be noticed that the crack initiation starts as the force reaches a critical value, and eventually, the crack propagates in a manner displaying a steady decline in the force measured. The deviation from linearity is smooth in both cases; however, it is slightly more pronounced for the GF/PP specimens. Moreover, after the crack initiation, the force increase is relatively higher. It could also be seen that for both the GF/PP and CF/PPS DCB specimens, the visual crack onset emerges after the point of non-linearity and prior to the peak load.

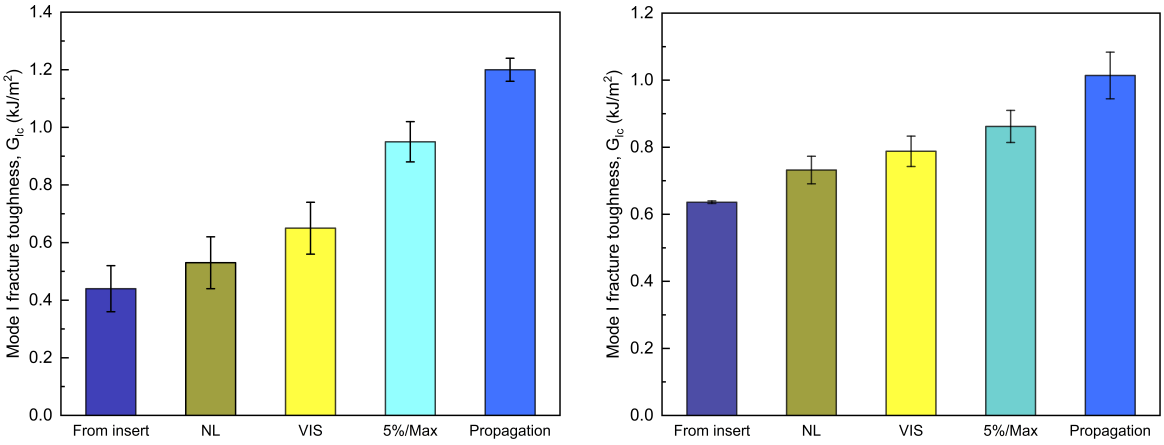
In the DCB test, it is not only essential to deduce the G_{Ic} as a function of delamination length; it is significantly vital to have a clear distinction between the initiation and the propagation mode I fraction toughness. ASTM standard proposes three different methods (NL, VIS, and 5 %/max) for determining the mode I initiation values and is defined in Section 5.1.



(a) GF/PP **(b)** CF/PPS

Figure 6.1: Characteristic force-displacement plots for UD GF/PP and UD CF/PPS DCB specimen.

The average values of mode I fracture toughness, G_{Ic}, and the standard deviation are shown in Figures **6.2a** and **6.2b** for UD GF/PP and UD CF/PPS specimens, respectively. It is apparent that the difference in the initiation values between the insert film and the precrack is higher in the GF/PP specimens, as predicted from the force-displacement curves. The mean propagation toughness, $G_{Ic_{prop}}$, is determined from the point of max peak force.



(a) GF/PP **(b)** CF/PPS

Figure 6.2: Mode I interlaminar fracture toughness

The resistance curve also known as R-curve presents the Mode I Interlaminar fracture toughness, G_{Ic}, as the function of the delamination length, which distinguishes the onset crack initiation and the subsequent propagation of the delamination. It could be noticed that the R-curve of the CF/PPS specimens (Figure **6.4**), after the initiation, converged to a steady phase earlier, following a minimal increment in the crack length.

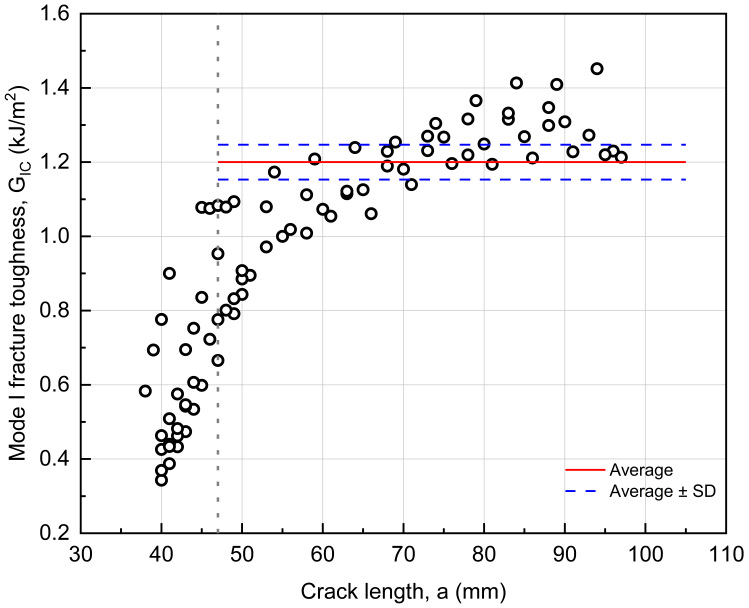


Figure 6.3: Mode I fracture toughness as a function of crack length (R-curve) of UD GF/PP specimens. Increasing resistance due to large scale bridging.

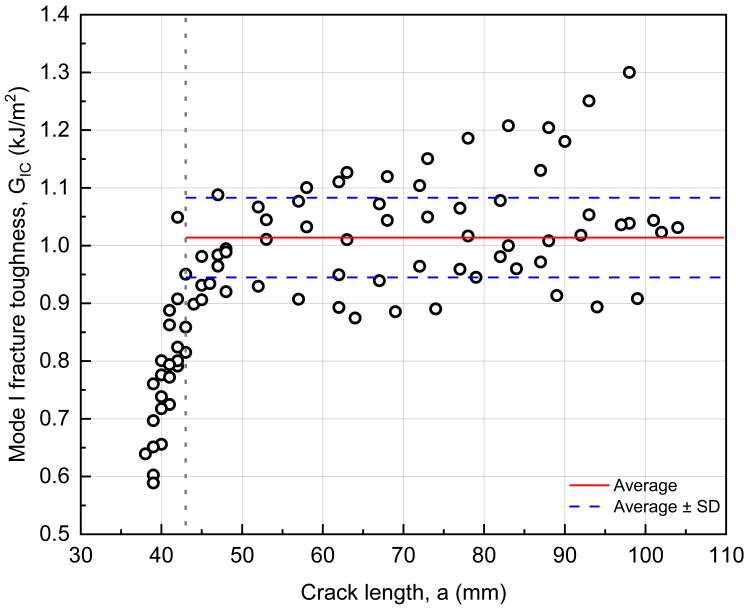


Figure 6.4: Mode I fracture toughness as a function of crack length (R-curve) of UD CF/PPS specimens. Converges to a steady state propagation around crack length 50 mm.

However, the GF/PP shows a gradually sharp increase in the critical energy release rate after the crack onset, and the propagation fracture toughness tends to reasonably reach a steady level after considerable crack propagation (Figure **6.3**). This resistance to delamination behavior can be associated with the fiber-bridging phenomenon, which is more typically observed at the interface between the unidirectional plies oriented in the 0° direction.

Another interesting aspect is that the NL, VIS, and the 5%/max point are almost closer to each other for the UD CF/PPS than the UD GF/PP specimens. Primarily, the higher fiber/polymer resin volume ratio and the lack of plastic deformation of the matrix might result in the visual crack onset at the edges to be observed as soon as the force-displacement curve starts exhibiting non-linearity, which lies closer to the peak max point. The effects of the blunt crack tip (due to insert film) and the resin-rich zone on the crack onset (G_{Ic} initiation) are discussed further.

The insert film generates a resin pocket locally disturbing fiber/matrix distribution near the insert film end. As the amount of resin might differ, the effect of the blunt crack tip together with the ductile PP resin-rich region presumably causes plastic deformation/ micro-cracking of the resin at the interface, which ultimately leads to scattering observed in the initiation fracture toughness values as seen in Figure 6.2a. Furthermore, the crack path depicted in Figure 6.5 indicating the presence of broken fibers makes it likely that the crack front (intralaminar) initiated and accelerated the bridging effects early, and this could explain the reason for the observed increase in the R-curve with the delamination length in the GF/PP. While due to considerably less resin near the insert film of the CF/PPS specimens, low plastic deformation of the PPS resin and low severity of the bridging phenomenon occurs at the start, ensuing in a lower scattering of the initiation values obtained at the insert film crack tip.

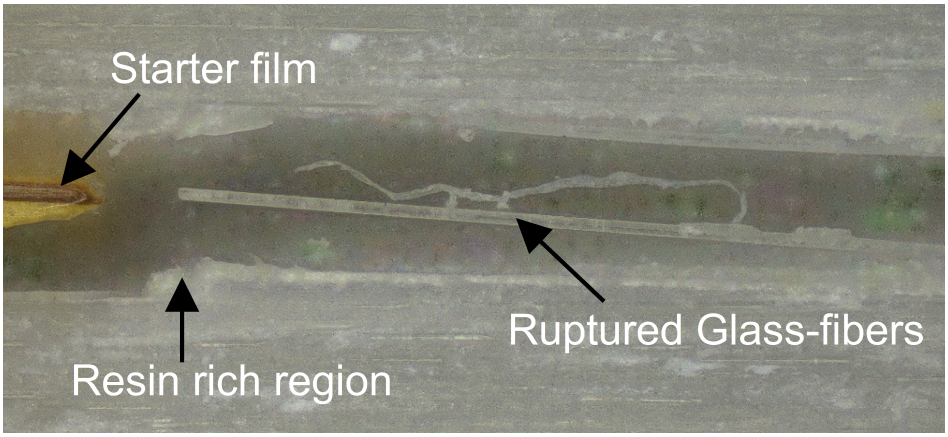


Figure 6.5: Image shows the crack path of the GF/PP specimen with the resin-rich region and broken fiber.

In addition, the propagation toughness was higher than a thinner specimen tested during the preliminary analysis. The processing condition, however, remained the same in both cases. The reason for this could be well understood from the works of Davies et al. [**113**], Bent F. Sorensen et al. [**112**], where an explanation considering the effects of the thickness on the fiber-bridging and the corresponding crack opening displacement was presented. The flexible thin specimens would enable accommodating larger crack displacement ensuing in the breakage of the bridged fibers at an earlier stage, in comparison with the thicker specimens

(stiffer), where it necessitates a considerable crack advancement before a balanced state of formation and breakage of fiber develops.

During the visualization of the experiments, the bridging of fibers was noticed between the arms of the DCB Specimens. Figures 6.6 and 6.7 illustrate the bridging of fibers for the GF/PP and CF/PPS specimens, respectively. Notice here the side view of the GF/PP specimens in Figure 6.7 revealing the extent of the bridging of glass fibers, which is found to be increasing along the crack length. This eventually explains the cause for the increasing R-curve. Additionally, the fracture surfaces reveal a limited quantity of bare carbon fibers in the CF/PPS specimens, substantiating the relationship between the fiber bridging and the loosened fibers.

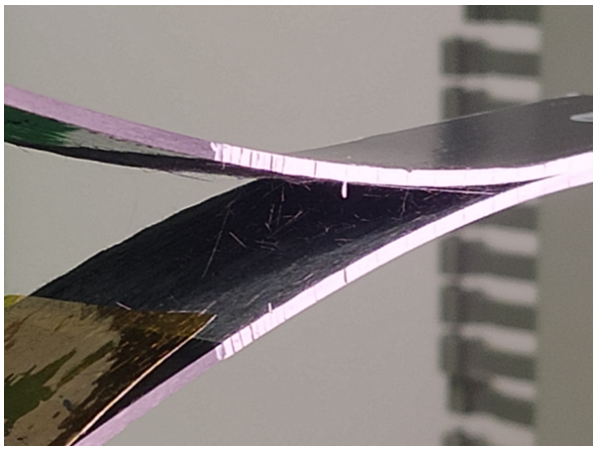
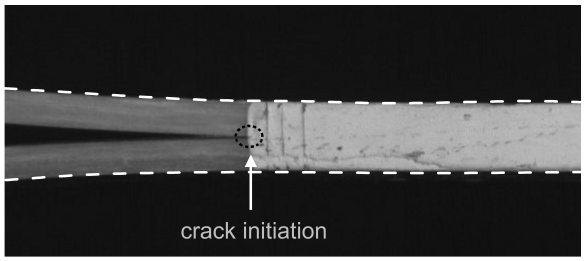
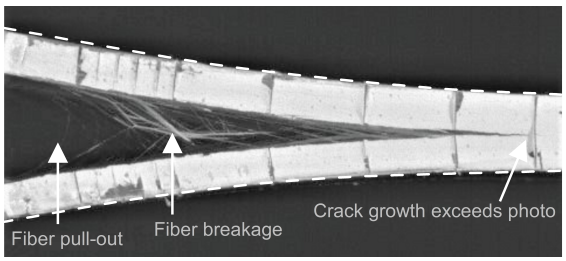


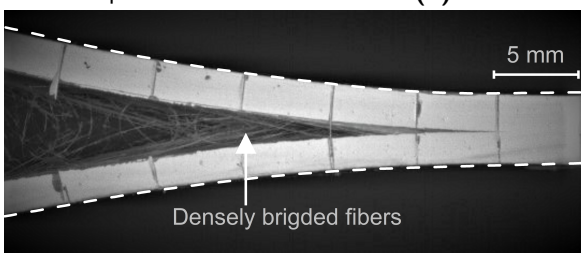
Figure 6.6: Fiber bridging observed in the CF/PPS specimen.



(a) At the insert film tip



(b) At ≈ 30 mm from the crack tip



(c) At ≈ 55 mm from the crack tip

Figure 6.7: Side-views of the GF/PP specimens displaying fiber bridging density with crack propagation.

The denuded loose glass fibers imply the extensive fiber bridging phenomenon, which is con-

siderably intrinsic due to the poor interfacial adhesion strength between the (glass) fiber and the matrix is more usual with glass-fiber composites [122]. In order to study the mode II fracture properties, ENF test was carried out. Section 6.2 continues more on this.

6.2 End - Notched Flexure Tests

The representative force - displacement plots for the two types of composite material systems measured during the ENF test are presented in Figures 6.8 and 6.9. Both curves represent the non-precracked (NPC) test.

Throughout the initial phase of the loading, a linear trend in the force-displacement curve can be observed for both composites. However, in the GF/PP specimens, an increase in the compliance of the beam (stiffness reduction) exhibiting prominent non-linearity following the linear segment can be distinguished prior to the maximum peak load. Davies P et al.[40] and a few other researchers [44][45] have noticed similar responses for the UD GF/PP composite. This phenomenon is a primary characteristic of the R- curve effect, which is generally observed once the crack growth has started [175].

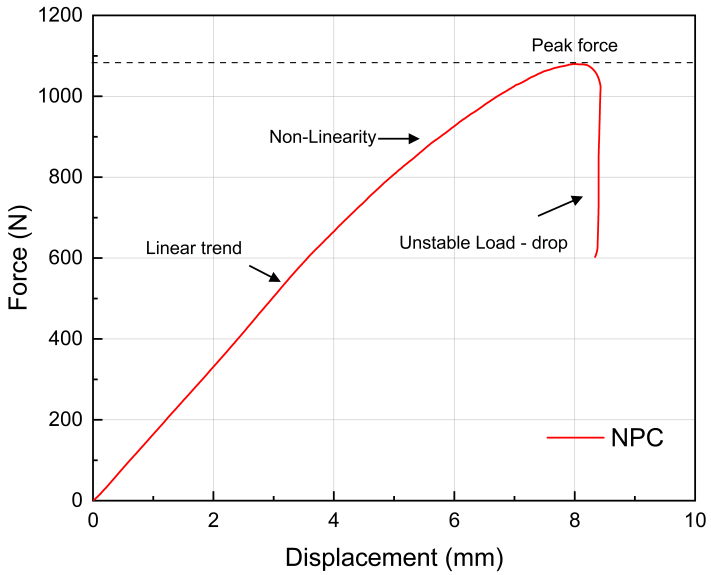


Figure 6.8: Typical ENF Force vs. Displacement plot of UD GF/PP specimens

Additionally, as the force reaches the peak, abrupt crack growth and a significant reduction in the force are observed, and it is possible to state that the crack growth/propagation is unstable, typically associated with snap-back instability [67][56]. Meanwhile, on the other hand, only a slight non-linear behavior could be noticed for the CF/PPS specimens, and the load tends to decrease steadily, showing a more stable crack growth behavior.

A snap-back instability ensues during the crack propagation when the strain energy released by the progressing crack exceeds the required energy for creating new fracture surfaces (zones).

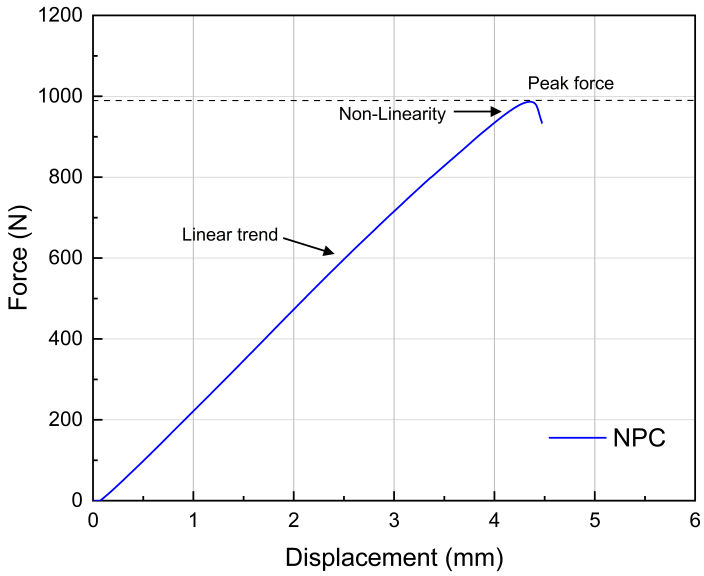


Figure 6.9: Typical ENF Force vs. Displacement plot UD CF/PPS specimens

During such situations, the force and displacement applied should reduce concurrently to maintain equilibrium, resulting in a snap-back behavior. This snap-back phenomenon depends on various factors, namely the material's properties, the specimen's geometric features, and the initial crack [176].

Besides, the unloading curve (GF/PP specimens) does not return to the origin, indicating hysteresis. Furthermore, the recorded hysteresis is plausibly attributed to the elastic snap-back instability action since no macroscopic (visible) plastic damage in the specimens (surface) was observed, and thus the material behavior is considered elastic. Nonetheless, owing to the fact that hysteresis is quite negligible, the critical energy is considered to be unaffected.

The non-linearity noticed precisely before the extension of the crack may presumably be related to the plastic deformation of the ductile polypropylene (thermoplastic resin) and formation/growth of the fracture process zone near the crack tip, which could be in the form of coalescence of sub-critical matrix cracking, delaying the unstable crack growth to a higher displacement [44][45][40][177]. This is highlighted by the SEM photograph in Figure 6.10, which indeed exhibits the damage zone at the crack tip substantiating the argument. Nevertheless, the non-linearity could not be ascribed to the geometric non-linearities for the reason that the same behavior was observed for a different specimen geometry during the preliminary analysis.

Figure 6.11 presents the force-displacement response obtained for different GF/PP specimen geometry. It could be noted that both specimen sizes exhibit the same behavior. Salviato et al. [67], in their size effect study on the interlaminar fracture of epoxy-based composite, reported the nonlinear phenomenon to be more significant in the small-sized samples relating it to the fracture process zone. At the same time, the unstable propagation was recorded for all the sizes tested, indicating the snapback instability.

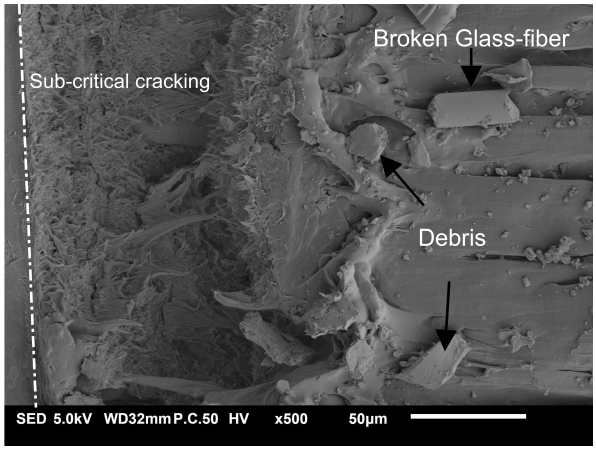


Figure 6.10: Fracture process zone near the crack tip exhibiting matrix microcracking (insert film) - GF/PP (x500)

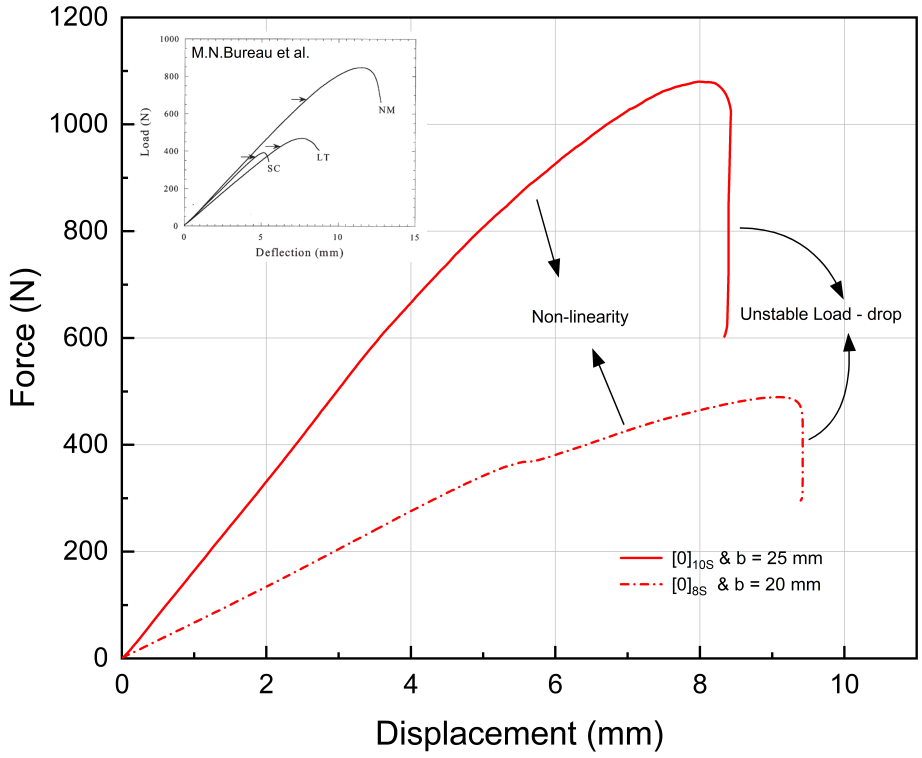
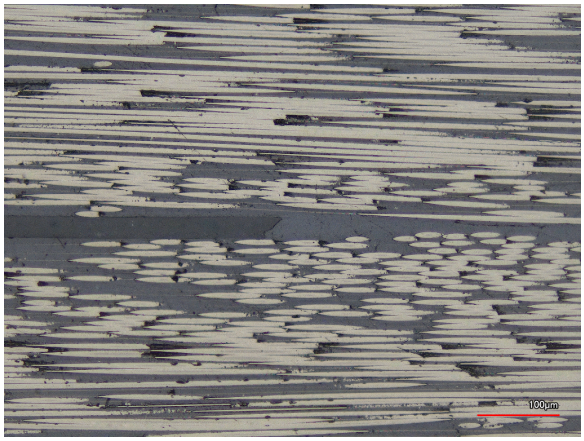


Figure 6.11: Typical ENF Force vs. Displacement plots for different specimen geometries - GF/PP

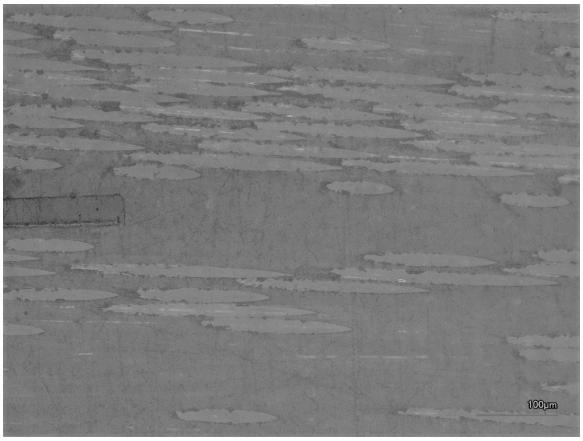
Additionally, the increase in the delamination resistance (fracture toughness) in the mode II loadings is also mainly ascribed to the damage zone and the typically observed crack-tip plasticity compared to the mode I, where the contribution of fiber-bridging is considerable and significant [56][45].

Figure 6.12a and 6.12b shows that the insert film generates resin pocket locally disturbing

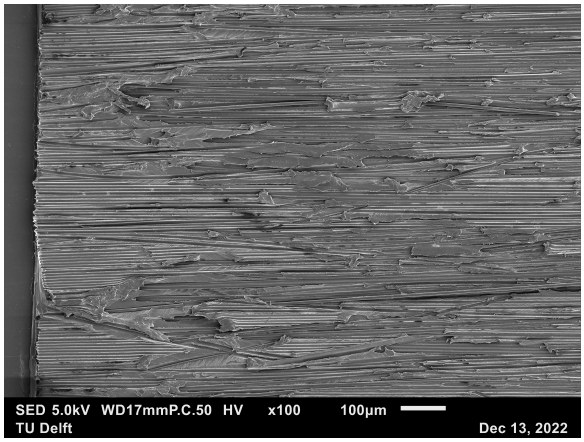
fiber/matrix distribution near the insert film end. Further, the resin-rich region is more in the GF/PP composite compared to the CF/PPS. This is also in good agreement with the fractographic micrographs shown in Figure 6.12d, which substantially reveal a more rough surface indicating matrix cracking at the crack initiation region in comparison with the Figure 6.12c, where the crack growth seems to be more directly advancing towards the fiber/matrix interface.



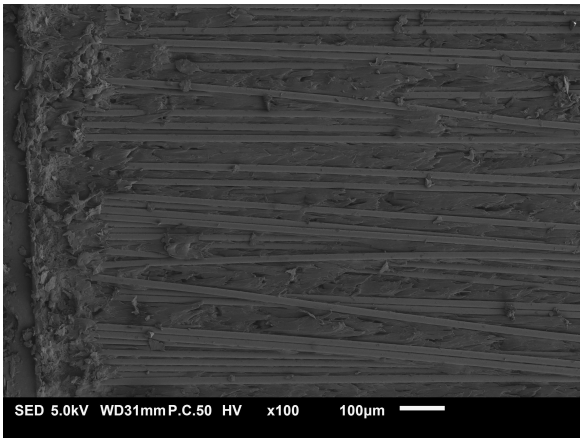
(a) CFPPS crack tip (starter film)



(b) GFPP crack tip (starter film)



(c) Fracture surface near the crack tip (insert film) - CF/PPS (x100)



(d) Fracture surface near the crack tip (insert film) - GF/PP (x100)

Figure 6.12: Condition of the crack tip near the starter film region and the corresponding fracture surface.

Material	P_{max} [N]						
	I	II	III	IV	V	**Average**	**SD**
GF/PP	940.92	928.89	1077.15	1079.85	1021.36	**1009.63**	**64.6**
CF/PPS	1000.22	1003.46	986.49	1061.57	1026.64	**1015.68**	**26.33**

Table 6.1: Values of the peak forces (P_{max}) recorded during the mode II ENF tests of UD GF/PP and UD CF/PPS.

Table 6.1 presents the values of the peak forces. As can be seen, the peak forces are high.

From the force-displacement curves, another interesting aspect that is worthy of attention is that in the CF/PPS specimens, the load drop magnitude is effectively controlled and arrests the unstable crack growth, contrary to the GF/PP composite, which shows a significant sharp drop in the magnitude of the load. It indicates the relation between the load drop magnitude (and behavior) and the potential suppression of the unstable crack growth, while the peak force signifies the capacity to control/resist the delamination. All the GF/PP specimens experienced unstable crack propagation, and in the tested specimens, the magnitude of the load drop ranged from 68 N to 379 N, whereas it was a stable load decrease for CF/PPS. Figure 6.13 summarizes the load drop and the corresponding delamination propagation length measured from the tip of the starter crack (insert film) after the NPC fracture test.

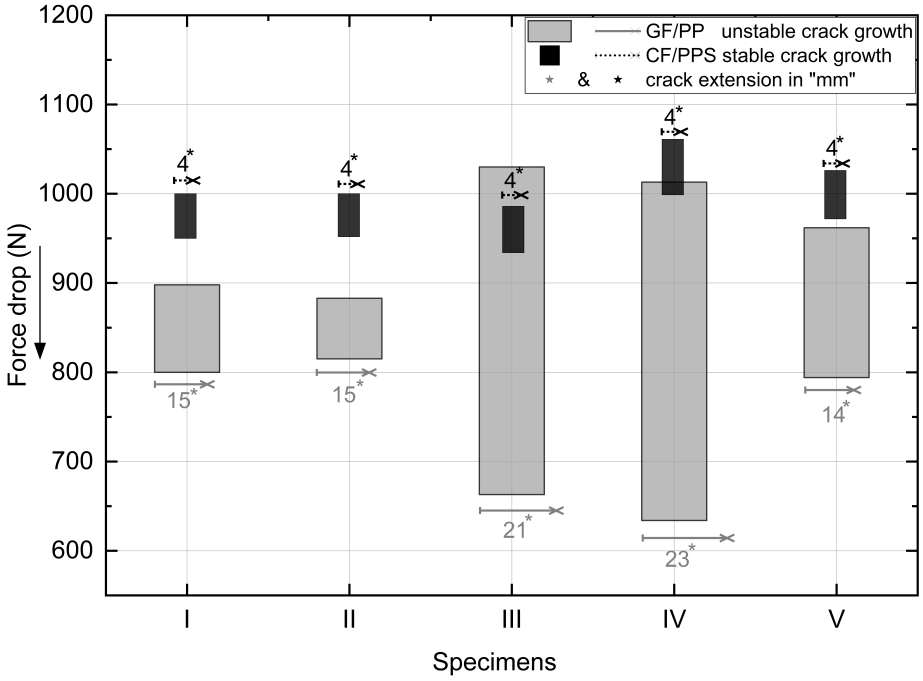
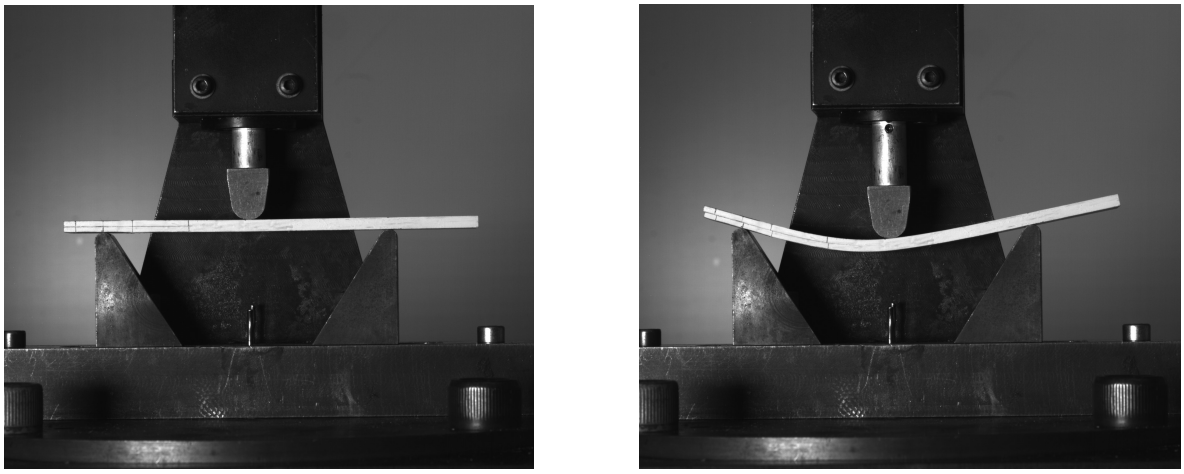


Figure 6.13: Indication of the force drop magnitude and the corresponding crack growth for the ENF specimens.

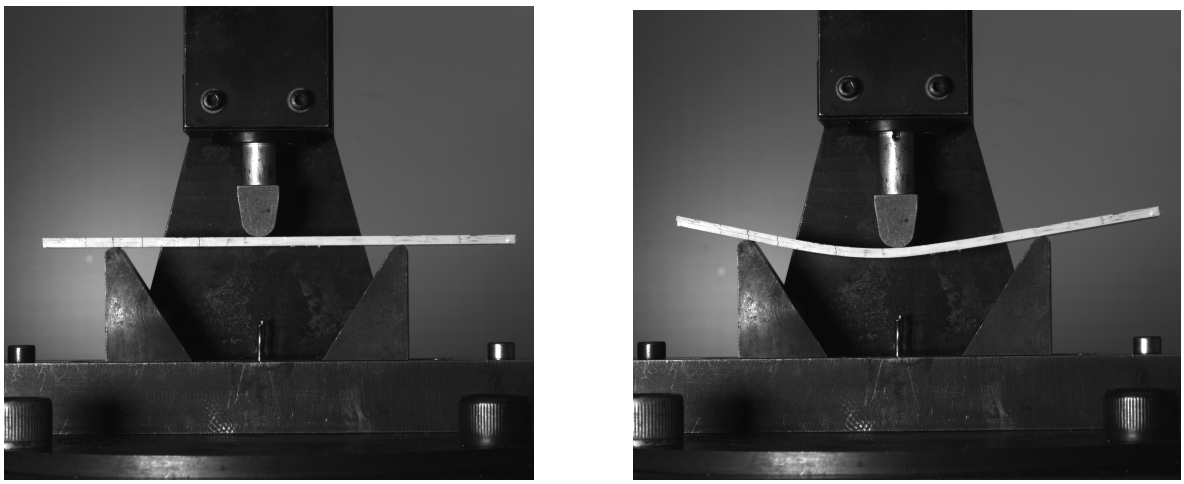
The pictures depict the macroscopic extension of the crack. Figure 6.14a and 6.15a illustrates the start of the NPC fracture test, while the extended crack and the resistance to delamination at the end of the test can be seen in Figure 6.14b and 6.15b for both materials, respectively. These photographs agree well with the corresponding P-δ results obtained and the data presented in Figure 6.13, where it is plausible to note that the GF/PP composite propagated a minimum of 15 mm, whereas a crack extension of 4 mm was observed for the CF/PPS. Also, the unstable crack extension stops at length greater than L/2 for GF/PP specimens III and IV.

The mode II interlaminar fracture toughness for the present study was determined at the crack initiation (from the insert), representing the onset fracture toughness. The accurate definition of the crack initiation point plays a crucial role in determining the G_{IIc}, and the corresponding force value is of utmost importance, according to the ASTM standard [52]. Uncertainty in identifying the delamination onset force could generate unreliable fracture



(a) Start of the NPC test **(b)** End of the NPC test

Figure 6.14: Macroscopic images of the ENF test of GF/PP composite



(a) Start of the NPC test **(b)** End of the NPC test

Figure 6.15: Macroscopic images of the ENF test of CF/PPS composite

toughness. Due to the complexities involved in identifying the exact crack initiation point, the non-linearity (NL) and the 5%/ max criteria are generally employed. Nonetheless, this becomes even more challenging if extensive non-linearity prior to the peak load is observed due to the fracture process zone. The ASTM standard thus recommends the maximum peak force as the only criterion for the crack initiation for the mode II ENF test. Although the standard suggests choosing other definitions (NL or 5% offset) if necessary for calculating the critical SERR but also mentions that these definitions do not specifically relate to any physical phenomena. Therefore, for the sake of consistency, it was decided to consider the peak load for determining G_{IIc}. Table **6.2** shows the Mode II interlaminar fracture toughness calculated based on the compliance calibration (CC) parameters summarised in Table **??** and **??** following the data reduction procedure outlined in Section **5.2** for respective material systems. Figure **6.16** indicates the average values and the standard deviation of the GF/PP

and CF/PPS specimens.

Material	G_{IIc} **[kJ/m^2]**						
	I	II	III	IV	V	**Average**	**SD**
GF/PP	2.86	2.32	3.12	3.14	2.81	**2.85**	**0.29**
CF/PPS	2.16	1.63	2.1	1.82	1.7	**1.88**	**0.22**

Table 6.2: Mode II Interlaminar fracture toughness, G_{IIc} data

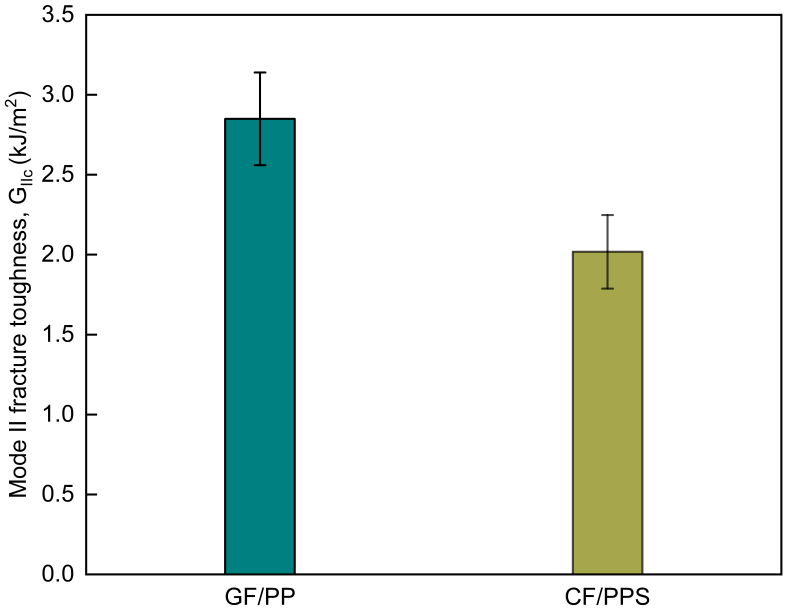


Figure 6.16: Mode II Interlaminar fracture toughness of the two composite systems (NPC)

Although matrix deformation was ascertained to be the characteristic behavior, nonetheless, since the plasticity is observed to be localized and confined only at the tip region of the insert film and the crack propagation path is along the interface, it could be asserted that at a macro level the linear elastic behavior of the tested specimens was maintained. On this basis, the experiments still satisfy the Linear elastic behavior assumption, and the energy release rate values hold good and are acceptable.

Section **6.3** continues on the test results of the MMB specimens.

6.3 Mixed - Mode Bending Tests

The mixed-mode bending tests performed for the UD GF/PP and UD CF/PPS specimens for three various mixed-mode ratios will be discussed here. The force-displacement plots for a mode mixture of 0.25 and 0.5 for the GF/PP specimens is shown in Figure **6.17**, while, it is represented in Figure **6.18** for the CF/PPS specimens measured during the MMB test. In the case of GF/PP for a mode mixity of 0.25, variability in the load-displacement response more

similar to the DCB specimens was observed. The relative stiffness between the specimens and the point of crack onset explicitly stands out, though the differences are insignificant. However, regarding the CF/PPS specimens, the crack initiation points exhibit less scattering. Another important and exciting feature with respect to the force-displacement response of the CF/PPS is that it appears to be closer to the behavior observed (in terms of stiffness) during the DCB test. On the other hand, the peak load registered for the MMB 25% is lower compared to its pure mode I peak force.

Nevertheless, as expected, the crack propagation was observed to be stable in both cases since the mode mixture is near the pure mode I and is more dominated by the mode I opening force. The steady flat propagation beyond the 6 mm crack opening displacement region, as seen for GF/PP, predicts a significant R-curve effect. The propagation toughness can be anticipated to be high, as the force response is almost stable with crack length. The experimental demonstration of this effect is depicted in Figure **6.19a**, where fiber bridging and numerous fiber fractures are observed.

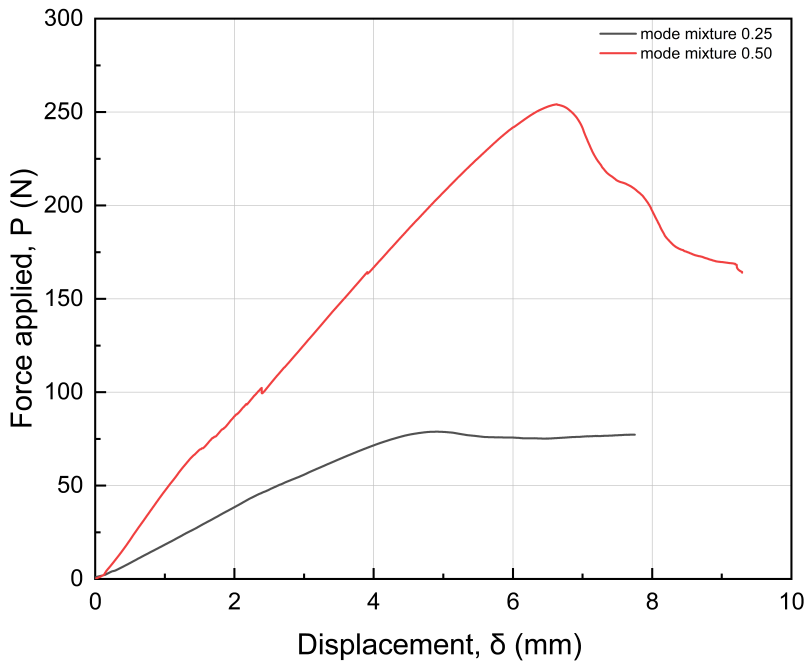


Figure 6.17: Typical MMB Force vs. Displacement plots for GF/PP specimens at various mode mixtures

Amongst the GF/PP specimens tested at a mode mixture of 0.5, variability in the force-displacement curves was observed, and the feature that attracts attention is the value of the peak load recorded. The onset and the subsequent crack advancement region evidently distinguish the randomized sampling between and within laminates; this clarifies that the cause for witnessed behavior could be primarily attributed to the condition of the delamination tip and the associated microscopic mechanisms. Meanwhile, the coefficient of variation is relatively low for CF/PPS specimens, and there is no considerable difference in the stiffness, despite the fact that the specimens were randomized between the laminates. With increasing mode II component, a higher force reduction rate and reduced fiber bridging effects (Figure

6.19b) are observed with the crack growth as far as the GF/PP specimens are concerned, whereas CF/PPS specimens displayed a steady decline in force. With CF/PPS specimens, the insufficient white light presented challenges in the visibility and identification of fiber-bridging effects during the experiments. However, the fracture surface analysis discussed in Section 6.4 detected a lack of fiber bridging.

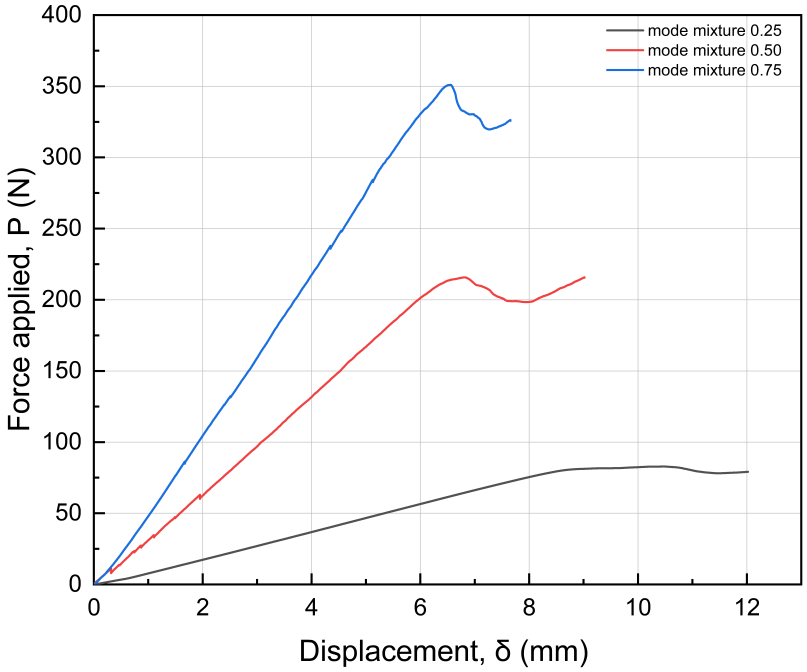
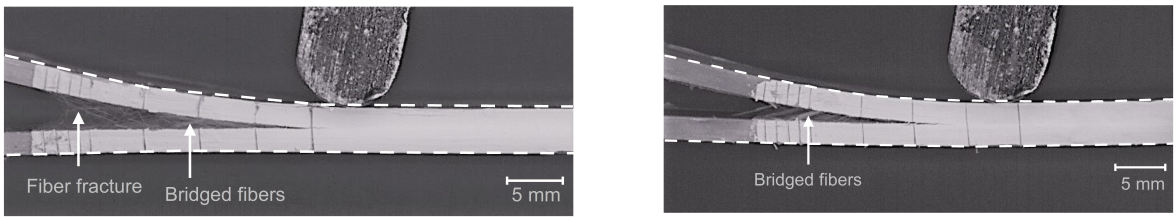


Figure 6.18: Typical MMB Force vs. Displacement plots for CF/PPS specimens at various mode mixtures.

Next, as can be seen (Figure 6.18), the initial compliance of the CF/PPS specimens with the mode mixture of 0.75 does not exhibit much relative deviation, quite similar to the mode II response. The delamination propagates with a steady force drop; the stiffness and the corresponding critical applied force necessary for crack initiation and propagation increase with increasing mode mixture toward mode II. The reason is that in most FRP composites, the interlaminar toughness in the shear direction is often higher than in the normal direction.



(a) MMB 25% **(b)** MMB 50%

Figure 6.19: Side-view of the GF/PP specimens displaying fiber bridging during MMB experiments.

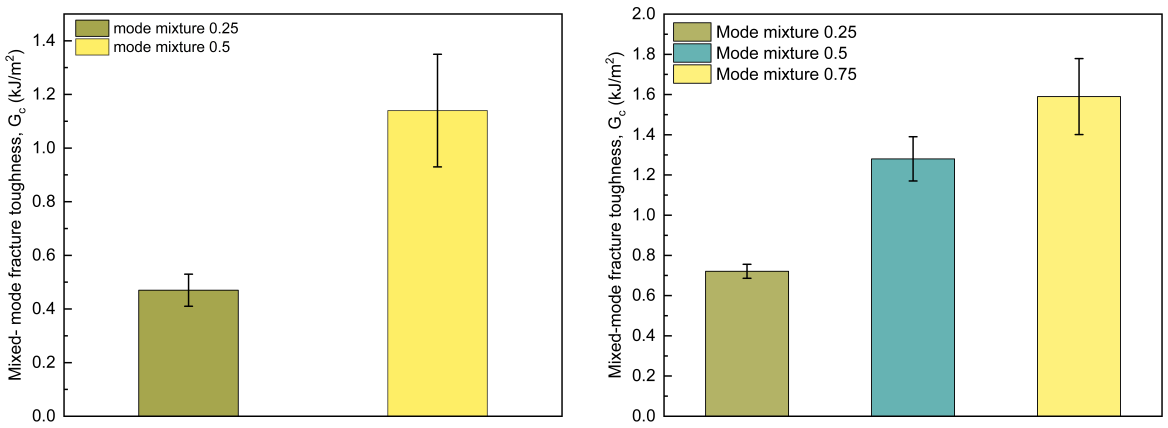
The delamination propagation may exhibit either stable or unstable behavior, primarily con-

trolled by the mode-mixture in the MMB tests, as was the case with the GF/PP specimens. Secondly, the initial crack length was long in CF/PPS specimens, which allowed for a short crack extension. However, the tests were stopped when the extended crack reached underneath the central roller. Due to all these reasons, the propagation option was not considered, as it was difficult to monitor the crack length. Therefore, the testing and the evaluation of mixed-mode fracture energy were limited to the crack initiation values.

Similar to the determination of pure mode I initiation (DCB), the ASTM standard [53] proposes the same three values (NL, 5%/max) for the MMB testing to calculate the mixed mode initiation toughness. In this study, the max load point in the force-displacement plot is considered for determining the total SERR. Table 6.3 provides the summary of the fracture energies at various mode mixtures for the two material systems and Figure 6.20 shows the mean fracture toughness with standard deviation.

Mode mixture (G_{II}/G_T)	$G_T(G_I + G_{II})$ **(kJ/m^2)**	
	GF/PP	**CF/PPS**
0.25	0.47 ± 0.07	0.71 ± 0.03
0.5	1.14 ± 0.21	1.27 ± 0.11
0.75	-	1.57 ± 0.19

Table 6.3: Summary of the experimental values of the mixed mode fracture energies from MMB tests.



(a) UD GF/PP **(b)** UD CF/PPS

Figure 6.20: Mixed-mode interlaminar fracture toughness of the UD GF/PP and UD CF/PPS composites.

The fracture toughness calculations presume a linear elastic behavior of the specimen being tested. However, if the displacement applied exceeds a certain level (δ_{max}), this assumption will no longer hold true, leading to inaccuracies due to geometric nonlinearity. The applied displacement recorded during the tests at different mode mixtures was below the δ_{max}.

The results demonstrate a correlation between the mode mixture and the fracture toughness for both materials examined. The observed increase in fracture toughness suggests that

an increase in mode mixture leads to improved resistance to crack propagation. The precise mechanisms underlying this phenomenon will be thoroughly investigated and elucidated through fractography studies.

6.4 Fractography Studies

Fractography studies of the fractured surfaces offer critical insights into the associated damage and failure mechanisms, principally the criteria for delamination failure. Further, understanding intricate damage mechanisms during the delamination growth for the known loading mode mixtures forms the basis for qualitative comparison with the morphology of the fracture surface generated during the Mandrel Peel testing (discussed in Chapter 7) and, eventually, the mode of failure and the corresponding loading conditions could be well ascertained.

Mode I Fracture Analysis

The macroscopic mode I fracture surface (Figure 6.21) of the GF/PP appears to be undulated rough texture with the presence of broken fibers and fiber bundles, whereas the CF/PPS exposes a relatively similar fracture surface with less fraction of broken fibers and limited/no traces of bundled fibers. Amongst other features of mode I, the bridging of fibers is the most inherent, and the scale depends on multiple factors. It is worth mentioning that the fiber bridging mechanism could ensue in fracture surfaces (upper and lower) featuring contrasting delamination propagation directions.

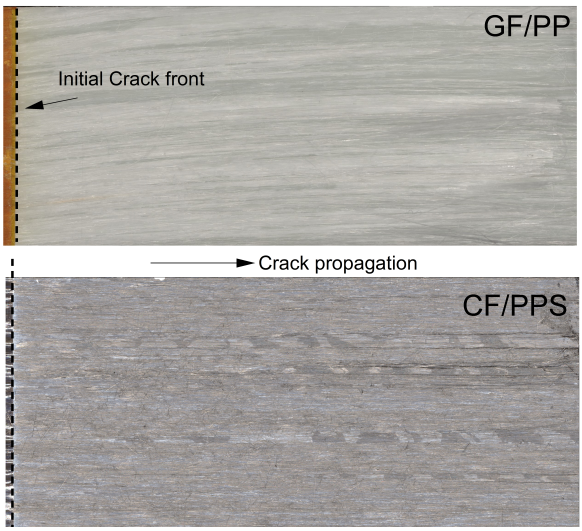
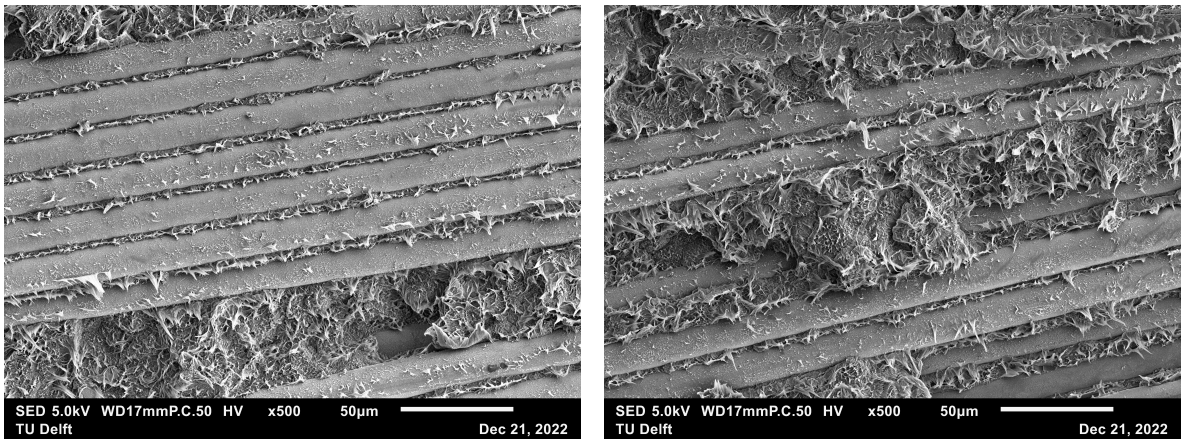


Figure 6.21: Fracture surface of mode I UD GF/PP and UD CF/PPS specimens indicating the tortuous path with fiber bundles and broken fibers.

Figure 6.22 reveals the mode I fracture features for the present GF/PP, where the polypropylene matrix over the fibers is peeled/pulled away, separating from the interfacial region. The degree of pulling differs relative to the position of the fibers and is highest at the central plane between the fiber spacings highly concentrated with the matrix volume fraction. Referring to Figure 6.22a, another interesting aspect that could also be evidenced is the tiny nodules of polypropylene resin on the surface of the glass fibers. This feature is classically representative of a fast fracture, and this occurrence, particularly in a fracture mode often considered

slow (0.5 mm/s in this case), is commonly associated with the phenomenological term "strain magnification. " Further, this is mostly observed at regions lacking matrix at the interface of the two adjacent plies [178].



(a) Resin nodules on the fiber surface and matrix stretching, x500

(b) Transpherulitic deformation in the matrix, x500

Figure 6.22: SEM micrographs of Mode I delaminated fracture surfaces of GF/PP.

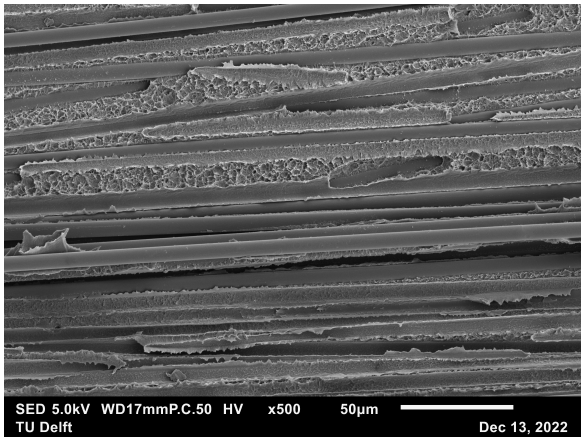
As can be seen (Figure 6.22b), the transpherulitic propagation with dimples exhibiting well-connected characteristic spherulitic matrix microstructure (between the fibers) was noticed and is more identical to the matrix structure (mode I fracture) reported by F. Perrin et al.[39] for GF/PP composites.

Similarly, denuded fibers with the matrix peeled completely were observed on the fracture surfaces of CF/PPS, as shown in Figure 6.23a. This suggests that the failure developed partially at the interface of the fiber and PPS matrix further implying adhesive type of fracture behavior which is more common for tough matrix materials. As expected this observation is more related to the relatively weak interfacial adhesion properties of CF/PPS which is consistent with the earlier studies reported in the literature [36][46]. While the ductile matrix drawing appears to be less, the morphology of the PPS matrix between the fiber spacings also shows the transpherulitic deformation failure with dimple features (Figure 6.23b).

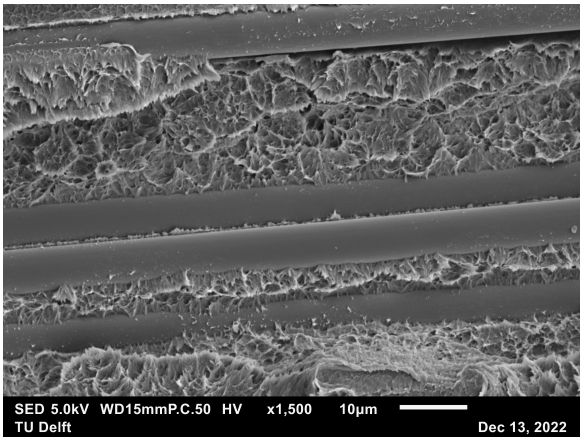
Mode II Fracture Analysis

It is plausible to note that the fracture surfaces generated under the mode II loading are abundant in features typically representing the characteristic shear damage mechanisms primarily at the regions rich with polymer matrix along with the occurrence of interfacial damage behavior.

The typical feature characteristic to the mode II loading was discerned to be the shear drag in both the materials. The occurrence of this feature during mode II loading is primarily due to the loading condition, which leads to the interlaminar shear effects at the interface of the matrix and fiber, associating with the movement of the two contacting crack surfaces. As can be seen in Figure ?? and 6.24b, denuded bare fibers were observed in both GF/PP and CF/PPS fractured surfaces. Thereby, the interfacial behavior appears to have been dependent on the mode of loading. In contrast to the mode I fracture surfaces, more inclined



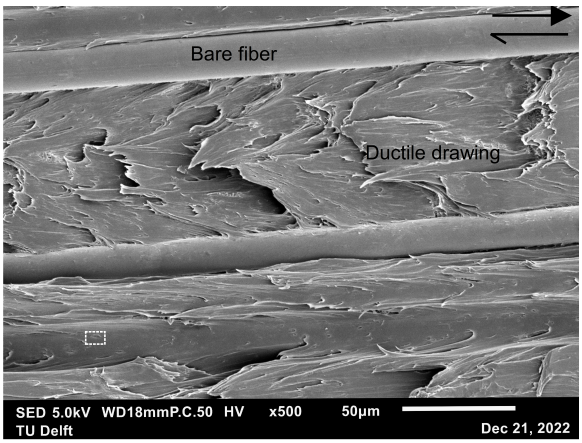
(a) Bare, denuded fibers indicating weak interface and matrix drawing, x500



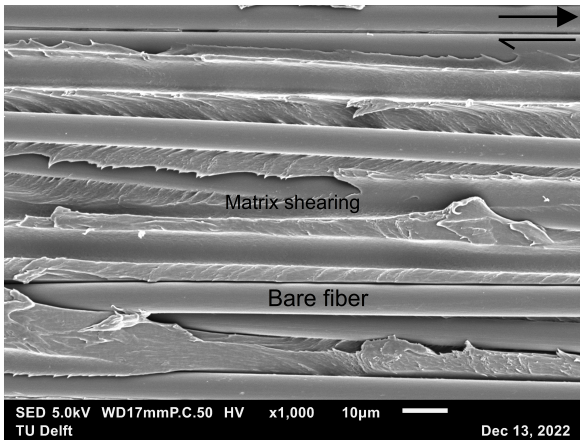
(b) Transpherulitic deformation with dimple features in the matrix, x1500

Figure 6.23: SEM micrographs of Mode I delaminated fracture surfaces of CF/PPS.

and flattened surfaces were found as the ductile drag or tearing emerges as the predominant mode of failure with increasing polymer matrix deformation.



(a) GF/PP



(b) CF/PPS

Figure 6.24: SEM micrographs of Mode II delaminated fracture surfaces.

Further, the direction of the ductile flattened surface reveals the shearing direction of the two crack surface such that as the ductile drag mark is oriented towards the left, the surface movement is from the left toward the right, +ve shear. Likewise, the right orientation of the ductile drag asserts the negative shearing movement at the opposite surface.

The fracture surface of the upper and lower sliding arm of the ENF specimen are shown in Figure **6.25**, respectively. While the lower fracture surface consists of fiber imprints and few fibers, the matching upper fracture surface shows more fibers, generally mentioned as the matrix and fiber-dominated fracture surfaces. The observation of this exhibited distinctive aspect and co-relating to the ductile drag orientation further allows postulating the crack growth direction from the morphology. The direction of the full arrow indicates the crack propagation direction, whereas the half arrow shows the shearing direction.

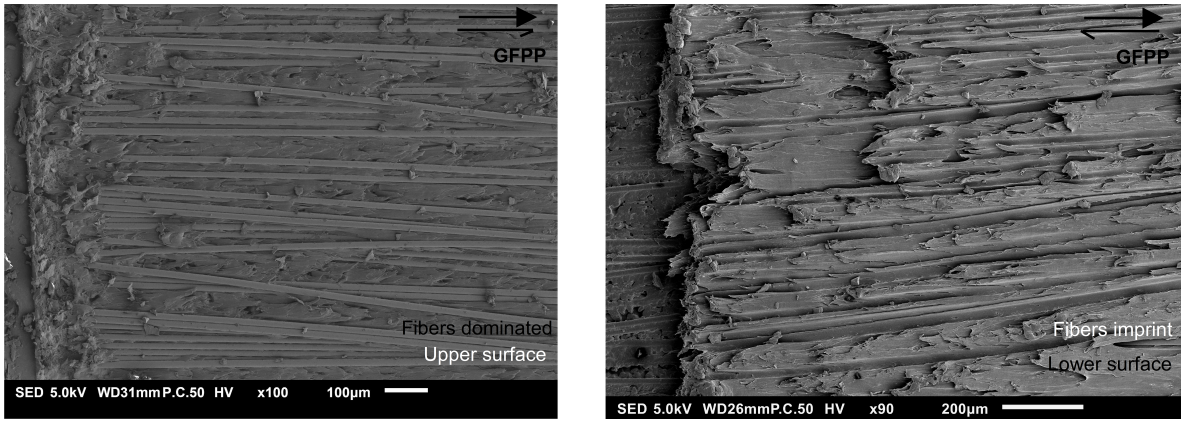


Figure 6.25: Fracture surface of the UD GF/PP ENF specimen indicating the fiber domination in the upper and fiber imprints in the lower arm, respectively.

Other features that could be well distinguished are the U-shaped dimples in the fiber imprints of GF/PP and the plastic shearing of the polypropylene matrix still adhering to the few glass fibers.

Mixed Mode Fracture Analysis

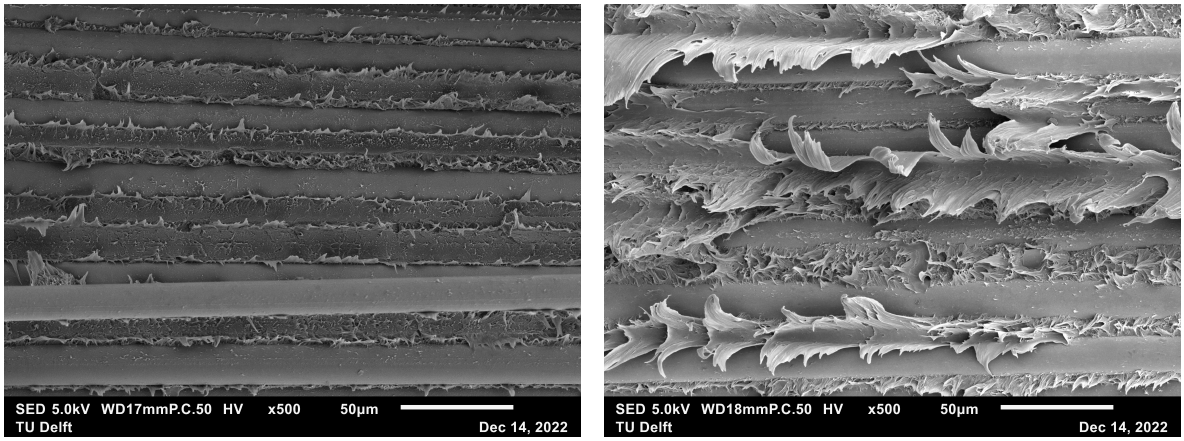
In general, from the viewpoint of fractography, the fracture surfaces under mixed (mode I and mode II) loading conditions are expected to exhibit a mixture of morphological features visualized for pure mode delamination surface. The mode mixture is the decisive factor influencing the semblance of the fracture surface features.

One of the distinctive aspect that emerges distinguishable from the mixed mode fracture surfaces is the inclination (tilt angle) of the matrix stretched/drawn. As discussed above, the mode I fracture surface illustrated fiber-peel, breakage, and failure at the interface. Under a mode mixture of 0.25 (G_{II}/G_T), fiber bridging was visible, and the fracture surface of the GF/PP specimen showed a ductile drawing of the PP matrix with the tip of the stretched fibril oriented in the direction normal to the surface. Also, matrix imprints on the fiber surface were seen, which indicates the dominance of the mode I energy component (Figure **6.26a**).

As the component of mode II loading increased, for a mode mixture of 0.5 (G_{II}/G_T), from the Figure **6.26b**, extensive ductile drawing of the matrix with fibrils tilted along the fiber surface and the fracture developed near the interface can be witnessed. Moreover, clearly defined U-shaped semi-circular dimples on the fiber track regions and comparatively clean fiber surfaces with fewer traces of PP matrix were noticed, exhibiting the shear component of loading.

The examined fracture features at varying mixed-mode conditions agree well with the fractographic observation reported for GF/PP by Ku- Hyun Jung et al.[**43**]. Based on this tendency, it could be speculated that for mode mixtures above 0.5, the degree of matrix deformation and the fibril alignment might vary and display higher inclination along the fiber axis, considering the domination of the mode II loading.

Figure **6.27** vividly imparts the delamination behavior of CF/PPS for varying mode mixtures revealing two distinctive differentiating aspects. With the increasing component of mode II



(a) Mode mixture 0.25 **(b)** Mode mixture 0.5

Figure 6.26: SEM micrographs of delaminated fracture surface of GF/PP in various mode mixtures.

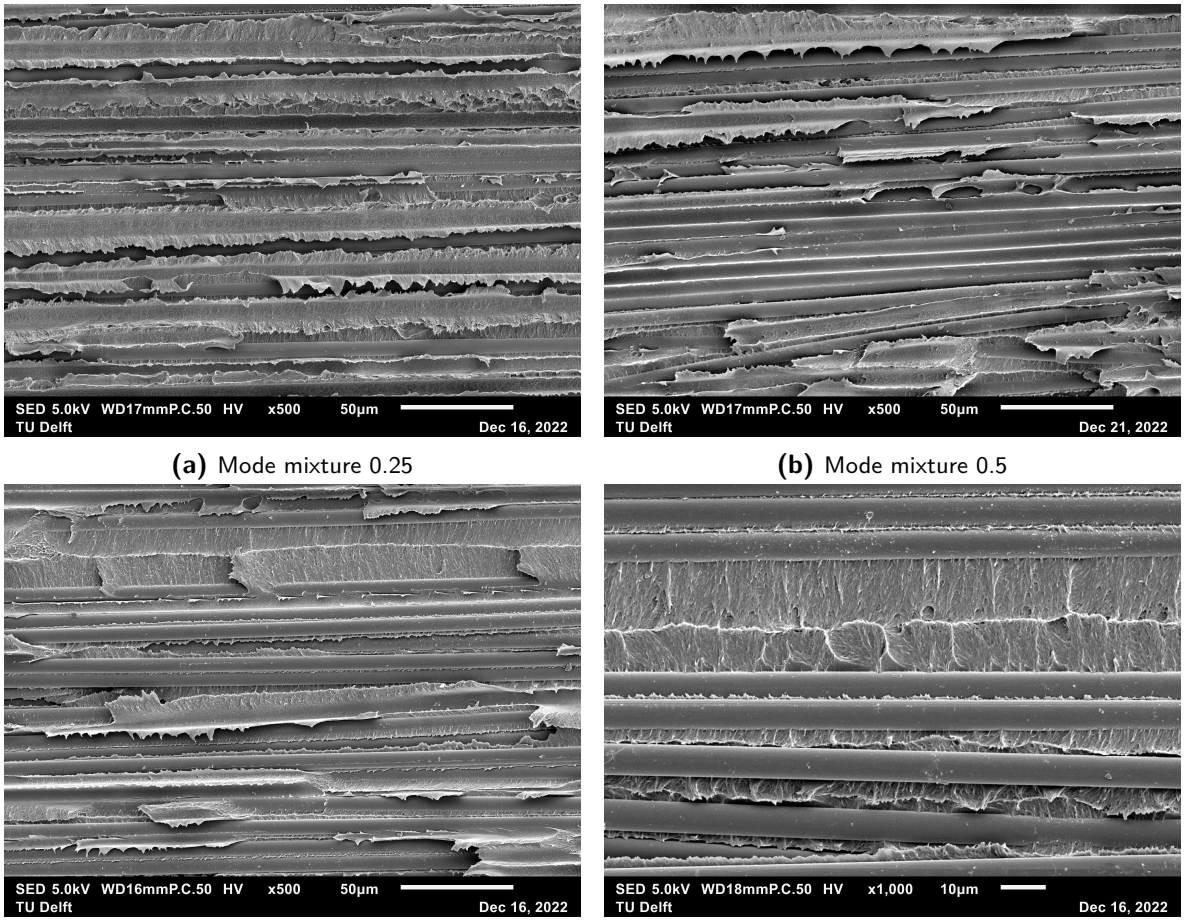
loading, trends of highly plastically deformed PPS matrix in the form of an extended lips-like feature referred to as "shear lips" along the periphery of fibers due to the ductile drawing were observed.

While the orientation of this extended PPS matrix looks thin and more upright for 0.25 mode mixture (Figure **6.27a**), as with decreasing mode I ratio, it tends to develop thick and align at an angle gradually depending on the mode-mixture, and the evolution can be interpreted from Figure **6.27b** and **6.27d**. In addition, smooth-denuded fibers were seen irrespective of the loading mode.

6.5 Effects of Processing Conditions

Even though the influence of processing conditions was not a part of this research campaign, as it was deemed imperative, a more comprehensive qualitative and quantitative reasoning has been discussed, exclusively on the basis of the limited literature of past studies for the GF/PP and the CF/PPS material systems arguing the critical effect of processing conditions, chiefly emphasizing the cooling rate on the mechanical performance explicitly focusing on the interfacial fracture properties.

It is significant to note that the fiber/matrix interface behavior depends on several factors. The processing conditions usually affect the properties of the polymer matrix, especially the crystallinity in the case of semicrystalline polymers (crystal size/distribution), and the glass transition temperature plays a vital role in the interfacial behavior of composites. The temperature plays a significant role in the growth of the crystals (spheroidal form known as **spherulites**) according to the crystallization kinetics. As a result, prior research has shown that it is the cooling rate that is observed to be the parameter that essentially governs the crystallinity, size, and morphology of the crystals, further reporting that an increase in cooling rate leads to a reduction in the degree of crystallinity and the spherulite size. Several researchers investigated the cooling rate's influence on the crystallinity level and the subsequent effect on fracture toughness.



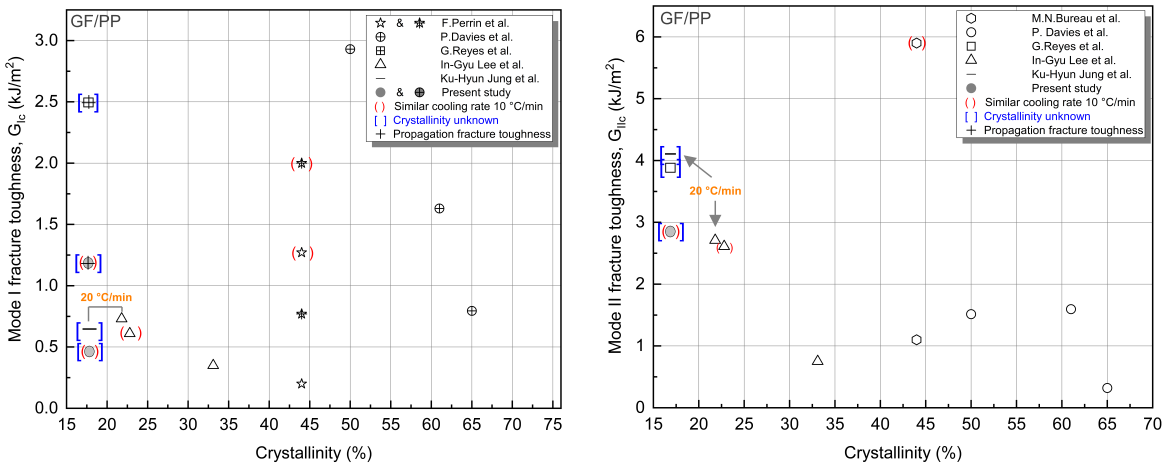
(a) Mode mixture 0.25 **(b)** Mode mixture 0.5

(c) Mode mixture 0.75 **(d)** Mode mixture 0.75

Figure 6.27: SEM micrographs of delaminated fracture surface of CF/PPS in various mode mixtures.

To this end, a comparative assessment of the correlation of the degree of crystallinity of the GF/PP and CF/PPS with the fracture toughness generated based on the literature findings is detailed in Figure **6.28 and 6.29**, respectively. Considering that the fracture toughness data correspond to different manufacturing methods and conditions, only the average fracture toughness values are shown and discussed. Also, in cases where the degree of crystallinity is unknown, especially in the present study, the "unknown crystallinity" is indicated by [ ] and by ( ) for toughness with the similar/same rate of cooling (compared with the present study), while "+" within the interior of the symbols denotes the propagation fraction toughness. The comparative evaluation represents only the interlaminar fracture toughness of continuous unidirectional (UD) fiber-reinforced composites. It is essential to acknowledge that the fiber volume fraction (of the prepreg and the laminate) differs, which might make the effective comparison of findings across studies challenging.

Recently, In-Gyu Lee et al.[42] reported for the GF/PP composites that the degree of crystallinity and the size of spherulites decreased with increasing cooling rate post-consolidation cycle. The mode I and mode II fracture toughness was found to be notably improved with the higher cooling rate, mainly attributing it to the enhanced adhesion strength between the



(a) Mode I **(b)** Mode II

Figure 6.28: Correlation of Interlaminar fracture toughness of GF/PP and the degree of crystallinity **[39][40][41][42][43][44, 45]**.

formed polypropylene spherulites. In the same way, P. Davies et al.[40] observed the fracture toughness increase in correlation with the cooling rate and formation of fine spherulites at higher cooling temperatures. This interlaminar fracture properties dependence on the cooling rate/molding temperature was also validated by the extensive works of M. N. Bureau et al.[44, 45], F. Perrin et al.[39], and G. Reyes et al.[41] on the GF/PP composites. Furthermore, it has been shown that the consolidation temperature also affects the properties (matrix microstructure and fracture toughness).

It could be stated that both the mode I and mode II initiation fraction toughness of UD GF/PP obtained in the present study is reasonably comparable to the reported values by In-Gyu Lee et al.[42]. In both the studies, the hot-pressed composites were cooled at a rate of 10°C/min; however, the consolidation temperature, pressure, and dwell time differ, and the GF/PP prepreg utilized had a fiber-volume fraction of approximately 45% and 34.5%, respectively.

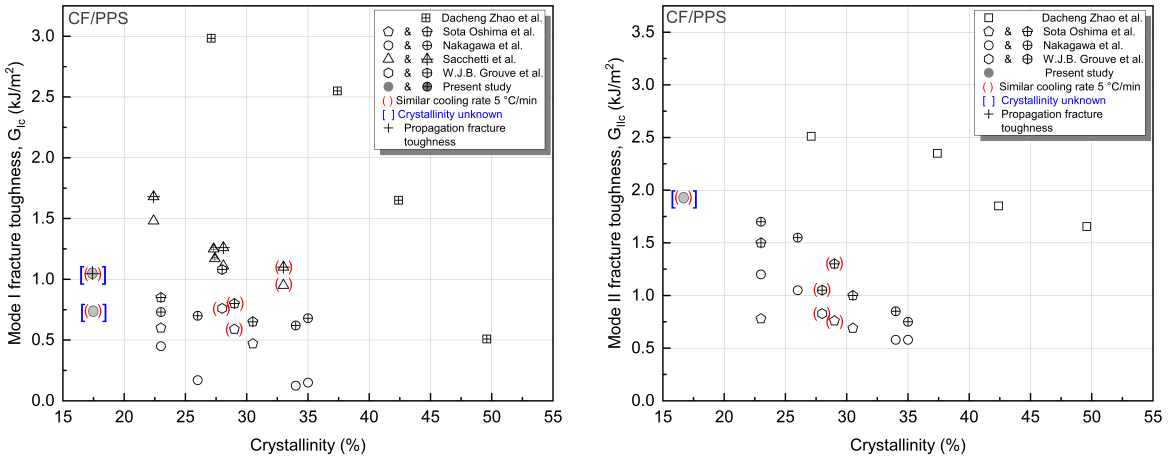
Interestingly, on the other hand, the investigations of In-Gyu Lee et al.[42] and Ku-Hyun Jung et al.[43] report different mode II fracture toughness values (initiation) for the same GF/PP with the same fiber volume fraction and same manufacturing conditions for a cooling rate of 20°C/min, whereas the mode I fracture toughness values is comparable, as can be seen from the figure.

A noteworthy aspect that merits attention is the interfacial adhesion between the matrix and fiber, which has been observed to decrease with an increase in cooling rate. Conversely, the adhesion strength within the matrix is enhanced owing to the formation of finer spherulite sizes, resulting in a higher strain energy release rate [179]. Furthermore, an increase in cooling rate (rapid cooling) is also found to improve the PP matrix's shear strength with increased ductile extension[180][42]. It is demonstrated that the morphology highly influences the crack growth path and fracture resistance within the polypropylene matrix (and semi-crystalline polymers in general) [181].

Although the crystallinity is not measured and the spherulite size is not quantified in this

study, from the fractographic analysis of GF/PP specimens, correlating the morphological aspects (spherulites, dimples, bare fibers indicating the weak glass fiber and polypropylene interfacial adhesion, ductile drag of the matrix) with the observations from the earlier investigations, the processing conditions effects on the matrix and in turn on the fracture toughness could be relatively understood. A reasonable argument is that the matrix dominated the contribution to the fracture energy in mode II determined in this study.

Proceeding with the discussion on CF/PPS, a recent study by Sota Oshima et al.[46] demonstrated that mode I initiation and propagation fracture toughness increased with the cooling rate. The study also revealed a similar trend for mode II fracture data, with higher propagation toughness observed in both mode cases for CF/PPS. This trend was consistent with the findings of Nakagawa et al.[47], where increased fracture toughness for modes I and II (initiation and propagation) fracture toughness was reported. Furthermore, increasing cooling rates (resulting in decreasing crystallinity) were noted to lead to higher mode I (propagation) and mode II (initiation) fracture properties (attributing to the improvement in the PPS matrix ductility resulting in higher energy absorption during deformation) by Dacheng et al.[48] during their investigation of the cooling rate effects.



(a) Mode I **(b)** Mode II

Figure 6.29: Correlation of Interlaminar fracture toughness of CF/PPS and the degree of crystallinity **[46][47][48][10][36]**.

According to the findings of the current study, from Figure **6.29a**, it can be inferred that the fracture toughness of CF/PPS in mode I exhibit consistency with the fracture toughness data reported in the previous studies on the same material (with a prepreg fiber volume fraction of around 59%) fabricated at a similar cooling rate of 5°C/min. Meanwhile, mode II initiation fracture toughness (Figure **6.29b**) has been observed to be relatively higher in comparison to the values recorded in the investigations mentioned above. It is comparable to the values documented by Dancheng et al. at the cooling rates of 2°C/min (49.6%) and 30°C/min (42.4%), where the difference in the resulting spherulite size was negligible.

Sota Oshima et al. also showed that the mode I toughness of the neat PPS resin increased with the decrease in the degree of crystallinity (decrease in spherulite size as well) and also argued that the rise in propagation fracture toughness of the CF/PPS in mode II could be related to the matrix deformation behavior. Since the cooling rate was not effectively

controllable during the manufacturing of the laminates in the current study, and also the degree of crystallinity is not known in this case, a speculative explanation is that, although the presence of the denuded bare fibers infers weak interface properties, (which often results in lower interlaminar fracture toughness); it is the high matrix toughness intrinsically that is likely to be reasoned for the higher mode II interlaminar fracture properties of the CF/PPS obtained in the current work. Moreover, the fractographic analysis also confirmed that mode II toughness is matrix-dominated, exhibiting extensive plastic deformation of the PPS matrix.

This assessment suggests that these fracture toughness outcomes are affected by morphological changes. Additionally, it is also clear that even similar materials (or, in some cases, material from the same manufacturer) have resulted in variability in the fracture toughness properties reported due to the sensitivity of the processing conditions that affect the mechanical performance of the composites produced, and this is well documented in the literature.

Further, the evaluation also indicates that the interfacial fracture properties are not only a function of the degree of crystallinity but also that the morphological characteristics of the crystalline phase play a significant role in making it a more complex relation as the crystallization is more heterogeneous. Most importantly, the resulting interlaminar fracture toughness of the fiber-reinforced thermoplastics is a balanced combination of several factors, such as the interfacial bonding strength of the fiber/matrix, the toughness of the matrix, the damage process zone formation, and finally, the loading mode.

6.6 Failure Criteria

Section **2.9** discussed the importance of the failure criterion that accounts for the synergetic effects of different modes for predicting delamination behavior under mixed mode conditions. In this work, Benzeggagh-Kenane (B-K) and Power Law criteria were employed amongst the various criteria reported in the literature to predict the mixed mode delamination behavior and establish the criteria which model the experimental fracture toughness data providing the best representation. The outcome of this assessment was utilized in the numerical models to validate the numerical simulation-based approach for predicting the mixed-mode delamination behavior and mode-partitioning. The collective data of the total critical SERR generated experimentally from the DCB, ENF, and MMB tests are shown in Table **6.4**. Different approaches were followed while fitting the Power Law and the B-K criterion. First, different limits of mode I and mode II fracture toughness are considered: minimum, average, and maximum values. Finally, the non-linear least squares curve fitting technique is implemented to obtain the best fit based on the average values of mode I and mode II fracture toughness. The curve fits established with different fracture toughness limits for different values of coefficients (β and η) were implemented, while only the best fit that represents the delamination behavior is presented and discussed.

Figure **6.30** shows the experimentally obtained fracture toughness as a function of different mode-mixtures of UD GF/PP and UD CF/PPS composite laminates. In this study, varying the B-K fitting parameter for the GF/PP composites between 1.5 -2.5 was a good range, with $\eta = 2$ resulting in a better fit, predicting the material behavior with reasonable accuracy. In this case, as it can be seen, the GF/PP exhibits a non-linear failure locus, with total fracture energy increasing with increasing mode mixture. The observed range of mixed-mode test results and the trend is in good agreement with the works of In-Gyu Lee et al.[**42**] and

Fracture Test	Mode ratio (G_{II}/G_T)	G_T ($G_I + G_{II}$) (kJ/m^2)	
		GF/PP	**CF/PPS**
DCB	0	0.436 ± 0.08	0.636 ± 0.04
MMB	0.25	0.469 ± 0.07	0.715 ± 0.03
MMB	0.5	1.143 ± 0.21	1.274 ± 0.11
MMB	0.75	-	1.578 ± 0.19
ENF	1	2.850 ± 0.29	1.882 ± 0.22

Table 6.4: Experimentally determined Interlaminar fracture toughness of UD GF/PP and UD CF/PPS composite laminates. The average initiation fracture toughness values are presented.

Ku-Hyun Jung et al.[43] (see [sub] Figure 6.30 - left). Furthermore, when considering the mode mixture of 0.25, minor disparities between the experimental findings and the fitted curve emerged, as the fracture toughness data is slightly outside the trend, such that the fit yields a higher value than obtained through the tests.

In the CF/PPS material system, the total energy shows, to some degree, an increasing linear trend in relation to the mode mixture. When implementing the B-K criteria, it was determined that an acceptable level of curve fits could be achieved within η in the range of 1-1.5 (Figure 6.30 - right). Nevertheless, when the criterion value is set to 1.5, there is a slight tendency to overpredict the fracture toughness in the lower mode II region. Conversely, employing η = 1 yields significantly unconservative estimations in fracture behavior characterized by low mixed mode ratios.

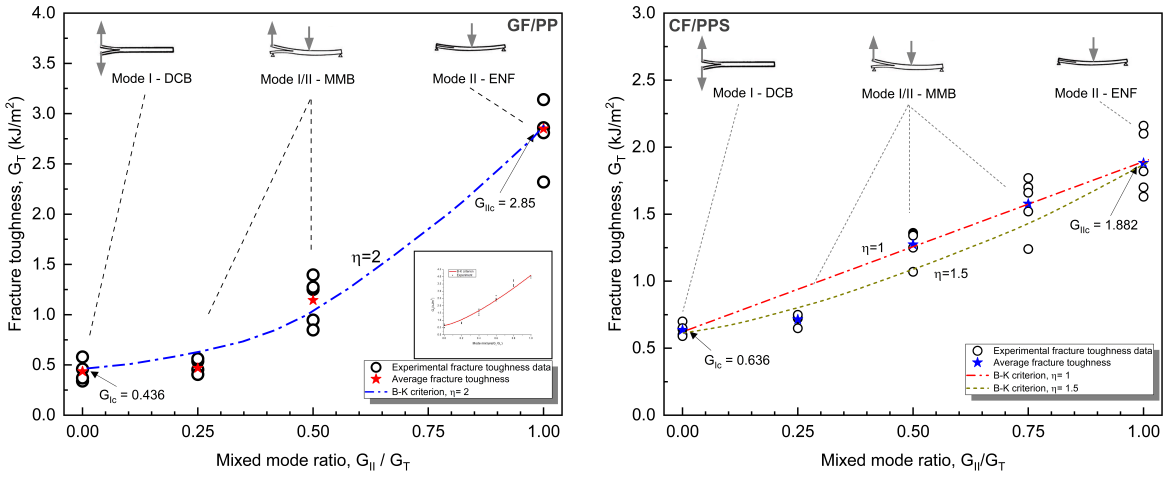


Figure 6.30: Fracture toughness as a function of different mixed mode ratios establishing the B-K delamination failure criterion for GF/PP and CF/PPS.

The power law criterion can more conveniently be represented based on the individual mode components G_I and G_{II}. Thus, the contributions of the mode I and mode II components of the various mixed mode ratios are depicted in Figure 6.31 in the form of mode II vs. mode I. In this study, the power law criterion employs a single fitting parameter with an assumption of $\alpha = \beta$ instead of utilizing two distinct fitting parameters, as described in the formulation.

It is noticeable from Figure 6.31 (right) that the power law criterion ($\beta = 1.5 - 2$) generates

agreeably adequate results for the estimation of the mixed mode fracture toughness of the CF/PPS composite. On the contrary, the effectiveness of power law criteria in accurately predicting delamination behavior for the GF/PP composites appears inferior compared to the B-K criterion (Figure **6.31** - left). This could also be due to insufficient fracture toughness data in the 0.5 to 1 mode mixture range. Additionally, it is worth noting that the power law criterion results in an overestimation of the mixed mode fracture toughness at a mode mixture of 0.25 for both material systems. The inefficiency of the power law criterion in predicting the mixed-mode fracture toughness, particularly in the mode I dominant mixed-mode regions, has also been reported in past works [182][183][184].

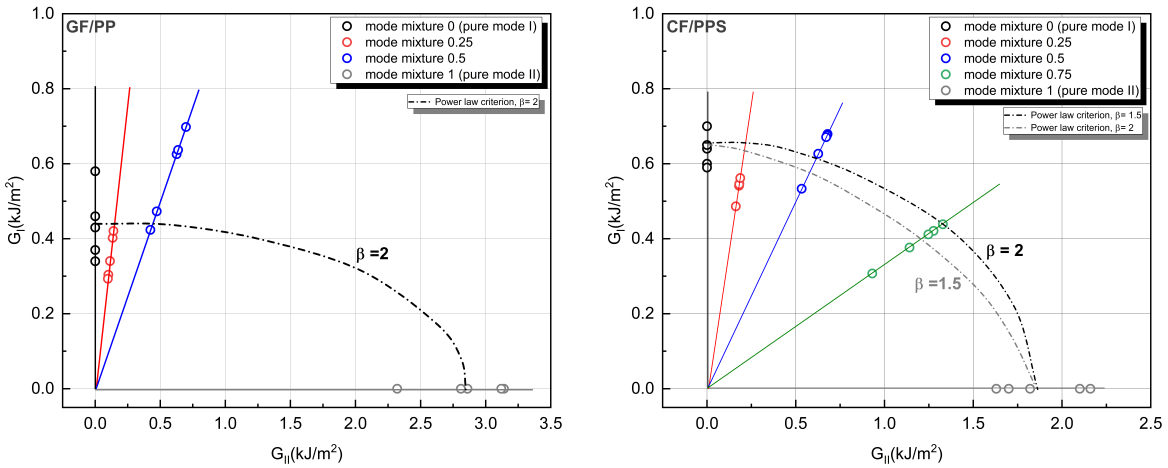


Figure 6.31: Mode II vs. Mode I (components of the various mixed mode ratios) and the Power Law curve fit for delamination behavior prediction.

In general, upon incorporating failure criteria into experimental data and evaluating their "Goodness of Fits," it is evident that the B-K criterion offers superior predictions for the material response in both investigated materials. Although the Power Law criterion successfully predicts the fracture behavior of CF/PPS (except low mode II regions), it exhibits ineffectiveness in accurately describing the material behavior of GF/PP, indicating that the Power Law criteria might not be appropriate for the GF/PP material modeling. Further, this demonstrates the significance of selecting appropriate failure criteria, as they can substantially influence delamination initiation and propagation behavior prediction.

To conclude, the significance lies in highlighting the importance of delineating the boundaries within which mode I and mode II fracture toughness data are taken into account during the curve fitting process for a specific delamination failure criterion. These limits serve to govern the fitting procedure and determine the optimal parameter that accurately characterizes the delamination behavior of the material.

Chapter 7

Mandrel Peel Tests

7.1 Experimental Results

This section presents a comprehensive analysis of the experimental findings obtained from the mandrel peel tests conducted. The primary objective of these tests was to investigate the influence of mandrel roller size and peel arm thickness on the peeling behavior and, in turn, on the interlaminar fracture toughness. A series of mandrel peel tests were performed using five different mandrel rollers with radii of 10 mm, 25 mm, 50 mm, 75 mm, and 100 mm to achieve this objective. A constant peeling rate of 12.5 mm/min was maintained throughout the tests. Two types of specimens, namely the UD GF/PP and UD CF/PPS, were utilized in the experiments. These specimens had peel arm thicknesses of one ply and two plies. In order to provide a systematic analysis, the results are presented separately for the one-ply tests followed by the two-ply tests. The G_c outcomes have been derived using the data processing procedure outlined in Section 5.4.

The Force – displacement plots for the one-ply peel specimens with the mandrel radius of 10 mm and 25 mm are shown in Figure 7.1. From the curves, it can be clearly seen that the peel force steadily increases along the path of crack propagation for both the material system investigated. The UD GF/PP specimens exhibit a more or less stable growth until a peel distance of approximately 20 mm, after which the forces increase slowly. Next, the degree of increase in the magnitude of the force from the insert film till the end of the advanced crack is relatively high for the 10 mm compared to the 25 mm mandrel roller radius. Likewise, the correlation between the force magnitude and peel displacement exhibited a similar trend in the case of UD CF/PP specimens (Figure 7.2). Nonetheless, the intensity was less comparatively. Interestingly, it is noteworthy that a similar relation (rising force) has been noted in the case of UD CF/PAEK with 0|0 interface during the ESIS TC4 Round Robin 1 testing of laminates' fracture toughness by mandrel peel loading. The aforementioned testing procedures also involved peeling single ply from the laminate utilizing a mandrel radius of 10 mm [137].

In addition, it was noted that the behavior described above was not evident in the experiments conducted using mandrels of 50 mm and 75 mm radii. The corresponding force-displacement curves are depicted in Figure Figure 7.1 and Figure Figure 7.2, respectively. As evident from

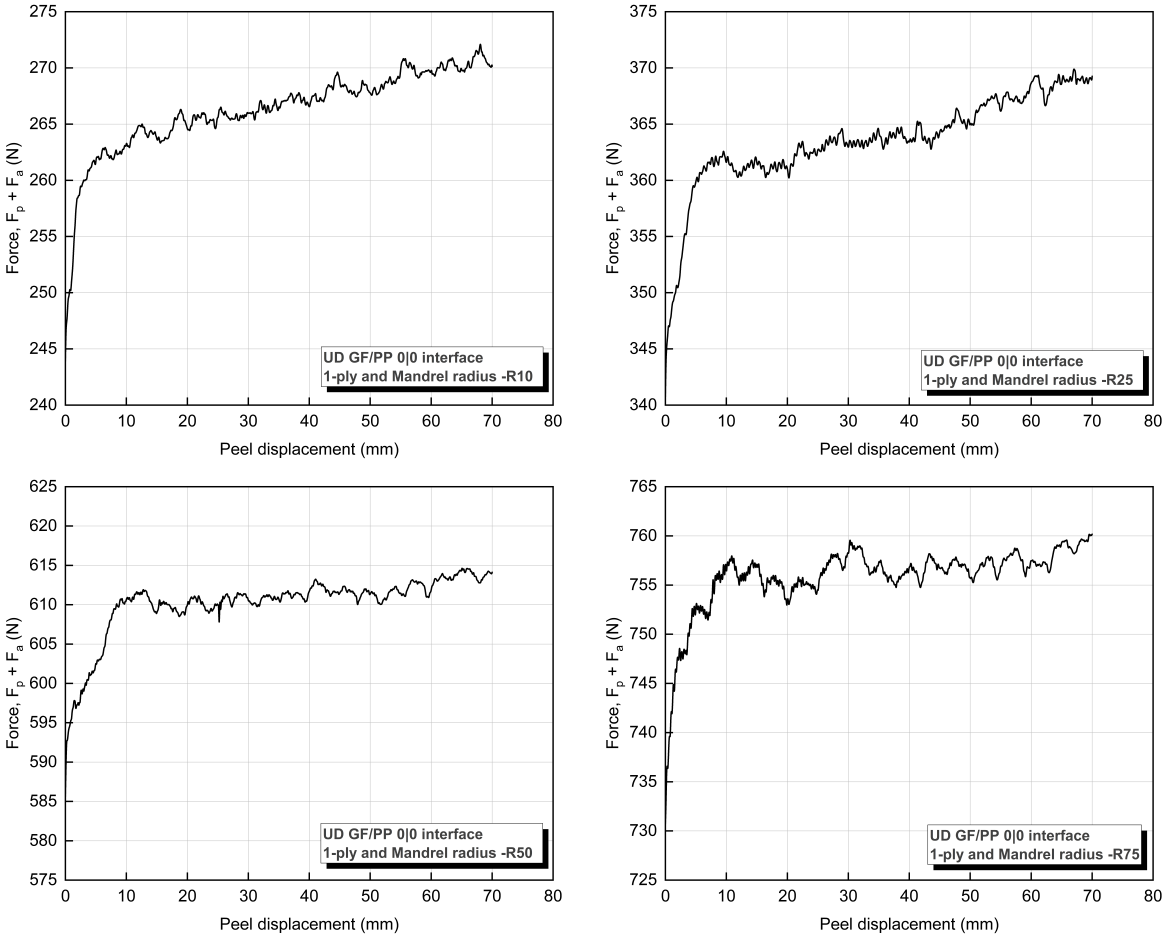


Figure 7.1: Peel force-displacement plots of 1-ply UD GF/PP peel specimens with 0|0 interface for various mandrel radii.

the plots, the peel force gradually approaches a stable plateau as the crack advances. It can be argued that with increasing mandrel size, the trend in the peel force response started to show a steady propagation.

In the study examining the effects of the peel arm thickness, the peeling results of the UD GF/PP and the UD CF/PPS specimens with a peel arm thickness of two plies follow. The presented Figure **7.3** illustrates the peel force vs. displacement curves for the UD GF/PP specimens. A representative curve for each mandrel size is shown. Notably, in all the cases, it can be observed that after the crack initiation, the force converges to a more steady state plateau along the crack growth. For a smaller mandrel radius (10mm and 25 mm), apparently, it could be said that the peel force behavior showed no drastic irregularities to a more considerable extent exhibiting a more stable delamination growth compared to what was realized during the peel test of the single ply with UD interface.

Further, as expected, the stick-slip behavior was not noticed primarily due to the establishment of proper mandrel-peel arm conformation. The occurrence of stick-slip is usually not confronted with the 0|0 interfaces, and the absence of this stick-slip behavior, particularly in the UD composites, could be attributed to the layup configuration.Moreover, it can be said

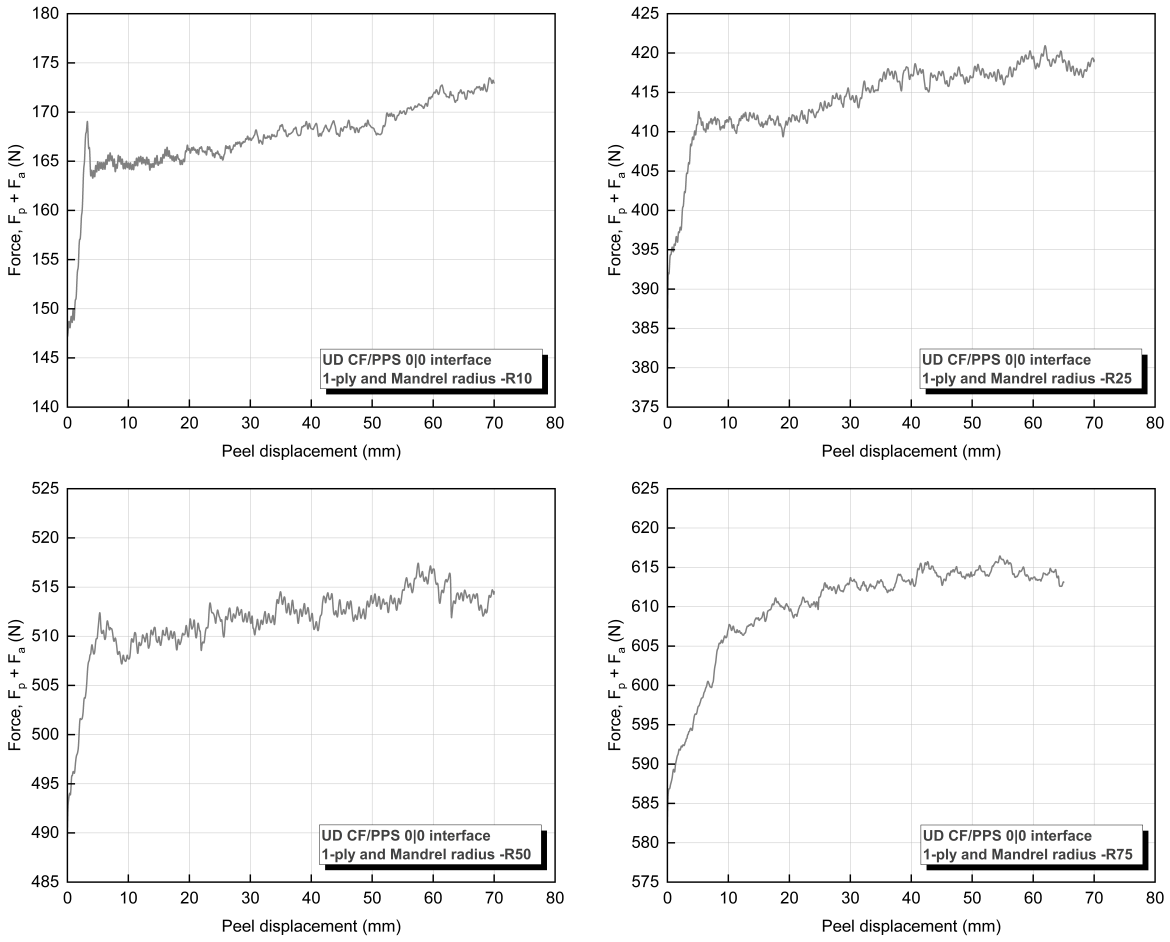


Figure 7.2: Peel force-displacement plots of 1-ply UD CF/PPS peel specimens with 0|0 interface for various mandrel radii.

that the peel arm had perfect conformation to the mandrel during the peeling test.

In the case of the CF/PPS (Figure 7.4), peel specimens tested with a 10 mm mandrel roller displayed a peel behavior slightly similar to the single-ply peel arm test. It is also important to mention that in a few experiments, tape fracture was noticed. The cause for this could be explained by referring to Figure 4.3, where it is possible to see that the bending strain of the peel arm (two plies thick) for a 10 mm radius is almost close to the failure strain of the carbon fibers. Also, the limiting critical radius to avoid the peel arm failure (for the thickness of 0.3 mm) is 9.375 mm.

The experiments with large mandrel radii (50 mm, 75 mm, and 100 mm) exhibited a stable delamination behavior. While the peel force–displacement curve for R = 50 mm illustrates a steady state, the peeling response for R = 100 mm features irregularities during crack growth for both the material systems. Furthermore, the effective peel force required for the crack to advance increased with the mandrel size.

Subsequently, the scope of this investigation was broadened to assess the suitability of the mandrel peel testing methodology and ultimately validate the hypothesis for the bi-material

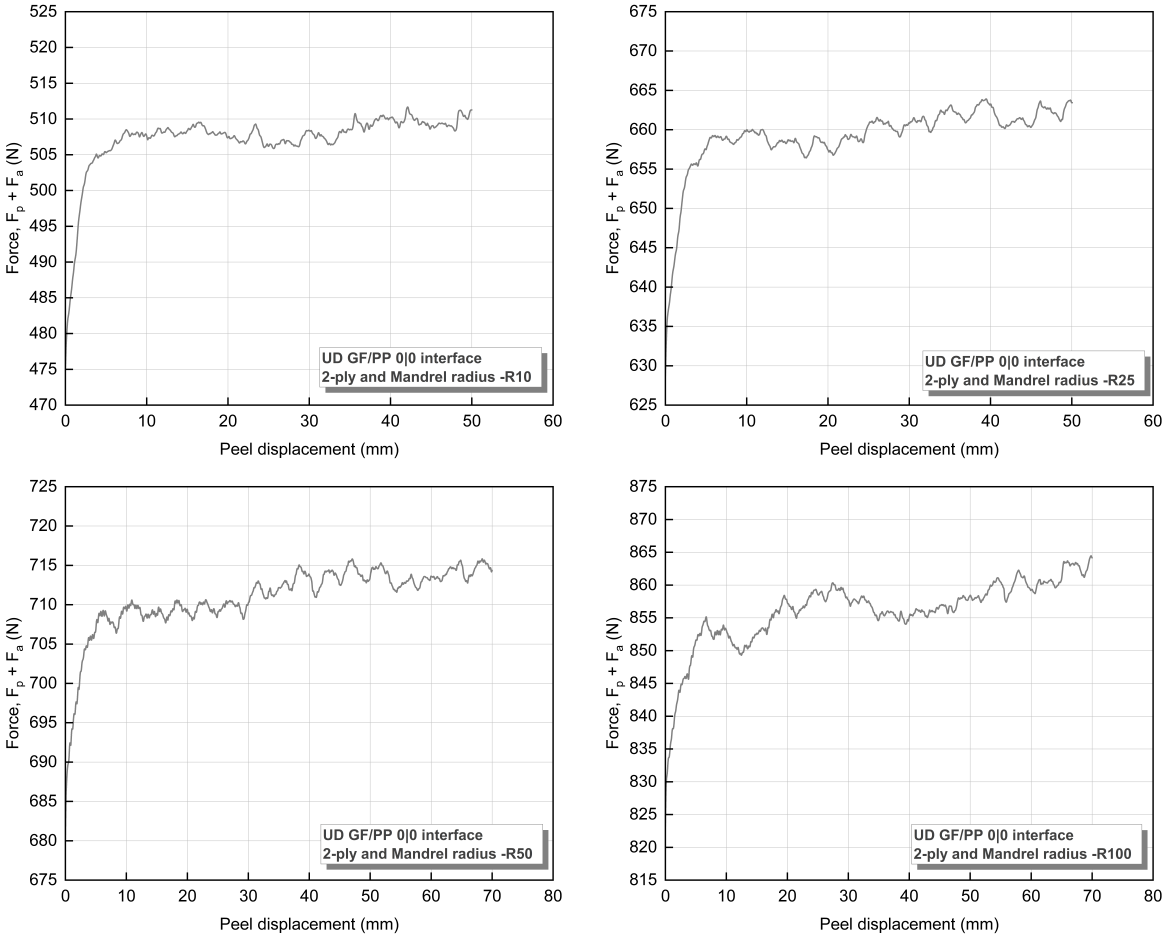


Figure 7.3: Peel force-displacement plots of 2-ply UD GF/PP peel specimens with 0|0 interface for various mandrel radii.

interface system, which constitutes a key aim of this research. To accomplish this objective, a composite laminate with a 0|90 interface was preferred since a delamination failure between the interface of two adjacent plies with fibers oriented at different directions $(0 - \theta^{o})$ within a composite is also deemed a bi-material interface failure.

Figure 7.5 shows the force vs. displacement curves for GF/PP 0|90 peel specimens for different mandrel radii. A slight irregular peel force response is recorded as the crack progresses and is relatively consistent along the peeling distance. This fracture propagation behavior is observed in all the tests irrespective of the mandrel roller size.

The peel specimens of CF/PPS with an interface orientation of 0|90 also display a low degree of irregularities in the peel force curve (Figure), similar to the GF/PP specimens. Additionally, a stick-slip phenomenon characterized by sudden drops and rises in the peel force was noticed in some of the specimens during the experiments Figure 7.6. The rationale behind such delamination behavior in both the material system is explored and articulated in Section 7.2.2.

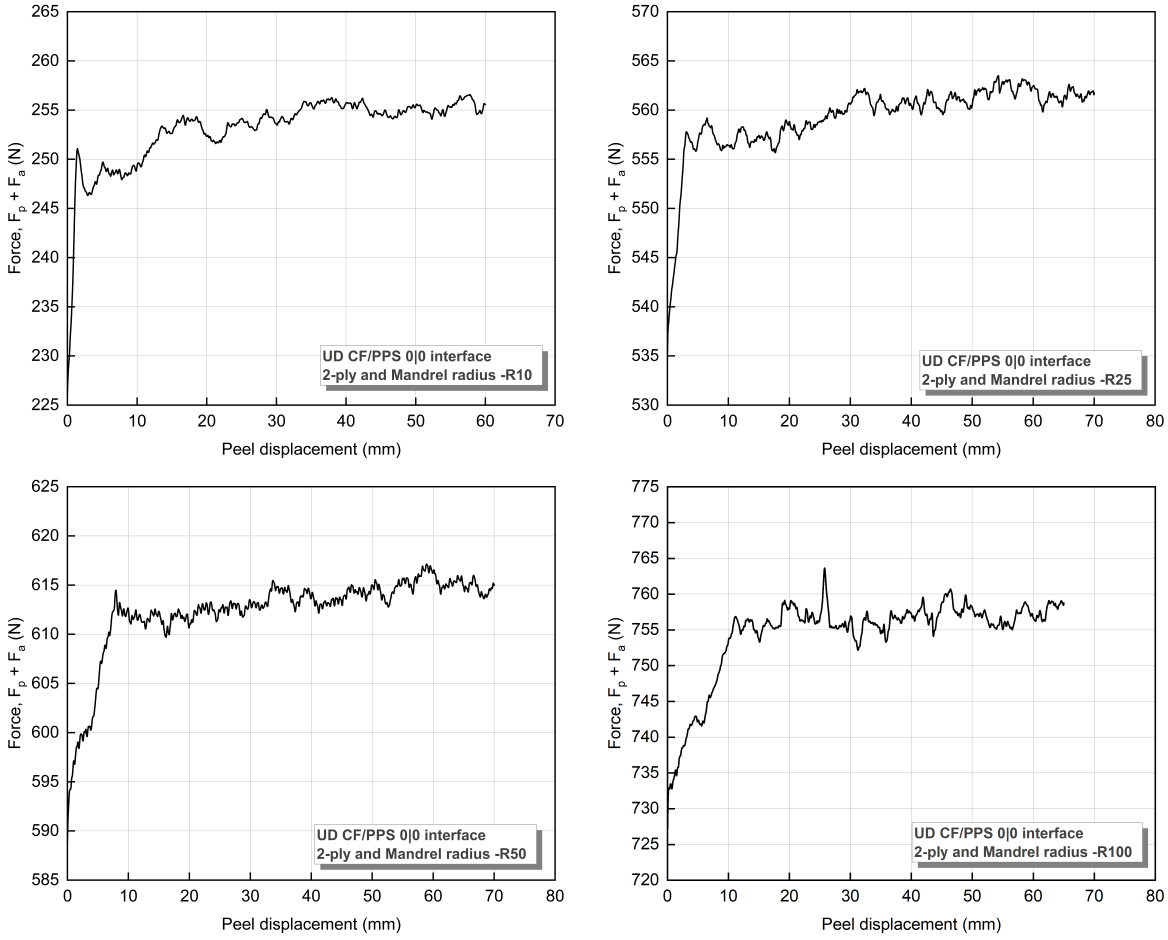


Figure 7.4: Peel force-displacement plots of 2-ply UD CF/PPS peel specimens with 0|0 interface for various mandrel radii.

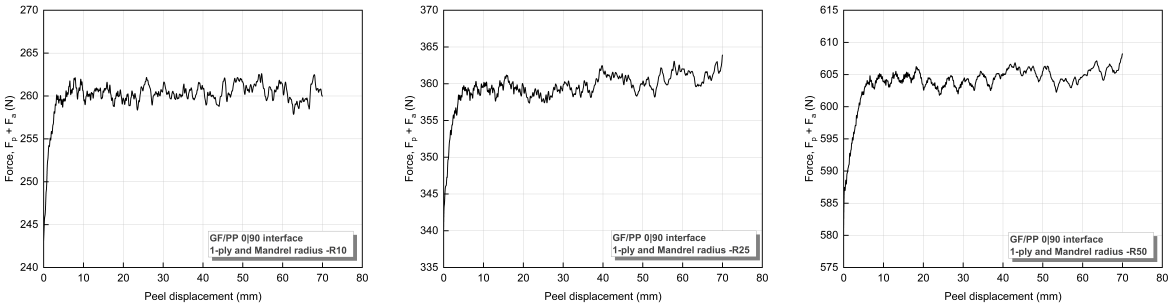


Figure 7.5: Peel force-displacement plots of 1-ply UD GF/PP peel specimens with 0|90 interface for various mandrel radii.

7.2 Discussion

In the following section, the mandrel peel test findings are consolidated and further analyzed with the objective of gaining a more profound comprehension of the underlying mechanisms

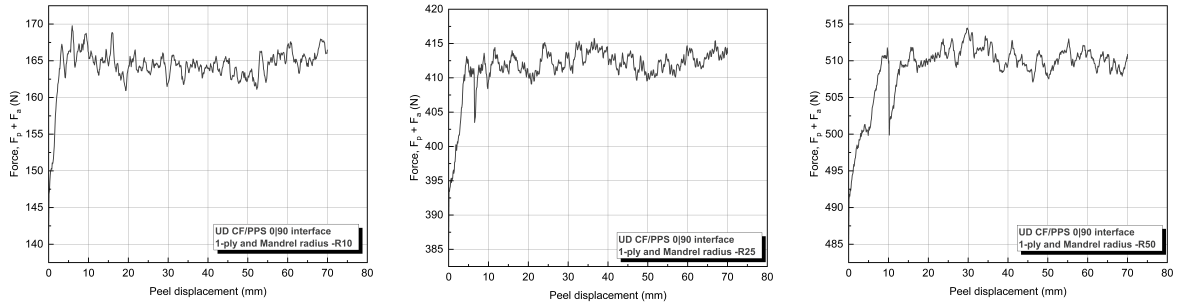


Figure 7.6: Peel force-displacement plots of 1-ply UD CF/PPS peel specimens with 0|90 interface for various mandrel radii.

(or factors) from the perspective of both material and testing configurations on the interlaminar fracture toughness.

7.2.1 Effect of Peel-arm Thickness and Mandrel Roller Radius

An integral aspect in the assessment of the interlaminar fracture toughness of composites involves a crucial element of investigating the propagation and its behavior. In Section 7.1, it is reported that the UD peel specimens (irrespective of the material system) displayed distinct crack propagation behavior for varying peel arm thickness and different mandrel rollers. An attempt to explain the cause of these unusual yet exciting delamination behaviors observed during mandrel peel testing of single-ply (also 2-ply) leads to a more detailed investigation, which is discussed further.

The video monitoring of the peel tests enabled the observation of the crack propagation and mandrel–peel arm conformation. It can be said that the peel arm had conformation to the mandrel throughout the peeling process. Following the post-processing and analysis of the videos, it was clearly noticed that the fibers of the peel arm were peeled off and jumped toward the substrate.

The fractographic image of the fracture surface shown in Figure 7.7 corresponds with the characteristic phenomenon and can be seen in all the specimens, which reveals the fibers of the peel arm adhering to the substrate, emphasizing the crack propagation path. Further, this implies that the crack path tends to migrate toward the peel arm away from the intended plane. Another interesting aspect that requires attention is that the adhering of fibers of the peel arm appears to develop from the start of the crack advancement (close to the insert end) and the degree of concentration of fibers gradually intensifies as the peeling proceeds, and the crack propagates, and this is more evident from the Figure 7.7.

In the case of the single-ply GF/PP specimens, it is essential to report that the crack migrated toward the peel arm in most tests. The rationale behind the migration from the predetermined interface could be reasoned to the PP resin-rich region (near the blunt crack tip) and the fiber-bridging. During the occurrence of the fiber bridging, the crack extends either by fiber pull-out, fiber breakage, or a combination of failure mechanisms that depend on the loading mode. The film inserted at the laminates' predetermined interface to generate the initial crack does not allow for the nesting of fibers in the initial delaminated area. Consequently,



Figure 7.7: Fracture surface of the UD GF/PP 1-ply peel arm and substrate indicating fibers of the peel arm adhering to the substrate.

the crack initiates pure delamination between the interface at the start. Further, as the crack advances, the fibers nested initiate the crack front to diverge.

In general, the UD composites, with the fiber orientation in the longitudinal direction (0), are more susceptible to fiber nesting. In the case of the multidirectional composites, the fiber oriented in a different direction could be determined straightforwardly at a microscopic level due to the presence of a small layer of resin free from the fiber between the reinforced matrix. However, this separation may be significantly less, particularly for the UD composites. During the process of consolidation or curing, the fibers might (partly) migrate within the adjacent plies or at the interface, known as nesting, eventually resulting in the bridging of fibers. The schematic of the fiber nesting is illustrated in Figure 2.8. The occurrence of fiber-bridging phenomena indicates the mingling of fibers at the interface (fibers of both the plies). More importantly, this mingling allows for more uniformity in the laminate, making it demanding (challenging) to trace the crack propagation/delamination path as it is not distinctive. This effect of fiber bridging impedes crack propagation, thereby increasing the resistance to delamination and the corresponding fracture toughness. Several studies show that the degree of fiber bridging is size dependent and demonstrate that the R-curves are influenced by specimen thickness in fiber-reinforced polymer composites. Amongst other parameters, the interlaminar fracture toughness is also shown to be affected by the ply thickness.

As the mandrel peel test deals with the characterization of the interlaminar (composites) or interfacial fracture toughness at a ply level, it is of specific interest to understand the effect of the ply thickness and microstructural uniformity on the fracture behavior. In order to address this issue and to further the understanding of this cause, the condition of the prepreg and consolidated laminated was analyzed on the basis of the cross-sectional microscopy. Furthermore, thickness measurements were taken across the prepreg width to access the thickness variation perpendicular to the fiber orientation.

A qualitative assessment of the characteristics of the prepreg revealed that the distribution of the fibers within the prepreg was not uniform. Densely packed glass fibers were discovered in addition to the polypropylene-rich regions due to the non-uniform distribution. This irregular distribution in the fiber-to-matrix volume ratio was observed frequently across the ply width, although the severity in the intensity varied. Specifically, there are notable disparities in the local fiber volume fraction and the prevalence of resin-rich areas throughout the composite.

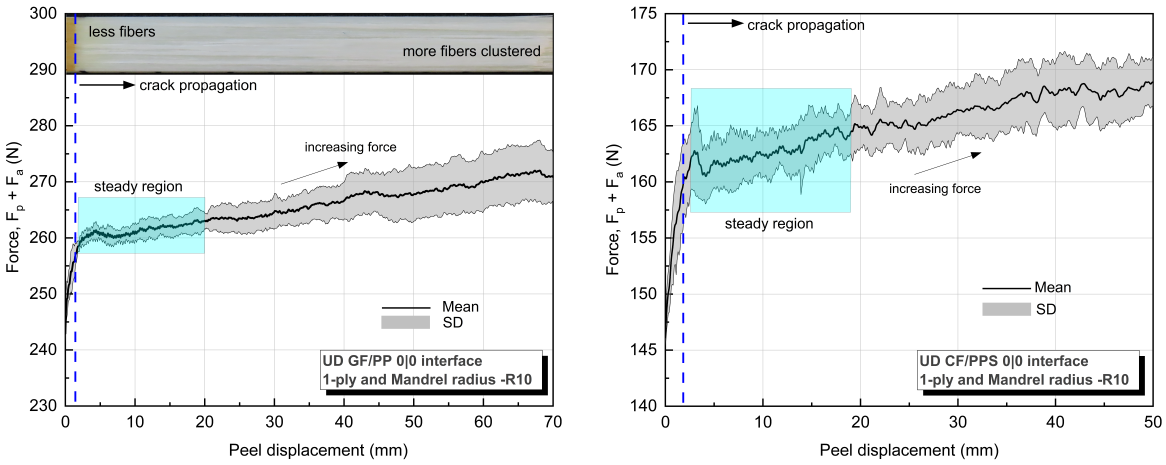
As the crack advances through these regions, the crack further has to extend either by fiber pull-out or fiber breakage, during which the matrix-rich enclosed fibers tend to either adhere to the substrate or the peel arm, as with the case observed with the interface investigated.

The thickness of the UD GF/PP and UD CF/PPS ply used in this study are 0.21 mm and 0.15 mm, respectively, which are considerably thick per commercial standards. It should be noted that the formation of clusters of dense fiber bundles is predominantly observed in standard/intermediate-ply(prepreg) and thick-ply(prepreg) and composite laminates fabricated, where the microstructure exhibits substantial heterogeneity [185][186][187]. Relatively the microstructure is more uniform and homogenous in thin plies (prepreg) due to the tow-spreading process technology, which enables the standard fiber tows to be spread.

The high heterogeneous microstructure that gets developed in the thick plies during the production of prepregs tends to contain regions with high concentrations of both matrix and fibers. Previous studies have shown these fiber-rich regions (in the laminates) to experience elevated levels of localized stress, which can lead to the development of distributed micro-cracks [186][4]. These cracks can then propagate in a non-uniform manner, resulting in a wavy crack front that extends through the entire specimen width. This phenomenon is responsible for the formation of fiber bundles that bridge the crack faces.

Moreover, the bridging fibers proximal to the initial crack (starter film) were predominantly individual in every specimen. However, with distance (from the initial crack), a significant number of fibers were found to be clustered in bundles. The quantity of bridging fibers present in these bundles is observed to be more significantly influenced by the thickness of the ply and varies. Based on these observations, it can be inferred that the presence of a varying degree of large fiber bundles is primarily responsible for the rising peel force. Figure 7.8a shows the representative normalized peeling force of the one-ply peel specimens with a mandrel radius of 10 mm, where it is possible to notice the range of force response. This is because the fiber bundles' strength is subject to variation based on the number of fibers it comprises, as stress is transferred to adjacent fibers in the event of a single fiber rupture. Consequently, these clustered fiber bundles are capable of bearing more stress compared to individual bridging fibers, leading to a prolonged and more effective bridging region. Again, as mentioned before, the bridged fibers either pull out or break for the crack to propagate. Figure 7.9 illustrates the peeling process (mandrel radius = 25 mm), and on observation, it could be realized that the fiber bundle is getting pulled (Figure 7.9 - b) and stretched as the peeling extends (Figure 7.9 -a), leading to the reasoning for the cause of increasing peel force in 1-ply UD GF/PP peel specimens with 0|0 interface.

Apart from the intrinsic heterogeneity, another reason could plausibly be attributed to the flow of molten polypropylene resin to the outer edges of the laminates. Further, this possibly allows for a higher fraction of the fiber volume to remain/occur at the laminates' central region. A higher fiber/matrix ratio might cause more bundles of fibers to bridge with a low volume of resin available to deform plastically at the interface. Next, if observed carefully, the peel force is almost steady in the initial 20 mm peeling and then rises gradually. This study suggests that the cause for this variation is the waviness and misalignment of fibers and the bridging action. The manufacturing procedure often results in fiber misalignments between the adjacent plies due to the manual stacking of the prepregs. The waviness of fibers in the in-plane orientation of the prepreg is also caused by the tow-spreading process. At a single-ply level, this misalignment/waviness of fibers and lack of matrix resulted in generating



(a) 1-ply UD GF/PP with 0|0 interface **(b)** 1-ply UD CF/PPS with 0|0 interface

Figure 7.8: Peel force-displacement plots of 1-ply UD GF/PP and UD CF/PPS peel specimens with 0|0 interface showing gradually increasing peel force for tests with R10.

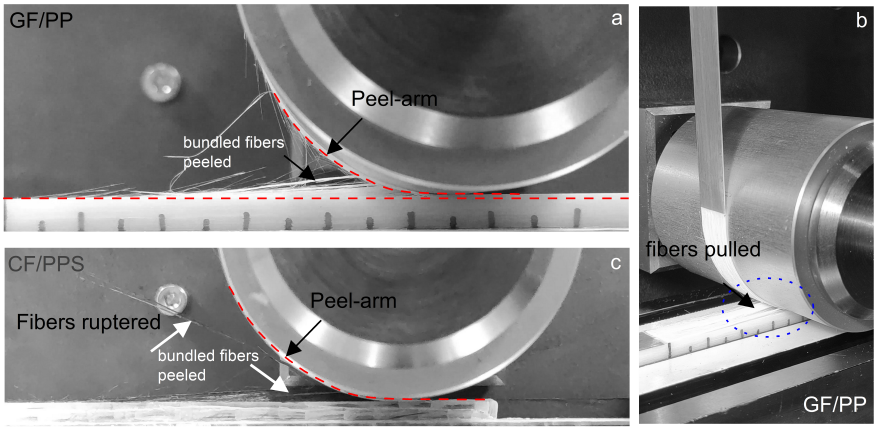


Figure 7.9: Crack propagation behavior of 1-ply UD GF/PP and UD CF/PPS peel specimens with 0|0 interface showing bundled fibers peeled and pulled increasing peel force for tests with small mandrel radius.

entanglements of fiber bundles that enable to sustain higher forces.

With the CF/PP single-ply specimens, (see Figure 7.9 -b), a similar mechanistic behavior could be noticed where the bridged fibers are detached and pulled. However, "layer-like" clusters are formed, and the number of fibers forming the cluster varies relative to the GF/PP specimens due to the different fiber volume fractions and the microstructure. The non-flat peeling force (Figure 7.8b) could reasonably be correlated to the strength of the carbon fibers as it is stretched before it fails after a large crack extension.

Despite the fact that the same phenomenon (crack shift/bridged fibers peeled off the peel arm) occurred during the peel test with 50 mm and 75 mm mandrel radius, it is expected that the large radius and the local peel angle synergistically stimulated each other resulting in a combination of both fiber-pull out and the breakage (at shorter distances) during the

crack progression, as shown in Figure 7.10 which features the broken fibers and fiber peeling, due to which the peel force showed a more stable behavior. Similar peeling behavior is also noticed with 1-ply CF/PPS peel specimens at large radius. This indicates that the peel angle at the crack front effectively contributes to the fracture behavior.

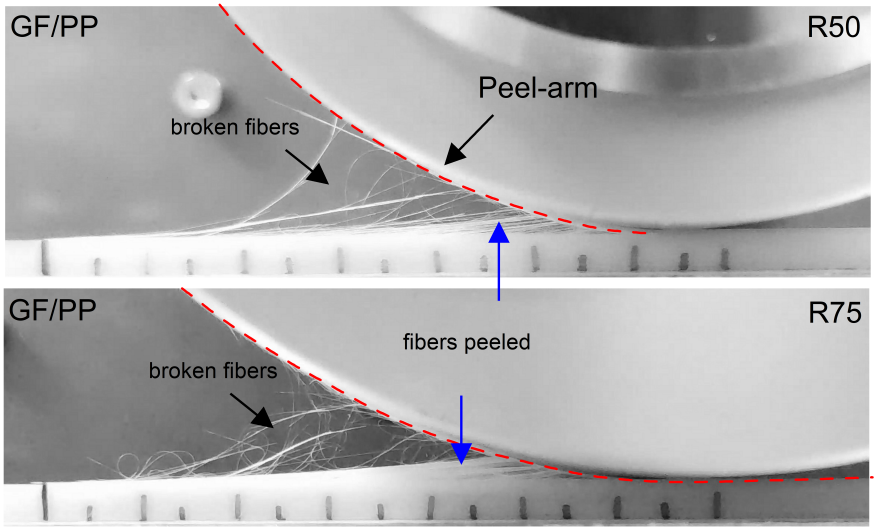


Figure 7.10: Crack propagation behavior of 1-ply UD GF/PP peel specimens with 0|0 interface showing fiber peeling and breakage resulting in a relatively stable behavior for R50 and R75.

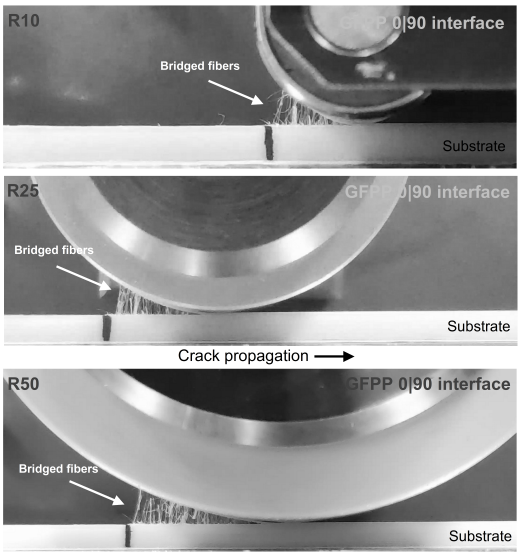
On the peel-arm effects, as mentioned earlier, the specimen thickness also affects the degree of fiber bridging and, in turn, the delamination behavior. The microstructure heterogeneity is assumed to be slightly reduced in a 2-ply thick peel arm at the interface, as the mingling of fibers allows for comparable uniformity (in the volume fraction). Additionally, especially in the UD laminates, irrespective of the thickness of the prepreg/ply, it is shown that due to the mingling of the adjacent layers, the delamination cannot be constrained within the interface, and consequently, the crack inevitably progresses partially intra-ply.

While it could be said that the crack remained in the intended plane with the 2-ply test, this argument for a UD composite could always be questioned, as it is challenging to distinguish a clear distinction due to more uniformity. Even with a consideration that the crack front migrates (this is dependent on the crack tip condition), in the case of interface with 0 orientation, as the initial delamination plane migrates to the adjacent upper ply, the fibers effectively impede further upward growth into the sub-adjacent ply, thereby maintaining the crack path to be parallel to the fibers of the first adjacent ply [7]. With the interface between the second and third ply for the 2-ply thick peel-arm, the crack propagation plane will be confined to the adjacent ply. At the same time, this is not the case with the 1-ply thick peel arm (interface between first and second ply), wherein a likely migration will always result toward the peel arm. The variation in the fiber migration at the interface (in the 1-ply and 2-ply thick peel specimens), along with the crack plane constraints and matrix deformation, plausibly rationalizes the reason for the observed relatively steady fracture propagation behavior in the 2-ply peel specimens, regardless of the mandrel size.

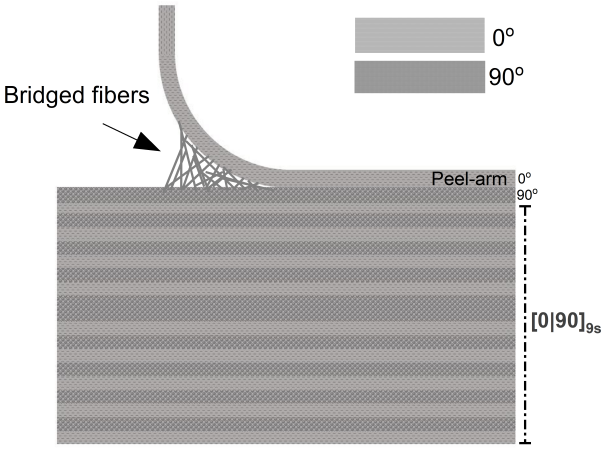
7.2.2 Applicability to 0|90 (Cross-ply) Interface

Even though the mandrel peel testing of 0|90 interface was carried out with a single-ply thick peel arm, the different fracture behavior (steady peel force) was observed in contrast to the tests with a single-ply 0|0 interface (rising peel force). Orienting the adjacent plies at large offset angles yielded in mitigating the nested fibers and ensued in different fiber bridging behavior, although it does not terminate the bridging effect entirely.

An explanation is offered based on the macroscopic observation of the crack propagation during the peeling test. Relating to the orientation of the ply at the interface, fibers aligned at 0 degrees tend to rupture at varying distances from the original plane of the crack. During this process, the fibers become detached from the resin matrix and are gradually peeled off as the crack grows, resulting in energy dissipation. On the other hand, it is worth noting that fibers oriented at the 0|90 interface exhibit a different bridging mechanism such that the height of the peel-off fibers, on average, remains relatively stable in the crack growth direction due to the mutually stimulating effect of fiber-breakage (Figure 7.11a). This critical finding helps reason the nearly steady propagation with the R-curve plateau. Eventually, the energy release ceases as the fibers are entirely peeled off. In this regard, the length (height) of the fibers peeled is considerably shorter in 0|90 (Figure 7.11b) interface specimens compared to that of fibers in 0|0 (specifically the behavior noticed in the single-ply peel), leading to a low strain energy release rate. The fracture resistance behavior, therefore, could be related to the height of the peel-out fibers, which is the outcome of a complex, randomized micro mechanistic synergistic process of fiber fracture and detachment.



(a) Fiber-bridging mechanism observed during the crack propagation showing the height of the peeled fibers.



(b) Schematic of the fiber bridging behavior.

Figure 7.11: Peeling behavior of 1-ply GF/PP specimens with 0|90 interface with different mandrel roller.

It can be further stated that from the fractured peel surface, the crack path was slightly tortous, and the observed phenomenon of crack growth behavior is also reflected in the fracture

resistance. The peel force response of the GF/PP 0|90 interface specimens demonstrates localized irregularities along the crack propagation, and a more detailed analysis revealed that the spacing between the peaks corresponds to the resin matrix enriched regions at the interface. A heterogeneously distributed fiber/matrix fraction remains even after the consolidation to a certain extent, and this eventually results in the crack front confronting two distinctive materials, which plausibly might intensify the possibilities of a shift in the crack path. In the GF/PP specimens, a few clustered fiber bundles (in 90^o direction) from the substrate could be seen adhering to the peel arm, and these are generally located at fiber-rich areas, which is emphasized in the macrograph and the SEM Image (Figure 7.12).



Figure 7.12: Fracture surface of the peel arm and substrate of the GF/PP specimen with a 0|90 interface, showing the fibers adhering on the peel arm (left), SEM image of the substrate exhibiting the corresponding region (right).

This shift could be reasoned based on the phenomenon of crack tip damage zone and its size. Previous research indicates that plastic damage zone is known to be affected by the inclusion of fibers. Further, the fiber volume fraction and its distribution in composite laminates are also crucial in crack propagation behavior. It has been postulated that if the size of the plastic zone exceeds the resin region at the interface, the crack may potentially grow by migrating toward the weakest zone in the crack plane [63][65][66]. The weakest zone here is the interface between the matrix and fibers. When the matrix becomes larger than the radius of the plastic zone in the interface (between the adjacent plies/layers), the crack growth will be confined within this region enriched with resin.

As stated earlier, the concentration of polypropylene matrix and glass fibers varies along the interface (peel arm-substrate), and as the crack tip confronts the regions rich with clustered fibers that lack resin, yields in the crack path to shift to the weak zone and propagate. This fracture behavior is eventually the cause for the fibers observed on the peel arm. Another aspect is that the consistently observed shift in the crack tends to be in the direction of 90^o-oriented ply in all tests, and the crack progression plane is confined within the 0|90 interface and(or) 90 ply, and it could be stated that the migration was not promoted to the upper and sub-adjacent (below the 90^o ply) plies with fibers in the 0 direction. A schematic of such a crack propagation behavior is demonstrated in Figure 7.13. To this end, the GF/PP cross-ply specimens' failure behavior can be regarded as both interlaminar (0|90 interface)

and intralaminar (within the 90 ply).

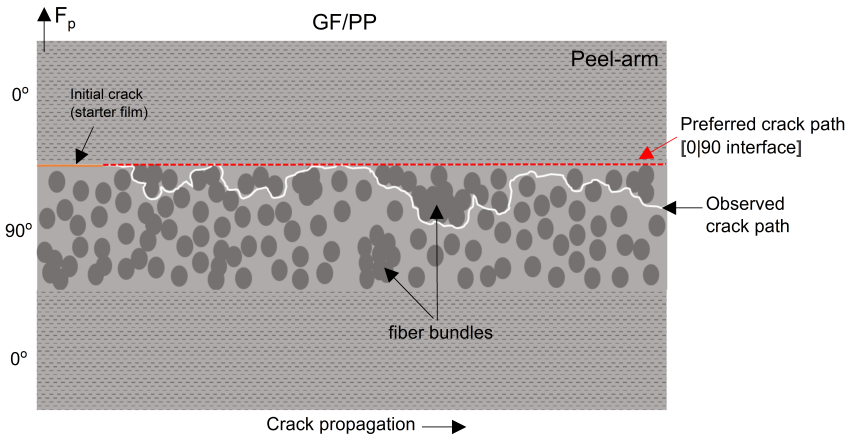
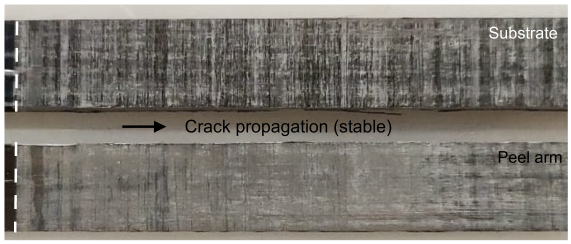
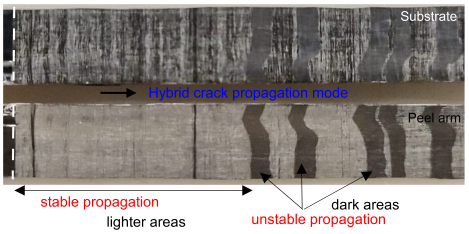


Figure 7.13: Schematic illustration of the crack propagation path in 0|90 GF/PP peel specimens indicating both interlaminar and intralaminar failure.

The peel testing of the CF/PPS 0|90 interface did not reveal any fiber bridging mechanism. In the absence of such bridging effects, the crack steadily propagated along the initial interface. However, the delamination also encountered unstable behavior characterized by abrupt load drop followed by a peak (crack growth re-initiation) in the force-displacement curve, indicating the typical phenomenon of stick-slip behavior, and this observation predominantly appeared at localized regions abundant in the PPS matrix, contributing to the instability of crack propagation. Figure 7.14, presents a visual representation of the fracture surface. The lighter areas on the surface consistently observed across all the tests indicates a gradually stable progression of the crack (Figure 7.14a). On the other hand, the darkest area, which was only noticed in a few tests where abrupt force drops were recorded, correlates to an unstable fracture behavior.



(a) Fracture surface indicating stable propagation.



(b) Fracture surface indicating stick-slip with hybrid propagation.

Figure 7.14: Fracture surface of the peel arm and substrate of the CF/PPS specimen with a 0|90 interface, showing no migration or fiber bridging trace.

It could be clearly argued that the crack propagation relates to the hybrid growth that combines the behavior of the stable and unstable modes (Figure 7.14b). At this juncture, it deems imperative to mention that the stick-slip behavior was noticed only in a few samples. Additionally, it is not attributable to any non-conformity in the mandrel and peel-arm con-

figuration. In fact, the mandrel is instrumental in suppressing such instabilities, as evidenced by prior literature and this current study.

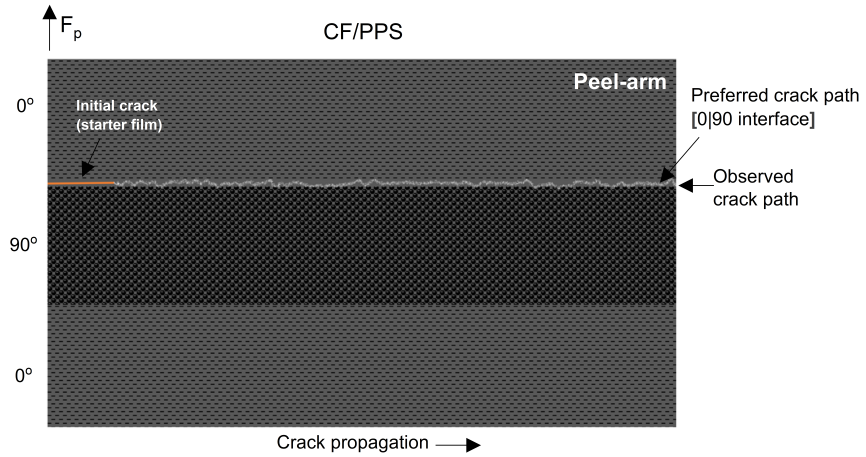


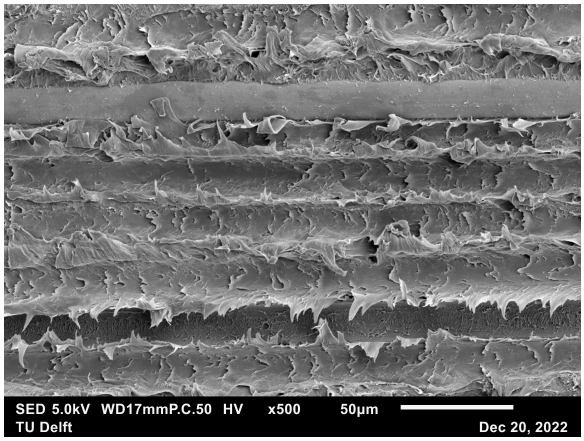
Figure 7.15: Schematic illustration of the crack propagation path in 0|90 CF/PPS peel specimens.

Across all tests (irrespective of the mandrel roller), it was observed that the crack growth progressed along the intended 0|90 interface without any indications of migration, except for the instabilities due to stick-slip (Figure 7.15). The macrograph (peel arm and the substrate) does not reveal the presence of features such as the fibers (0) on the substrate or 90 oriented fibers adhering onto the peel arm, further substantiating the absence of crack plane shift (see Figure 7.14).

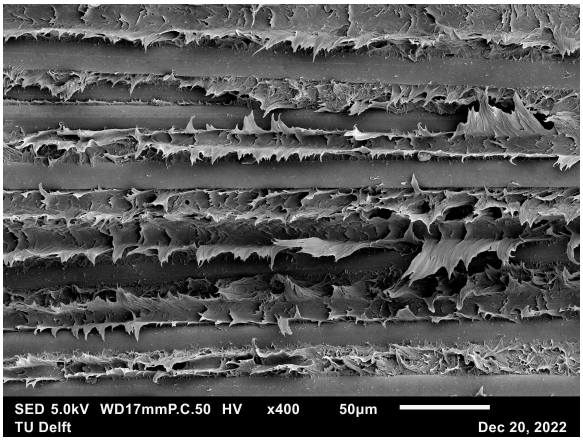
7.2.3 Mode of Failure

The fracture behavior of two materials investigated under different configurations (mandrel radius, interface) is discussed in this section using SEM micrographs. The fracture surface of the GF/PP mandrel peel specimens illustrates features of fiber-peel and breakage. Fiber bridging is evident, and the (0|0 interface) fracture surface of the GF/PP specimen exhibited a ductile drawing of the PP matrix with the stretched fibril's tip oriented (Figure 7.16a). In addition, impressions of the matrix on the fiber surface were observed. With increasing mandrel radius, the fracture surface shows extensive ductile deformation of the matrix with fibrils inclined along the fiber surface, and fracture near the interface was observed from Figure 7.16b. Additionally, well-defined U-shaped semi-circular dimples were identified in the fiber track regions, and relatively clean fiber surfaces with lesser traces of PP matrix were apparent, demonstrating the presence of the shear component of loading.

On the other hand, similar features such as "shear lips" in the form of a highly plastically deformed PPS matrix along the fiber surface could be evidenced in the CF/PPS mandrel peel fracture surface (0|0 interface) (Figure 7.17a). Furthermore, with a larger mandrel radius, the matrix deformation is significant with thick extended matrix inclination to the fiber surface (Figure 7.17b). The bare fibers implicative of matrix separation were noticed. The aspects, such as the deformation morphology of the matrix, degree of deformation, and inclination, indicate the mixed-mode fracture behavior.

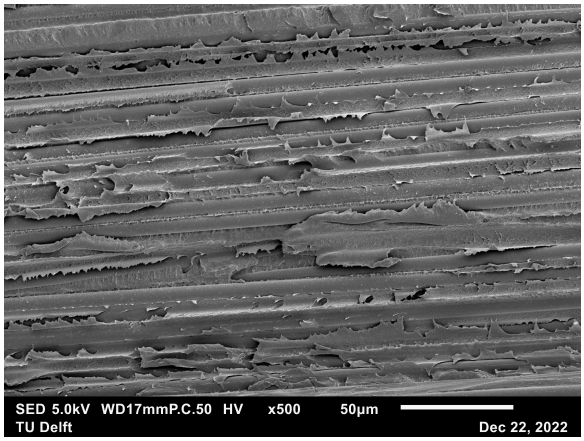


(a) Mandrel radius, R10

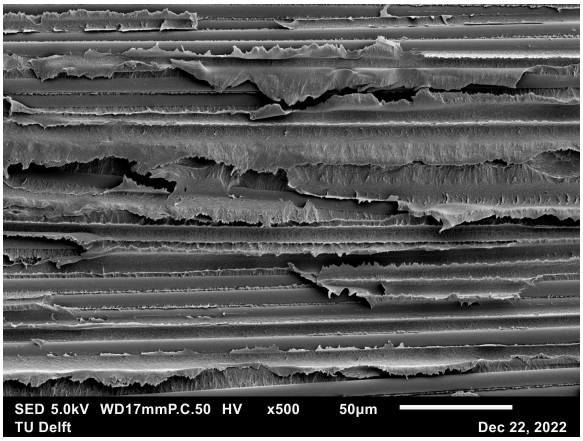


(b) Mandrel radius, R50

Figure 7.16: SEM micrographs of the delaminated fracture surface of UD GF/PP in various mandrel radii.



(a) Mandrel radius, R10



(b) Mandrel radius, R50

Figure 7.17: SEM micrographs of the delaminated fracture surface of UD CF/PPS in various mandrel radii.

7.3 Analysis of Fracture Toughness

The following section details the findings of the mandrel peel tests providing the fracture toughness data. Initially, the general observations during the experimental testing and the resultant peel-force response are outlined, followed by the guidelines adopted in this study for the fracture data analysis. Ultimately, the outcomes of the peel-tested specimens are integrated to develop a fracture envelope, which depicts the relationship between the mandrel radius, peel-arm thickness, and interlaminar fracture toughness.

General observations

Different crack propagation behavior leading to various characteristic peel force vs. displacement curves could be noticed during the Mandrel peel testing for various reasons for different material systems, as discussed in the preceding section. A few challenges which were expe-

rienced were the occurrence of the rising R -curve (fracture toughness vs. the peel length) and small crack growth region with conformance during peeling with a larger mandrel radius (R>75 mm). While the former highlights the plausible deviations in the delamination growth mechanisms, namely crack path and bridging of fibers, the latter emphasizes the importance of alignment load. In addition, hybrid crack propagation displaying both stable and unstable (stick-slip) behavior was also recorded. Since this complexifies the data processing analysis, two guidelines were established to generate the data set for evaluation. A Peel specimen was used for evaluation if that showed a minimum of 10 -20 mm interlaminar delamination prior to migration. In the case of specimens exhibiting stick-slip, only the steady-state propagation region is considered for calculating fracture energy.

Initiation Fracture Toughness

Within this study, it is pertinent to note that there is no clear distinction for the crack initiation point for the mandrel peel tests. It is also known that the interlaminar fracture toughness initiation values cannot be evaluated with the peeling tests. As explained in the previous sections, the blunt crack tip, in combination with a resin-rich zone, could have an influence effectively. Similarly, the cross-sectional micrographs also reveal that the concentration of the resin-rich zone at the insert film end and along the interface varies. Interestingly, for peel tests using a 10 mm mandrel size, a sharp peak was observed during the initiation for the CF/PPS, irrespective of the peel arm thickness. Nevertheless, this elevation in the peak diminished for the tests with different mandrel radii. On the contrary, Grouve et al.[36] did not observe any sharp elevated peak in the force-displacement response during the peel tests for the UD CF/PPS, further re-confirming that the crack tip condition near the insert film plays a role in the initiation fracture behavior at the interface during the peel tests as well. Considering all these into account and for the reason of consistency, only the propagation fracture toughness values are reported and discussed.

Propagation Fracture Toughness:

The total energy release rate or the fracture toughness is evaluated considering the steady state peel force using the data reduction procedure described in Section 5.4. In the case of peel tests with a single-ply peel arm, especially with a mandrel radius of 10 mm and 25 mm, the initial regions where the steady-state propagation is observed are considered for calculating fracture energy. Figure 7.18 shows the mean overall fracture toughness and its standard error for the tested peel specimens with different mandrel radii for UD GF/PP and UD CF/PPS, respectively.

Comparing the propagation fracture toughness data of 1-ply and 2-ply specimens, it can be noted that the average fracture toughness values for the two-ply specimens are generally higher than those for the one-ply specimens. Furthermore, it can be seen that the standard deviation values for the two-ply specimens are generally lower than those for the 1-ply specimens. This indicates that the fracture toughness values for the two-ply specimens are more consistent and less variable than those for the 1- ply specimens. However (excluding the data of the R-75 mm and R -100 mm from comparison), based on the standard deviation of the fracture toughness results within the 1-ply peel specimens (for R-10 and R-25mm), the sensitivity analysis between the 1-ply and 2-ply should be treated with care.

Nevertheless, in terms of the effect of mandrel radius on fracture toughness, it can be observed that for both 1-ply and two-ply specimens, the average fracture toughness values generally

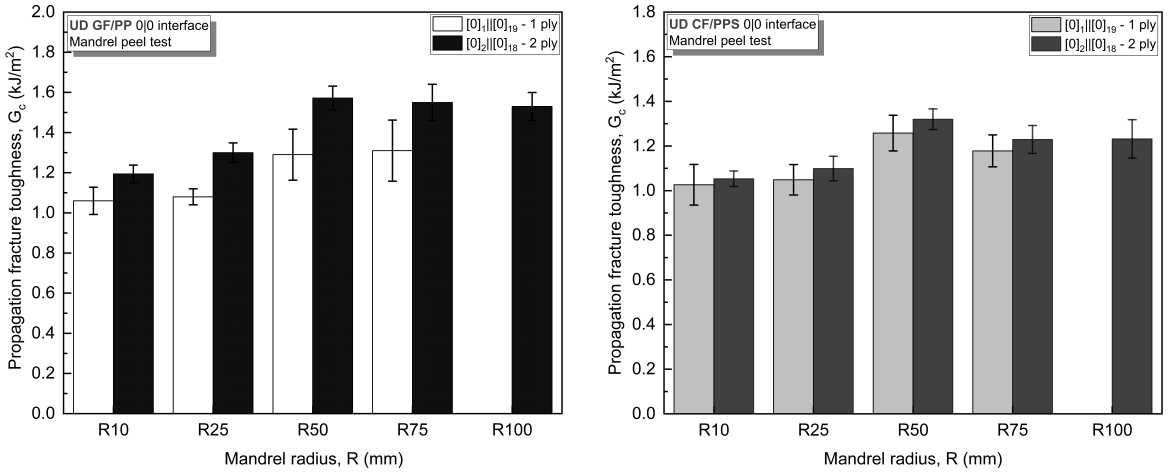


Figure 7.18: Propagation fracture toughness of 1 and 2-ply peel specimens as a function of various mandrel radii for UD GF/PP and UD CF/PPS composites.

increase as the mandrel radius increases. With the exclusion of the R75 and R100 data, it can be noticed that the difference in toughness values between the 1-ply and 2-ply specimens is more pronounced, and the trend of increasing difference in toughness with increasing mandrel radius is more apparent. This observation suggests that the data for R75 and R100 might be outliers or affected by some other factors, and hence, the exclusion of these data points leads to more meaningful conclusions.

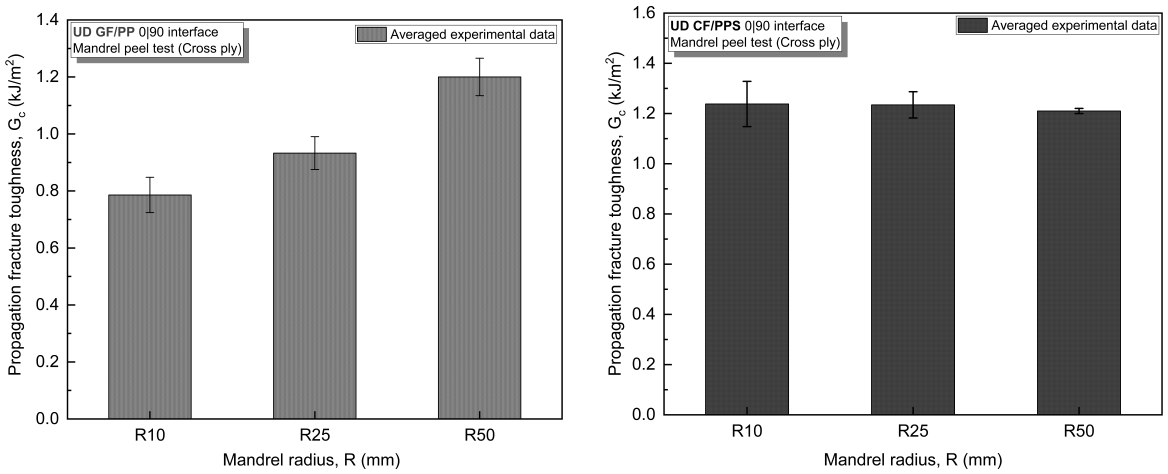


Figure 7.19: Propagation fracture toughness of GF/PP and CF/PPS peel specimens with 0|90 interface as a function of various mandrel radii.

With the 0|90 interface, an observation can be made regarding the influence of mandrel radius on the average fracture toughness within the GF/PP material system (Figure **7.19** - left). Specifically, an increase in the mandrel radius was found to correspond to a higher average fracture toughness. On the contrary, when examining the CF/PPS peel test results associated with the 0|90 interface, no significant changes in the overall fracture toughness were evident in relation to the mandrel radii (Figure **7.19** - right).

From these observations, it is essential to note that the relationship between mandrel radius and fracture toughness may not be linear, and the specific trend may depend on the material being tested. Additionally, the effect of mandrel radius may depend on other factors such as material thickness, orientation, and fracture energy at pure modes.

7.4 Comparative Assessment

This section presents an analysis and comparison of the results obtained from three standardized tests, namely the DCB, ENF, and MMB tests and the Mandrel Peel (MP) test. The primary objective is to evaluate the suitability of the MP test for determining the critical strain energy release rate experimentally and developing a failure envelope. To achieve this goal, the comparison considers both global criteria, such as G_c values, and local criteria, including the crack front shape and failure mode from the fracture surfaces obtained from different test configurations. Chapter **6** and Section **7.1** - **7.2** provide a detailed discussion of the results obtained from the standardized tests and the Mandrel peel test.

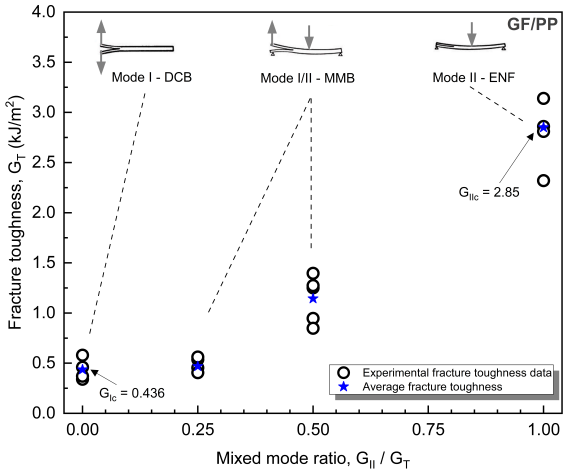
"*The question is whether the G_c values obtained through the MP test method could be comparable to those obtained from standard Mode I, Mode II, and Mixed Mode I/II tests.*"

The graphical representation of the interlaminar fracture toughness of the two material systems studied is presented. The results are summarized for ease of comprehension. Figures **7.20a** and **7.21a** shows the critical failure envelope developed based on the initiation fracture toughness data of various mixed mode ratio combinations from the classical tests for the UD GF/PP and UD CF/PPS composites, respectively.

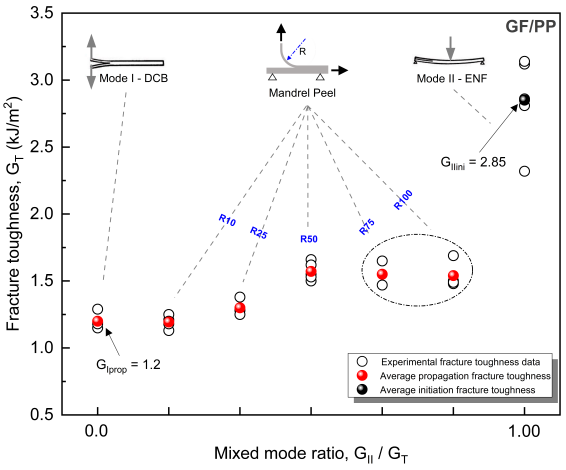
The critical failure envelope describes the fracture toughness dependence as a function of mixed-mode loading. The mixed mode ratio refers to the ratio of the mode II strain energy release rate (SERR) G_{II} to the total SERR G_T ($G_I + G_{II}$), expressed as G_{II}/G_T. While the mixed mode ratio of 0 indicates pure mode I, pure mode II is identified with G_{II}/G_T of 1.

Pertinently, the literature indicates that the evaluation of fracture toughness through the mandrel peel test primarily signifies the propagation of fractures under mixed mode conditions. Consequently, based on this, the interlaminar fracture toughness measurements obtained from the mandrel peel test are expected to be within the range from the fracture values of pure mode I to pure mode II. With this hypothesis, the corresponding interlaminar fracture toughness values for the UD GF/PP and UD CF/PPS generated from the mandrel peel test for various mandrel roller size elaborated in the form of a failure window is represented in Figures **7.20b** and **7.21b**.

The presented findings demonstrate a clear relationship between the fracture toughness values and the mode mixture, as evidenced by the standard tests. Specifically, an increase in mode mixture leads to higher fracture toughness values. Interestingly, this relationship is also evident when examining the influence of mandrel roller radii on the fracture toughness values in the mandrel peel tests. A similar trend is observed in the mandrel peel tests when the mandrel roller radii are increased. Notably, the fracture toughness obtained with a small mandrel radius (R10) closely aligns with the propagation fracture toughness obtained from the mode I DCB tests, indicating strong consistency with previous findings and correlation documented in the literature [**36**][**30**][**34**][**137**]. Moreover, as the mandrel roller radius increases, the fracture toughness also shows a corresponding increase. This trend is more apparent by

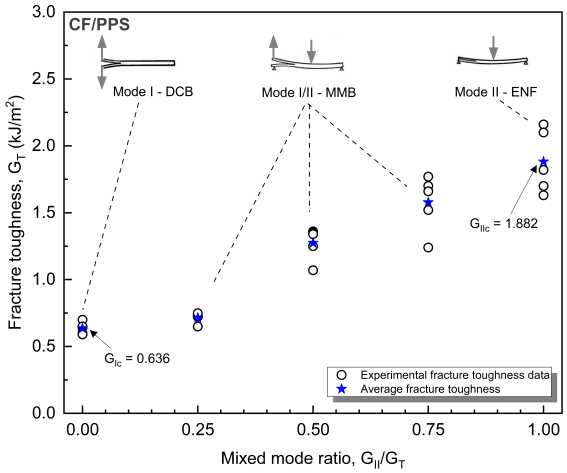


(a) Initiation fracture toughness as a function of different mixed mode ratios developed from the classical standardized tests.

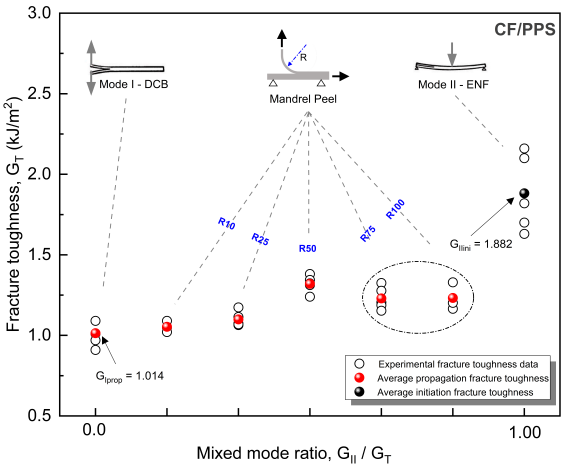


(b) Propagation fracture toughness as a function of different mandrel roller radii developed from the mandrel peel tests.

Figure 7.20: Critical failure envelope comparison for the GF/PP material system based on various testing methods.



(a) Initiation fracture toughness as a function of different mixed mode ratios developed from the classical standardized tests.



(b) Propagation fracture toughness as a function of different mandrel roller radii developed from the mandrel peel tests.

Figure 7.21: Critical failure envelope comparison for the CF/PPS material system based on various testing methods.

excluding the fracture toughness data corresponding to R75 and R100, which was affected by slight non-conformity issues. Consequently, excluding these data allows for more meaningful conclusions to be drawn. From the global perspective in terms of fracture toughness, these observations suggest that the mandrel roller influences fracture toughness.

7.4.1 Crack Front

Macroscopic images of the fracture surfaces were captured using optical microscopy to acquire apparent salient details of the crack growth and the crack front shapes. An illumination source was employed at a tilting oblique angle such that the light gets projected at the sample surface to improve the visibility of the delamination features.

In general, GF/PP and CF/PPS composites tended to be more opaque, and visually observing the front crack shapes was challenging, and this was mainly for the DCB, ENF, and MMB specimens. However, the CF/PPS ENF specimens offered some insights into the delamination front. The shapes generated by the Mode II ENF loading are relatively convex compared to the frontal shape formed by the starter film. Figure 7.22 shows the fracture surface of the CF/PPS specimen, which suggests that the mean length of the crack along the width is higher than the measured crack length on the specimen's longitudinal edges. Next, it is also clearly discerned that the crack fronts are asymmetric often and not symmetric about the center axis along the specimen width as the crack advances incrementally.

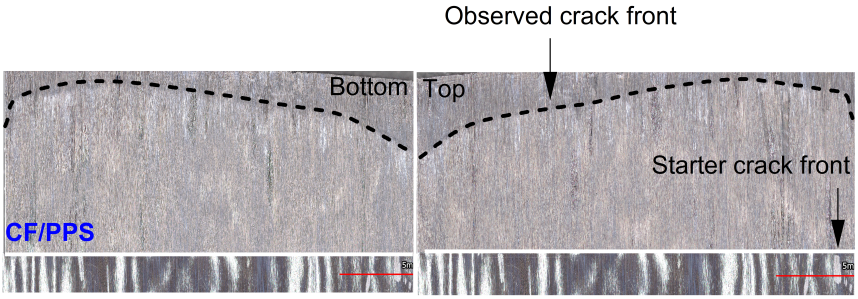


Figure 7.22: Propagation of crack in CF/PPS ENF specimen showing the crack front curvature.

While it is worth noting that the peel specimens still allowed some degree of light transmission into the peel arm, enabling to capture crack front. This was possible because the degree of opacity can vary depending on the percentage of glass fibers, the fibers' size and distribution, and the composite material's thickness.

Nonetheless, the obtained images necessitated further post-processing, such as color thresholding. Following the thresholding, the surface appears to exhibit enhanced clarity revealing the shape of the delamination front as shown in Figure 7.23. As it can be visualized, the crack front is straight in the peel specimens with various mandrel sizes. Delamination propagation with a straight front could be consistently observed even with the peel specimens with a 0|90 interface for both GF/PP and CF/PPS composites.

These observations further confirm that irrespective of the stacking sequence and the interface configuration, the delamination front essentially remains relatively straight in the mandrel peel test. This aspect is as anticipated, as the kinematics of the mandrel peel test (and specimen) primarily maintained by the mandrel enables establishing a relatively straight crack growth front controlling the crack tip location, leading to a better strain energy distribution across the width, unlike the standard tests.

Even though the direct visualization and macroscopic examination of the fracture surface did not reveal distinctively visible indications (due to the employed technique) of the delamination front shape in a few standardized test specimens in this work for effective comparison;

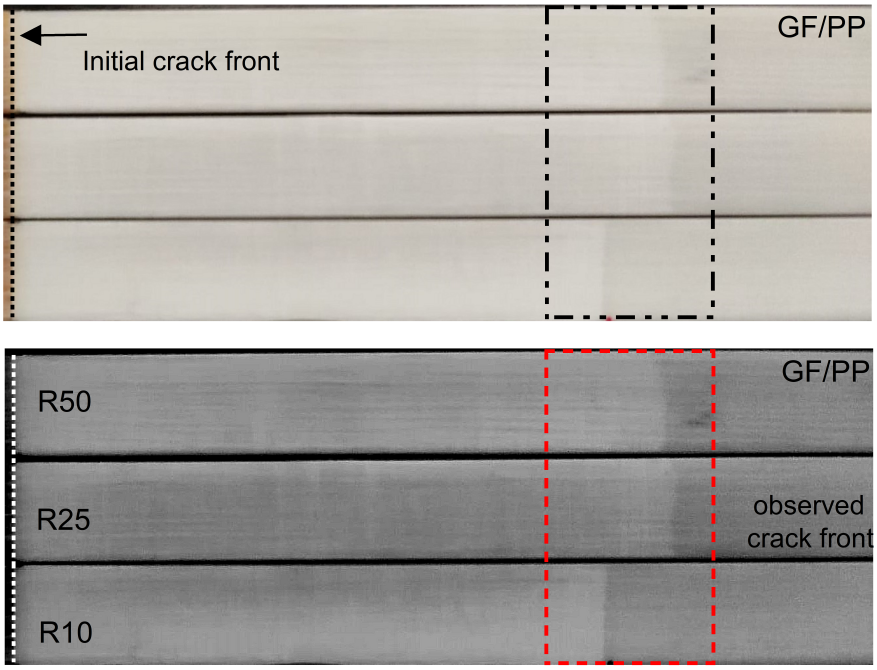


Figure 7.23: Propagation of crack in GF/PP mandrel peel specimens showing relatively straight crack front.

however, there are numerous studies in the literature to substantiate the argument that the delamination front suffers from curvature and skewness, contributing to the variation in fracture toughness, as discussed in Chapter 2.

While an advanced technique, such as X-ray tomography with (without) penetrant, would yield more accurate details of the crack front pattern, at this point, the macroscopic observation presented in this study on this aspect at the preliminary level provides sufficient information to conclude that the mandrel peel test generates a relatively straight front compared to the standard tests.

7.4.2 Failure Mode

The fractography analysis of the fractured surfaces of UD GF/PP and UD CF/PPS discussed in Section 6.4 offered critical information on the failure and damage mechanisms during the crack propagation under known loading mode mixtures. This serves as a foundation for qualitatively comparing the fracture surface morphological features (as detailed in Section 7.2.3) observed during the Mandrel peel test. Ultimately, this enables a comprehensive understanding of the failure mode and the corresponding loading conditions. The micrography images of the fracture surfaces of standardized tests and the mandrel peel tests are illustrated again for easier comparison and interpretation.

Based on the fractography analysis, the observed characteristics, such as the deformation morphology of the matrix, degree of deformation, and inclination, provide evidence of mixed-mode fracture behavior. These features exhibit a strong correlation between the fracture aspects observed in the mixed mode tests and the mandrel peel tests conducted with different

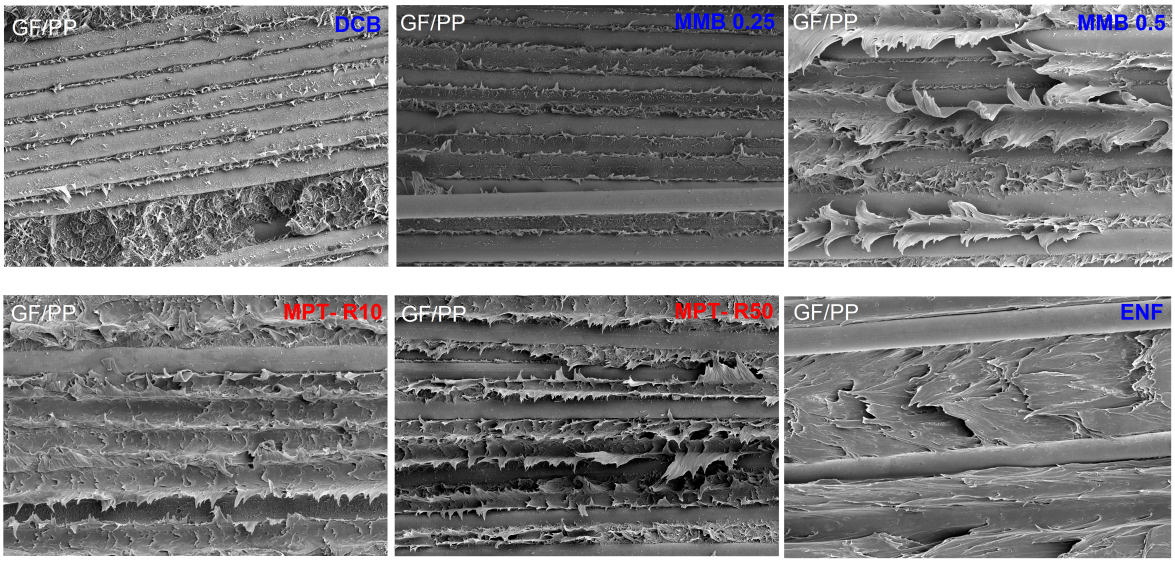


Figure 7.24: Micrography images of the fracture surface of DCB, MMB, ENF specimens, and the MP specimens of UD GF/PP composite.

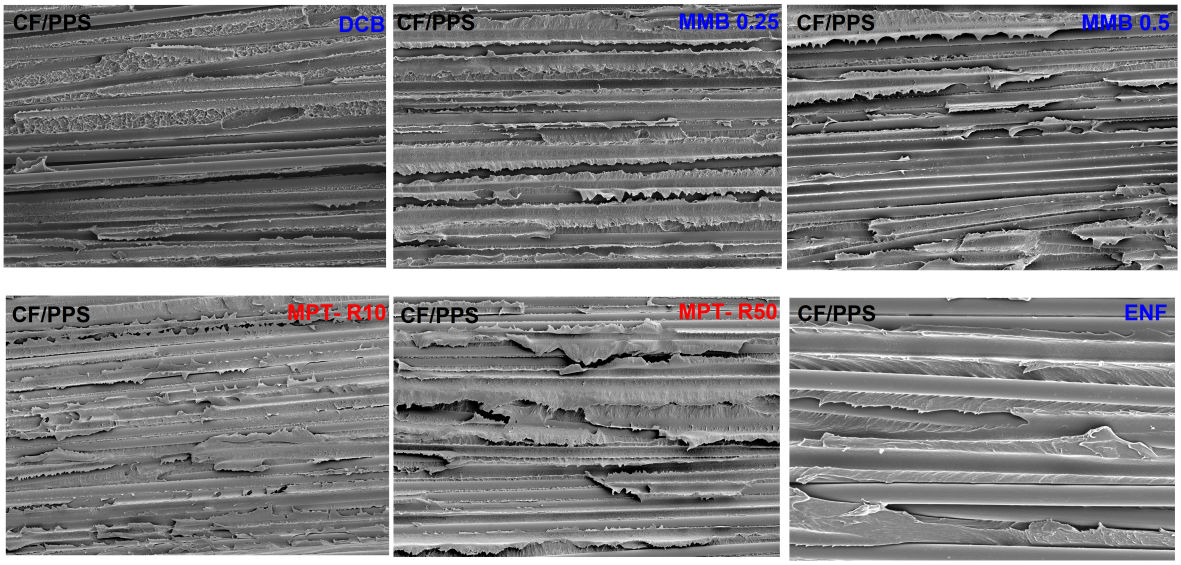


Figure 7.25: Micrography images of the fracture surface of DCB, MMB, ENF specimens, and the MP specimens of UD CF/PPS composite.

mandrel radii for both material systems. The fracture surfaces obtained from the mandrel peel tests with R10 and R50, as shown in Figure 7.24, demonstrate similar fracture features to those observed in the MMB tests with mode mixtures of 0.25 and 0.5. This similarity is also evident in the CFPPS analysis (Figure 7.25).

The behavior of mandrel peel specimens with varying mandrel radii exhibits distinct failure modes. In the case of mandrels with small radii, the primary mode of failure is predominantly characterized by mode I fracture-dominated features. However, as the mandrel radius increases, there is a noticeable shift towards an increasing dominance of the shear component

in the failure mechanism. This observation highlights the influence of mandrel radius on the failure characteristics of the mandrel peel specimens. It should be noted that although the mandrel peel tests demonstrate similar mixed-mode fracture behavior, the exact degree of mode mixity may or may not correspond precisely to the mixed loading conditions in the MMB tests. In order to quantify the loading conditions and the degree of mode mixity, a numerical-based mode-partitioning approach was considered, which is discussed in the next Chapter.

Chapter 8

Numerical Validation

In order to examine the mixed mode fracture behavior of the UD GF/PP and UD CF/PPS composites and validate the experimental results, finite element analysis-based numerical simulations of the Mandrel Peel test was conducted using various mandrel radius. For this purpose, the numerical modeling of the delamination behavior utilized two primary approaches: the Virtual Crack Closure technique, the so-called VCCT, and the Cohesive Zone modeling technique (CZM). Subsequently, the peel force-displacement plots obtained from both CZM and the Virtual Crack Closure Technique (VCCT) simulations were compared to experimental results.

Figure 8.1 shows the Mandrel peel test configuration in 2D with specific boundary conditions considered. While the alignment balancing load is applied in the x-direction to ensure proper mandrel roller and peel arm conformation, a frictionless interaction is assumed between the mandrel and the peel arm.

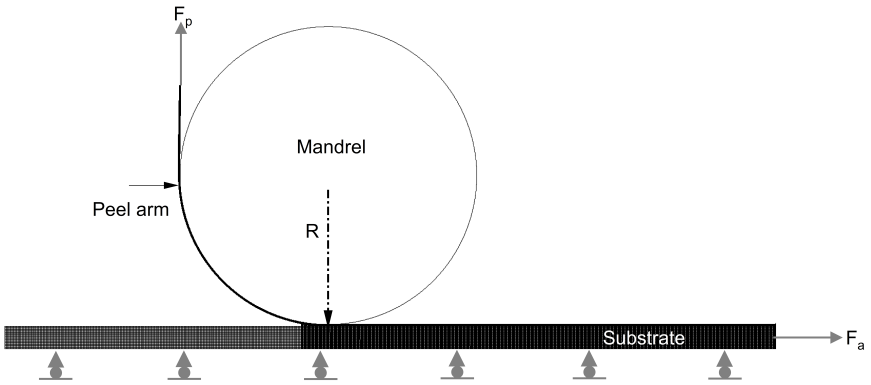


Figure 8.1: FE model (2D) of the Mandrel Peel test configuration with boundary conditions.

In this work, the VCCT-based mode-partitioning approach was considered to determine the degree of mode mixity in the mandrel peel tests. This study uses both Power Law and B-K

criterion for the mixed-mode propagation behavior based on the failure criteria implemented in Section 6.6.

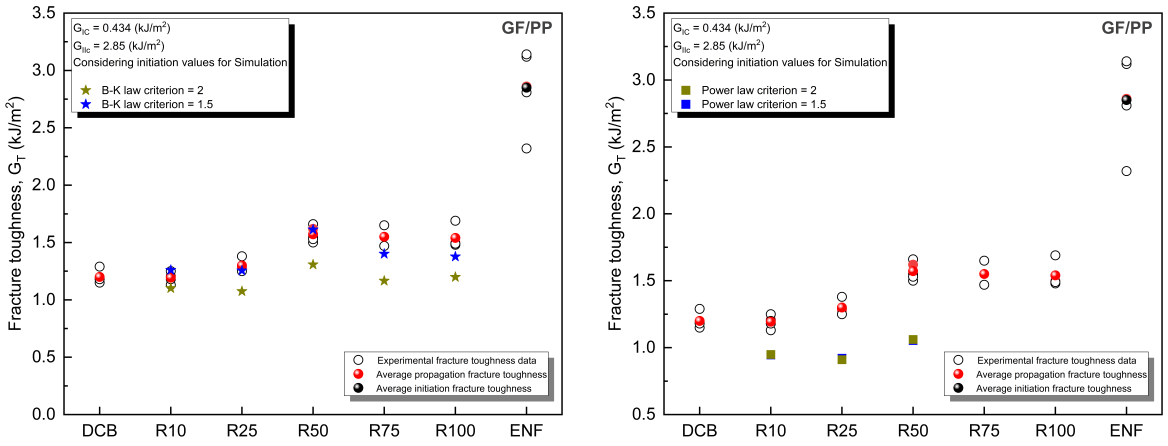


Figure 8.2: Numerically simulated fracture toughness for various mandrel radius compared with the experimental results of the UD GF/PP composite. B-K criterion (left) and Power Law criterion (right).

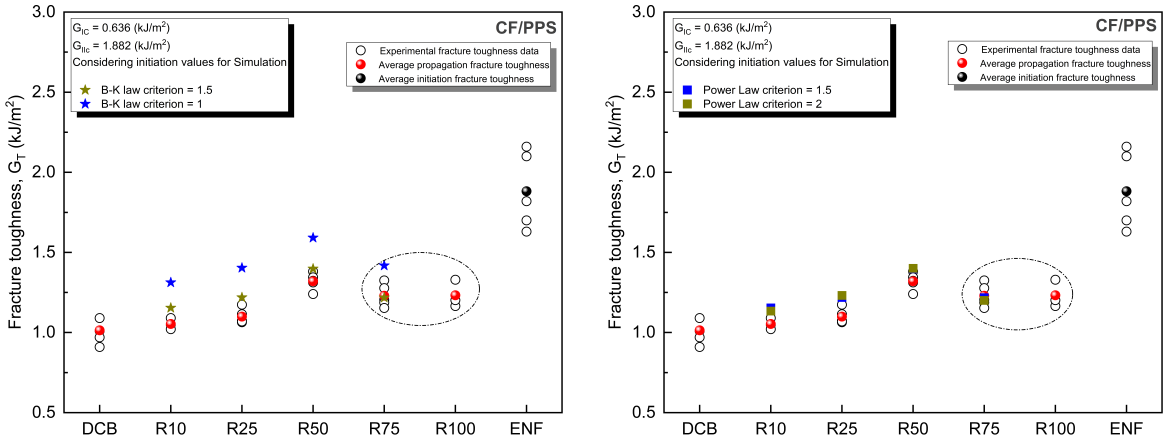


Figure 8.3: Numerically simulated fracture toughness for various mandrel radius compared with the experimental results of the UD CF/PPS composite. B-K criterion (left) and Power Law criterion (right).

The numerical simulations demonstrate a clear relationship between the increase in mandrel radius and the corresponding increase in fracture toughness, which aligns with experimental findings. Notably, when applying the B-K criterion with a value of $\eta = 1.5$, the simulated fracture toughness reveals a satisfactory agreement with reasonable accuracy. However, simulations using a criterion value of $\eta = 2$ underestimate the fracture toughness, leading to conservative estimations for the GF/PP composite (Figure 8.2 - left). Conversely, the simulated results obtained using the Power law criterion fail to predict the peel behavior effectively (Figure 8.2 - right). This ineffectiveness was further evident during the curve fitting process, as it failed to produce satisfactory fits.

With the CF/PPS composites, implementing numerical simulations using the B-K criterion

at a value of $\eta = 1.5$ produces fracture toughness results that are reasonably approximated (Figure 8.3 - left). However, when the value of the criterion is set to $\eta = 1$, an overprediction in the simulated fracture toughness values is observed. It is worth noting that numerical simulations using the Power criterion at values of $\beta = 1.5$ and 2 yield similar fracture toughness values, indicating a good estimation (Figure 8.3 - right). Moreover, the similarity in the fracture toughness obtained for different Power Law fitting parameters also holds true for the GF/PP material.

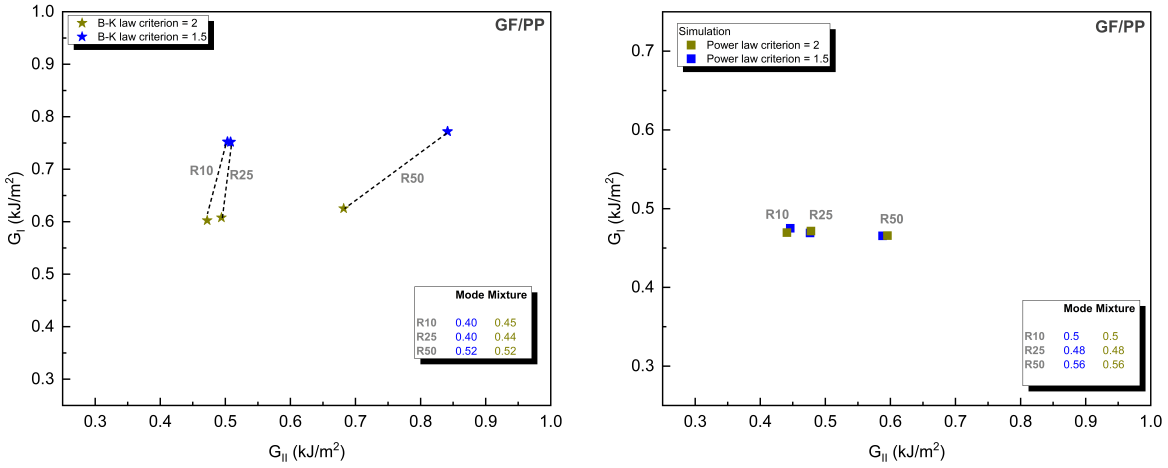


Figure 8.4: Simulated fracture toughness represented as Mode II vs. Mode I for UD GF/PP peel tests indicating the mode mixity: B-K criterion (left) and Power Law criterion (right).

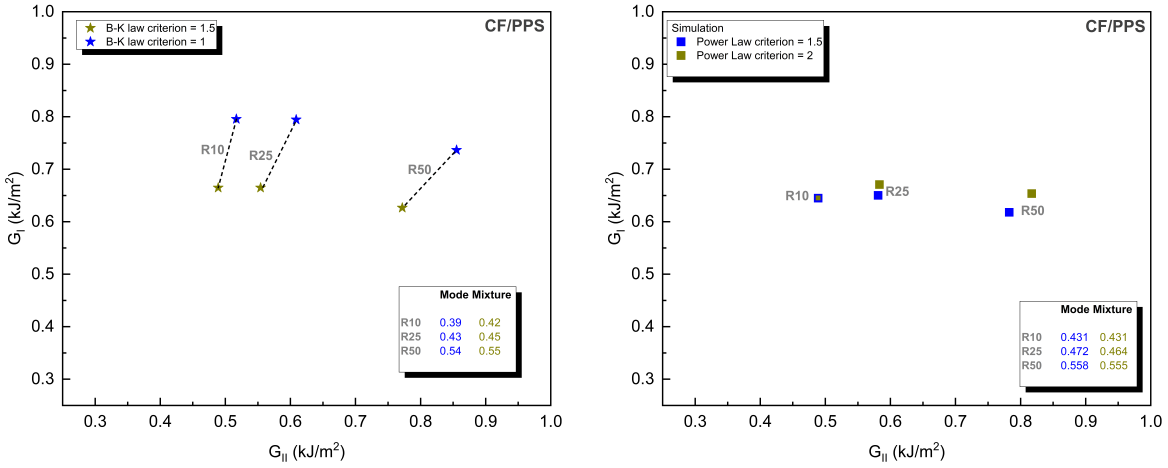


Figure 8.5: Simulated fracture toughness represented as Mode II vs. Mode I for UD CF/PPS peel tests indicating the mode mixity: B-K criterion (left) and Power Law criterion (right).

The results obtained from numerical simulations provide clear illustrations of the relationship between the radius of the mandrel and the associated changes in the peel front angle, consequently leading to the dominance of mode II. Specifically, as the mandrel radius increases, a decrease in the peel front angle is observed, indicating the transition toward mode II domination.

Furthermore, the findings of this study demonstrate that the degree of mode mixture increases with larger mandrel radii (Figure **8.4** and **8.5**). In instances where the mandrel radius is relatively small, mode I exhibit a significantly higher level of dominance. Conversely, mode II becomes highly dominant when the mandrel radius is large. Interestingly, the simulation results obtained using the Power law criterion exhibit consistent mode ratio values for each mandrel radius, regardless of the fitting parameter employed. On the other hand, employing the B-K law for the mode-partitioning approach reveals minor variations in the mode ratios when different fitting parameters are utilized.

Generating fracture toughness data with a significant dominance of mode II (mode ratio $>$ 0.7) poses practical challenges that must be acknowledged. From an experimental standpoint, achieving such a high mode ratio fracture toughness through the Mandrel Peel test is not feasible. A mandrel roller with an exceedingly large radius is necessary to generate a local peel angle of 0 at the crack tip, which, in turn, would lead to the failure of the peeling arm based on the principles of peel mechanics. Therefore, using the aforementioned method, it is impossible to experimentally obtain mixed-mode fracture toughness data with a mode ratio exceeding 0.7. Alternatively, one potential approach involves conducting experiments to generate mixed-mode data with mode ratios below 0.7. Additionally, numerical simulations could be employed to investigate the effects of larger radii on the fracture toughness data. Such an approach holds promise as a viable option for acquiring relevant information in the absence of experimentally feasible high mode II dominance conditions.

In summary, the numerical simulations consistently support the conclusion that the radius of the mandrel plays a pivotal role in determining the peel front angle and the mode of fracture, with mode II becoming increasingly dominant as the mandrel radius increases. Conversely, mode I exhibit higher dominance when the mandrel radius is relatively small.

Chapter 9

Conclusions and Recommendations

The objectives of this thesis were to investigate and gain insights into the sensitivity of specimen configuration and testing parameters on different thermoplastic materials systems and evaluate the suitability of the Mandrel Peel test method for establishing a relationship between mandrel roller size and mixed mode fracture behavior. A comparative assessment was also conducted between the multi-mandrel radii peel test and the standardized DCB, ENF, and MMB tests. The intention was to establish a correlation between the fracture energy observed during the mandrel peel tests and the fracture toughness obtained from DCB (Double Cantilever Beam), ENF (End-Notched Flexure), and MMB (Mixed-Mode Bending) standardized tests conducted on the same material system. The experimental tests on UD GF/PP and UD CF/PPS composites were performed, along with subsequent extensive qualitative fractography-based studies and a numerical approach to gain further insights and understand the mode components of the energy release rate in the mandrel peel tests and address the research questions. The findings and conclusions of this research are presented in this chapter.

Effect of Peel arm Thickness

The propagation fracture toughness data between 1-ply and 2-ply (UD GF/PP and UD CF/PPS) peel arm specimens reveals that the average fracture toughness values are generally higher for the two-ply specimens with better consistency and less variability than the one-ply specimens. This is attributed to the microstructure of the ply and its influence on the associated damage mechanism and fracture propagation behavior.

As the mandrel peel test deals with the characterization of the interlaminar (composites) or interfacial fracture toughness at a ply level, the thickness of the ply influences the delamination propagation behavior due to the microstructural uniformity. In general, thicker plies exhibit a non-uniform distribution of fibers and matrix, resulting in the formation of fiber-rich regions, which lead to the development of fiber bundles that bridge the crack faces in the case of a unidirectional interface. This heterogeneity especially in 1-ply peel arm specimens. results in crack migration and is more likely toward the peel arm. In 2-ply thick peel arm specimens, the increase in thickness results in a more even distribution of stress in the region in front of the crack tip. This leads to a larger crack bridging zone near the crack tip, thereby increasing

toughness during propagation. The increase in toughness can be attributed to various factors, such as enhanced plastic resin deformation, increased fiber breaking, and fiber pull-out.

Effect of Mandrel Roller Size

The results of the experimental investigation indicate that the average fracture toughness values of UD GF/PP and UD CF/PPS with 0|0 interface exhibit an increase as the mandrel radius increases. This conclusion is more meaningful when the fracture toughness data of mandrel radius R75 and R100 are excluded, as it was affected by slight non-conformity issues. The UD GF/PP with 0|90 interface configuration also shows a similar increase in fracture toughness. It should also be mentioned that the fracture toughness of CF/PPS peel specimens with a 0|90 interface showed limited variation with respect to the mandrel radius. This observation may be attributed to the comparable range of pure mode I and mode II fracture toughness at the 0|90 interface, where the fracture toughness of mode I (G_{IC}) could be speculated to be approximately equal to that of mode II (G_{IIC}). However, to establish a more solid rationale, additional numerical investigations are necessary in order to substantiate this explanation. Furthermore, it is important to acknowledge that the relationship between mandrel radius and fracture toughness may not follow a linear pattern, and the specific trend observed can vary depending on the material under investigation and the fracture energy at pure loading modes. Moreover, the study suggests that the influence of mandrel radius on the fracture toughness behavior depends on factors, such as material thickness and interface orientation.

Comparative assessment between Standardized Tests and Mandrel Peel Test

- In the standard tests (DCB, MMB and ENF), an increase in mode mixture showed an increase in fracture toughness values. A similar trend is observed in the mandrel peel tests when the mandrel roller radii are increased. The **fractography analysis** conducted in this study has provided valuable insights into the fracture behavior of the tested materials. The behavior of the mandrel peel specimens with varying mandrel radii reveals distinct failure modes. A strong correlation has been identified between the fracture aspects observed in the mixed mode tests and the mandrel peel tests, performed with different mandrel radii for both material systems. The fractography based findings highlight the importance of considering mixed-mode fracture behavior and the influence of mandrel radius when analyzing the failure characteristics of materials. The combination of fractography analysis and multi-mandrel peel tests offers a comprehensive approach to studying fracture behavior under mixed-mode loading conditions.

- From the **crack front** perspective, the findings of this study reinforce the fact that during the mandrel peel test, the delamination front remains relatively straight, regardless of the stacking sequence and interface configuration. This observation aligns with the anticipated behavior of the mandrel peel test, wherein the kinematics of both the mandrel and the specimen plays a crucial role. The mandrel effectively controls the position of the crack tip during the propagation and enables maintaining a straight crack growth front. As a result, a more uniform distribution of strain energy across the specimen's width is achieved, distinguishing it from standard tests. This advantageous characteristic highlights the potential benefits of utilizing the mandrel peel test in delamination studies.

- The aspect worthy of attention is that the utilization of multiple mandrel radii in assessing the mixed-mode fracture toughness of a particular material system offers the possibility of extrapolating pure mode I and II fracture toughness values from the obtained mixed-mode data. The failure envelope developed based on the mandrel peel tests with various mandrel rollers in this work significantly validates this claim. It is shown in this study that the fracture toughness obtained with a small mandrel radius (R10) closely aligns with the propagation fracture toughness derived from mode I DCB tests for both UD GF/PP and UD CF/PPS indicating a solid consistency. This approach presents a viable tool for characterizing composites' pure mode I and mode II fracture energy with non-zero oriented interfaces that cannot be effectively assessed using classical tests. By considering these findings, further advancements can be made in understanding and characterizing fracture properties in hybrid material systems.
- It is essential to note that the practical feasibility of generating mixed-mode fracture toughness with high dominance of mode II (mode ratio > 0.7) is limited. Experimental realization of fracture toughness data with a high mode ratio using the Mandrel Peel test would require a mandrel roller of a large radius to achieve a local peel angle of 0^o at the crack tip. This, however, would result in peeling arm failure based on the principles of peel mechanics. In such cases, it is shown that numerical simulations could be employed to investigate the effects of larger radii on the fracture toughness data. Such an approach holds promise as a viable option for acquiring relevant information in the absence of experimentally feasible high mode II dominance conditions.

The present study's hypothesis stated that an increase in mandrel roller size would lead to changes in the degree of mode-mixity, and the findings presented herein provide substantial evidence to support this claim. Specifically, a clear and well-established relationship between mandrel roller size and mixed-mode fracture behavior is demonstrated from both fractography and numerical fea-based mode-partitioning approach. These findings not only strengthen the validity of the hypothesis but also emphasizes the significance of considering mandrel size when assessing mode-mixity in fracture phenomena.

Finally, this work shows that utilizing the **multi-mandrel concept** with both experimental and numerical approaches is an important and promising method for predicting material systems' pure-mode I and II fracture toughness by extrapolating the mixed-mode fracture data. This approach proves particularly useful for assessing the interfacial behavior of hybrid material systems that cannot be evaluated using traditional test methods. Consequently, this research in this master thesis opens avenues for further exploration in this area of investigation.

References

[1] D. Svensson, "Experimental methods to determine model parameters for failure modes of cfrp," 2013.

[2] Y. Hu, Y. Zhang, X. Fu, G. Hao, and W. Jiang, "Mechanical properties of ti/cf/pmr polyimide fiber metal laminates with various layup configurations," *Composite structures*, vol. 229, p. 111408, 2019.

[3] I. Raju and T. O'brien, "Fracture mechanics concepts, stress fields, strain energy release rates, delamination initiation and growth criteria," in *Delamination behaviour of composites*, pp. 3–27, Elsevier, 2008.

[4] G. Frossard, "Fracture of thin-ply composites effects of ply thickness," *PhD thesis*, vol. 8032, p. 188, 2017.

[5] M. Laffan, "Testing the toughness of polymer matrix composites," in *Failure Mechanisms in Polymer Matrix Composites*, pp. 110–128, Elsevier, 2012.

[6] T. L. Anderson, *Fracture mechanics: fundamentals and applications*. CRC press, 2017.

[7] E. S. Greenhalgh, "Characterisation of Mixed-Mode Delamination Growth in Carbon-Fibre Composites," no. August, pp. –, 1998.

[8] R. Khan, "Delamination growth in composites under fatigue loading," 2013.

[9] Y. Zhou, Y. Xiao, Q. Wu, and Y. Xue, "A multi-state progressive cohesive law for the prediction of unstable propagation and arrest of mode-i delamination cracks in composite laminates," *Engineering Fracture Mechanics*, vol. 248, p. 107684, 2021.

[10] F. Sacchetti, W. J. Grouve, L. L. Warnet, and I. F. Villegas, "Effect of resin-rich bond line thickness and fibre migration on the toughness of unidirectional Carbon/PEEK joints," *Composites Part A: Applied Science and Manufacturing*, vol. 109, no. February, pp. 197–206, 2018.

[11] W. S. Johnson and P. Mangalgiri, "Investigation of fiber bridging in double cantilever beam specimens.," tech. rep., NATIONAL AERONAUTICS AND SPACE ADMINISTRATION HAMPTON VA LANGLEY RESEARCH ..., 1986.

[12] E. Zile and V. Tamuzs, "Mode ii delamination of a unidirectional carbon fiber/epoxy composite in four-point bend end-notched flexure tests," *Mechanics of composite materials*, vol. 41, pp. 383–390, 2005.

[13] M. May, "Measuring the rate-dependent mode i fracture toughness of composites–a review," *Composites Part A: Applied Science and Manufacturing*, vol. 81, pp. 1–12, 2016.

[14] W. X. Wang, M. Nakata, Y. Takao, and T. Matsubara, "Experimental investigation on test methods for mode II interlaminar fracture testing of carbon fiber reinforced composites," *Composites Part A: Applied Science and Manufacturing*, vol. 40, no. 9, pp. 1447–1455, 2009.

[15] W. J. B. Grouve, L. Warnet, B. Rietman, and R. Akkerman, "On the weld strength of in situ tape placed reinforcements on weave reinforced structures," *Composites Part A: Applied Science and Manufacturing*, vol. 43, no. 9, pp. 1530–1536, 2012.

[16] P. Davies, G. D. Sims, B. R. K. Blackman, a. J. Brunner, K. Kageyama, M. Hojo, K. Tanaka, G. Murri, C. Rousseau, B. Gieseke, and R. H. Martin, "Comparison of test configurations for the determination of G_{IIC}: Results from an international round robin," *Plastics, Rubber and Composites*, vol. 28, no. September, pp. 432–437, 1999.

[17] F. Caimmi, R. Frassine, and A. Pavan, "A new jig for mode ii interlaminar fracture testing of composite materials under quasi-static and moderately high rates of loading," *Engineering fracture mechanics*, vol. 73, no. 16, pp. 2277–2291, 2006.

[18] M. R. Eplett, *Experimental methods for the study of mixed-mode fractures*. PhD thesis, Loughborough University, 2017.

[19] C. Fan, P.-Y. B. Jar, and J.-J. R. Cheng, "Internal-notched flexure test for measurement of mode ii delamination resistance of fibre-reinforced polymers," *Journal of Composites*, vol. 2013, 2013.

[20] R. Krueger, "A summary of benchmark examples to assess the performance of quasi-static delamination propagation prediction capabilities in finite element codes," *Journal of Composite Materials*, vol. 49, no. 26, pp. 3297–3316, 2015.

[21] B. D. Davidson, R. D. Bialaszewski, and S. S. Sainath, "A non-classical, energy release rate based approach for predicting delamination growth in graphite reinforced laminated polymeric composites," *Composites science and technology*, vol. 66, no. 10, pp. 1479–1496, 2006.

[22] J. Reis, M. de Moura, R. Moreira, and F. Silva, "Mixed mode i+ ii interlaminar fracture characterization of carbon-fibre reinforced polyamide composite using the single-leg bending test," *Materials Today Communications*, vol. 19, pp. 476–481, 2019.

[23] Z. Jiang, S. Wan, Z. Zhong, S. Li, and K. Shen, "Effect of curved delamination front on mode-i fracture toughness of adhesively bonded joints," *Engineering Fracture Mechanics*, vol. 138, pp. 73–91, 2015.

[24] D. A. Dillard, H. K. Singh, D. J. Pohlit, and J. M. Starbuck, "Observations of decreased fracture toughness for mixed mode fracture testing of adhesively bonded joints," *Journal of Adhesion Science and Technology*, vol. 23, no. 10-11, pp. 1515–1530, 2009.

[25] M. D. Bartlett, S. W. Case, A. J. Kinloch, and D. A. Dillard, "Peel tests for quantifying adhesion and toughness: A review," *Progress in Materials Science*, p. 101086, 2023.

[26] A. Rudawska, *Surface treatment in bonding technology*. Academic Press, 2019.

[27] J. Cañas, L. Távara, A. Blázquez, A. Estefani, and G. Santacruz, "A new in situ peeling test for the characterisation of composite bonded joints," *Composites Part A: Applied Science and Manufacturing*, vol. 113, pp. 298–310, 2018.

[28] F. Daghia, C. Cluzel, L. Hébrard, F. Churlaud, and B. Courtemanche, "The double drum peel (ddp) test: a new concept to evaluate the delamination fracture toughness of cylindrical laminates," *Composites Part A: Applied Science and Manufacturing*, vol. 113, pp. 83–94, 2018.

[29] A. Kapshammer, M. C. Miron, L. Dangl, and Z. Major, "Interface characterization of consolidated ppgf tapes on ppgf mat material," *Polymers*, vol. 15, no. 4, p. 935, 2023.

[30] F. Sacchetti, W. J. Grouve, L. L. Warnet, and I. F. Villegas, "Woven fabric composites: Can we peel it?," *Procedia Structural Integrity*, vol. 2, pp. 245–252, 2016.

[31] L. N. Grafen and W. J. B. Grouve, "On the applicability of the mandrel peel test to characterize the fracture toughness of non-symmetric interfaces," 2020.

[32] L. F. Kawashita, A. J. Kinloch, D. R. Moore, and J. G. Williams, "The influence of bond line thickness and peel arm thickness on adhesive fracture toughness of rubber toughened epoxy-aluminium alloy laminates," *International Journal of Adhesion and Adhesives*, vol. 28, no. 4-5, pp. 199–210, 2008.

[33] L. Kawashita, A. Kinloch, D. Moore, and J. Williams, "A critical investigation of the use of a mandrel peel method for the determination of adhesive fracture toughness of metal-polymer laminates," *Engineering fracture mechanics*, vol. 73, no. 16, pp. 2304–2323, 2006.

[34] F. Sacchetti, W. J. Grouve, L. L. Warnet, and I. F. Villegas, "Interlaminar fracture toughness of 5hs carbon/peek laminates. a comparison between dcb, els and mandrel peel tests," *Polymer testing*, vol. 66, pp. 13–23, 2018.

[35] Y. Su, M. De Rooij, W. Grouve, and L. Warnet, "Characterisation of metal-thermoplastic composite hybrid joints by means of a mandrel peel test," *Composites Part B: Engineering*, vol. 95, pp. 293–300, 2016.

[36] W. J. B. Grouve, L. Warnet, and R. Akkerman, "Critical assessment of the mandrel peel test for fiber reinforced thermoplastic laminates," *Engineering fracture mechanics*, vol. 101, pp. 96–108, 2013.

[37] R. Krueger, "Virtual crack closure technique: History, approach, and applications," *Applied Mechanics Reviews*, vol. 57, no. 1-6, pp. 109–143, 2004.

[38] A. Turon, P. P. Camanho, J. Costa, and C. Dávila, "A damage model for the simulation of delamination in advanced composites under variable-mode loading," *Mechanics of materials*, vol. 38, no. 11, pp. 1072–1089, 2006.

[39] F. Perrin, M. N. Bureau, J. Denault, and J. I. Dickson, "Mode I interlaminar crack propagation in continuous glass fiber/polypropylene composites: Temperature and molding condition dependence," *Composites Science and Technology*, vol. 63, no. 5, pp. 597–607, 2003.

[40] P. Davies and W. J. Cantwell, "Fracture of glass/polypropylene laminates: influence of cooling rate after moulding," *Composites*, vol. 25, no. 9, pp. 869–877, 1994.

[41] G. Reyes V. and W. J. Cantwell, "The mechanical properties of fibre-metal laminates based on glass fibre reinforced polypropylene," *Composites Science and Technology*, vol. 60, no. 7, pp. 1085–1094, 2000.

[42] I. G. Lee, D. H. Kim, K. H. Jung, H. J. Kim, and H. S. Kim, "Effect of the cooling rate on the mechanical properties of glass fiber reinforced thermoplastic composites," *Composite Structures*, vol. 177, pp. 28–37, 2017.

[43] K. H. Jung, D. H. Kim, H. J. Kim, S. H. Park, K. Y. Jhang, and H. S. Kim, "Finite element analysis of a low-velocity impact test for glass fiber-reinforced polypropylene composites considering mixed-mode interlaminar fracture toughness," *Composite Structures*, vol. 160, pp. 446–456, 2017.

[44] M. N. Bureau, J. Denault, and J. I. Dickson, "Effect of the molding conditions on mode II interlaminar crack propagation in continuous glass fiber/polypropylene composites," *Journal of Thermoplastic Composite Materials*, vol. 14, no. 5, pp. 374–403, 2001.

[45] M. Bureau, J. Denault, F. Perrin, and J. Dickson, *Crack Propagation in Continuous Glass Fiber/Polypropylene Composites: Matrix Microstructure Effect.* Plastics Design Library, 2001.

[46] S. Oshima, R. Higuchi, M. Kato, S. Minakuchi, T. Yokozeki, and T. Aoki, "Cooling rate-dependent mechanical properties of polyphenylene sulfide (PPS) and carbon fiber reinforced PPS (CF/PPS)," *Composites Part A: Applied Science and Manufacturing*, vol. 164, no. September 2022, p. 107250, 2023.

[47] Y. Nakagawa, S. Oda, N. Uda, Y. Shinmoto, H. Nagai, Y. Ono, and S. Takeda, "Effect of forming cooling rate on mode i and ii interlaminar fracture properties of cf/pps thermoplastic composites," *Journal of the Japan Society for Composite Materials*, vol. 45, no. 6, pp. 242–250, 2019.

[48] D. Zhao, T. Li, H. Zhang, W. Liu, G. Yue, and L. Pan, "Effect of the cooling rate on the fracture toughness of carbon fiber reinforced thermoplastic composites," *Journal of Thermoplastic Composite Materials*, vol. 0, no. 2999, pp. 1–14, 2022.

[49] T. E. Tay, "Characterization and analysis of delamination fracture in composites: An overview of developments from 1990 to 2001," *Applied Mechanics Reviews*, vol. 56, no. 1, pp. 1–31, 2003.

[50] S. Heimbs, "Bird strike simulations on composite aircraft structures," in *SIMULIA Customer Conference, Barcelona*, pp. 73–86, 2011.

[51] ASTM D5528-01, "Standard test method for mode I interlaminar fracture toughness of unidirectional fiber-reinforced polymer matrix composites," *American Standard of Testing Methods*, vol. 03, no. Reapproved 2007, pp. 1–12, 2014.

[52] ASTM D7905, "Standard test method for determination of the mode II interlaminar fracture toughness of unidirectional fiber-reinforced polymer matrix composites," *Astm*, pp. 1–18, 2014.

[53] A. D6671M, "Standard Test Method for Mixed Mode I-Mode II Interlaminar Fracture Toughness of Unidirectional Fiber Reinforced Polymer Matrix Composites," *ASTM International*, vol. i, no. Mode I, p. 15, 2006.

[54] M. Laffan, S. Pinho, P. Robinson, and A. McMillan, "Translaminar fracture toughness testing of composites: A review," *Polymer testing*, vol. 31, no. 3, pp. 481–489, 2012.

[55] J. Williams, "On the calculation of energy release rates for cracked laminates," *International Journal of Fracture*, vol. 36, pp. 101–119, 1988.

[56] S. Hashemi, A. Kinloch, and J. Williams, "The effects of geometry, rate and temperature on the mode i, mode ii and mixed-mode i/ii interlaminar fracture of carbon-fibre/poly (ether-ether ketone) composites," *Journal of Composite Materials*, vol. 24, no. 9, pp. 918–956, 1990.

[57] M. Charalambides, A. J. Kinloch, Y. Wang, and J. G. Williams, "On the analysis of mixed-mode failure," *International Journal of Fracture*, vol. 54, no. 3, pp. 269–291, 1992.

[58] S. Hashemi, A. J. Kinloch, and J. Williams, "The analysis of interlaminar fracture in uniaxial fibre-polymer composites," *Proceedings of the Royal Society of London. A. Mathematical and Physical Sciences*, vol. 427, no. 1872, pp. 173–199, 1990.

[59] N. Blanco Villaverde *et al.*, *Variable mixed-mode delamination in composite laminates under fatigue conditions: testing & analysis*. Universitat de Girona, 2005.

[60] D. Purslow, "Matrix fractography of fibre-reinforced epoxy composites," *Composites*, vol. 17, no. 4, pp. 289–303, 1986.

[61] X. Gong, A. Hurez, and G. Verchery, "On the determination of delamination toughness by using multidirectional dcb specimens," *Polymer testing*, vol. 29, no. 6, pp. 658–666, 2010.

[62] M. B. M. Rehan, J. Rousseau, S. Fontaine, and X. Gong, "Experimental study of the influence of ply orientation on dcb mode-i delamination behavior by using multidirectional fully isotropic carbon/epoxy laminates," *Composite Structures*, vol. 161, pp. 1–7, 2017.

[63] M. Hojo, T. Ando, M. Tanaka, T. Adachi, S. Ochiai, and Y. Endo, "Modes i and ii interlaminar fracture toughness and fatigue delamination of cf/epoxy laminates with self-same epoxy interleaf," *International journal of fatigue*, vol. 28, no. 10, pp. 1154–1165, 2006.

[64] P. Davidson and A. M. Waas, "Non-smooth mode i fracture of fibre-reinforced composites: an experimental, numerical and analytical study," *Philosophical Transactions of the Royal Society A: Mathematical, Physical and Engineering Sciences*, vol. 370, no. 1965, pp. 1942–1965, 2012.

[65] F. Ozdil and L. Carlsson, "Plastic zone estimates in mode i interlaminar fracture of interleaved composites," *Engineering Fracture Mechanics*, vol. 41, no. 5, pp. 645–658, 1992.

[66] A. Aksoy and L. Carlsson, "Crack tip yield zone estimates in mode ii interlaminar fracture of interleaved composites," *Engineering fracture mechanics*, vol. 39, no. 3, pp. 525–534, 1991.

[67] M. Salviato, K. Kirane, Z. P. Baant, and G. Cusatis, "Mode i and II Interlaminar Fracture in Laminated Composites: A Size Effect Study," *Journal of Applied Mechanics, Transactions ASME*, vol. 86, no. 9, 2019.

[68] S. Heide-Jørgensen and M. K. Budzik, "Crack growth along heterogeneous interface during the dcb experiment," *International Journal of Solids and Structures*, vol. 120, pp. 278–291, 2017.

[69] S. Heide-Jørgensen, S. T. de Freitas, and M. K. Budzik, "On the fracture behaviour of cfrp bonded joints under mode i loading: Effect of supporting carrier and interface contamination," *Composites Science and Technology*, vol. 160, pp. 97–110, 2018.

[70] D. Purslow, "Matrix fractography of fibre-reinforced thermoplastics, part 1. peel failures," *Composites*, vol. 18, no. 5, pp. 365–374, 1987.

[71] D. Purslow, "Matrix fractography of fibre-reinforced thermoplastics, part 2. shear failures," *Composites*, vol. 19, no. 2, pp. 115–126, 1988.

[72] D. Nicholls and J. Gallagher, "Determination of gic in angle ply composites using a cantilever beam test method," *Journal of Reinforced Plastics and Composites*, vol. 2, no. 1, pp. 2–17, 1983.

[73] R. Khan, "Fiber bridging in composite laminates: A literature review," *Composite Structures*, vol. 229, no. July, 2019.

[74] W. L. Bradley and R. N. Cohen, *Matrix deformation and fracture in graphite-reinforced epoxies*. ASTM International, 1985.

[75] A. B. Pereira and A. B. de Morais, "Mode I interlaminar fracture of carbon/epoxy multidirectional laminates," *Composites Science and Technology*, vol. 64, no. 13-14, pp. 2261–2270, 2004.

[76] M. De Moura, R. D. Campilho, A. Amaro, and P. Reis, "Interlaminar and intralaminar fracture characterization of composites under mode i loading," *Composite Structures*, vol. 92, no. 1, pp. 144–149, 2010.

[77] P. Davies, P. Casari, and L. Carlsson, "Influence of fibre volume fraction on mode ii interlaminar fracture toughness of glass/epoxy using the 4enf specimen," *Composites Science and Technology*, vol. 65, no. 2, pp. 295–300, 2005.

[78] A. A. Griffith, "Vi. the phenomena of rupture and flow in solids," *Philosophical transactions of the royal society of london. Series A, containing papers of a mathematical or physical character*, vol. 221, no. 582-593, pp. 163–198, 1921.

[79] G. R. Irwin, "Analysis of stresses and strains near the end of a crack traversing a plate," 1957.

[80] M. F. Kanninen, A. McEvily, and C. H. Popelar, "Advanced fracture mechanics," 1986.

[81] G. R. Irwin and J. Kies, "Critical energy rate analysis of fracture strength," *Spie Milestone series MS*, vol. 137, pp. 136–141, 1954.

[82] P. Hine, B. Brew, R. Duckett, and I. Ward, "Failure mechanisms in carbon-fibre-reinforced poly (ether sulphone)," *Composites science and technology*, vol. 43, no. 1, pp. 37–47, 1992.

[83] K. D. Cowley and P. W. Beaumont, "The interlaminar and intralaminar fracture toughness of carbon-fibre/polymer composites: The effect of temperature," *Composites science and technology*, vol. 57, no. 11, pp. 1433–1444, 1997.

[84] I. 15024, *Fibre-reinforced plastic composites—Determination of mode I interlaminar fracture toughness, GIc, for unidirectionally reinforced materials.* International Organization for Standardization Geneva, Switzerland, 2001.

[85] A. J. Brunner, B. R. Blackman, and P. Davies, "A status report on delamination resistance testing of polymer-matrix composites," *Engineering Fracture Mechanics*, vol. 75, no. 9, pp. 2779–2794, 2008.

[86] L. A. Carlsson, J. W. Gillespie, and R. B. Pipes, "On the Analysis and Design of the End Notched Flexure (ENF) Specimen for Mode II Testing," *Journal of Composite Materials*, vol. 20, no. 6, pp. 594–604, 1986.

[87] L. Carlsson, J. Gillespie, and B. Trethewey, "Mode ii interlaminar fracture of graphite/epoxy and graphite/peek," *Journal of Reinforced Plastics and Composites*, vol. 5, no. 3, pp. 170–187, 1986.

[88] C. Bouvet, J. Serra, and P. G. Perez, "Strain rate effect of mode ii interlaminar fracture toughness on the impact response of a thermoplastic peek composite," *Composites Part C: Open Access*, vol. 2, p. 100031, 2020.

[89] M. J. Mathews and S. R. Swanson, "Characterization of the interlaminar fracture toughness of a laminated carbon/epoxy composite," *Composites science and technology*, vol. 67, no. 7-8, pp. 1489–1498, 2007.

[90] P. S. Vanderkley, *Mode I-mode II delamination fractrue toughness of a unidirectional graphite/epoxy composite*. PhD thesis, Texas A&M University, 1981.

[91] I. 15114, "Fibre-reinforced plastic composites—determination of the mode ii fracture resistance for unidirectionally reinforced materials using the calibrated end-loaded split (c-els) test and an effective crack length approach," 2014.

[92] R. H. Martin, "Interlaminar fracture characterization: a current review," 1991.

[93] H. Wang and T. Vu-Khanh, "Use of end-loaded-split (els) test to study stable fracture behaviour of composites under mode ii loading," *Composite structures*, vol. 36, no. 1-2, pp. 71–79, 1996.

[94] K. Kageyama, M. Kikuchi, and N. Yanagisawa, "Stabilized end notched flexure test-characterization of mode ii interlaminar crack growth," *Composite Materials: Fatigue and Fracture. Vol. 3*, vol. 3, pp. 210–225, 1991.

[95] B. Blackman, A. Brunner, and J. Williams, "Mode ii fracture testing of composites: a new look at an old problem," *Engineering fracture mechanics*, vol. 73, no. 16, pp. 2443–2455, 2006.

[96] R. Martin and B. Davidson, "Mode ii fracture toughness evaluation using four point bend, end notched flexure test," *Plastics, Rubber and Composites*, vol. 28, no. 8, pp. 401–406, 1999.

[97] K. Tanaka, T. Yuasa, and K. Katsura, "Continuous mode ii interlaminar fracture toughness measurement by over notched flexure test," in *4 th European Conference on Composites: Testing and Standardisation*, pp. 171–179, 1998.

[98] F.-G. Buchnolz, R. Rikards, and H. Wang, "Computation analysis of interlaminar fracture of laminated composites," *International journal of fracture*, vol. 86, pp. 37–57, 1997.

[99] J. H. Crews Jr and J. R. Reeder, "A mixed-mode bending apparatus for delamination testing," tech. rep., 1988.

[100] A. De Morais and A. Pereira, "Application of the effective crack method to mode i and mode ii interlaminar fracture of carbon/epoxy unidirectional laminates," *Composites Part A: Applied Science and Manufacturing*, vol. 38, no. 3, pp. 785–794, 2007.

[101] C. Schuecker and B. D. Davidson, "Evaluation of the accuracy of the four-point bend end-notched flexure test for mode ii delamination toughness determination," *Composites Science and Technology*, vol. 60, no. 11, pp. 2137–2146, 2000.

[102] B. D. Davidson and X. Sun, "Effects of friction, geometry, and fixture compliance on the perceived toughness from three-and four-point bend end-notched flexure tests," *Journal of reinforced plastics and composites*, vol. 24, no. 15, pp. 1611–1628, 2005.

[103] X. Sun and B. D. Davidson, "Numerical evaluation of the effects of friction and geometric nonlinearities on the energy release rate in three-and four-point bend end-notched flexure tests," *Engineering fracture mechanics*, vol. 73, no. 10, pp. 1343–1361, 2006.

[104] A. Szekrényes and J. Uj, "Mode-ii fracture in e-glass-polyester composite," *Journal of Composite Materials*, vol. 39, no. 19, pp. 1747–1768, 2005.

[105] J. R. Reeder and J. Crews Jr, "Nonlinear analysis and redesign of the mixed-mode bending delamination test," tech. rep., 1991.

[106] S. Hashemi, A. Kinloch, and G. Williams, "Mixed-mode fracture in fiber-polymer composite laminates," *ASTM Special Technical Publication*, no. 1110, pp. 143–168, 1991.

[107] B. Davidson and V. Sundararaman, "A single leg bending test for interfacial fracture toughness determination," *International Journal of Fracture*, vol. 78, pp. 193–210, 1996.

[108] P. Davies, B. Blackman, and A. Brunner, "Standard test methods for delamination resistance of composite materials: current status," *Applied composite materials*, vol. 5, pp. 345–364, 1998.

[109] C. Sun and S. Zheng, "Delamination characteristics of double-cantilever beam and end-notched flexure composite specimens," *Composites Science and Technology*, vol. 56, no. 4, pp. 451–459, 1996.

[110] B. Davidson, R. Krüger, and M. König, "Three-dimensional analysis of center-delaminated unidirectional and multidirectional single-leg bending specimens," *Composites Science and Technology*, vol. 54, no. 4, pp. 385–394, 1995.

[111] T. Sebaey, N. Blanco, C. Lopes, and J. Costa, "Numerical investigation to prevent crack jumping in double cantilever beam tests of multidirectional composite laminates," *Composites Science and Technology*, vol. 71, no. 13, pp. 1587–1592, 2011.

[112] B. F. Sørensen and T. K. Jacobsen, "Large-scale bridging in composites: R-curves and bridging laws," *Composites Part A: Applied Science and Manufacturing*, vol. 29, no. 11, pp. 1443–1451, 1998.

[113] P. Davies, M. Benzeggagh, and F. De Charentenay, "Delamination behavior of carbon-fiber-reinforced pps," *SAMPE Q.;(United States)*, vol. 19, no. 1, 1987.

[114] Z. Suo, G. Bao, and B. Fan, "Delamination r-curve phenomena due to damage," *Journal of the Mechanics and Physics of Solids*, vol. 40, no. 1, pp. 1–16, 1992.

[115] E. Farmand-Ashtiani, J. Cugnoni, and J. Botsis, "Specimen thickness dependence of large scale fiber bridging in mode i interlaminar fracture of carbon epoxy composite," *International Journal of Solids and Structures*, vol. 55, pp. 58–65, 2015.

[116] M. Shokrieh, M. Heidari-Rarani, and M. Ayatollahi, "Delamination r-curve as a material property of unidirectional glass/epoxy composites," *Materials & Design*, vol. 34, pp. 211–218, 2012.

[117] C. Blondeau, G. Pappas, and J. Botsis, "Influence of ply-angle on fracture in anti-symmetric interfaces of cfrp laminates," *Composite Structures*, vol. 216, pp. 464–476, 2019.

[118] J. Schoen, T. Nyman, A. Blom, and H. Ansell, "A numerical and experimental investigation of delamination behaviour in the dcb specimen," *Composites Science and Technology*, vol. 60, no. 2, pp. 173–184, 2000.

[119] A. Ramji, Y. Xu, M. Yasaee, M. Grasso, and P. Webb, "Delamination migration in cfrp laminates under mode i loading," *Composites Science and Technology*, vol. 190, p. 108067, 2020.

[120] T. Sebaey, N. Blanco, J. Costa, and C. Lopes, "Characterization of crack propagation in mode i delamination of multidirectional cfrp laminates," *Composites Science and Technology*, vol. 72, no. 11, pp. 1251–1256, 2012.

[121] J. Andersons and M. König, "Dependence of fracture toughness of composite laminates on interface ply orientations and delamination growth direction," *Composites Science and Technology*, vol. 64, no. 13-14, pp. 2139–2152, 2004.

[122] E. S. Greenhalgh, C. Rogers, and P. Robinson, "Fractographic observations on delamination growth and the subsequent migration through the laminate," *Composites Science and Technology*, vol. 69, no. 14, pp. 2345–2351, 2009.

[123] A. Pereira and A. De Morais, "Mixed mode i+ ii interlaminar fracture of carbon/epoxy laminates," *Composites Part A: Applied Science and Manufacturing*, vol. 39, no. 2, pp. 322–333, 2008.

[124] Y. Gong, B. Zhang, and S. R. Hallett, "Delamination migration in multidirectional composite laminates under mode i quasi-static and fatigue loading," *Composite structures*, vol. 189, pp. 160–176, 2018.

[125] J. A. Nairn, "Energy release rate analysis for adhesive and laminate double cantilever beam specimens emphasizing the effect of residual stresses," *International Journal of Adhesion and Adhesives*, vol. 20, no. 1, pp. 59–70, 2000.

[126] J. W. Hutchinson *et al.*, "Mixed mode fracture mechanics of interfaces," *Metal-ceramic interfaces*, vol. 1990, pp. 295–306, 1990.

[127] W. Wang, S. T. De Freitas, J. A. Poulis, and D. Zarouchas, "A review of experimental and theoretical fracture characterization of bi-material bonded joints," *Composites Part B: Engineering*, p. 108537, 2020.

[128] ASTM, "Standard test method for peel adhesion of pressure-sensitive tape," 2018.

[129] I. 8510-1, "Adhesives—peel test for a flexible-bonded-to-rigid test specimen assembly—part 1: 90 degree peel," 1990.

[130] A. D903-98, "Standard test method for peel or stripping strength of adhesive bonds," *ASTM International*, 2017.

[131] A. SEkULIC, "Experimental identification of adhesive properties between epoxy and glass," *These de Doctorat de l'Ecole Polytechnique Fédérale de Lausanne*, 2008.

[132] Y. Su, M. de Rooij, W. Grouve, and L. Warnet, "Characterisation of metal–thermoplastic composite hybrid joints by means of a mandrel peel test," *Composites Part B: Engineering*, vol. 95, pp. 293–300, 2016.

[133] A. D1781-98, "Standard test method for climbing drum peel for adhesives," *ASTM international,West Conshohocken, PA: https://www.astm.org/*, 2021.

[134] R. Okada and M. Kortschot, "The role of the resin fillet in the delamination of honeycomb sandwich structures," *Composites Science and Technology*, vol. 62, no. 14, pp. 1811–1819, 2002.

[135] F. Daghia and C. Cluzel, "The climbing drum peel test: An alternative to the double cantilever beam for the determination of fracture toughness of monolithic laminates," *Composites Part A: Applied Science and Manufacturing*, vol. 78, pp. 70–83, 2015.

[136] L. F. Kawashita, D. R. Moore, and J. G. Williams, "Comparison of peel tests for metal-polymer laminates for aerospace applications," *Journal of Adhesion*, vol. 81, no. 6, pp. 561–586, 2005.

[137] S. Michel, F. Hauf, and A. J. Brunner, "Evaluation of a climbing drum laminate peel test to determine the interlaminar mode i fracture toughness of thin cfrp laminates—comparison with the standard mode i dcb test and a mandrel laminate peel test proposed by esis tc4," *Frontiers in Materials*, vol. 10, p. 981647, 2023.

[138] A. T. Nettles, E. D. Gregory, and J. R. Jackson, "Using the climbing drum peel (cdp) test to obtain a gic value for core/face sheet bonds," *Journal of composite materials*, vol. 41, no. 24, pp. 2863–2876, 2007.

[139] D. O. Adams, J. A. Kessler, B. Kuramoto, J. Bluth, C. Weaver, and A. Gill, "Development and evaluation of fracture mechanics test methods for sandwich composites," *Advanced material and structure*, 2012.

[140] L. F. Kawashita, D. R. Moore, and J. G. Williams, "The development of a mandrel peel test for the measurement of adhesive fracture toughness of epoxy-metal laminates," *Journal of Adhesion*, vol. 80, no. 3, pp. 147–167, 2004.

[141] E. Breslauer and T. Troczynski, "Experimental determination of the peel adhesion strength for metallic foils," *Journal of Adhesion Science and Technology*, vol. 12, no. 4, pp. 367–382, 1998.

[142] W. Grouve, L. Warnet, R. Akkerman, S. Wijskamp, and J. Kok, "Weld strength assessment for tape placement," *International journal of material forming*, vol. 3, pp. 707–710, 2010.

[143] Y. Su, M. de Rooij, W. Grouve, and R. Akkerman, "The effect of titanium surface treatment on the interfacial strength of titanium – Thermoplastic composite joints," *International Journal of Adhesion and Adhesives*, vol. 72, no. October 2016, pp. 98–108, 2017.

[144] T. Peters, C. Kukla, H. Janssen, and C. Brecher, "System improvement for laser-based tape placement to directly manufacture metal / thermoplastic composite parts," *ICCM International Conferences on Composite Materials*, vol. 2017-Augus, no. August, pp. 20–25, 2017.

[145] V. M. Marinosci, W. J. Grouve, M. B. de Rooij, S. Wijskamp, and R. Akkerman, "Effect of grit-blasting on the fracture toughness of hybrid titanium-thermoplastic composite joints," *International Journal of Adhesion and Adhesives*, vol. 109, no. May, p. 102893, 2021.

[146] L. F. Kawashita, *The peeling of adhesive joints*. PhD thesis, Imperial College London (University of London), 2006.

[147] L. Kawashita, D. Moore, and J. Williams, "The development of a mandrel peel test for the measurement of adhesive fracture toughness of epoxy–metal laminates," *The Journal of Adhesion*, vol. 80, no. 3, pp. 147–167, 2004.

[148] H. M. Jensen, "Elastic fracture mechanics of the peel-test geometry," *The Journal of Adhesion*, vol. 38, no. 3-4, pp. 185–197, 1992.

[149] M. D. Thouless and Q. D. Yang, "A parametric study of the peel test," *International Journal of Adhesion and Adhesives*, vol. 28, no. 4-5, pp. 176–184, 2008.

[150] L. F. Kawashita, D. R. Moore, and J. G. Williams, "The development of a mandrel peel test for the measurement of adhesive fracture toughness of epoxy-metal laminates," *Journal of Adhesion*, vol. 80, no. 3, pp. 147–167, 2004.

[151] E. M. Wu and R. Reuter Jr, "Crack extension in fiberglass reinforced plastics," tech. rep., ILLINOIS UNIV AT URBANA DEPT OF THEORETICAL AND APPLIED MECHANICS, 1965.

[152] M. L. Benzeggagh and M. Kenane, "Measurement of mixed-mode delamination fracture toughness of unidirectional glass/epoxy composites with mixed-mode bending apparatus," *Composites science and technology*, vol. 56, no. 4, pp. 439–449, 1996.

[153] P. P. Camanho and C. G. Dávila, "Mixed-mode decohesion finite elements for the simulation of delamination in composite materials," tech. rep., 2002.

[154] J. Reeder, "An evaluation of mixed-mode delamination failure criteria," tech. rep., 1992.

[155] J. W. Hutchinson and Z. . Suo, *Mixed Mode Cracking in Layered Materials*, vol. 18. 1978.

[156] M. D. Thouless, "Fracture of a model interface under mixed-mode loading," *Acta Metallurgica et Materialia*, vol. 38, no. 6, pp. 1135–1140, 1990.

[157] M. Thouless and H. Jensen, "Elastic fracture mechanics of the peel-test geometry," *The Journal of Adhesion*, vol. 38, no. 3-4, pp. 185–197, 1992.

[158] R. Schapery and B. Davidson, "Prediction of energy release rate for mixed-mode delamination using classical plate theory," 1990.

[159] C. M. Harvey and S. Wang, "Experimental assessment of mixed-mode partition theories," *Composite Structures*, vol. 94, no. 6, pp. 2057–2067, 2012.

[160] Q. Luo and L. Tong, "Analytic formulas of energy release rates for delamination using a global–local method," *International Journal of Solids and Structures*, vol. 49, no. 23-24, pp. 3335–3344, 2012.

[161] M. Conroy, A. Kinloch, J. Williams, and A. Ivankovic, "Mixed mode partitioning of beam-like geometries: A damage dependent solution," *Engineering Fracture Mechanics*, vol. 149, pp. 351–367, 2015.

[162] P. Tsokanas and T. Loutas, "Fracture mode partitioning: A review," *Available at SSRN 4405085*.

[163] E. F. Rybicki and M. F. Kanninen, "A finite element calculation of stress intensity factors by a modified crack closure integral," *Engineering fracture mechanics*, vol. 9, no. 4, pp. 931–938, 1977.

[164] A. De Morais and A. Pereira, "Mixed mode i+ ii interlaminar fracture of glass/epoxy multidirectional laminates–part 1: Analysis," *Composites science and technology*, vol. 66, no. 13, pp. 1889–1895, 2006.

[165] P. Prombut, L. Michel, F. Lachaud, and J.-J. Barrau, "Delamination of multidirectional composite laminates at $0/\theta$ ply interfaces," *Engineering fracture mechanics*, vol. 73, no. 16, pp. 2427–2442, 2006.

[166] P. S. Valvo, "A revised virtual crack closure technique for physically consistent fracture mode partitioning," *International Journal of Fracture*, vol. 173, pp. 1–20, 2012.

[167] A. Turon, P. P. Camanho, J. Costa, and C. G. Dávila, "An interface damage model for the simulation of delamination under variable-mode ratio in composite materials," tech. rep., 2004.

[168] A. Turon, P. Camanho, J. Costa, and J. Renart, "Accurate simulation of delamination growth under mixed-mode loading using cohesive elements: Definition of interlaminar strengths and elastic stiffness," *Composite structures*, vol. 92, no. 8, pp. 1857–1864, 2010.

[169] L. Ye, "Role of matrix resin in delamination onset and growth in composite laminates," *Composites science and technology*, vol. 33, no. 4, pp. 257–277, 1988.

[170] R. Moreira, M. de Moura, F. Silva, F. Ramírez, and J. Rodrigues, "Mixed-mode i+ ii fracture characterisation of composite bonded joints," *Journal of Adhesion Science and Technology*, vol. 34, no. 13, pp. 1385–1398, 2020.

[171] F. M. Ramírez, M. F. de Moura, R. D. Moreira, and F. G. Silva, "Experimental and numerical mixed-mode i+ ii fracture characterization of carbon fibre reinforced polymer laminates using a novel strategy," *Composite Structures*, vol. 263, p. 113683, 2021.

[172] S. Mudunuru, "Finite Element Model For Interfaces In Compatibilized Polymer Blends: A Comparative Study on the Mixed-Mode Response of Cohesive Zone Models Implemented With Small and Large Displacement Assumptions."

[173] A. Tabiei and W. Zhang, "Composite laminate delamination simulation and experiment: A review of recent development," *Applied Mechanics Reviews*, vol. 70, no. 3, 2018.

[174] A. E122-09, "Standard practice for calculating sample size to estimate, with specified precision, the average for a characteristic of a lot or process," 2011.

[175] P. G. Perez, C. Bouvet, A. Chettah, F. Dau, L. Ballère, and P. Peres, "Effect of unstable crack growth on mode ii interlaminar fracture toughness of a thermoplastic peek composite," *Engineering Fracture Mechanics*, vol. 205, pp. 486–497, 2019.

[176] X. Li, S. Lu, and G. Lubineau, "Snap-back instability of double cantilever beam with bridging," *International Journal of Solids and Structures*, vol. 233, p. 111150, 2021.

[177] L. C. M. Barbosa, D. B. Bortoluzzi, and A. C. Ancelotti Jr, "Analysis of fracture toughness in mode ii and fractographic study of composites based on elium® 150 thermoplastic matrix," *Composites Part B: Engineering*, vol. 175, p. 107082, 2019.

[178] D. Purslow, "Fractography of fibre-reinforced thermoplastics, Part 3. Tensile, compressive and flexural failures," *Composites*, vol. 19, no. 5, pp. 358–366, 1988.

[179] L. Ye, A. Beehag, and K. Friedrich, "Mesostructural aspects of interlaminar fracture in thermoplastic composites: Is crystallinity a key?," *Composites science and technology*, vol. 53, no. 2, pp. 167–173, 1995.

[180] H. Wafai, G. Lubineau, A. Yudhanto, M. Mulle, W. Schijve, and N. Verghese, "Effects of the cooling rate on the shear behavior of continuous glass fiber/impact polypropylene composites (gf-ipp)," *Composites Part A: Applied Science and Manufacturing*, vol. 91, pp. 41–52, 2016.

[181] K. Friedrich, "Analysis of crack propagation in isotactic polypropylene with different morphology," in *Physik der Duroplaste und anderer Polymerer: Vorträge der Frühjahrstagung der Deutschen Physikalischen Gesellschaft Fachausschuß „Physik der Hochpolymeren "in Rothenburg o. T. vom 28. bis 31. März 1977*, pp. 103–112, Springer, 2007.

[182] J. R. Reeder, "3-d mixed mode delamination fracture criteria-an experimentalist's perspective," in *American Society for composites 21st annual technical conference*, 2006.

[183] P. P. Camanho, C. G. Davila, and M. De Moura, "Numerical simulation of mixed-mode progressive delamination in composite materials," *Journal of composite materials*, vol. 37, no. 16, pp. 1415–1438, 2003.

[184] E. S. Greenhalgh, *Characterisation of mixed-mode delamination growth in carbon-fibre composites*. PhD thesis, Imperial College London (University of London), 1998.

[185] A. Arteiro, C. Furtado, G. Catalanotti, P. Linde, and P. Camanho, "Thin-ply polymer composite materials: A review," *Composites Part A: Applied Science and Manufacturing*, vol. 132, p. 105777, 2020.

[186] G. Frossard, J. Cugnoni, T. Gmür, and J. Botsis, "Mode I interlaminar fracture of carbon epoxy laminates: Effects of ply thickness," *Composites Part A: Applied Science and Manufacturing*, vol. 91, pp. 1–8, 2016.

[187] J. Galos, "Thin-ply composite laminates: a review," *Composite Structures*, vol. 236, p. 111920, 2020.